UNIVERSITY OF LEEDS

MECHANISMS OF AMYLOID FIBRIL-MEDIATED TOXICITY

Kevin William Tipping

Submitted in accordance with the requirements for the degree of Doctor of Philosophy.

The University of Leeds

Astbury Centre for Structural Molecular Biology

September 2014

Intellectual Property and Publication Statements

The candidate confirms that the work submitted is his/her own, except where work which has formed part of jointly authored publications has been included. The contribution of the candidate and the other authors to this work has been explicitly indicated below. The candidate confirms that appropriate credit has been given within the thesis where reference has been made to the work of others.

The work in Chapter 2 contains data from a jointly authored paper which was published in 2014. Specifically, data presented in Figure 2.3.5 was performed and analysed by Dr Sophia Goodchild and is acknowledged as such in the figure legend. The candidate contributed to the work presented in (Goodchild, SC., Sheynis, T., Thompson, RT., Tipping, KW., Xue, WF., Ranson, NA., Beales, PA., Hewitt, EW. And Radford, SE. (2014) β2-microglobulin amyloid fibril-induced membrane disruption is enhanced by endosomal lipids and acidic pH, *PloS ONE. **9;**e104492*) *by characterising fibrils used in the study, in addition to contributing to the experimental design and editing of the manuscript. S.C. Goodchild performed and designed the experiments and wrote the original manuscript of the paper, T. Sheynis performed confocal microscopy analyses and R.T. Thompson performed cryo-electron microscopy. N.A. Ranson, P.A. Beales, E.W. Hewitt and S.E. Radford provided help with scientific discussions, data interpretation and manuscript preparation.*

Acknowledgements

First and foremost I would like to thank my Supervisors, Professor Sheena Radford and Dr Eric Hewitt, for affording me the freedom to experiment through a variety of different means in my attempts to answer a singular question. Your enthusiasm and ambition has opened my eyes to what it truly means to be a successful scientist.

There are many people without whom this project would not have worked: I would like to thank Dr Theo Karamanos, for assistance with NMR experiments, Toral Jakhria, for kindly sharing her cell-based Hsp70 data with me, Dr Matt Iadanza and Rebecca Thompson, for their attempts to structurally characterise oligomers using electron microscopy, Drs Jef Clark, Alex Boradavka, and Roman Tuma, for assistance with various aspects of FCS and MEM, and Dr James Ault and the whole mass spectrometry group, for helping and allowing me to book time and play with their instruments. Finally, I would like to thank Dr Sophie Goodchild and Dr Tania Sheynis whose work preceded that presented in this thesis (apart from Section 2.3.3, which was performed entirely by Sophie).

In addition to technical assistance, I would like to thank the whole Radford group (past and present) for the great environment they provide in the lab. A special thanks to Nasir Khan, for feeding me at least one seventh of the meals I've eaten during my PhD, and your hard work in making life as simple as possible for those of us carrying out research. Also, a special shout-out to Jan, Rachel, and the Beast, for tolerating me during caffeine-fuelled lapses into adolescent behaviour.

I would like to thank my family, in particular my parents, who have managed to provide a sense of realism by reminding me (in the case of my Dad – incessantly so) that some things are more important, such as spending time with them.

And lastly, but not leastly, thank you to my amazing wife, Kira, and the Magipones, who have been somewhat neglected during the writing of this thesis. Thank you for your patience, love, encouragement, and for believing in me. I owe you one big time!

Abstract

Amyloid diseases are a group of protein misfolding disorders characterised by the formation of highly ordered filamentous assemblies known as amyloid fibrils. Soluble aggregation intermediates whose formation precedes that of mature fibrils are commonly considered the major source of toxicity in amyloid diseases.

Oligomer toxicity has often led to mature amyloid fibrils being referred to as inert end products of aggregation. Recent evidence, however, has shown that fibrils themselves are capable of facilitating toxicity by a variety of mechanisms. One such protein, β_2-microglobulin (β_2m), has been shown to form amyloid fibrils that bind to liposome membranes causing deformations and disruption in a pH dependent manner.

In this thesis, the *in vitro* mechanisms of β_2m fibril-induced membrane disruption are explored to elucidate why reducing the pH from 7.4 to 6.4 leads to an enhancement in fibril membrane disruption. A combination of chemical kinetics, NMR and liposome dye-release assays show that at both pH values, membrane disruption is mediated through the shedding of soluble species induced upon diluting fibrils formed at low pH into either buffer. Fibril depolymerisation at pH 6.4 leads to the persistence of membrane-active non-native species, whereas depolymerisation at pH 7.4 is driven rapidly to membrane-inactive native monomer. Further analysis reveals that these non-native species are structurally disordered, spherical particles that display significant surface-exposed hydrophobicity.

The observed pH-dependent formation of oligomers shed during depolymerisation is likely to play an important role in mediating cellular effects upon incubation with fibrils. Consistent with this, chemical cross-linking of fibrils and co-incubating fibrils with Hsp70-1A prevents the depolymerisation of β_2m fibrils at both pH 7.4 and 6.4 *in vitro* and reduces metabolic defects associated with β_2m fibril depolymerisation. The results suggest that kinetically stabilising fibrils to prevent molecular shedding could be a means of helping to remedy amyloid-associated toxicity.

Table of Contents

Table of Figures

Table of Tables

Abbreviations

Aβ Amyloid β

AC Autocorrelation curve

AFM Atomic force microscopy

ANS 8-Anilinonaphthalene-1-sulphonate

AUC Analytical ultracentifugation

ApoE Apolipoprotein E

β_2m Beta-2-microglobulin

BMP Bismonoacylphosphate

C_f Fibril concentration

CryoEM Cryo-electron microscopy

CPY Carboxypeptidase Y

DMEM Dulbecco's Modified Eagles Medium

DNA Deoxyribonucleic acid

DRA Dialysis-related amyloidosis

DTT Dithiothreitol

EDTA Ethylenediaminetetraacetic acid

EGCG (-)-Epigallocatechin

ER Endoplasmic reticulum

ESI-IMS-MS Electrospray ion-mobility spectrometry mass spectrometry

FCCS Fluorescence cross correlation sprectroscopy

FCS Fluorescence correlation spectroscopy

FLD Fibril length distribution

FRET Forster resonance energy transfer

FO Fibrillar oligomer

GAG Glycosaminoglycan

GdmHCl Guanidine hydrochloride

hIAPP Human islet amyloid polypeptide

HMW High molecular weight

HSQC Heteronuclear single quantum correlation

HTT Huntingtin exon 1

Ig Immunoglobulin

LMW low molecular weight

LTP long-term potentiation

LUV large unilamellar vesicle

MEM maximum entropy method

MHC Major histocompatibility complex

MTT 3-(4,5-Dimethylthiazol-2yl)-2,5-diphenyltetrazolium Bromide

Neg-stain TEM Negative stain transmission electron microscopy

NMR Nuclear magnetic resonance

PAGE Polyacrylamide gel electrophoresis

PBS Phosphate buffered saline

PDB Protein data bank

PFO Pre-fibrillar oligomer

PM Plasma membrane

POPC 1-palmitoyl-2-oleoyl-sn-glycero-3-phosphocholine

POPE 1-palmitoyl-2-oleoyl-sn-glycero-3-phosphoethanolamine

PrP^{SC} Prion protein scrapie isoform

R_H Hydrodynamic radius

RNA Ribonucleic acid

SCA Single component analysis

SDS Sodium dodecyl sulphate

TTR Transthyretin

TCCD Two colour coincidence detection

TF Transcription factor

ThT Thioflavin T

UPR Unfolded protein response

V_H Hydrodynamic volume

Wt Wild-type

INTRODUCTION

1.1 Forethought

Amyloid diseases are an expanding class of disorders typically characterised by the formation of protein aggregates defined by their gain-of-toxic-function (1–4). The ubiquity of amyloid diseases are increasing as the onset of many are linked to ageing. With an ageing population worldwide, the prevalence of amyloid diseases is set to increase (5).

The relationship between amyloid and ageing is complex, although it is likely to be related to the down-regulation of proteostatic mechanisms commonly associated with ageing; as the proteostatic capacity decreases, the deposition of specific proteins into amyloid assemblies increases, which upon meeting a critical aggregate concentration threshold, leads to the manifestation of pathological features (6–8). Not all amyloid disorders are age-related however, familial variants associated with early-onset phenotypes often carry mutations within amyloidogenic polypeptide sequences that accelerate amyloid aggregation (9–13). Early-onset phenotypes can also be the result of mutations that render proteins responsible for processing and clearing amyloidogenic precursors significantly impaired in comparison with their wild-type (*wt*) counterparts (14–17). These features add weight to the amyloid aggregate toxic gain-of-function hypothesis in mediating disease, and hence has been the focus of intense research activity for more than two decades (18).

The ubiquity of amyloid diseases (see Table 1.1.1 for some well-known examples), with around 50 known disorders currently classified by amyloid deposition (19), and the common biochemical and biophysical signatures of amyloid aggregation, to which you shall be introduced, led to initial efforts to identify a unifying cytotoxic entity amongst many of these diseases (20, 21). Hitherto, it has become increasingly clear that a single pathological event does not underlie the complex mechanisms of cytotoxicity associated with amyloid diseases. For example, in Alzheimer's disease, perhaps the best known amyloid disease, a vast array of aggregates have been characterised *in vitro* and display varying degrees of toxicity *in vivo,* via highly diverse cellular mechanisms (22–25). The reality is that, *in vivo*, an ensemble of structures are just as likely to form than any individual species predominating, thus creating a complex network of pathological cascades which require intervention to

inhibit disease progression. Therefore, a paradigm shift in the approach to tackling and classifying amyloid diseases is required; instead of the development of therapeutic strategies focusing on pacifying a single cytotoxic entity, the array of amyloid structures, and other genetic abnormalities, that contribute to disease progression must be elucidated before effective therapies can be developed.

With this in mind, this thesis presents work towards our attempts to understand the complex mechanisms that underpin amyloid fibril-mediated toxicity by using the model protein β_2-microglobulin. Traditional theories have often cast amyloid fibrils as inert end-stage products of amyloid assembly, whose contribution towards toxicity is negligible (26–28). By using a range of biochemical, biophysical and cell biological assays, I hope this in-depth investigation, along with other recently published studies, will help to establish the role of amyloid fibrils in an array of processes critical to the multi-faceted nature of amyloid diseases.

Table 1.1.1 A selection of diseases associated with amyloid formation

Precursor protein	Disease
	Neurodegenerative diseases
α-synuclein	Parkinson's disease
Amyloid precursor protein (APP)	Alzheimer's disease
PolyQ-expanded huntingtin	Huntington's disease
Prion protein	Spongiform encephalopathies
Superoxide dismutase 1, TDP-43	Amyotrophic lateral sclerosis
Transthyretin mutants	Familial amyloid polyneuropathy
	Systemic amyloidosis
β_2m	Dialysis related amyloidosis
Immunoglobulin light chain	Amyloid light chain (AL) amyloidosis
Lysozyme	Lysozyme amyloidosis
wt Transthyretin	Senile systemic amyloidosis
	Localised amyloidosis
Islet Amyloid polypeptide	Type II diabetes mellitus
Insulin	Injection localised amyloidosis

1.2 Protein folding in the cell

Proteins are the chief mediators of the majority of cellular processes and are therefore of critical importance to understanding the fundamental principles of life. From an essential tool kit of 20 amino acids, a vast number of polypeptide sequences can be derived whose range of functions is diverse, including processes such as DNA replication, cargo transport, ATP synthesis, muscle contraction, light sensing, smell, digestion and so on. In order to carry out their encoded functions, the majority of proteins must obtain a native fold. It has long been known that the information encoded within a polypeptide sequence can be sufficient for the folding of a protein to its native functional state (29). However, the study of protein folding is perhaps the last paradigm of 20th century biology that remains to be fully chartered. Even in the age of computer assisted experimental design and analysis, correctly predicting the fold of an existing polypeptide sequence, or predicting the fold of a novel sequence, is not a trivial exercise. This is because polypeptide sequences have evolved to encode a vast array of different characteristics; folds, functions, lengths and dynamic behaviours. These impede our ability to spot trends within sequence motifs that determine not just three-dimensional structure but function (30). The ability to design *in silico* polypeptide sequences and fully recapitulate the predicted structure and function therefore remains a significant challenge. The serendipitous acquisition of mutations that lead to novel or altered functions *in vivo* occludes the composition of a generalised set of rules for *de novo* protein design (31, 32).

Even so, we have learnt much over the last 50 years about how proteins obtain their three dimensional structures. Principally, obtaining the native fold *in vitro* requires a fully synthesised polypeptide to traverse a downhill energy landscape to reach a low energy 'native conformation' (33) (Figure 1.2.1). This spontaneous folding activity is largely inaccessible to the majority of proteins within the cell however, and is exacerbated by the hugely crowded cellular environment (34). In response, the cell has developed a catalogue of proteins, known as molecular chaperones, whose predominant function is to promote the correct folding of polypeptide sequences. Wherever protein folding takes place, such as the endoplasmic reticulum (ER) or the cytosol, a wealth of cellular resources is dedicated to guiding a variety of client proteins to reach the functional, folded, native state.

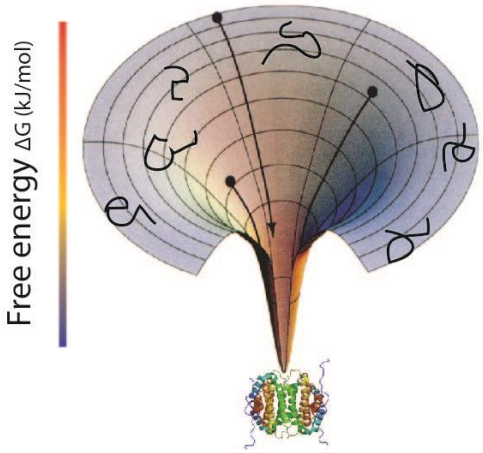

Figure 1.2.1 Free energy landscape depicting an idealised view of downhill protein folding. A fully synthesised, unfolded polypeptide chain (black lines) folds spontaneously to a low energy well that is the native state. Adapted from (33)

Obtaining a native state is not the only means of controlling protein activity in the cell. Other phenomena can equally affect protein structure and function in addition to post-translational misfolding. These processes are often critical for tuning protein activity and are therefore tightly coordinated throughout a protein's life cycle. One such regulatory process is time, as different proteins are required for distinct periods of a cell's life cycle. Some, such as collagen, exist for the entire lifespan of the cell. Others, such as HIF-1α, exist for minutes (35, 36). The regulated half-life of a protein is a necessary feature of a cell being able to tune its chemistry in response to the environment. Therefore, the existence of the functional native state must also be tightly regulated temporally. In addition, proteins undergo a library of different post-translational modifications which affect function, structural stability and turn-over of proteins (37). Some proteins also require assembly into higher order macromolecular machines for function and folding. Most, if not all, also undergo extensive modifications during ageing which, left unchecked, can have damaging consequences for the fold and function of a protein (38).

These limited examples begin to illustrate the inherent plasticity of proteins *in vivo* and the subsequent importance of cellular monitoring of protein folding throughout the lifetime of the cell. Given the unique features of individual proteins, it is perhaps surprising that damaging protein misfolding events do not take place more frequently than they do. In order to minimise the aberrant misfolding of proteins, or the accumulation of redundant or aged-damaged species, the cell has also developed a

myriad of protein quality control networks that ensure the misfolded protein burden is maintained at levels that are safe for the health of the entire proteome (39).

The turnover of proteins is not restricted to those that have aged or outlived their function. Processes of regulated turnover begin with monitoring of protein folding even before the full synthesis of a polypeptide has taken place. Up to 300 proteins have been characterised as participants in the process of translation, with many of these involved in controlling translation rates and correct folding of the nascent polypeptide chain during synthesis (40). Both of these processes are equally important in facilitating a protein to reach and maintain its native fold. Translation rates are tempered by the sequence of the polypeptide being synthesised and the corresponding mRNA codons used. The rate of translation is often slowed during the synthesis of hydrophobic stretches of amino acids. Slowing translation affords more time for chaperones to bind and mask aggregation prone sequences as they emerge from the ribosome (41). For other proteins, the rate of translation can be increased or decreased to ensure a greater percentage of folding of the nascent chain towards a native state (42, 43). This is especially true for the synthesis of enzymes, where translation rates can impact upon the efficiencies of down-stream catalytic processes (44).

The rate of translation of mRNA into individual polypeptides is therefore an important step for determining the folding outcome of a protein, but there are processes that affect the global translation network. Whole-scale control of protein translation is usually initiated through the induction of particular stress responses. These responses are designed to afford the cell additional time to redress proteostatic imbalance when a critical protein-misfolding threshold has been exceeded. Examples of these so called stress responses include the induction of translation inhibition through the unfolded protein response (UPR) or after acute heat shock (45, 46). In both, the general strategy of preventing the synthesis of new proteins enables the cell to concentrate resources towards redressing the initial seeding event of proteostatic imbalance. Only once the cell has overcome such stresses will translation be re-initiated. The induction of stress responses are therefore rapid and involve concerted activities of a large array of different proteins. For example, the UPR is initiated upon sensing of terminally misfolded secretory proteins within the lumen of the ER. Terminal misfolding of proteins in the ER can be sensed via a variety of different

mechanisms. Distinct, but integrated, signalling pathways sense ER protein misfolding and transduce signals to the cytosol via transmembrane sensors in order to shut down translation through phosphorylation of translation initiation regulatory factor eIF2α (47, 48). Shutting down standard 5'-cap dependent translation initiation is coupled to increased translation of UPR mRNAs such as the transcription factor (TF) ATF-4 (49, 50). ATF-4 and other UPR up-regulated TFs increase the expression of genes designed to alleviate ER stress. Only once the ER misfolded protein burden has recovered is the UPR 'switched off' and translation re-initiated. Translation is similarly affected upon acute heat shock which is most commonly associated with protein misfolding in the cytosol. Upon induction of the heat shock response, Hsp40 and Hsp70 chaperones, proteins that have evolved to assist protein-folding, are re-distributed from nascent chains emerging from ribosomes in order to catalyse the refolding of stress induced unfolded sequences (51). In both these cases, the reduction in translation prevents the production of aberrantly folded proteins which otherwise would lead to a catastrophic protein misfolding event.

These are only a few of the mechanisms that have evolved to keep the cell safe from the consequences of protein misfolding. Others include chaperone-mediated autophagy, lysosome-mediated degradation, ubiquitin-dependent proteasomal degradation of cytosolic proteins, retro-translocation of terminally misfolded proteins from the ER, co-translational ubiquitin tagging of proteins for degradation, juxtanuclear positioning of membrane-bound misfolded protein clusters, formation of insoluble cytosolic inclusions, and nuclear shuttling of proteins for degradation. Together, these form complex communicative networks that ensure the general health of the proteome is maintained (52–59) (Figure 1.2.2). These compartmentalized defence mechanisms can also involve signalling between different cells (60).

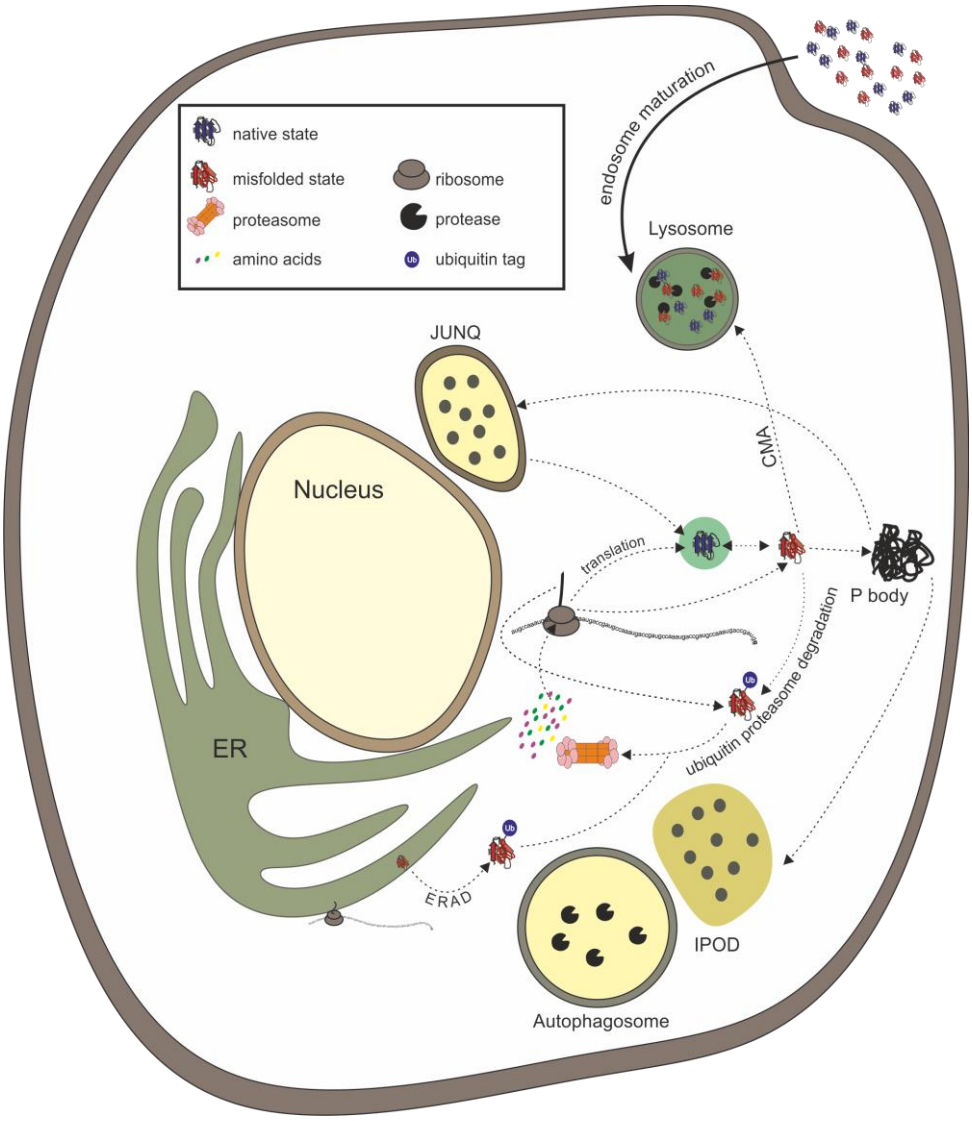

Figure 1.2.2 Integrated protein quality control mechanisms within the cell. The cell has developed a myriad of compartments and processes to alleviate protein misfolding. Terminally misfolded proteins can be degraded through the ubiquitin proteasome system, by forming cytosolic p body inclusions that sequester into IPOD for phagosomal degradation or chaperone –mediated autophagy in the lysosome (CMA). Proteins can also be ubiquitin-tagged for degradation during translation, or retro-translocated from the ER (ERAD) for proteasomal degradation. P bodies can also position themselves into juxtanuclear inclusions (JUNQ), where they can undergo chaperone-assisted refolding or be degraded.

The array of resources dedicated to maintaining specialised protein function in the cell is not only an indicator of the importance of obtaining (and maintaining) the native fold, but also of preventing misfolding events from accumulating. Genetic abnormalities that perturb the folding landscape of a single protein can manifest in significant metabolic defects, leading to disorders such as lysosomal storage diseases (61). Perhaps the most well-known loss-of-function protein misfolding disease is cystic fibrosis, where mutations within the CFTR chloride ion channel prevent

correct protein folding. Many of the clinical features of cystic fibrosis are the result of this single protein misfolding event (62). These diseases help illustrate the biological impact of incorrect protein folding.

In addition to loss-of-function protein misfolding disorders, there are also an expanding class of protein misfolding diseases that are more typically characterised by a gain-of-toxic function of misfolded protein aggregates. These diseases, known as amyloid, are unique in that disease progression is thought to be due to the aberrant activity of proteins that can adopt toxic conformations (1, 2, 4). Amyloid disorders are commonly associated with ageing due to the decline in protein homeostasis that allows the accumulation of disease-associated proteins and their subsequent 'misfolding' into tightly packed, and highly ordered macromolecular assemblies. The formation of these species can be thought of as taking place within a partitioned energy landscape not normally accessible within a healthy cellular environment (63) (Figure 1.2.3). The assembly of amyloid is driven by the formation of inter- as opposed to intra-molecular contacts that usually define protein folding. It is the formation of these species that is often associated with within the onset of amyloid disease, and not the loss of the native function of the misfolded protein, as is the case for the protein misfolding diseases discussed above.

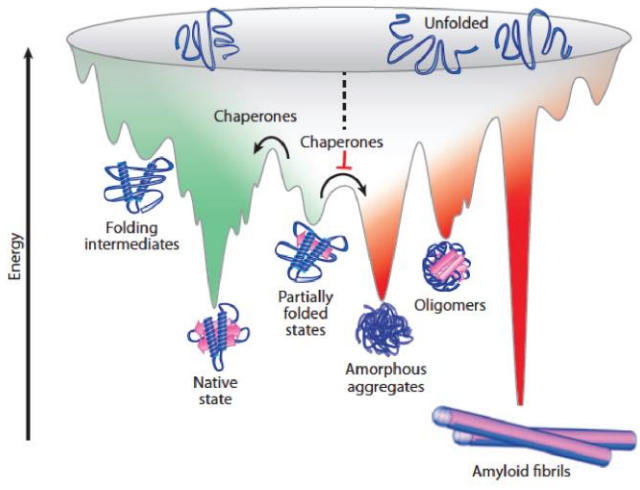

Figure 1.2.3 The alternative folding landscape of amyloidogenic aggregates. Amyloidogenic precursors can be partitioned within a separate energy landscape that is dominated by intermolecular contacts that drive amyloid formation. Proteins can transition to the amyloid landscape via a partially folded conformation that leads to the exposure of aggregation prone sequences. Molecular chaperones have evolved to prevent to the prolonged exposure of aggregation-prone sequences during protein folding to prevent amyloid formation taking place Adapted from (63).

1.3 Amyloid – A beginners guide

The term amyloid is actually a misnomer, originally coined due to the unusual capacity of tissue deposits to develop a blue colour upon binding to an iodine stain in the presence of sulphuric acid (64). This property was described over 150 years ago in the first documented cases of amyloid diseases, with the name giving reference to the starch-like behaviour of the deposits characteristic of the disease. It has henceforth been established that this starch-like behaviour of amyloid *in vivo* is due to the associated carbohydrates (glycosaminoglycans (GAGs)) that bind tightly to amyloid assemblies (3). Although it is now a well-known fact that deposits are overwhelmingly composed of protein, the term amyloid has remained very much in use (65).

1.3.1 Generic features of amyloid fibrils

All amyloid assemblies share a common set of characteristics. This is despite the large-scale sequence heterogeneity of amyloid precursors. The ability of a wide range of sequences to form amyloid has also raised intriguing questions as to whether the amyloid fold is theoretically accessible from almost any polypeptide sequence (4, 66, 67). These generic features are also used to ascertain whether a newly described aggregate is an amyloid or not. Chief among these properties are the long, unbranched filamentous structures seen upon observing amyloid fibrils using techniques such as transmission electron microscopy (EM) or atomic force microscopy (AFM) (Figure 1.3.1a). The core of the amyloid fibril is typically rich in β-sheet, whereby β-strands are arranged perpendicularly to the length of the fibril axis in a highly ordered fashion (Figure 1.3.1b). This arrangement, known as cross-β, is often diagnosed by the conserved X-ray fibre diffraction pattern observed for a large subset of fibril types (68). Two scattering arcs are usually seen, ~4.8Å meridonal reflections and ~10 Å equatorial reflections, which arise from the highly regular molecular spacings of intra-sheet β-strand packing and the inter-sheet distance of two individual units that typically associate to generate the final fibril architecture (68, 69) (Figure 1.3.1c). The core is frequently arranged in a parallel in-register array, whereby β-strands are bound tightly by neighbouring segments through side chain and backbone hydrogen bonds. Protruding side chains tend to inter-digitate between two sheets to form a self-complementing, dry interface (70, 71). This vast hydrogen bonding network is thought to be responsible for the

remarkable thermodynamic stability of amyloid fibrils, which make them looked upon favourably as materials within the nanotechnology industry (72–76).

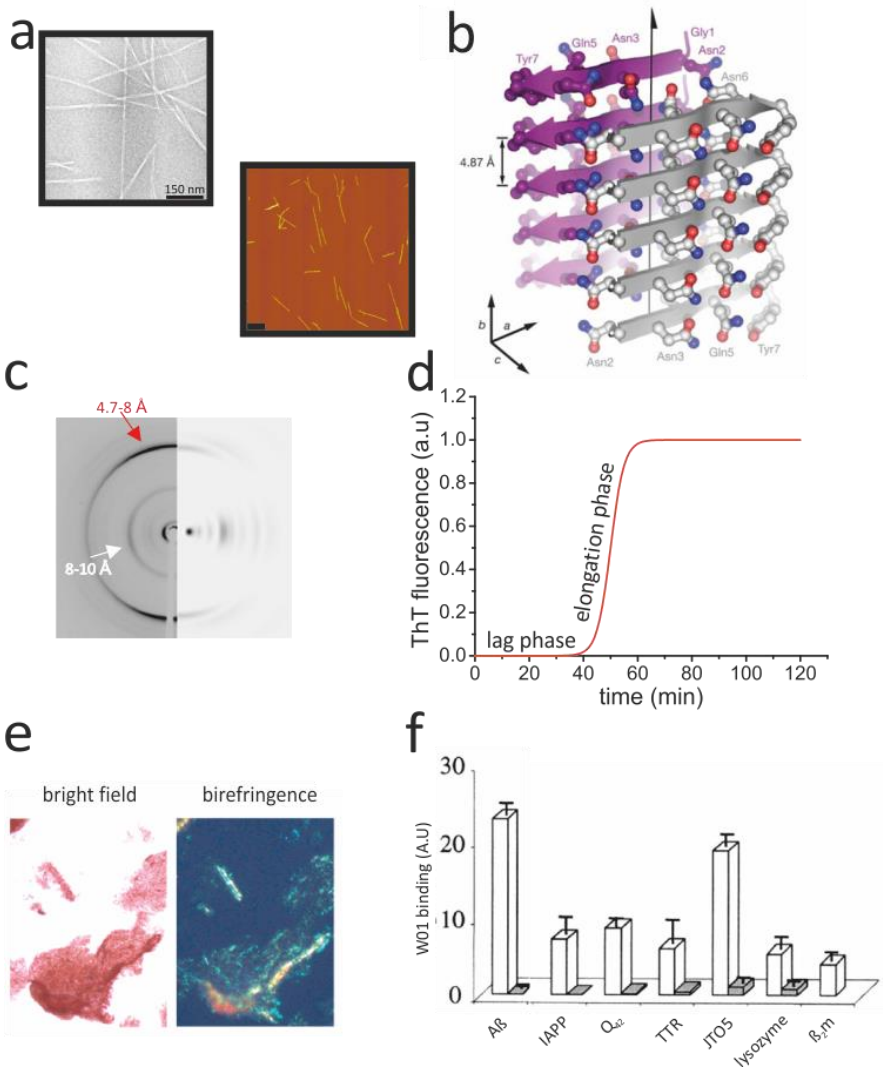

Figure 1.3.1 The generic morphological features of amyloid fibrils. Amyloid fibrils exhibit a classic, unbranched filamentous morphology as viewed by EM (a) and AFM (b, scale bar 1µm). (b) X-ray crystal structure of the steric zipper motif of an amyloid fibril core (70). (c) The X-ray fibril diffraction pattern of TTR(105-115) amyloid fibrils. Red and white arrows indicate the meridonal and equatorial scattering arcs respectively (69). (d) Amyloid fibrils formed after an initial lag phase bind and enhance the fluorescence of ThT. (e) Congo Red red/green birefringence exhibited under polarised light upon binding amyloid (82). (f) Amyloid fibrils composed of a range of precursor sequences bind the monoclonal W01 antibody. Monomer controls are in grey (80).

Amyloid fibrils also tend to display conserved tinctorial properties, including exhibiting red/green birefringence under polarised light upon binding the dye Congo Red (77, 78), binding and increasing the fluorescent properties of aromatic compounds such as Thioflavin T (79) and they usually contain a conformational epitope recognised by the monoclonal W01 antibody (80, 81) (Figure 1.3.1d-f).

Many of these properties as conserved between amyloid fibrils isolated *ex vivo* and those which are formed from the same precursor sequence *in vitro* (82). These similarities make amyloid fibrils formed *in vitro* an invaluable tool for elucidating fundamental processes that underlie amyloid formation and mechanisms of amyloid-associated toxicity.

1.3.2 Structural heterogeneity of amyloid fibrils at the macroscopic level

Although the above features are required for an aggregate to be defined as amyloid, as the number of known diseases in which insoluble assemblies form increases, so does the polymorphism within the resulting fibril architecture. The definition of amyloid has become looser in order to encompass fibril polymorphs that exhibit large degrees of heterogeneity from these classical amyloid properties (19, 83). These fibril types are often called 'amyloid-like' and display many of the pathological and biophysical features that one expects from a true amyloid, such as the presence of the cross-β spine (84–86). Amyloid-like fibrils include those formed as intracellular inclusions, or *in vitro*, as traditionally amyloid is a term associated with the extracellular deposition of insoluble, highly ordered aggregates (1, 71, 85).

Amyloid polymorphisms can be observed at the level of secondary structure and are not restricted to structural heterogeneity observed between assemblies composed of different precursors. Fibrils composed from the same precursor have been shown to exhibit entirely different packing arrangements within the fibril core. For example, in addition to the parallel in-register cross-β array described above, $A\beta_{40}$ fibrils have been shown to form out-of-register, parallel cross-β cores, or entirely antiparallel cross-β architecture (87–89). These large-scale polymorphisms have been most frequently described within amyloid fibrils composed of smaller peptides (70, 88, 90–92), but polymorphisms are still observed in fibrils formed from longer amyloidogenic precursor sequences (87, 93–97). Numerous factors, including ionic strength and pH influence the final fibril architecture. Therefore, assembly conditions can promote the formation of entirely distinct fibril morphologies which often, but not always, retain the classical hallmarks of amyloid (98–104). Polymorphisms have also been observed within fibril populations grown in identical solution conditions (87, 91).

Structural polymorphisms of amyloid fibrils formed from the same precursor can significantly influence the biophysical properties of amyloid assemblies (93, 94, 98, 105–112). The consequences of propagating a distinct polymorph can also manifest in unique biological activities. For one such example, two fibrillar polymorphs of α-synuclein, the causative agent of Parkinson's disease, possess entirely distinct seeding capacities *in vivo* (108). Seeding is the process by which amyloid fibrils catalyse the aggregation of soluble pools of the amyloidogenic precursor. Similarly, distinct α-synuclein 'strains' were shown to induce differing degrees of aggregation of not just endogenous α-synuclein, but also of pathological tau inclusions (108). Different fibrillar polymorphs found to predominate within the brains of Alzheimer's patients have also been suggested as a possible explanation for the difference in disease progression between sufferers (113). The difference in seeding capacity can have dramatic consequences for the propagation of 'infectious' amyloids, thus enhancing or repressing the progression of the disease. Whether the predominant fibril morphology propagating within patients of Alzheimer's disease can be used to serotype the severity of disease is now being investigated (113). Amyloid polymorphism may therefore be an important determinant of the aggressiveness of disease, which adds an additional layer of complexity towards treating amyloid disorders. The variety of pathological mechanisms associated with amyloid polymorphisms is further compounded by the newly emerging phenomenon of co-polymerisation, or cross-seeding, of distinct precursors and by the ability of familial variants of precursors to favour certain polymorphs over another (87, 90, 114–119).

Nevertheless, most amyloid and amyloid-like structures exhibit a parallel, in-register, cross-β core. The greatest degree of heterogeneity is present at the quaternary level, where proto-filaments can arrange into an array of higher-order assemblies. The ability to build atomic models of amyloid fibrils has only become a reality within the last decade. This is primarily due to advances in structural techniques like cryo-electron microscopy and solid-state NMR (120). These techniques have helped to reveal differences in parallel, antiparallel, and β-helical cross-β arrays that can arrange to generate structures that differ significantly, but still retain the majority of the classical amyloid characteristics as described above (87, 91, 92, 95, 97, 113, 120–125). A selection of amyloid fibril atomic models are shown in Figure 1.3.2.

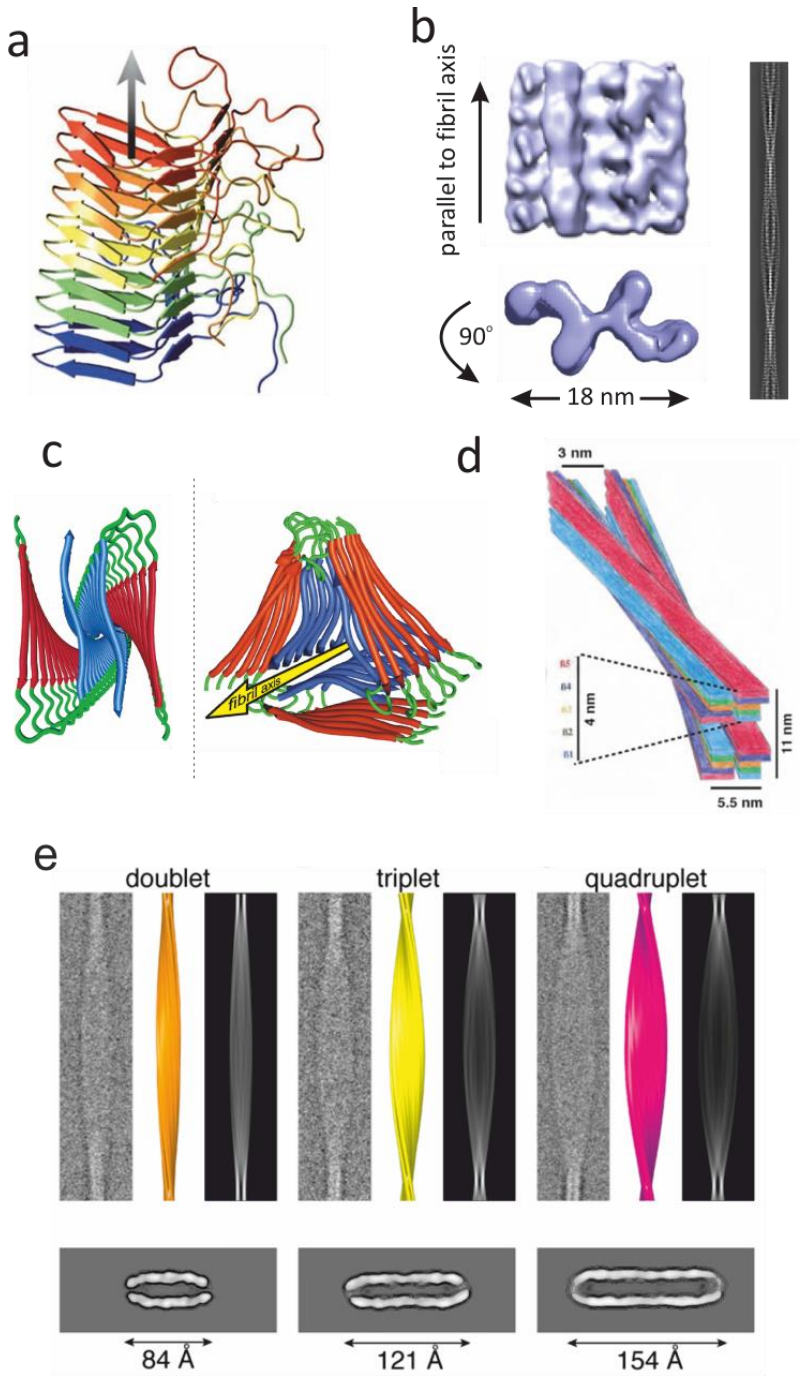

Figure 1.3.2 The structural polymorphisms within amyloid fibrils. (a) The β-solenoid arrangement of the Het-S amyloid-like fibril core solved by solid-state NMR (121). (b) Cryo-EM-derived electron density map of *wt*-β_2m fibrils formed at pH 2.0 (92). The fibril is composed of 6 protofilaments arranged in two banana-like arrays as seen from the top-down view. (c) Structural polymorphisms of $A\beta_{1\text{-}40}$ fibrils shown with fibres containing two-fold or three-fold symmetry (95, 97). Models were derived using ss-NMR. (d) Model of the α-synuclein amyloid fibril derived from ss-NMR and HDX-NMR (125). Each tricoloured filament is composed of stacked α-synuclein monomers arranged in a parallel in-register array. (e) Polymorphism of TTR (105-115) peptide-derived amyloid fibrils seen to propagate in identical solution conditions. Below shows cross-sectional view of the fibril cores (91)

1.3.3 Exploiting the cross-β fold in nature – functional amyloid

While the formation of amyloid is most often associated with disease, there has been a significant increase in the discovery of 'functional' amyloids. Functional amyloids are normally soluble proteins that adopt an alternative conformation in order to exhibit altered function. Functional amyloids were first described in yeast, and are perhaps more commonly known as prions. The conversion of soluble proteins into insoluble and inheritable amyloid-like fibres is an established epigenetic mechanism of phenotypic inheritance though the adoption of an altered protein conformation (126). The cytoplasmic inheritance of amyloid-like aggregated prions in yeast normally provides a selective advantage for the cells in which they are propagated (127).

Yeast prions contain a prion-determining domain that is dispensable for the function of the 'soluble' domain. The typical physiological function of the non-prion-like domains vary and include regulatory control of transcription or translation of particular subsets of genes. For example, the yeast prion Ure2p expressed in *Saccharomyces cerevisiae*, is a transcriptional repressor of *Gln3*, a protein involved in nitrogen catabolism. When nitrogen sources are rich soluble Ure2p suppresses *Gln3* transcription (128). Under conditions where nitrogen sources becoming limiting, however, Ure2p forms amyloid-like fibrils, thus preventing the transcriptional repression of *Gln3* to allow the host to exploit alternative nitrogen sources. In a second well-known example in yeast, the formation of amyloid-like fibrils from Sup35 takes place in particular strains of *S.cerevisiae*. Sup35 sequestered into insoluble amyloid-like assemblies reduces the efficiency of global translation termination. Reducing the efficiency of translation termination promotes phenotypic diversity by allowing the expression of previously untapped biological code (129, 130). Although the suggestion these mechanisms of epigenetic inheritance were once a laboratory artefact, more recent examples have determined the existence of epigenetic prions in a variety of wild yeast strains. The formation of prions confer selective advantages within a wide range of environmental conditions (131–133). The rapid conversion of soluble proteins into prion-like aggregates and back can be a fluid process, allowing the yeast to optimise its proteome in response to environmental triggers. In many ways inheritance and persistence of a prionogenic trait is a mechanism of adaptive memory (134) (Figure 1.3.3).

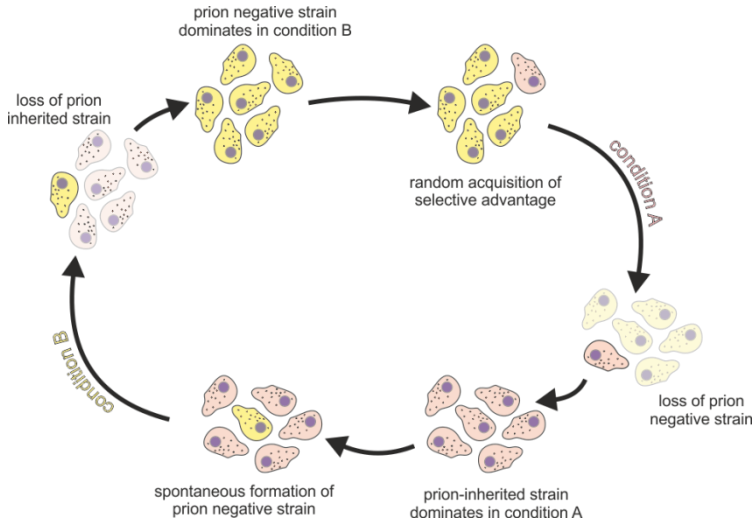

Figure 1.3.3 Prion-based epigenetic inheritance of phenotypic traits. Starting from the top left, yeast cells lacking the inherited prion state are favoured under condition B. Spontaneous processes confer a selective advantage upon prion formation. The prion strain is especially favoured under condition A, thus prion inherited cells dominate. The metastability of the prion state means a small pool will convert back to the prion negative, which upon changing back to condition B is re-favoured, thus ensuring the yeast thrives under both conditions. Inspired from (134).

In addition to yeast prions, several high profile examples of functional amyloid in more complex eukaryotes are beginning to emerge. In mammals, peptidic hormones have been found to be stored in high concentrations as amyloid fibrils within secretory granules of the endocrine system (135). Mammalian amyloid-like fibrils composed of RNA and RNA-binding proteins were recently discovered *in vivo* localised within cell nuclei (135–138). The sequestration of such biological molecules into highly dynamic heterogeneous assemblies is thought to provide a mechanism for the control of gene expression in response to environmental changes. Sequestering these protein:RNA complexes into amyloid assemblies provides a means of compartmentalisation without the presence of a lipid membrane, thus allowing for complex dissolution to take place rapidly in order to effect an immediate biological response. Amyloid fibrils are not the only type of aggregate deemed to be a functional amyloid. In *Drosophila melanogaster* amyloid-like oligomers composed from the cytoplasmic polyadenylation-element binding protein Orb2 have been implicated in the persistence and maintenance of long term memory (139, 140). These are just a selection of functional amyloids that continue to be discovered and classified. Additional examples from an array of organisms can be found in the following references (141–145).

1.3.4 Formation of disease-associated amyloidogenic species

The previous sections have described the generic and heterogeneous features of pathogenic amyloid fibrils and also the emerging concept of functional amyloid, but how does amyloid form? The majority of amyloidogenic proteins display nucleation-dependent growth kinetics *in vitro* (146–149), whereby a lag phase - a dynamic equilibrium of soluble oligomeric species formed from a partially or fully unstructured monomeric conformation - precedes an exponential growth phase, where monomers and oligomers are rapidly consumed via a mechanism of templated elongation at the nucleating particle ends (Figure 1.3.4a). This primary nucleation process can be readily monitored through ThT fluorescence. The lag phase of amyloid fibril assembly can be bypassed by the addition of preformed seeds, or fibrils (Figure 1.3.4a – black dashed line). Exhibiting a capacity to seed is another defining characteristic of an amyloid. The nucleating particles, such as fibrils, can multiply through secondary nucleation processes to further increase the rate of elongation (99, 150, 151). The most common secondary nucleation pathway is through fibril fragmentation, where additional fibril ends are generated to increase the elongation rate via the more rapid consumption of fibril subunits (Figure 1.3.4b). In a conventional ThT fluorescence experiment, the increased contribution of secondary nucleation pathways towards amyloid formation manifests itself by a steeper transition from the lag to the stationary phase (Figure 1.3.4b). Additional mechanisms of secondary nucleation will be discussed in greater detail later (152).

This overview of how amyloid formation proceeds is the most simplistic and generic mechanism for describing the aggregation of many amyloidogenic precursors. There are, however, considerable differences within aggregation landscapes, such as what may be the rate-limiting step of amyloid formation (146, 153, 154). This can either be the formation of an energetically unfavourable nucleating particle, the conformational conversion of an existing oligomer, or even the dissociation of stable native complexes to release the aggregation-prone precursor in a process known as downhill polymerisation (146, 153, 154). Each parameter of the aggregation kinetic profile, such as the length of the lag phase, the rate of elongation and the final fibril yield, are highly dependent on the precursor sequence as well as the solution conditions used to promote aggregation *in vitro* (99, 155, 156).

Much effort has been afforded to decipher the mechanisms of amyloid formation and to elucidate the structural properties of soluble species that form within the lag phase (Figure 1.3.4a). Reasons for this are two-fold; firstly, understanding the initial events that promote amyloid formation would mean that the fundamental processes underlying aggregation can be targeted for therapeutic intervention, and secondly, soluble species that form during the lag phase of amyloid fibril formation, not the aggregation end-stage products, are purported to be the primary source of cytotoxicity in a wide range of amyloid disorders (see next Section). In addition, especially for proteins with defined native structures, the fundamental processes that drive the conformational conversion of a metastable, soluble, natively folded protein into a partially folded, amyloid-competent state is a question of fundamental intrigue within the amyloid field that remains to be fully understood (156–162).

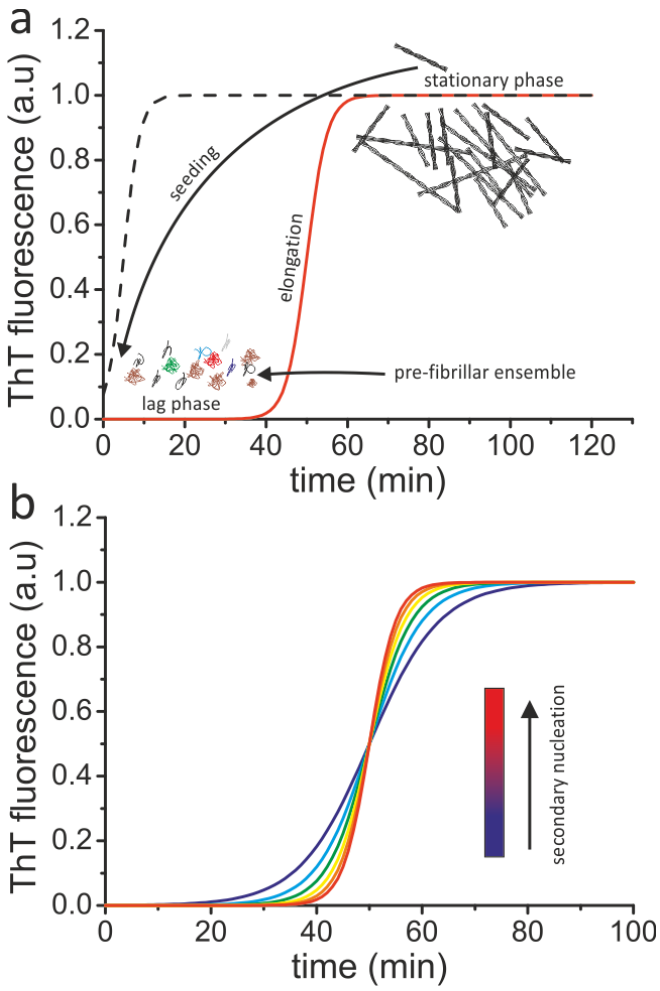

Figure 1.3.4 The amyloid aggregation cascade. (a) Typical ThT fluorescence kinetics observed during *de novo* (red line) and seeded (black dashed line) fibril formation. (b) Secondary nucleation mechanisms increase the rate of elongation.

1.3.5 Amyloid-β oligomer toxicity: a case study

As just mentioned the species purported to be the most cytotoxic are those that form during the lag phase of amyloid assembly. Initially, the general consensus was that oligomers derived from amyloidogenic precursors display conserved structural characteristics, indicating a potential generic toxicity mechanism. This was, in part, due to two pioneering studies performed between 2002-2003 which showed that sequences derived from proteins known to be involved in amyloid disease, along with several that were not, were able to form species that caused toxicity in cultured cells (20, 21). Between them, these studies indicated that soluble species are typically spherical in origin, ranging from 10 – 70 nm in size, and display a conserved A11 antibody binding epitope. Importantly, these species were significantly more cytotoxic than their fibrillar counterparts, and toxicity could be prevented by pre-incubating oligomers with the A11 antibody prior to addition to cells (21). These studies paved the way for the hypotheses of amyloid toxicity that largely persists today; oligomers are toxic, while fibrils are essentially inert.

Subsequently, it has become obvious that whole arrays of soluble species are capable of forming within the lag phase, most of which display varying degrees of toxicity (Figure 1.3.5). These species can be broadly characterized as pre-fibrillar or fibrillar, which is a reflection on their gross morphology. In short, pre-fibrillar oligomers (PFO) tend to display the A11-binding epitope, while fibrillar oligomers (FO) bind an OC antibody (163). The OC antibody also recognizes the mature amyloid fibril, thus suggesting FOs may be structurally reminiscent of the mature amyloid fibril. Within each class of oligomer, however, there exists a high degree of structural heterogeneity, even for oligomers composed from the same precursor sequence.

The best examples of oligomer heterogeneity arising from a single precursor come from investigations performed on Aβ peptides. This is largely due to the volume of research performed on these sequences due to their association with Alzheimer's disease. Within the lag phase of Aβ amyloid assembly, species ranging from dimers to Alzheimer's Derived Diffusible Ligands (ADDLs – 24mers) have been reported to form and cause toxicity when applied ectopically to cellular models of disease (23, 164, 165). In between, the array of different species that have been classified include trimers, 5-6mers, low number oligomers (LNOs), globulomers (12mers),

amylospheroids (APSDs), Aβ*56 oligomers, annular protofibrils, $A\beta_{40:42}$ mixed oligos and transglutaminase 2-induced oligomers (21, 23, 166–174). Interestingly, all of these oligomer preparations have been shown to inhibit long-term potentiation (LTP) in hippocampal brain slices, a process thought to mediate the decline in cognitive function in Alzheimer's patients. In addition, all of the species (apart from APSDs) have been shown to bind with varying degrees of affinity the A11 antibody and are predominantly spherical in character. This is where the similarities between distinct species end, as the different species contain varying degrees of unstructured and/or parallel or anti-parallel β-sheet content, as well as being either on or off-pathway towards mature amyloid fibril formation (25, 175). The formation of each species *in vitro* also generates a range of 1) stoichiometries, especially for larger aggregates (e.g. granular protofibrils), and 2) conformations for smaller ones (for example, dimers). The dynamism, range of stoichiometries and transient nature of oligomers has (for the most part) precluded their atomic-level characterization.

Although the toxic effects of oligomers are undeniable, with several having been isolated from the brain tissue of Alzheimer's patients (173, 176, 177), the sheer variety of species that form within the aggregation landscape make targeting oligomeric species as a therapeutic strategy in any amyloid disorder highly challenging. This is further complicated by the ability of species to readily interconvert between different structures and the potential co-existence of different species *in vivo* (Figure 1.3.5) (25). The multiple Aβ-derived peptide fragments that are known to co-aggregate with full length $A\beta_{40-42}$ also significantly increases oligomer heterogeneity (153, 167, 178). In addition, as mentioned previously, there is another class of oligomers that have also been shown to induce cellular defects. These oligomers, known as FOs, share a greater degree of structural homology to mature amyloid fibrils. The structural similarities of FOs and fibrils, such as the appearance of cross-β architecture, suggests FOs may form at later stages of the aggregation landscape (24, 179).

Despite this section detailing Aβ-derived oligomers, heterogeneity is observed within all amyloidogenic cascades, including α-synuclein, the causative agent in Parkinson's Disease (180–187). Oligomers composed of α-synuclein are also dynamic. A recent study showed that oligomers formed of α-synuclein were able to

interconvert between two structurally distinct types (188). The formation of a more tightly-packed, protease resistant oligomer led to an increase in the generation of reactive oxygen species in neurons – a key feature of Parkinson's pathology – while less compact oligomers were relatively innocuous (189). Similar differences are seen for oligomers composed of Hyp-FN, a yeast protein, which can form two structurally similar, but distinct, aggregate pools. Conversely to what was found for α-synuclein, Hyp-FN oligomers that have a higher degree of structural flexibility and enhanced surface hydrophobicity were more cytotoxic than their rigid counterparts (190).

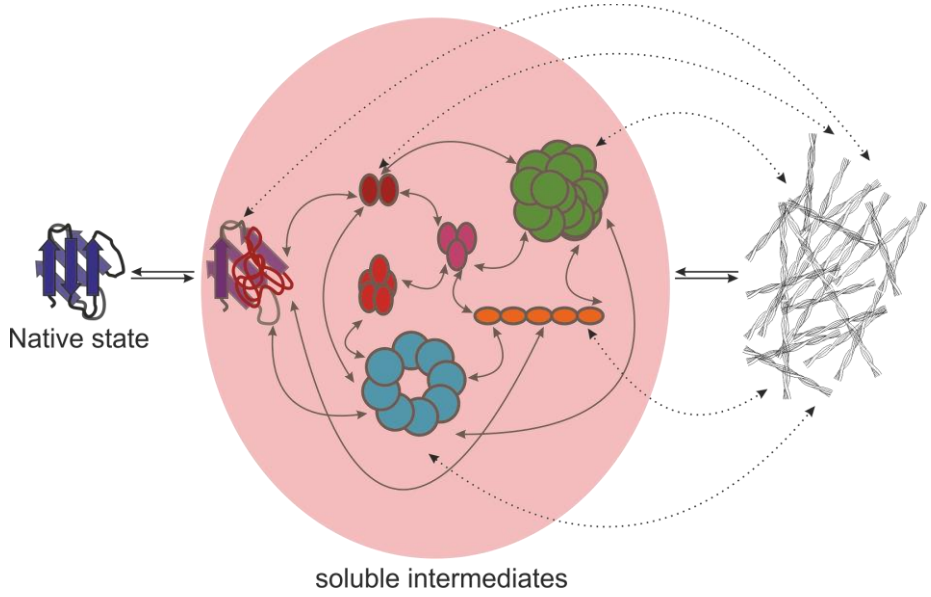

Figure 1.3.5 Conformational and stoichiometric plasticity of soluble intermediates of amyloid fibril assembly.. An array of species have been isolated *in vitro*, which may be on- or off-pathway to amyloid fibril formation. Different coloured oligomers represent altered sub-unit conformations as well as heterogeneous stoichiometries. Each species can induce toxicity via independent mechanisms, while several may co-exist at any one time. Fibrils may also act as reservoirs of soluble intermediates *in vivo* (dashed lines).

1.3.6 Mechanisms of toxicity of soluble amyloidogenic species

In general there are two main mechanisms of amyloid-mediated toxicity. The first, which has been primarily linked to amyloid deposited extracellularly, is through membrane disruption (191–193). The ability of amyloid to disrupt membranes has been a consistent theme irrespective of precursor identity. Moreover, amyloid-membrane interactions have been well documented both *in vitro* and in cellular and animal models of amyloid diseases (170, 184, 194–197). Despite the conserved affinity of amyloid for membranes, the mechanisms that lead to membrane disruption are quite diverse (Figure 1.3.7). Pore-forming oligomers have been

identified for a range of different amyloids (198). Oligomeric pores that pre-form in solution and embed within the lipid bilayer cause *in vitro* membrane disruption and/or calcium influx at the plasma membrane (Figure 1.3.7$_1$) (190, 199, 200). For other amyloidogenic proteins, such as hIAPP and α-synuclein, unstructured, hydrophobic monomers embed within the lipid bilayer where amyloid formation proceeds (Figure 1.3.7$_{2\text{-}3}$) (201–203). Embedding within the lipid bilayer can lead to a conformational conversion of the precursor protein into an amyloid-competent state. The growth of amyloid aggregates at the membrane surface damages membrane integrity, leading to disruption (201, 204). Similar nucleation events at the membrane surface have been shown to generate membrane-active pores, as opposed to fibrils, of hIAPP (196, 205). The formation of pores within the membrane, as opposed to pre-formation in solution, has been proposed to induce a greater degree of membrane disruption (173). Recent X-ray crystallographic studies have elucidated the structure of a potentially pore-forming oligomer composed of a fragment of the amyloidogenic αβ-crystallin (Figure 1.3.6). The oligomer exhibited many of the properties of other oligomeric species, including binding to the A11 antibody and causing toxicity in cell models. The crystallographic structure revealed the oligomer to be formed from 6 antiparallel β-strands (known as cylindrin), offering intriguing insights into how pore-forming oligomers may induce membrane disruption (206).

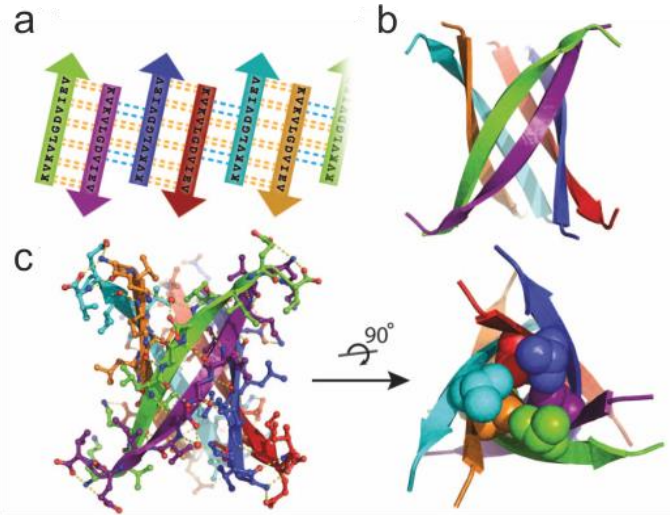

Figure 1.3.6 Atomic resolution structure of a toxic amyloidogenic oligomer. (a) Rolled out schematic representation of 'cylindrin' structure, showing β-strand orientation and main chain and salt-bridge mediated hydrogen bonds between strands (yellow and blue dashed lines). (b) Paired strands form anti-parallel dimers that orientate about a three-fold axis of symmetry within the cylindrin structure. (c) Side chain positioning within the cylindrin structure with H bonds shown in yellow. Taken from (206).

The cylindrin structure is only applicable to oligomers of sufficiently low order (for example, hexamers vs. 20-30mers) that are rich in β-sheet secondary structure. However, as many oligomeric species are composed of highly unstructured material (190). Nevertheless, unstructured oligomers still induce membrane disruption. Several mechanisms have been proposed as to how this may be facilitated. As unstructured oligomers can exhibit high degrees of surface exposed hydrophobicity, it is more entropically favourable for these types of species to embed within the hydrophobic bilayer (Figure $1.3.7_4$). Embedding of a large, bulky protein oligomer is proposed to cause membrane thinning, which can cause membranes to become leaky (207–210). Membrane leakage has also been proposed to be mediated *in vivo* via receptor-mediated mechanisms. Oligomers have been shown to bind to cell surface receptors as opposed to directly embedding within the bilayer. Recent experiments have proposed that PrP acts as a cell-surface receptor for aggregates of Aβ, potentially mediated through copper binding (211–213). Similar receptor-mediated mammalian cell surface interactions have also been proposed for non-pathological, but toxic, amyloid assemblies composed from the yeast prion Sup35 (214).

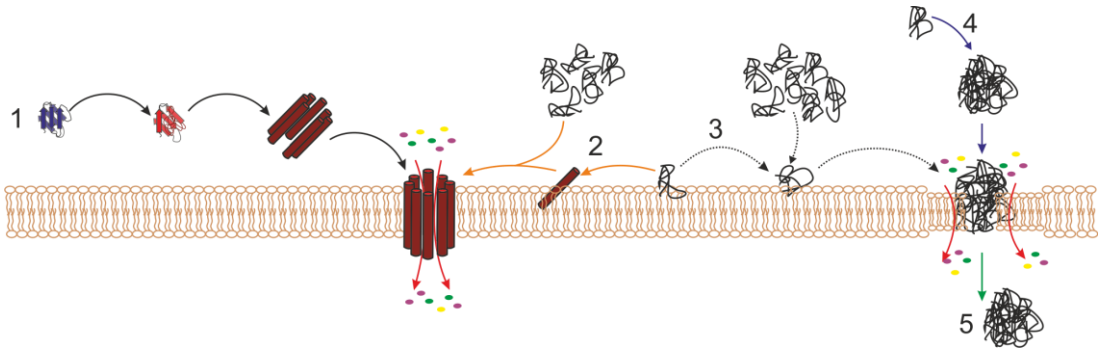

Figure 1.3.7 Mechanisms of amyloid-mediated membrane disruption. (1) Oligomeric pores can form due to partial denaturation of the native state of an amyloidogenic precursor (blue to red). (2) Partially structured or intrinsically disordered proteins can undergo conformational conversion upon embedding within the bilayer to form pores. (3) IDPs and unstructured monomers that interact with the bilayer can also seed the formation of non-pore like aggregates, leading to membrane thinning and leakage. (4) Non-pore aggregates can also form in solution prior to embedding within the bilayer. (5) Finally, aggregates can also traverse the membrane, enabling seeding and propagation of the amyloid.

Although membrane interactions have been extensively documented *in vitro* and in cells, *in vitro* membrane disruption does not always correlate with cytotoxicity (197). This is not surprising when considering the long incubation times over which amyloid diseases emerge. Sometimes symptoms of disease can take decades to manifest, which would not be the case if cellular membrane integrity were so easily

compromised. This is not meant to downlay the importance of amyloid-lipid interactions in disease, but just to suggest that the cellular effects may be more subtle than those observed *in vitro* using liposomes (197). The majority of *in vitro* studies are performed at protein concentrations that would typically exceed those found *in vivo*, and as aggregation of amyloid is normally a concentration dependent process (146, 148, 215), the concentration of toxic oligomers are likely to be much higher *in vitro*. Nevertheless, the formation of ionic pores and oligomer-membrane interactions has been documented at physiologically relevant concentrations (25, 213). Indeed, apart from the consequences outlined above, amyloid-lipid interactions must take place *in vivo* in order for the prion-like propagation of infectious amyloid particles (Figure $1.3.7_5$). For a series of different amyloid-like aggregates, including tau, α-synuclein and SOD1, infectious particles are able to transmit from the endocytic pathway to the cytosol, where they can seed new amyloid formation (98, 216–218). This must take place through the disruption of cellular membranes without any immediate consequences for the viability of cells (108, 188, 216, 218, 219). Evidence to support endosomal membrane disruption is supported by the release of cathepsins into the cytosol upon incubation with Aβ aggregates (220).

The second mechanism of amyloid toxicity is generally mediated via cytosolic inclusions through the disruption of cellular proteostasis (Figure 1.3.8). Large intracellular aggregates have been shown to co-aggregate with various cellular factors that lead to a loss-of-function of the co-aggregated protein. Which cellular proteins interact within inclusions appears to be functionally indiscriminate, with various cellular pathways affected as a result (221). An enrichment of proteins involved in mechanisms of proteostasis are commonly found enriched with inclusions, however. These can include molecular chaperones and factors critical for ubiquitin-mediated proteasomal degradation. This makes sense, as cytosolic inclusions are often enriched in ubiquitin, but their increased stability upon aggregation means they are not effectively cleared (222–224). What's more, sequestration of cellular factors by cytosolic inclusions does not always manifest in obvious metabolic defects until secondary stresses appear (225). In a study performed in yeast, cytosolic huntingtin exon 1 (HTT) inclusions were found enriched with the molecular chaperone Sis1p. Toxicity was not observed until a secondary, non-amyloidogenic inclusion of carboxypeptidase Y (CPY) was formed.

In the absence of HTT inclusions, CPY aggregates were degraded quickly, but competition for cellular resources upon HTT inclusion formation prevented clearance of CPY and led to cellular toxicity. Toxicity could be reversed upon over-expression of Sis1p, which led to the clearance of CPY aggregates, but not HTT aggregates. This chaperone competition has also been shown to impede clathrin-mediated endocytosis through the sequestration of intracellular Hsc70. Endocytic trafficking defects were observed in the presence of a variety of different cytosolic inclusions, including those of ataxin-3, SOD1 and HTT (226). Chaperone competition as a mechanism of amyloid toxicity could well be applicable to all amyloid diseases. It can also explain why so many amyloid diseases are age-related; as mechanisms of proteostasis decline, depleted chaperone pools are overwhelmed by increased aggregate deposition, reducing the clearance of misfolded, aged and non-functional proteins (6, 7). The reduced clearance of proteins may then induce a range of cellular defects.

The disruption of endocytic trafficking (as outlined above (226)) is especially pertinent for neurodegenerative amyloid disorders. The correct trafficking of signalling molecules is fundamental to the maintenance of communicative neuronal networks. The disruption of these processes is likely to be a key contributor to the onset of symptoms. Similar trafficking defects have been observed in models of Alzheimer's and Parkinson's diseases. Aggregates of Aβ were shown to perturb the function of PICALM, a scaffold protein required for the correct assembly of clathrin-coated vesicles (16, 227). In yeast and *C.elegans* models of Parkinson's disease, α-synuclein cytosolic inclusion formation induced a range of lipid-associated defects (228, 229). In both instances, correcting trafficking defects using small molecules was able to ablate amyloid toxicity in yeast and in Parkinson's disease patient-

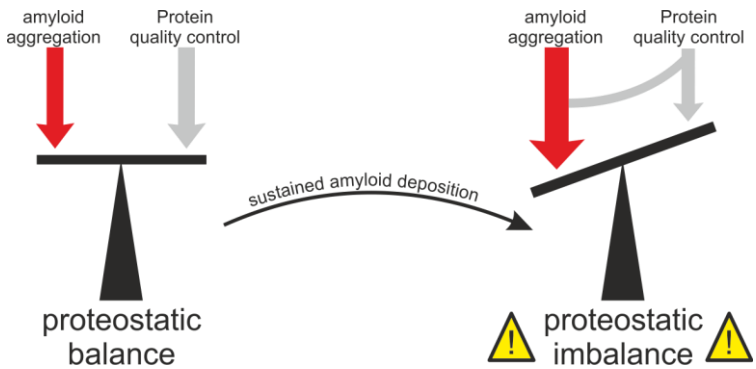

Figure 1.3.8 Proteostatic imbalance as a mechanism of amyloid-induced cytotoxicity.

derived induced pluripotent stem cells (230–232).

Disruption of cellular homeostasis is not only restricted to the sequestration of cytosolic chaperones. Over-expression of aggregation-pone PrP^{SC} in the ER attenuates translation through activation of UPR in mice. Restoring translation by inhibiting phosphorylation of eIF2α delays the onset of PrP^{SC}-induced cell death, without reducing PrP^{SC} aggregation (233). PrP^{SC} aggregates are proposed to mediate toxicity by preventing the synthesis of critical cellular proteins to replace those that have been turned over (233). Translation attenuation as a mechanism of amyloid toxicity has also been observed for other aggregates (234, 235). Irrespective of whether mediated by translation attenuation or chaperone competition, amyloid toxicity in both of these instances is mediated through the disruption of critical cellular pathways leading to a loss in concentration of functional proteins.

1.3.7 Amyloid fibrils – inert end products of aggregation?

The cytosolic inclusions mentioned in Section 1.3.6 are often insoluble in nature and can display morphological features similar to those observed in amyloid fibrils. This observation raises questions regarding whether amyloid fibrils are truly inert (28), or whether they contribute towards toxicity via mechanisms such as chaperone competition. Several amyloid fibrils have been shown to interact with a range of molecular chaperones *in vitro* (221, 236–239). For example, the interaction of Aβ amyloid fibrils with ATP-independent chaperones has been shown to reduce the rate at which fibril subunits exchange with soluble species (237, 238). The reduced rate of subunit exchange upon chaperone binding illustrates the functional relevance of amyloid fibril:chaperone interactions. Therefore, amyloid fibrils deposited extracellularly, as well as intracellular inclusions such as those described above, may mediate elements of chaperone competition-based toxicity through the sequestration and inhibition of chaperone function.

Can amyloid fibrils illicit toxicity via other mechanisms? As mentioned above, amyloid fibrils exhibit dynamic behaviour post-formation by subunit exchange with material that remains soluble under fibril growth conditions. Can the extent to which soluble species exchange with fibrils be modulated in order to increase the concentration of potentially membrane-active soluble species in solution (Figure $1.3.9_c$)? For functional amyloid, the formation of (some) amyloid provides a means

of membrane-free compartmentalization to suppress protein function under certain conditions. The dissolution of these amyloid assemblies upon encountering specific environmental triggers allows resolubilised protein to mediate a rapid biological response. (136–138). Similarly, amyloid fibrils composed of peptidic hormones dissolute into functional, soluble units upon encountering different physiological conditions once trafficked and released into the extracellular environment (135, 240). There are several more recent examples describing the role of dynamic amyloid formation, including controlling the ability of yeast to acquire facultative multi-cellularity, and higher order assembly of metabolic enzymes into filamentous assemblies in response to pH induced starvation (133, 241). In the latter, assembly into insoluble filaments inactivates the enzymes to avoid excessive consumption of cellular resources when nutrient supplies are deficient.

As mentioned, the dynamic nature of pathological amyloid fibrils is an established fact. A study in 2005 was the first to document such activity in fibrils assembled from an SH3 domain. Using NMR and hydrogen exchange mass spectrometry, Carulla et al revealed that exchange within the fibril was dominated by a mechanism of dissociation and re-association of soluble species in solution at an exchange rate of $1x10^{-4}.s^{-1}$ (242). Similar observations were subsequently made for fibrils composed of Aβ and α-synuclein, where dissociating species for the latter were cytotoxic oligomers (188, 243). Although the reported exchange rates are relatively slow (complete exchange of subunits over a time scale of weeks), exchange of soluble species was only investigated under the conditions employed for fibril growth. The exchange of species may be accelerated by subtle changes in solution conditions, a situation that is likely to be reflective *in vivo*, as extracellular amyloid fibrils can be routinely trafficked to environments that are distinct from those in which they form (188, 216–218, 220, 244–246).

In addition to amyloid fibrils acting as reservoirs for cytotoxic oligomers (Figure 1.3.9), the fibril surface has been shown to be an important driving force in the propagation of cytotoxic species (Figure 1.3.9d). Aβ amyloid fibrils were recently shown to increase the pool of soluble intermediates when incubated in the lag phase of amyloid fibril formation, through a mechanism of surface-induced conformational conversion of monomeric precursors to an amyloid-competent state (151, 152).

Secondary nucleation processes such as these illustrate the pathological potential of amyloid fibrils in driving the formation of toxic species in amyloid disorders.

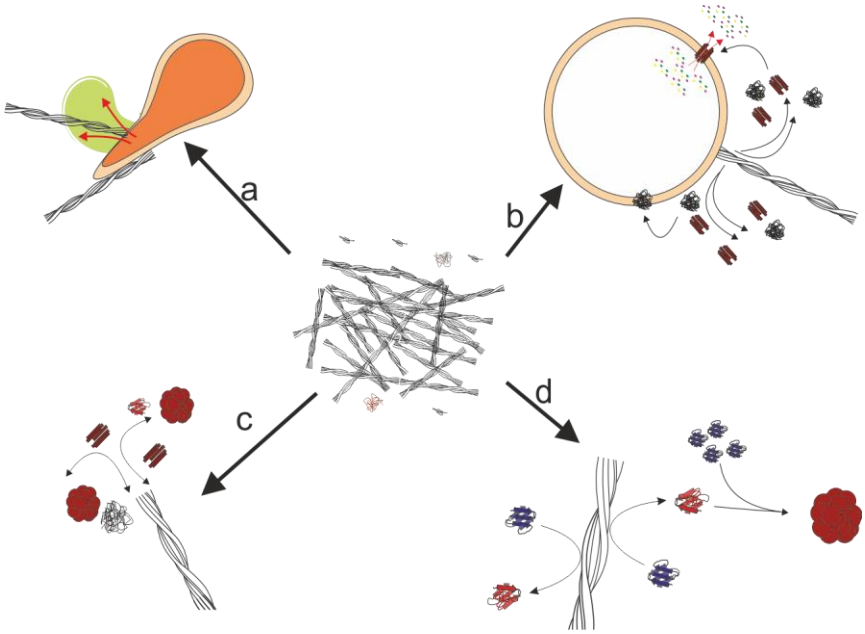

Figure 1.3.9 Mechanisms of amyloid fibril-mediated toxicity. (a) Amyloid fibrils have been shown to interact directly with, and perturb, the architecture of membrane bilayers. (b) Amyloid fibrils composed of Aβ have been shown to release cytotoxic protofibrils upon interacting with membranes. (c) Fibrils composed of a range of amyloidogenic precursors are also dynamic, with subunits exchanging with soluble material under stable conditions. (d) Fibril surfaces have also been shown to be important catalytic surfaces for the propagation of cytotoxic oligomers.

As for soluble intermediates of amyloid assembly, mature amyloid fibrils have also been reported to mediate membrane disruption *in vitro* (Figure 1.3.9). This has been shown for fibrils composed of α-synuclein or HTT, where fibrils were shown to bind to unilamellar vesicles of a variety of different compositions (247). The binding of α-synuclein to synthetic vesicles is coincident with calcein dye-release from the vesicular interior. Plasma membrane (PM) disruption was also observed upon the addition of α-synuclein fibrils to cells, as evidenced by an increase in intracellular calcium levels (248). Calcium influx into the cytosol is associated with, among other things, the onset of apoptosis. PM disruption was also shown for fibrils composed of the yeast prion Sup35. In this instance, PM disruption is modulated by the presence of GM-1 expression at the cell surface (214). This shows that fibril-induced PM disruption can also be receptor-mediated. PM interactions have also been reported for fibrillar assemblies of Aβ, which induce LTP in models of Alzheimer's disease (194). As previously mentioned, disruption of LTP is thought to be the driving force behind cognitive decline in patients with Alzheimer's disease. Aβ fibril-induced LTP

disruption is independent of PrP, the purported cellular receptor for toxic assemblies of Aβ, suggesting that fibril-induced LTP disruption in this instance is mediated by direct binding between fibrillar assemblies and the lipid bilayer (212).

An additional study also observed the reversion of Aβ fibrillar assemblies into protofibrillar oligomers upon interacting with biological membranes (Figure 1.3.9b) (249). These oligomers were structurally homologous to those that form on-pathway to fibril formation *in vitro* and were shown to induce memory defects in Alzheimer's disease mice models. The different mechanisms by which amyloid assemblies of the same precursor induce toxicity may be related to the structural heterogeneity observed within mature amyloid fibril assemblies (Section 1.3.2). This supports the hypothesis of 'strain' dependent phenotypes for amyloid disorder, where the range of symptoms observed and the aggressiveness of disease may be related to the predominating fibril morphology found *in vivo* (113).

1.3.8 How to treat a problem like amyloid?

Targeting the precursor

As a result of the multitude of mechanisms of amyloid-derived toxicity, developing therapeutic strategies to intervene within this class of disorders is extremely challenging. Major research efforts have been focused in understanding the mechanisms that underlie aggregate formation in an attempt to find points within the amyloid cascade that are most amenable to intervention. The premise of this strategy is that preventing the formation of aggregate species will preclude the need to intervene downstream of amyloid-mediated toxicity. Intervening at the most initial stages also means that the wild-type function of the amyloidogenic precursor can be maintained, providing the native fold is stabilised (250). So far, this strategy has yielded the only commercially available treatment for any amyloid disorder: Familial amyloid neuropathy (FAP).

FAP is a deadly neurodegenerative disorder caused by the aggregation of transthyretin (TTR) into amyloid species (251). TTR in its wild-type form assembles into functional tetramers whose physiological role in the blood is to transport holo-retinol binding protein (252). Like all amyloidogenic precursors that possess a defined tertiary or quaternary structure, partial unfolding of the native state is

required for TTR assembly into amyloidogenic structures (253, 254). The misfolding of TTR is exacerbated by the presence of familial mutations that destabilise the native state and accelerate amyloid formation and the emergence of disease (255). There are more than 100 familial mutations known to be associated with various TTR amyloidoses and, in general, the more destabilising the mutation to the native tetramer, the earlier the onset of disease (256, 257). The rate governing step for TTR aggregation is related to the kinetic stability of the tetramer, although monomer unfolding is required for aggregation to proceed (Figure 1.3.10) (258, 259).

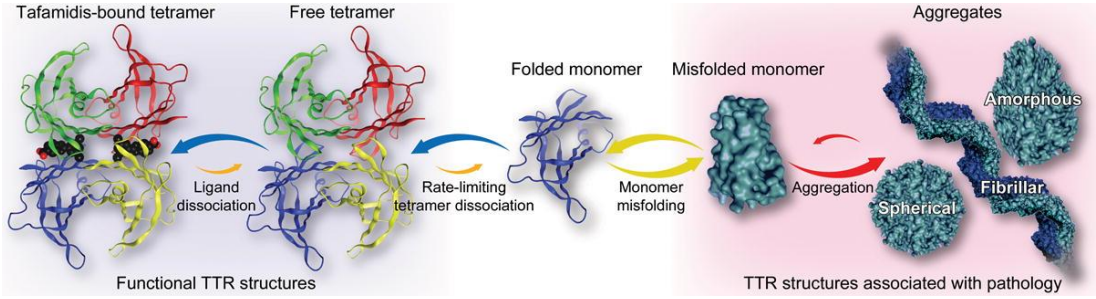

Figure 1.3.10 Mechanism of action of Tafimids Transthyretin aggregation into amyloid is dependent first upon monomer dissociation from the native tetramer prior to partial unfolding of the monomer into an amyloid competent state. The rate limiting step of TTR aggregation is tetramer dissociation. Tafimidis binds within the thyroxine binding pocket of TTR between the weak dimer interfaces, increasing dimer contacts and improving the kinetic stability of the native tetramer. Increasing tetramer kinetic stability prevents monomer dissociation and subsequent amyloid formation. Figure taken from (432).

For FAP, if aggregation of TTR could be prevented by kinetically stabilising the native tetramer to prevent monomer dissociation, disease progression could be slowed. Evidence for the effectiveness of this strategy is supported by the presence of a familial variant that reduces monomer-tetramer dissociation in families that also carry TTR familial variants associated with FAP (260, 261). The variant, I119M, increases the stability of the native tetramer by increasing the intermolecular contacts between the weak dimer interfaces (Figure 1.3.10). To this end, the Kelly group developed the small molecule ‘pharmacological’ chaperone, Tafimidis, that kinetically traps the native TTR tetramer to prevent monomer dissociation and amyloid fibril formation (Figure 1.3.10) (262, 263). They were able to do this by targeting the evolutionary conserved but functionally redundant (in humans) thyroxine binding pocket that resides within the subunit interface of native TTR, by using a structure-guided drug design strategy (264). Tafimidis essentially mimics the inhibitory I119M variant by stabilising the dimer contact interface to prevent complex dissociation. Phase III clinical trials reported that patients with the V30M

FAP-associated familial mutation experienced a slowing down of neurological defects associated with TTR amyloidosis, showing the value of pharmacological chaperones in treating amyloid disorders (255).

Despite the obvious success of this strategy, how applicable pharmacological chaperones are to other amyloid diseases is unclear. For disorders that require partial native state denaturation, such as for lysozyme or immunoglobulin heavy and light chain amyloidoses, stabilising the native state against unfolding is a promising therapeutic strategy. For other amyloid disorders, amyloigoneic precursors are natively unstructured. As little to no information exists regarding the monomeric conformations of these proteins, it is not possible to use a structure based design strategy to develop small molecule inhibitors of aggregation. Therefore other means are required. The most conservative strategies generally involve depletion of the monomeric precursor, due to the difficulties in targeting multiple toxic aggregates and the concentration dependent aggregation of most amyloidogenic proteins. For Aβ in particular, this can involve modulation of the activity of processing enzymes responsible for generating amyloidogenic Aβ fragments from the APP transmembrane precursor (265). Monoclonal antibodies targeted against monomeric or soluble oligomeric forms of Aβ have also been developed as a potential treatment (266). The value of monomer depletion in treating Alzheimer's disease was recently shown in two papers that alleviated and even reversed Aβ-induced cognitive impairment by up-regulating cellular proteins that increased the removal of Aβ from the CNS into the circulating plasma (267, 268). In one of these studies, Cramer *et al* found that Bexarotene, an FDA-approved anti-cancer drug molecule, increased the production of apolipoprotein E (ApoE) and reduced the levels of soluble Aβ in the brain of Alzheimer's mice (268). Mutations within ApoE are one of the greatest risk factors in early-onset Alzheimer's (269). Despite the initial and continuing excitement surrounding this publication, several studies have attempted to recapitulate these findings with varying degrees of success (270–273). In addition, the strategy of monomer depletion is certainly not limited to Aβ, but as usual provides the greatest variety of examples for the types of approaches being developed due to its association with Alzheimer's disease. Other monomer depletion strategies can be found here, such as RNA interference of precursor mRNA levels within the cell (274, 275).

Remodelling toxic species

Another heavily investigated strategy for ameliorating amyloid toxicity is to remodel soluble oligomeric species into aggregate structures that are benign (26, 276–280). There are many different mechanisms of small molecule interference of the aggregation cascade, with lead compounds often identified through screening large libraries of molecules. Screening programmes are usually performed *in vitro* and typically rely on changes to the aggregation kinetics observed using amyloid binding compounds such as Thioflavin T (Figure 1.3.11a and b). Screening protocols that observe the kinetics of fibril formation are the most efficient way to identify compounds that modulate the aggregation landscape, as little structural information is known about intermediates of amyloid formation that cause cytotoxicity; therefore structural based drug design strategies cannot be performed (281).

Most typically, compounds that inhibit or delay the formation of amyloid species are

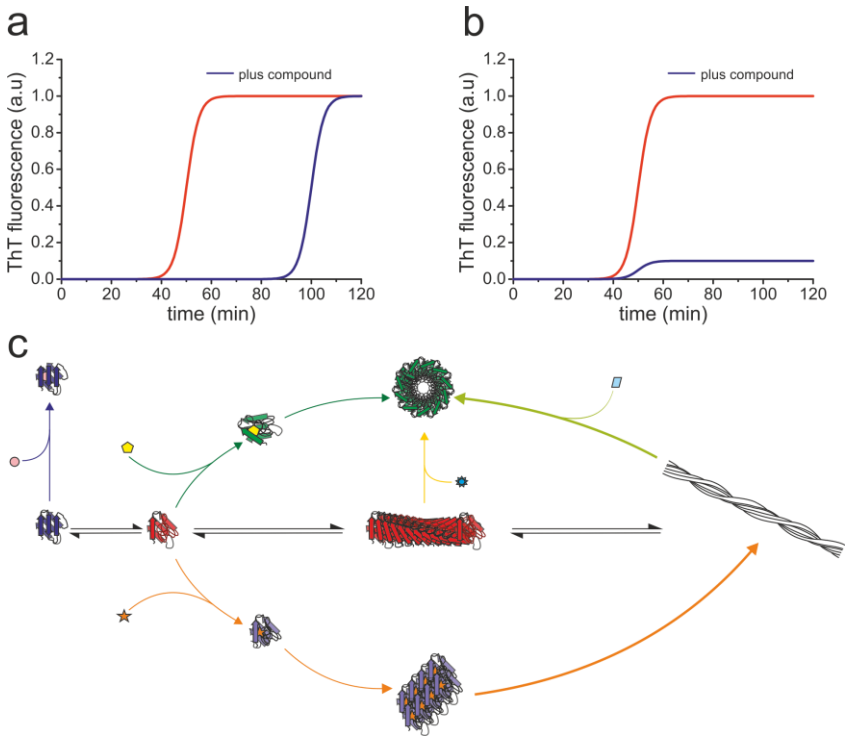

Figure 1.3.11 Pharmacological modulation of the amyloid aggregation cascade. Observing the kinetics of fibril formation are typically used to identify compounds that modulate amyloid aggregation. Positive hits either result in an increased lag time (a) or a reduction in ThT fluorescence amplitude (b), or both. (c) Aggregation can be inhibited by stabilisation of the native state (blue arrow). Partially unfolded monomers can also be bound by inhibitors that re-direct aggregation towards non-amyloidogenic species (green arrows). Small molecules can be used to drive amyloid fibril formation to prevent the accumulation of cytotoxic species (orange arrows), or can be used to bind and remodel cytotoxic species (yellow and lime arrows).

considered hits in screens that utilise fluorescence kinetics of amyloid formation as a read-out (281). This manifests in an increased or infinite lag phase (Figure 1.3.11a), or a reduction in the amplitude of ThT fluorescence within the stationary phase, due to a lower fibril yield (Figure 1.3.11 b). Using a single analytical method such as ThT fluorescence is not wholly reliable and can provide false negative results due to competitive binding between small molecules and ThT to the cross-β fibril core (282). Competitive binding takes place as many amyloid-binding compounds share structural homology with ThT, in that they are rich in aromatic functional groups (283, 284). The mode of binding is thought to be largely hydrophobic with additional specificity provided by salt bridges or hydrogen bonds from small molecule functional groups (285). Nevertheless, monitoring the kinetics of amyloid fibril formation by ThT fluorescence remains at the forefront of efforts to identify agents that can pharmacologically intervene with amyloid aggregation and thus possibly prevent or ameliorate disease (281).

One thing that should be considered when screening for amyloid aggregation inhibitors is the inherent heterogeneity within toxic oligomer ensembles. As the origins of toxicity within oligomer populations are not defined by a single species, it can be difficult to inhibit or divert the aggregation pathway down a route that favours the formation of a non-toxic aggregate. In addition, cytotoxic oligomers do not have to be those that form on-pathway to fibril formation, so preventing fibril formation by diverting aggregation down alternate routes does not necessarily mean that toxicity will be ablated (Figure 1.3.11c). For example, the small molecule rifamycin-SV was shown to divert the aggregation of β_2m into non-amyloidogenic species. Despite inhibiting fibril formation, rifamycin-SV-generated aggregates still exhibit significant cytotoxic potential (286).

Nevertheless, compounds discovered by *in vitro* screening have been reported to bind to oligomeric species and inhibit the aggregation cascade, often leading to reduced aggregate toxicity (26, 276, 278, 287–290). Similar anti-aggregation activities have been reported for a variety of other molecules, including molecular chaperones, antibiotics, metal chelators, anti-inflammatory agents and antibodies (291–298). In addition, *de novo* designed β breakers have recently been shown to end-cap oligomeric species and prevent further elongation into amyloid fibrils (299,

300). These β-breakers were designed based on the structure of oligomeric species formed from fragments of Aβ peptides resolved by X-ray crystallography (301–303).

Small molecules that modulate amyloid toxicity are not restricted to those that inhibit amyloid formation (Figure 1.3.11c). Compounds have also been identified that accelerate fibril formation, leading to reduced overall toxicity of Aβ peptide preparations (26). Similarly, small molecules have been shown promote fibril disaggregation, in the process generating soluble species with varying degrees of toxicity (277, 304, 305). The competing pathways in which small molecules have been discovered to modulate amyloid toxicity further illustrate the heterogeneous mechanisms of amyloid toxicity. Therefore, the therapeutic benefit of a single small molecule identified through such screens remains to be established.

Although changes in aggregation kinetics are most usually monitored using fluorescent amyloid dyes, other techniques, such as ion mobility spectrometry mass spectrometry (IMS-MS), can provide additional information as to the mode of action of particular small molecule modulators of amyloid aggregation (306–308). This is achieved through the high mass to charge resolution of MS, which can detect binding stoichiometries of small molecules to defined oligomeric species, and determine whether binding is specific to a particular oligomeric state (Figure 1.3.12). Because IMS-MS resolves species based on shape and well as m/z, this technique can also determine whether small molecules bind to particular oligomer conformations.

IMS-MS has been used to reveal differences in the mode of aggregation inhibition of the well-established small molecule inhibitors silbinin and (-)-epigallocatechin (EGCG) against hIAPP aggregation (278, 308, 309) (Figure 1.3.12). Young *et al*. were able to show that although both molecules inhibit aggregation, EGCG binds specifically only to monomer conformations of hIAPP, preventing the formation of higher order species (Figure 1.3.12c and d). Silibinin, however, binds specifically to a particular expanded conformation of monomeric hIAPP. Binding to a specific conformer and preventing aggregation suggests this particular monomer conformation is an on-pathway species towards fibril formation (308). These results show that IMS-MS is more than a simple screening strategy and can reveal information regarding the role of particular oligomeric species in the aggregation

cascade. Techniques such as this may become the new standard bearer for high throughput screening for amyloid inhibitors able to target specific conformers, but are not, as yet, routinely used.

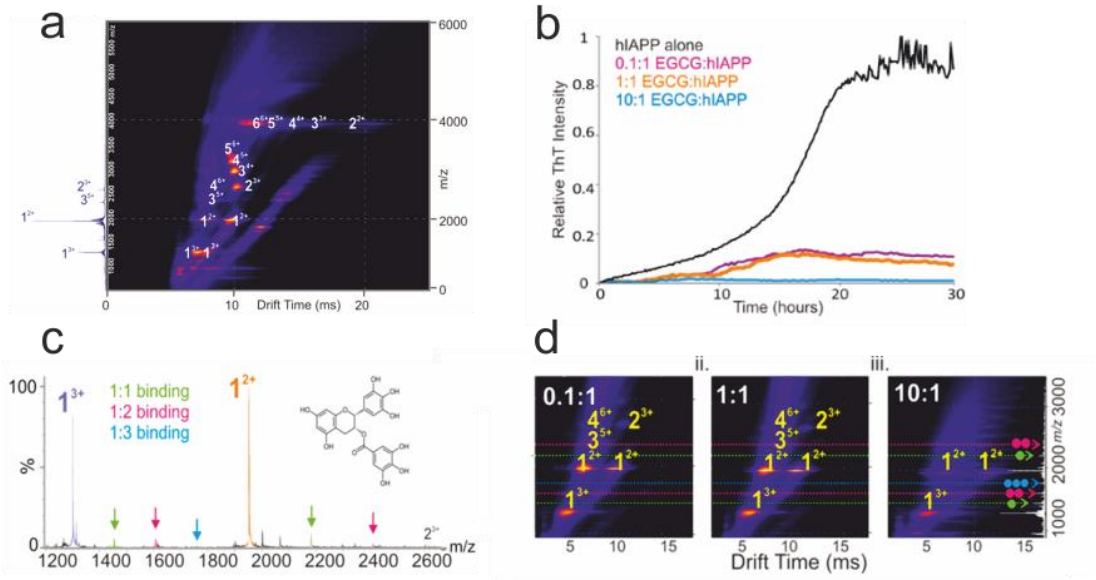

Figure 1.3.12 IMS-MS as a tool to determining mechanisms of amyloid inhibition. (a) Drift plot displaying the formation of oligomeric species within the lag phase of hIAPP amyloid aggregation. The large number gives oligomer stoichiometries, with the superscript indicating charge state. The 1-D m/z spectrum is shown on the left hand y-axis. (b) ThT kinetics if hIAPP alone (black) and in the presence of increasing amounts of EGCG. (c) m/z spectra of hIAPP with EGCG shows binding to both hIAPP monomer 2+ and 3+ charges with a range of binding stoichiometries (inset shows structure). (d) Drift plots of hIAPP in the presence of increasing amounts of EGCG indicates binding to monomer prevents the formation of higher order oligomers. Compound to protein ratios are defined on the drift plots. Figure adapted from (308).

Intervention through modulation of the proteostatic network

The strategies outlined so far rely on the premise of the gain-of-toxic function for amyloidogenic aggregates. However, a new wave of research has identified the loss of protein homeostasis in the presence of aggregates as a defining feature of the onset of amyloid disease (6, 8, 250, 310). These were discussed in the latter half of Section 1.3.6. Several high profile papers have shown that reversing the defects within the proteostatic network can alleviate symptoms associated with amyloid deposition. In some examples, this reversal can be achieved without affecting the concentration of aggregate deposition. In particular, small molecule inhibition of PERK kinase, a key mediator of the UPR, prevents translation inhibition in mice with prion disease and rescues cognitive defects associated with PrP^{sc} replication.

Importantly, pharmacological intervention was beneficial even after the emergence of disease symptoms (311).

More recently, similar pharmacological rescue of translation inhibition was shown to be beneficial for amyloid disorders associated with the deposition of cytoplasmic inclusions in amyolotrophic lateral sclerosis (ALS). Toxicity associated with TDP-43 and ataxin-2 cytoplasmic stress granule formation were modulated by inhibiting PERK kinase in Drosophilia models of the disease. This further confirms the role of the dys-proteostasis in the progression of at least some amyloid diseases (234).

1.4 β_2-microglobulin, a model system for studying amyloid diseases

1.4.1 β_2m and dialysis-related amyloidosis

Despite the progress made towards understanding the biophysical and pathological features of amyloidogenic proteins, there is still significant mileage ahead until curative, or indeed palliative, treatments for amyloid diseases become readily available. So, what is the rate-limiting step inhibiting the development of therapeutics? One thing in particular is that modulators of amyloid aggregation discovered *in vitro* are not similarly effective at ameliorating toxicity *in vivo* (312). This is likely to be due to the multifaceted nature of amyloid toxicity not normally accounted for during *in vitro* screening protocols. Therefore, in order to combat toxicity effectively, all species that facilitate pathological processes, and indeed the associated mechanisms of toxicity, need to be characterised within an amyloidogenic ensemble. This is especially pertinent today due to the limited number of routine screening protocols designed to detect early events associated with the onset of most amyloid disorders. Therefore, there is a significant need for treatments that intervene once amyloid formation has already commenced.

In order to investigate the mechanisms of amyloid-associated toxicity we here utilise β_2-microglobulin (β_2m) as a model system. Under normal physiological conditions, β_2m plays a central role in cellular immunology by associating non-covalently with the major-histocompatibility complex type 1(MHC-1) (Figure 1.4.1a). MHC-1 is involved in antigenic peptide presentation of short peptide fragments derived from proteolytically cleaved cytoplasmic proteins in all nucleated cells. β_2m is a small, 99 residue protein with a immunoglobulin-like fold that contains a stabilising disulphide bridge between cysteine residues at positions 25 – 80 on opposing β-sheets (313–

315) (Figure 1.4.1b). Although non-covalently associated with MHC-1, β_2m is essential for the correct folding of MHC-1 and thus antigen presentation. Because of the requirement of β_2m for correct folding of the antigen presentation complex it is often referred to as the MHC-1 chaperone (316, 317).

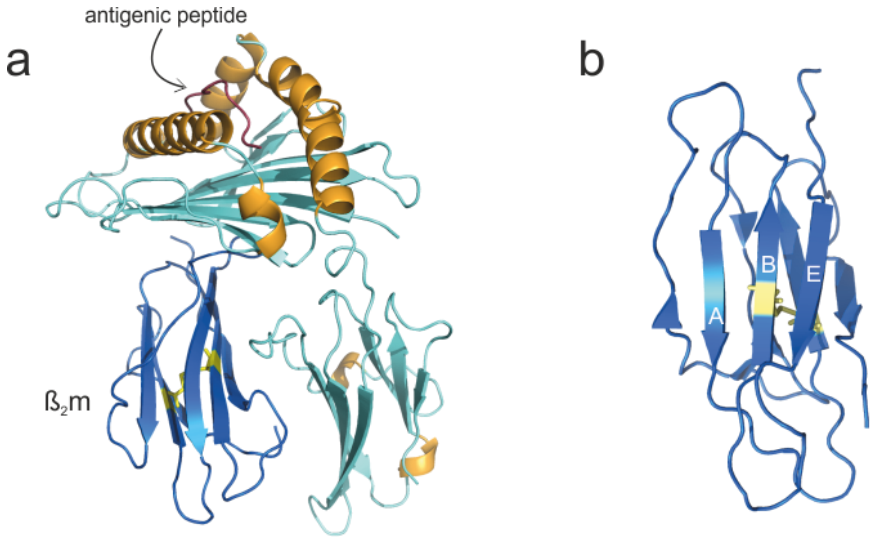

Figure 1.4.1 Structure of human β_2-microglobulin. (a) β_2m in complex with the MHC-1 heavy chain. The antigenic peptide is displayed in red. The β_2m light chain component is shown in blue (PDB code 1QEW). (b) Structure of β_2m in isolation. The ABE β-sheet is shown orientated towards the front of the page. Cysteine residues 25and 80 are shown in yellow (PBD code 1J1N) (433).

As part of its catabolic cycle, β_2m dissociates from the heavy chain into the blood where it is trafficked to the kidneys for renal clearance (318). For patients undergoing long-term haemodialysis treatment due to kidney failure, β_2m undergoes an increase in plasma concentrations (up to 60-fold) as it cannot be cleared effectively through dialysis membranes (319, 320). This increase in concentration is ultimately responsible for the tissue-specific deposition of β_2m into amyloid plaques associated with pathological joint and bone destruction in a condition known as dialysis-related amyloidosis (DRA) (321–323) (Figure 1.4.2). The tissue specific deposition of β_2m into synovial joints is thought to result from an affinity of β_2m and collagen (324, 325). More recently, a familial variant of β_2m (D76N) was discovered to be associated with localised systemic amyloidosis, increasing the spectrum of β_2m-associated amyloidoses (10).

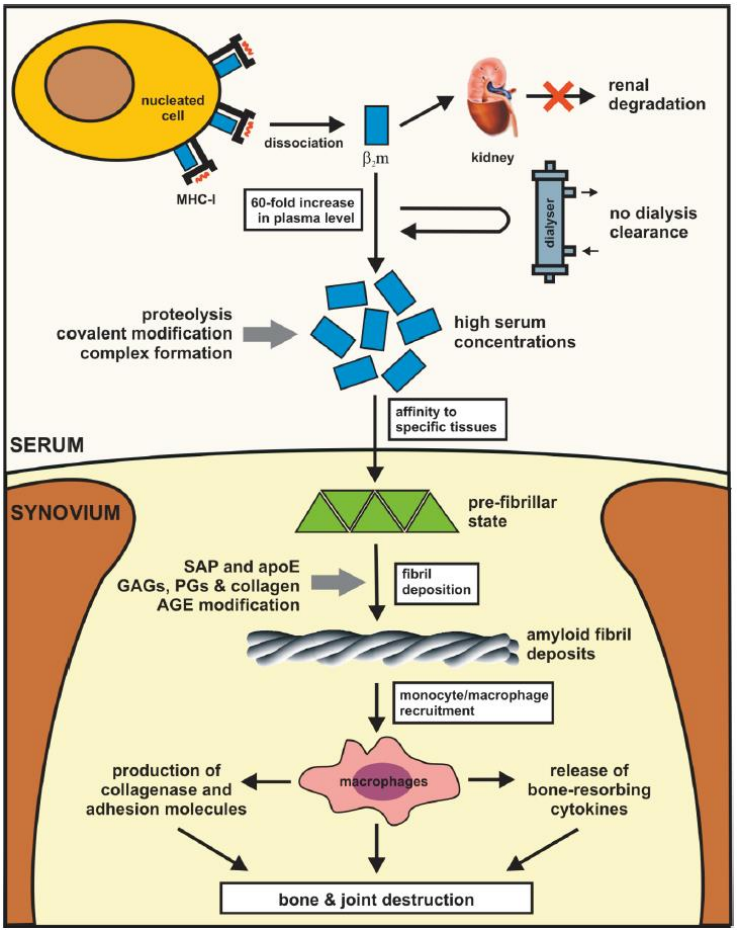

Figure 1.4.2 Dialysis-related amyloidosis. This cascade of events leads to tissue-specific β_2m deposition, conversion to a fibrillar state and ultimately pathological joint and bone destruction. Factors known to associate with deposits of β_2m *in vivo*, such as collagen, are indicated. Taken from (434).

1.4.2 Mechanisms of β_2m amyloid formation

Like other amyloid diseases, the pathological origins of β_2m amyloid formation are unclear. Similarly, the mechanisms that promote the aggregation of the natively folded protein into the amyloid cross-β fold also remain unresolved in atomic detail. The increase in β_2m concentration, however, is fundamental to the aggregation of β_2m (326, 327). The increased persistence of β_2m in the blood also means that proteolytic products of β_2m are often found in patients with DRA. In particular, the N-terminally truncated variant, ΔN6, in which the N-terminal 6 residues are proteolytically cleaved, can compose up to 30% of the total β_2m concentration associated with amyloid plaques (328, 329). The enrichment of ΔN6 within amyloid plaques of β_2m suggests that proteolysis may play a role in initiating amyloid formation – *wt* β_2m cannot form amyloid fibrils, at least *in vitro*, at neutral pH (330). *In vitro* studies showed that the removal of the 6 N-terminal residues provides a

greater degree of conformational flexibility within the β_2m molecule, which upon a slight reduction in pH from 7.2 – 6.2 leads to a cis-trans peptidyl-prolyl isomerisation at residue proline 32 (157). The trans orientation of Pro32 in ΔN6 enables the protein to adopt a conformation reminiscent of the folding intermediate I_T (157, 159). Although highly homologous in main chain structure to *wt* β_2m, ΔN6 exhibits a significant rearrangement of side-chains involved in the formation of the hydrophobic core (157) (Figure 1.4.3). The concentration of I_T can also be increased by mutating residue 32 to glycine, indicating the role of cis-Pro32 is restricting the conformational freedom of β_2m to prevent amyloid formation (159, 331). The I_T state is thought to be a structural intermediate critical for amyloid formation. The

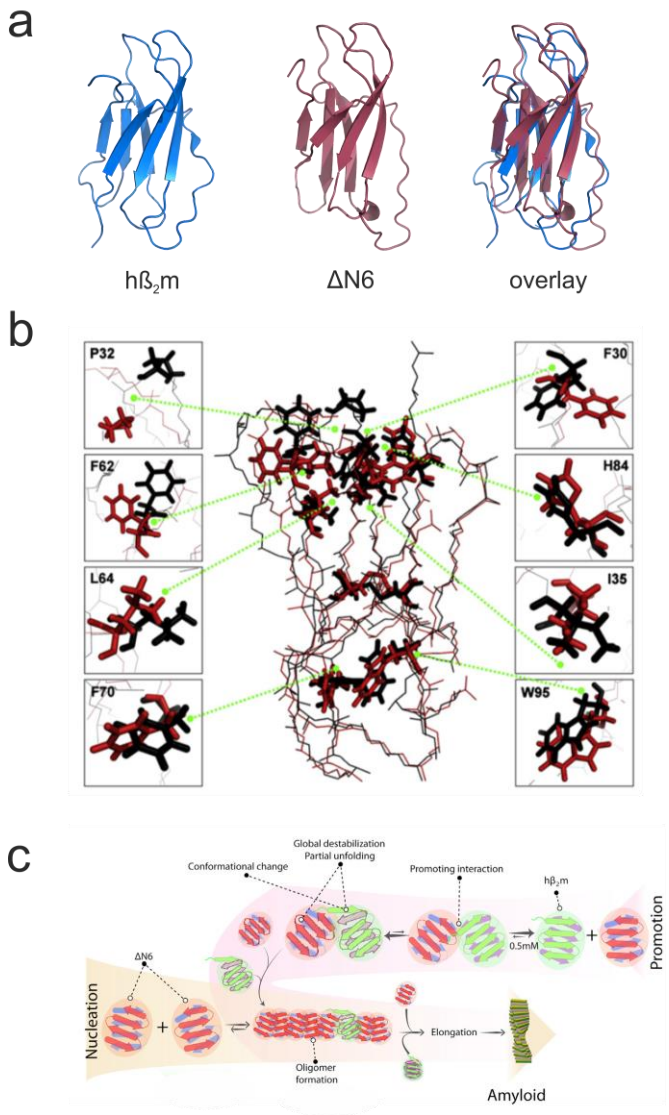

Figure 1.4.3 The β_2m amyloidogenic variant ΔN6. (a) The lowest energy structures of *wt* β_2m(blue), ΔN6 (raspberry) and the overlaid structures (far right) (PBD codes 2XKS and 2XKU respectively). (b) Side chain reorientation within the hydrophobic core of ΔN6 (red). Shown in comparison with hβ_2m(black) (157). (c) Model of proposed activity of ΔN6 (red) in promoting the aggregation of hβ_2m (green) (332).

presence of large concentration of ΔN6, a structural mimic of the I_T state, may therefore accelerate/initiate the formation and deposition of β_2m into amyloid fibrils. More recent studies have shed light on the possible role of ΔN6 in promoting the formation of *wt* β_2m into amyloid fibrils at near-neutral pH. Using detailed NMR studies, Karamanos *et al*. showed recently that ΔN6 can act as a catalytic converter to promote conformational changes within *wt* β_2m at pH 6.2 into an amyloid-competent state (332) (Figure 1.4.3). The interaction between ΔN6 and *wt* β_2m involved the formation of weakly associated, transient head-to-head interactions, which was enough to destabilise the native state to allow fibril formation of *wt* β_2m to proceed (Figure 1.4.3c). The partial unfolding/denaturation of β_2m as an initiating event of fibril formation is further supported by additional *in vitro* analyses that have highlighted particular conditions under which β_2m aggregation is promoted. At neutral pH, β_2m amyloid formation can proceed in the presence of Cu^{2+} ions and urea; by mutagenic removal of the 6 N-terminal residues of β_2m; by adding tetrafluoroethylene; or by destabilising the N- and C- terminal stands of β_2m (329, 333–335). Furthermore, β_2m fibril formation has been shown to proceed rapidly at low pH under a variety of conditions. Acid denaturation of *wt* β_2m in solutions with low ionic strength promotes the formation of β_2m amyloid fibrils with all the characteristic hallmarks of amyloid fibrils (155, 336, 337). In addition, β_2m amyloid fibrils obtained under these conditions are morphologically similar to those isolated *ex vivo* from patients with DRA (82). The similarities of fibrils formed at low pH with those isolated *ex vivo* highlight the value of *in vitro* experiments in determining the mechanisms of β_2m amyloid fibril formation. They also make *in vitro* β_2m amyloid fibrils a valuable resource for deciphering the mechanisms of amyloid formation and amyloid-associated toxicity.

1.4.3 Morphological features of β_2m amyloid fibrils

Recent advances in structural biology have helped to elucidate the structural properties of β_2m amyloid fibrils. Chief among the techniques used to investigate β_2m fibril architecture are cryo electron microscopy (cryoEM) and solid-state NMR (SS-NMR). In 2009, White *et al* used cryoEM to elucidate the quaternary packing of protofilaments within the mature fibril core, and also determined the subunit packing arrangement within the protofilaments themselves (92). The study revealed that β_2m

amyloid fibrils have a diameter of approximately 20 nm and contain a characteristic cross over repeat of variable length parallel to the fibril axis (Figure 1.4.4a). The fibril core is composed six protofilaments which arrange into two crescent-shaped half-fibrils (protofibrils Figure 1.4.4b and c). Each protofilament has an approximate dimension of 3 x 4 nm when viewed top-down and has a regular subunit repeat length of 5.25 nm parallel to the long fibril axis (Figure 1.4.4b). Scanning transmission electron microscopy (STEM) analysis of fibrils revealed a packing density of 52 kDa/nm, indicating that each repeat length must be composed of 24 β_2m monomers ((52 kDa/nm x 5.25 nm)/11.86 kDa). Taking into account the six protofilaments within the fibril, subunit repeats are most likely to be a set of stacked dimers of dimers, consistent with two distinct regions of density within the fibril subunit repeat length (Figure 1.4.4c).

Subsequent to this analysis, SS-NMR and electron paramagnetic resonance (EPR) have revealed that monomers within the fibril core are arranged in a parallel in-register array (106, 338). This architecture, as previously mentioned, is found in many amyloid fibrils. Similar SS-NMR analysis of fibrils composed of the N-terminally truncated variant ΔN6 also showed a parallel in-register subunit orientation; albeit with a slightly different subunit packing arrangement (94, 117). Comparative limited proteolysis of the two fibrils revealed ΔN6 fibrils possess an additionally accessible cleavage site within the C-terminal region of the subunit in comparison with *wt* β_2m fibrils (339) (Figure 1.4.4d). In addition, SS-NMR revealed an increase in the number of identifiable backbone Nα-Cα cross-peaks in ΔN6 fibril spectra (94). Thus, although a similar number of residues in ΔN6 participate in the formation of the fibril core, the region may possess elevated rigidity compared with fibrils formed of *wt* β_2m at low pH.

ΔN6 and *wt* β_2m have also been shown to co-polymerise to form heteropolymers with distinct biophysical properties compared with the two homopolymers (117). The co-polymerisation of two distinct amyloidogenic sequences to expand the number of accessible fibril polymorphs has become an increasingly frequent phenomenon among pathogenic amyloidogenic precursors (118). More structural information regarding the fibril core of β_2m:ΔN6 heteropolymorphs have yet to be determined.

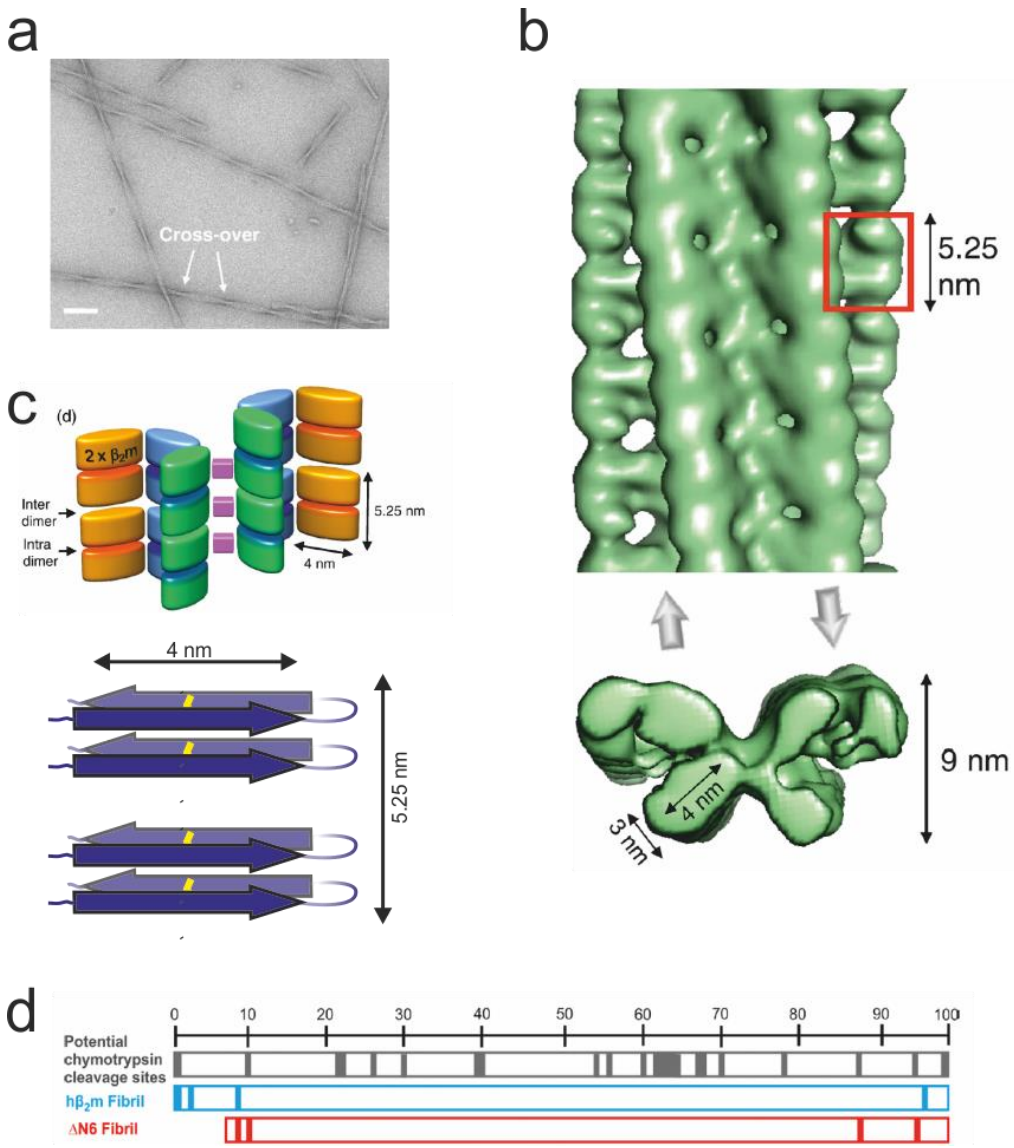

Figure 1.4.4 Structure of β_2m amyloid fibrils. (a) Negative stain TEM of β_2m amyloid fibrils illustrating cross-over repeat motif (92). (b) His resolution cryoEM map showing regions of density with β_2m fibril (92). The cross sectional view is shown below. (c) Subunit organisation within β_2m amyloid fibrils. The parallel in-register array of monomers with the subunit repeat is shown below. Accessible cleavage sites within fibrils composed of β_2m or ΔN6. Potential cleavage sites are shown in grey, with actual cleavages illustrated by blue of red vertical lines (117).

1.4.4 Studying mechanisms of β_2m amyloid fibril-mediated toxicity

The disease-association of β_2m amyloid formation coupled with the well-characterised and reproducible nature of β_2m aggregation makes this protein an attractive model system for elucidating mechanisms not only DRA and familial amyloidosis, but also perhaps generic features of amyloid diseases. Because β_2m amyloid formation is very well described, it provides a powerful resource for identifying species that form during amyloid assembly and disassembly that mediate cellular dysfunction. Samples can be made and characterised *in vitro* prior to being

incubated with cells to ensure that the identity of the entire aggregate population is known at the starting point of the investigation (245). Even if aggregates undergo structural evolution during incubation with cells, whatever structure is causing cellular dysfunction must be accessible from the known starting conformation. In this thesis work is focused on investigating whether amyloid fibrils, as opposed to soluble aggregation intermediates, can induce cellular defects and which features of amyloid fibrils are responsible for potentially mediating metabolic defects. This is performed first by extensive characterisation of samples prepared *in vitro* from recombinant protein using the wealth of tools developed developed in the Radford group. Discoveries made will be discussed in more detail in a brief introduction to the following chapters before describing work performed as part of this thesis.

1.5 Aims of this Project

The principal aim of the work described in this thesis was to expand our knowledge of the mechanisms associated with β_2m amyloid fibril-mediated cellular metabolic dysfunction and membrane disruption *in vitro*. As mentioned, studying these mechanisms using β_2m provides an exciting opportunity to perform an in-depth analysis of how amyloid fibrils in general can contribute towards amyloid pathologies. Opinions concerning the role of amyloid fibrils in disease are varied, such an analysis, therefore, could reveal the importance of fibrils in facilitating toxicity, and whether the long accepted view that fibrils are simply inert end products of aggregation can be re-assessed. In order to investigate this question, a range of analytical techniques were performed to investigate the behaviour of β_2m amyloid fibrils *in vitro* under competing sets of conditions. The presentation of results within this thesis is listed below. Relevant methods used are detailed in each chapter.

Chapter 1 hopefully provides a general overview as to the current state of the amyloid research field.

Chapter 2 provides an introduction to the construction and characterisation of β_2m amyloid fibrils used throughout this thesis. These fibrils are then used to investigate the response of amyloid fibrils under two sets of conditions in which the capacity of fibrils to disrupt membranes is significantly different. More specifically, changes in

dynamic behaviours of fibrils are probed using ThT fluorescence kinetics, ESI-IMS-MS and NMR, as well as documenting attempts to elucidate whether the dynamic behaviour of β_2m amyloid fibrils is responsible for metabolic defects upon incubation with cultured mammalian cells. The work builds on several collaborations in which the mechanisms of pH-dependent membrane disruption were established and the mechanisms of β_2m fibril-mediated cellular dysfunction were investigated (340–342).

Chapter 3 details the use of fluorescence correlation spectroscopy (FCS) to investigate how the subtly different solution conditions used in Chapter 2 have dramatic consequences upon the equilibrium of species that populate upon dilution into solutions that differ by only a single pH unit. Attempts to structurally characterise the novel species are also described and the implications for amyloid-associated cellular dysfunction are discussed.

Chapter 4 describes a comparative analysis between the mechanisms of β_2m amyloid fibril polymerisation and depolymerisation through ThT kinetic analysis and FCS. The results show that, at least kinetically, the two processes are not mutually exclusive, with fundamental differences in relation to the end-dependent nature of fibril polymerisation and depolymerisation existing. Moreover, FCS suggests that the intermediate species formed during the lag phase of β_2m amyloid assembly are distinct from those that form during depolymerisation. This finding may expand the structural repertoire of oligomeric species known to cause toxicity in amyloid diseases.

Finally, **Chapter 5** summarises all the key findings established from the studies above and places them in the context of β_2m amyloidosis as well as that of the generic principles of amyloid toxicity. Future work will also be discussed that aims to investigate in more detail whether the molecular shedding phenomenon is applicable to other fibril types and how such a process may be therapeutically intervened.

CHAPTER 2

The molecular mechanism of amyloid fibril-mediated membrane disruption

2.1 Introduction

Characterising the array of amyloid species that mediate mechanisms of toxicity is a key prerequisite for the development of therapeutic strategies to combat these disorders. Although the inherent toxicity of amyloid fibrils is lower than that of their oligomeric counterparts, the prevalence of fibrils at the site of toxicity (1, 343), and their persistence due to increased thermodynamic stability in comparison with soluble species (75, 93, 107, 117, 156, 344–346), means that the role of amyloid fibrils in contributing to disease processes needs to be investigated more thoroughly.

The role of β_2m amyloid fibrils in mediating toxicity was established in 2009, when Xue *et al.* showed a fibril length dependent relationship of amyloid-mediated metabolic dysfunction (245, 347). In essence, fibrils fragmented to reduce the average particle length displayed enhanced cytotoxicity compared with their longer, unfragmented counterparts at monomer equivalent concentrations (Figure 2.1.1a). This length dependent phenomenon was observed for α-synuclein and lysozyme amyloid fibrils and was also replicated in an *in vitro* liposome dye release assay (Figure 2.1.1b and c, respectively). Subsequent to this, it was found that upon incubation with cells, fibrils are internalised into lysosomes. Inhibition of clathrin-mediated endocytosis using the dynamin inhibitor, Dynasore (348), reversed β_2m fibril-mediated metabolic defects (Figure 2.1.2a), indicating that fibrils illicit toxicity from inside the cell (Figure 2.1.2b) (340). In addition, β_2m amyloid fibrils were also shown to inhibit the development of bone resorbing osteoclasts and impair the viability of osteoblasts, the cell type that produces bone, indicating the potential role of fibrils in mediating the pathological joint and bone destruction observed in DRA (349).

Considering the alleged importance of amyloid – lipid interactions in mediating cellular toxicity (190, 191, 200–202, 213, 214, 220, 244, 247, 350–357), these observations inspired a systematic investigation into the molecular mechanisms of β_2m fibril-mediated membrane disruption and cellular dysfunction. Several hypotheses were put forward as potential explanations for the length dependent

phenomenon, including the potential importance of fibril ends; shorter fibrils at monomer equivalent concentrations will possess a significantly greater number of fibril ends. Thus, if fibril ends mediate *in vitro* membrane disruption, then shorter fibrils will possess greater activity in this regard. In 2012, using cryo-electron microscopy, Milanesi *et al*. observed a direct interaction predominantly between β_2m amyloid fibril ends and synthetic lipid bilayers which, if responsible for mediating *in vitro* liposome disruption, could explain the greater activity of short fibril samples (Figure 2.1.1d) (358).

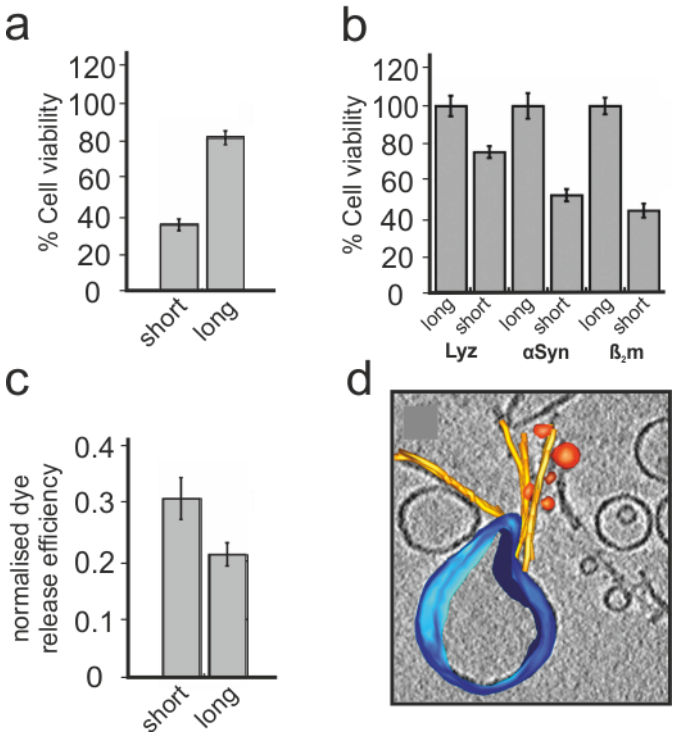

Figure 2.1.1 Biological activity of β_2m amyloid fibrils. (a) β_2m amyloid fibrils cause length dependent metabolic dysfunction as judged by the MTT assay. (b) Similar phenomenon were observed for fibrils composed of lysozyme (b) and α-synuclein (αSyn). (c) β_2m fibrils also cause length dependent carboxyfluorescein dye release from synthetic liposomes (245). (d) Direct observation of β_2m fibril – lipid interactions highlights the role of fibrils ends in perturbing membrane architecture (358). The lipid bilayer is shown in blue, fibril in yellow and released lipids in orange.

Subsequent to this, our understanding not only of fibril-mediated membrane disruption, but of the biological consequences of incubating cells with β_2m amyloid fibrils, has expanded greatly. This chapter describes a body of work that has attempted to elucidate these processes, with special focus on *in vitro* studies of the causative agents of membrane disruption. The range of techniques encompassed within this work, including biochemical, biophysical and ultimately cell biological assays, is the result of fruitful collaborations with members of the Radford and

Hewitt groups past and present, who are acknowledged for their contribution in the appropriate figure legends. The systematic investigation of lipid composition and pH upon β_2m fibril-mediated membrane disruption presented in Section 2.3.3 (341) was primarily performed by Dr Sophia Goodchild, using fibrils samples of defined length provided by myself. The results are shown to provide a narrative as to the evolution of our understanding of the mechanisms behind β_2m amyloid fibril-mediated membrane disruption and cellular metabolic dysfunction.

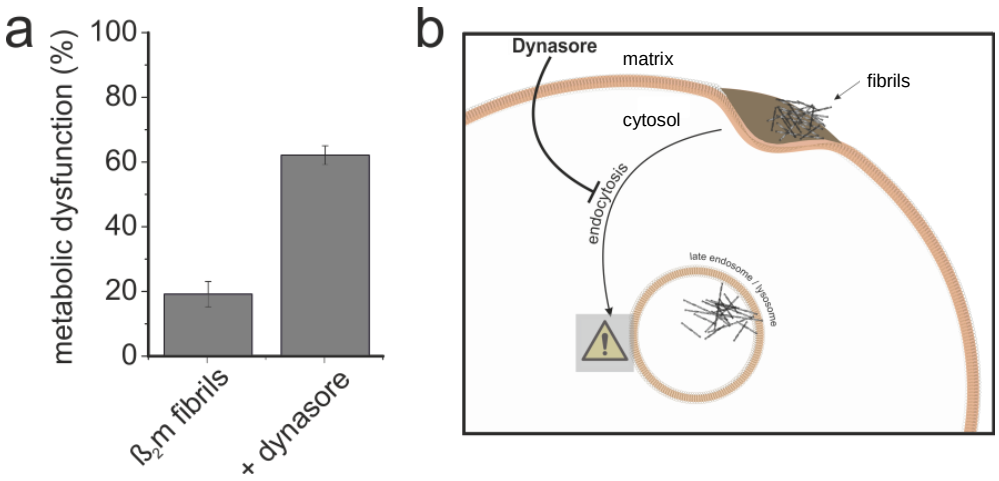

Figure 2.1.2 Inhibiting clathrin-mediated endocytosis reverses fibril-mediated metabolic dysfunction. (a) MTT viability of 1.2 μM β_2m fibrils in the presence (+ dynasore) and absence of the clathrin mediated endocytosis inhibitor dynasore (340). (b) Schematic representation of fibril-mediated toxicity. Fibrils are internalised and trafficked to lysosomes. Restricting fibril internalisation with CME inhibitors prevents metabolic defects associated with β_2m fibril incubation.

2.2 Materials and Methods

All chemicals (unless otherwise stated) were purchased from Sigma Aldrich and were of analytical grade.

2.2.1 General analytical methods

2.2.1.1 Quantifying protein concentration using UV absorption at 280 nm

Proteins were diluted where necessary to obtain UV absorption values of between 0.1 and 1 for determination of protein concentration. In general, protein solutions were diluted into water containing 6 M guanidinium hydrochloride (GdmHCl) to a final volume of 100 μl. All absorption values were acquired using a reference standard of buffer-only solutions. Protein concentrations were determined using Beer-Lambert's law. Wild-type β_2m has an extinction coefficient of 20065$M^{-1}.cm^{-1}$ which was determined using Gill and Von Hippel's method (359).

2.2.1.2 DNA quantification

DNA quantification was performed by diluting DNA samples into sterile water (typically 1 to 200) before measuring the absorbance at 260 nm given that Abs_{260} of 1 is the equivalent of 50 $\mu g.ml^{-1}$ of DNA. The correct concentration was calculated using the appropriate programme on an Ultraspec 2100 proUV-vis spectrophotometer (Amersham Biosciences).

2.2.1.3 Preparation of agar plates

2.5 g of Luria Bertani medium (containing per L, 10 g bacto-tryptone, 5 g yeast extract and 10 g NaCl, Melford) and 1.5 g of bacto-agar (Melford) were added to 100 ml of deionised water. The solution was autoclaved for 20 min at 121°C min prior to cooling to approximately 45°C before the addition of the appropriate antibiotic. About 25 ml of autoclaved, cooled solution was poured into each 100 mm diameter petri dish before allowing setting at room temperature. Agar plates were kept chilled at 4°C and stored for up to one week.

2.2.1.4 SDS-polyacrylamide gel electrophoresis

A two layered gel system consisting of a stacking gel for protein loading and a 15% Tris-Tricine resolving gel was used throughout. Components of the stacking and resolving gels are detailed in Table 2.2.1.

Table 2.2.1 Composition of stacking and resolving gels for SDS-PAGE

Solution Component	Resolving gel (ml)	Stacking gel (ml)
30% (*w/v*) Acrylamide 0.8% (*w/v*) *bis*-acrylamide	7.5	0.83
3 M Tris-HCl, 0.3% (*w/v*) SDS pH 8.45	5.0	1.55
H_2O	0.44	3.72
Glycerol	2	-
10% (*w/v*) ammonium persulphate	0.1	0.2
Tetramethylethylenediamine (TEMED)	0.01	0.01

Gels were electrophoresed using anode buffer (200 mM Tris-HCl pH 8.8) and Tris/Tricine cathode buffer (100 mM Tris, 100 mM Tricine, 0.1 % (*w/v*) Sodium dodecyl sulphate (SDS) pH 8.3,Bio-Rad) at a constant current of between 35 – 50 mA.

Samples were prepared for SDS-PAGE by adding 2.5 µl each of 1 M dithiotheritol (DTT) and 6 x loading buffer (150 mM Tris-HCl pH 6.8, 600 mM DTT, 6% (*w/v*) SDS, 0.3% (*w/v*) bromophenol blue and 30% glycerol) to approximately 10 µl of sample. After electrophoresis gels were stained for 1 h with Instant Blue (Expedeon) and de-stained by washing in water for 3 x 5 min.

2.2.1.5 Transmission electron microscopy imaging

Samples were applied to a freshly glow discharged copper EM grid coated with a thin layer of carbon, blotted with Whatman filter paper, washed with 18 MΩ water, and stained with 1% (*w/v*) uranyl acetate for approximately 30 sec. Images were

recorded using a BM Ultrascan 2k x 2k CCD (Gatan) on a Technai T12 TEM (FEI) operating at 120 keV.

2.2.1.6 Electrospray ionisation mass spectrometry

All spectra acquired to confirm protein identity were performed using samples ranging from 50 – 100 µM in protein concentration in 50 – 100 mM ammonium bicarbonate buffer, pH 7.4. Mass spectra were acquired using a Synapt HDMS instrument (Micromass UK Ltd., Waters Corp, Manchester, UK) interfaced to a NanoMate automated sample infusion device operating in positive ion mode (Advion Biosciences Inc., Ithaca, NY). All spectra were calibrated using cluster ions generated from a separate introduction of cesium iodide solution (2 mg/ml, 1:1 water:methanol). The spectra were smoothed using the Savitzsky-Golay method and analysed using MassLynx software.

2.2.2 General cloning methods

2.2.2.1 Transformation of plasmid DNA

The gene encoding *wt* human β_2m was cloned into a pET23a vector using Hind III and Nde I restriction sites under the control of the T7 promoter (NEB, USA). The vector, known as the pINK plasmid, was originally constructed and designed by Dr Neil Kad (336). Gene-harbouring vectors were then transformed into competent *E.coli* BL21 DE3 pLysS cells (E.coli B F-dcm ompT hsdS(rB- mB-) gal λ(DE3)pLysS (Camr), Agilent) using the 'heat shock' method. In brief, 5 µl of the *wt* β_2m vector was added to 50 µl of chilled (on ice) BL21 DE3 pLysS cells and gently agitated prior to returning to ice for 30 min. Cells were then 'heat shocked' by submerging in a water bath set to 42^{o}C for 45 sec before returning to ice for 2 – 3 min. 500 µl of pre-warmed LB media (Section 2.2.1.3) was then added to cells before incubating at 37^{o}C 200 rpm for 1 h. Two pre-warmed agar plates were streaked with either 50 µl or 200 µl of transformed cells and left to incubate at 37^{o}C overnight in agar plates containing 50 µg.ml^{-1} carbenicillin.

2.2.3 Expression and purification of wild-type β_2m

For expression and purification of *wt* β_2m, colonies of BL21 DE3 pLysS cells transformed with the pINK plasmid were picked and used to inoculate 100 ml LB

medium supplemented with 50 μg.ml^{-1} carbenicillin and 50 μg.ml^{-1} chlormaphenicol. Starter cultures were grown overnight at 37°C shaking at 200 rpm. Once overnight cultures had reached an OD_{600nm} > 1, 10 ml of overnight starter culture was used to inoculate 11 x 2 litre flasks each containing 1 L of LB medium pre-warned to 37°C and supplemented with 100 μg.ml^{-1} carbenicillin. Cells were grown at 37°C, 200 rpm and protein expression induced once an OD_{600nm} 0.6 was reached by adding isopropylthiogalactopyranoside (IPTG, Generon) to a final concentration of 0.8 mM. Protein expression was subsequently allowed to continue for 16 h.

Cells were harvested using a continual action centrifuge at 15000 rpm (Heraus) and the pellet re-suspended in approximately 50 ml per 20 g of cell pellet of lysis buffer (25 mM Tris.HCl pH 8.0, 100 μg.ml^{-1} lysozyme, 100 nM phenylmethanesulfonyl fluoride (PMSF), 20 μg.ml^{-1} deoxyribonuclease and 1 mM ethylenediaminetetraacetic acid (EDTA)) by vigorous agitation. The homogenised cell pellet was incubated at room temperature with vigorous agitation (using a magnetic stirring bar) for 30 min before being further disrupted using a cell disrupter operating at 20 kPSi (Constantsytem). The resulting cell debris and β_2m inclusion bodies were pelleted by centrifugation at 15,000 rpm using a Beckmann JLA 16.250 rotor for 30 min at 4^{o}C. The supernatant was discarded and a lipid film on top of the protein inclusion body removed by gently scraping with a spatula before re-suspending the inclusion body in 100 ml 25 mM Tris.HCl pH 8.0. Inclusion bodies were then re-pelleted and cleaned (typically 5 cycles) as described above until a clean pellet devoid of cellular debris was obtained.

The inclusion body pellet was re-suspended in 25 mM Tris.HCl pH 8.0 containing 8 M urea (MP Biomedicals) and incubated at room temperature while gently stirring overnight to re-solubilise β_2m. Soluble β_2m was then dialysed (3,000 kDa cut-off, Fisher Scientific) against 5 L of 25 mM Tris.HCl pH 8.0 at 4^{o}C for 24 h to refold with at least 4 buffer changes. Insoluble material was removed by centrifugation at 15,000 rpm 4^{o}C for 30 min using a Beckmann JLA 16.250 rotor. Refolded β_2m was further purified by anion exchange chromatography by loading the protein sample onto a fast flow Q-Sepharose (GE healthcare) column self-packed (200-300 ml) and previously equilibrated with 600 ml of 25 mM Tris.HCl pH 8.0 at a flow rate of approximately 5 ml.min^{-1}. Once loaded the column was washed with 600 ml 25 mM

Tris.HCl pH 8.0. β_2m was eluted using a linear gradient of 0 – 400 mM NaCl in 25 mM Tris-HCl over 800 ml at a flow rate of 5 ml.min^{-1}, collecting fractions 10 ml in size. Fractions containing β_2m as judged by SDS-PAGE were pooled and dialysed (3000 kDa cut-off) for 48 h against 5 L 18 MΩ water with at least five buffer changes at 4°C prior to freeze drying the sample and storing at -20^{o}C. β_2m was then purified to >95% purity by gel filtration using a Superdex 75 Prep column (GE Healthcare) equilibrated with 25 mM sodium phosphate buffer, pH 7.4 and calibrated with a standard gel filtration calibration kit (GE healthcare). Freeze-dried protein was re-suspended in the same buffer at an approximate concentration of 10 mg.ml^{-1} and filtered using a 0.2 μm syringe filter (Millipore) before 5 ml was loaded onto the column using an injection loop. Protein was eluted at a flow rate of 3 ml.min^{-1} while collecting fractions of 3 ml after 100 ml of buffer had passed through into waste. Fractions containing purified β_2m as judged by SDS-PAGE were concentrated to approximately 2.5 mM using cenitrifugal3 kDa cut-off filtration units (Centricon) according to manufacturer's instructions, prior to snap freezing in liquid nitrogen and storage at -80^{o}C. The identity of β_2m was confirmed by mass spectrometry (see section 2.2.1.6).

2.2.4 Fibril sample preparation

Fibril seeds were prepared by diluting concentrated β_2m solutions stored at -80°C in 25 mM sodium phosphate buffer pH 7.4 to 120 μM in 10 mM sodium phosphate buffer, containing 50 mM NaCl, pH 2.0 (fibril growth buffer). 500 μl aliquots were then placed and sealed in screw top 1.5 ml glass vials (Chromacol) containing a 3 x 8 mm magnetic stirring beads and placed on a custom-made precision stirrer (University of Leeds Physics Workshop) rotating at 1,000 rpm for 3 days at 25°C.

These seeds were then stored under quiescent conditions at room temperature and used in all subsequent fibrils growth experiments in the fibril growth buffer at a seeding concentration of 0.1% (*w/w*) unless otherwise stated. Typical fibril growth experiments were performed by diluting stored β_2m to 120 μM into fibril growth buffer before adding 0.1 % (*w/w*) seed and incubating at room temperature for a minimum of 48 h unless stated otherwise.

2.2.5 Tapping mode atomic force microscopy

Samples were prepared for tapping-mode AFM by diluting samples to 0.4 µM monomer equivalent concentrations in 18 MΩ water to ensure good sample dispersion and uniform coverage upon the imaging surface. After dilution, 20 µl of sample was immediately placed on to a freshly cleaved surface of mica and incubated at room temperature for 5 min. Surfaces were then washed with 1 ml of 18 MΩ water before gently aspirating the surface with a stream of N_2 gas to complete dryness. Samples were imaged using a Dimension 3100 scanning probe microscope (Veeco Instruments) and PPP-NCLR silicon cantilever probes (Nanosensors, Neuchatel, Switzerland) with a nominal force constant of 48 N/m. Typically, 10 μm^2 images at a pixel ratio of 1024 x 1024 were collected for analysis.

Images were analysed using scripts generated in Matlab (Mathworks) by Dr Wei-Feng Xue (360). The script automatically picks fibrils from image surfaces to avoid subjective analysis of sample distributions. In order to correct for the inherent bias in favour of analysing short fibrils, an empirical power function was applied to the distributions to correct for the under-representation of long fibrils (360). Long fibrils are more often excluded from the analysis due to reduced surface-deposition efficiencies and greater frequency in which long fibrils are cut-off by image boundaries or overlap with other fibrils. The bias correction factor is calculated by assuming that since the identical original monomer concentrations of samples under analysis, the average weight of material observed should be equal within each image.

2.2.6 Liposome dye release assay

Lipid films (all lipids were obtained from Avanti Lipids) containing 12 mol% bis(monooacylglycero)phosphate (BMP), 7 mol% sphingomyelin (porcine brain), 36 mol% 1-palmitoyl-2-oleoyl-sn-glycero-3-phosphocholine (POPC), 20 mol% 1-palmitoyl-2-oleoyl-sn-glycero-3-phosphoethanolamine (POPE) and 25 mol% cholesterol (ovine wool) and 0.1 mol% rhodamine-PE (for lipid quantification) were re-suspended in 50 mM sodium phosphate buffer, pH 7.4 containing 50 mM carboxyfluorescein, 10 mM NaCl and 1 mM EDTA and left overnight at 4°C. Up to four freeze-thaw cycles were performed the following morning using dry ice, prior to sonicating for 30 sec in a water bath. Free lipids at a concentration of 3.6 mM were

then extruded by passing through a 0.4 µm polycarbonate pore (Whatmann) up to 35 times to generate 400 nm large unilamellar vesicles (LUVs). LUVs were subsequently washed by successive rounds (up to 5) of centrifugation at 13,000 x rpm for 30 min at 4°C using a bench-top centrifuge and re-suspension of the lipid pellet in 50 mM citric acid/sodium phosphate buffer, pH 7.4 containing 107 mM NaCl and 1 mM EDTA (dye release buffer). After 5 rounds, the concentration of lipid was determined by comparing the rhodamine Abs_{595nm} from before and after the extrusion process using a UV-vis spectrophotometer. The concentration was adjusted to 0.5 mM in dye release buffer and LUVs were stored on ice prior to use withing 48 h.

For the dye release assay, 120 µM β_2m fibrils formed as described (section 2.2.4) were diluted 4-fold to 30 µM (monomer equivalent concentration) in duplicate samples to a final volume of between 50 – 100 µl in either pH 7.4 buffer (50 mM sodium phosphate buffer, containing 30 mM NaCl and 3 mM KCl) or pH 6.4 buffer (50 mM sodium phosphate buffer, containing 85 mM NaCl and 3 mM KCl) and incubated at 25°C for 30 or 60 min, respectively. The concentration of NaCl was altered to maintain an equivalent ionic strength between buffers of 164 mM, equivalent to that of commercial 1 x PBS. After the initial incubation period, one sample was syringe filtered using a 0.2 µM small-volume syringe filter (Millipore) to remove fibrillar material while the second identical sample remained untreated. 40 µl of either syringe-filtered or untreated sample was then added to 2 µl of 0.5 mM 400 nm LUVs diluted in 158 µl dye release buffer at pH 7.4 (for pH 7.4-diuted fibril samples) or the same buffer at pH 6.4 (for pH 6.4-diluted fibril samples) and incubated at 37°C for 10 min. Carboxyfluorescein dye release was then assayed by adding 1 ml of pH 7.4 dye release buffer before recording the emission at 513 nm after excitation at 492 nm using a PTI QuantaMaster spectrometer with excitation and emission slit widths set to 4 nm. 100% dye release values were then recorded for each sample by the addition of Triton X-100 to a final concentration of 0.25% (*v/v*). Normalised dye release values for each sample were then calculated using the following equation, where I_s is the fluorescence intensity of the sample, I_0 is the background dye release (carboxyfluorescein fluorescence from LUVs in the absence of fibril samples) and I_{100} is the fluorescence intensity after the addition of Triton X-100.

$$\%\ Dye\ Release = \frac{I_s - I_0}{I_{100} - I_0}$$

Detailed experimental protocols for dye release experiments investigating the effect of pH and lipid composition on the amplitude of dye release, and those performed in the presence of small molecules can be found in the following references (341, 342).

2.2.7 Kinetic stability assay

β_2m fibril stability was determined by diluting 120 μM pre-formed β_2m fibrils to 30 μM (monomer equivalent concentration) in either pH 7.4 buffer or pH 6.4 buffer pre-equilibrated to 25°C and each supplemented with 10 μM Thioflavin T (see Section 2.2.3 for detailed buffer composition). The assay was performed at 25°C in black, clear bottomed 96 well plates (Costar) at a final reaction volume of 100 μl. ThT fluorescence (excitation wavelength 440±10 nm, emission wavelength 480±10 nm) was monitored under quiescent conditions using a BMG Labtech Optima plate reader working in plate mode with a gain value of set to 75% of the total fluorescence signal of one of the sample replicates. ThT fluorescence was recorded for up to 360 min and curves were normalised to the highest ThT fluorescence reading of each sample, with a baseline value used from monitoring the ThT fluorescence of monomer controls recorded at equivalent concentrations under each condition. Curves were best fit to the double exponential function shown below using OriginPro v8.6, where A and k_1, and B and k_2 are the amplitude and rate constant associated with the first and second exponential phases, respectively. Rate constants for samples from both pH values were calculated from at least six independent measurements.

$$y = -A.e^{-k_1 t} + Be^{-k_2 t} + c$$

Variations of this experiment, such as those presented in the presence of Hsp70, using diazirine-labelled β_2m-containing fibrils, or at increased β_2m monomer equivalent concentrations, were performed using an identical experimental set up to that outlined above with a constant ThT:β_2m molar ratio. Where the initial concentration of fibrils within the assay, the buffer used, or temperature is different to that outlined above it is indicated in the text. All experiments were analysed using baseline ThT fluorescence values obtained from controls of the exact composition of

the sample except substituting fibrils for the monomer equivalent concentration of native β_2m. All curves plotted are an average of at least three independent replicate measurements.

2.2.8 Soluble release assay

The release of soluble material was quantified by densitometry from SDS-PAGE gels made and electrophoresed as described in section 2.2.1.4. Multiple aliquots of 120 μM pre-formed fibrils were diluted to 30 μM (monomer equivalent concentration) in either pH 7.4 or pH 6.4 buffer (see section 2.2.6 for detailed buffer composition) to a final volume of 50 μl and incubated at 25°C under quiescent conditions. Samples diluted in pH 7.4 buffer were syringe filtered using a 0.2 μm reduced volume syringe filter (Millipore) 0, 2, 5, 10, 20, 40, 60 or 120 min after the initial dilution, or 0, 10, 20, 40, 60, 90, 120, 150 min for samples diluted in pH 6.4 buffer. 10 μl of each filtrate was then prepared for gel electrophoresis as described in Section 2.2.1.4 along with three standards containing known amounts of β_2m of 1.25 μg, 0.625 μg and 0.3125 μg. Standards were prepared by diluting samples of native β_2m quantified using Beer-Lambert's law (Section 2.2.1.1). Gels were stained and de-stained as previously described and the mass of β_2m released from fibrils and isolated by filtration was calculated by quantifying the intensity of bands on gels using Gene Tools. The known sample volume loaded for each sample was then used to determine the concentration of released β_2m from a linear calibration curve constructed from the band intensities of the three standards plotted versus their known protein masses.

2.2.9 Diazirine labelling of β_2m

Diazirine labelling of β_2m was performed by diluting purified β_2m to between 5 – 10 $mg.ml^{-1}$ in 25 mM sodium phosphate buffer, pH 7.2. Immediately before use, succinimidyl 6-(4,4'-azipentanamido) hexanoate (LC-SDA Diazirine, Pierce Net) was dissolved in 18 MΩ water to a concentration of 7.66 mM. LC-SDA diazirine was then added to β_2m in a 10-fold molar excess over the β_2m concentration and left to react at room temperature for 15 minutes with infrequent agitation. Excess LC-SDA diazirine was quenched to arrest labelling by adding a 5-fold molar excess of Tris.HCl pH 8.0. Excess label was removed using a PD-10 desalting column

previously equilibrated with 25 mM sodium phosphate buffer, pH 7.2 (GE healthcare) according to manufacturer's instructions. An aliquot was prepared for ESI-MS by diluting to between 50 – 100 μM in 50 mM ammonium bicarbonate, pH 7.2 and buffer exchanging using a Zeba spin desalting column (Piercenet, 7 kDa cut-off) according to manufacturer's instructions. Labelling stoichiometry was confirmed by ESI-MS operated as outlined in Section 2.2.1.6. Diazirine-labelled β_2m was then concentrated using a Centricon 3 kDa cut-off centrifugal filter unit according to manufacturers, and stored at -80°C in 50 μl aliquots of between 800 – 900 μM by snap freezing in liquid nitrogen.

2.2.10 Incorporation of diazirine-labelled β_2m into seeded β_2m fibrils

To determine the maximum concentration at which diazirine-labelled β_2m could be incorporated into amyloid fibrils a titration was performed from 10% to 100% of diazirine-labelled β_2m into seeded fibril growth assays at a final total protein concentration of 120 μM. All fibril samples were prepared as outlined in Section 2.2.4 by substituting *wt* β_2m for diazirine-labelled β_2m for the appropriate diazirine-labelled β_2m concentrations. The amount of soluble material remaining in solution after 48 h of fibril growth was determined by ultra-centrifuging 20 μl samples of each titrant for 1 h at 4°C at 400000 x *g* (Sorvall). The concentration of protein in the supernatant was then determined using Beer Lambert's law (Section 2.2.1.1).

To ensure labelled protein was incorporated into β_2m fibrils, fibril pellets were re-suspended in 20 μl 18 MΩ water and 50 μl of hexafluoroisopropanol (HFIP) was added. Samples were incubated at 37°C 200 rpm for 5 min, heated to 55°C for 5 min with no shaking before returning to 37°C 200 rpm for an additional 5 min. Depolymerised fibrils were then lyophilised to complete dryness using a speedvac and re-suspended in 50 mM ammonium bicarbonate buffer pH 7.2. Samples were desalted using a Zeba spin desalting column (7 kDa cut-off) according to manufacturers instructions prior to analysis by ESI-MS as detailed in Section 2.2.1.6.

2.2.11 Photo-activation of diazirine-labelled fibrils

Cross-linking of diazirine-labelled β_2m-containing fibrils was photo-induced by UV irradiation for 20 min at 345 nm using a 6 watt hand-held UV lamp (Stratalinker)

(Figure 2.2.1). Samples were placed 1 cm away from the UV source in upturned lids cut from sterile 1.5 ml Eppendorf tubes. Samples were agitated every 2 min by gently pipetting solutions up and down. Cross-linking efficiency was determined by analyzing the production of higher order species by performing SDS-PAGE as outlined in Section 2.2.1.4. The dependence of the extent of crosslinking on the concentration of protein was also determined by serially diluting samples from 120 μM to 7.5 μM (monomer equivalent concentration) in fibril growth buffer (see section 2.2.2) prior to UV irradiation as outlined above. Aliquots of each sample were then prepared for SDS-PAGE by diluting each to the same concentration of 7.5 μM to facilitate comparative analysis of the degree of higher order cross-linking.

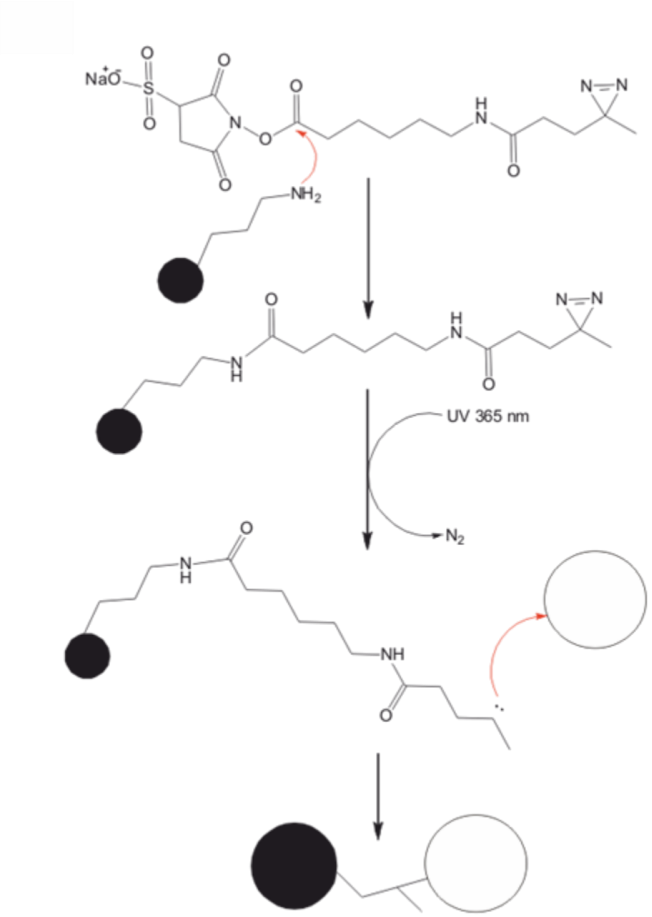

Figure 2.2.1 Schematic of photo-induced diazirine cross-linking. LC-SDA diazirine labels proteins on free primary amines such as lysine side chains through nucleophilic substitution of the NHS-succinimidyl ester. Once labelled, the diazirine moiety can be activated through UV irradiation, releasing N_2 gas to expose a reactive carbene centre. The carbene group can form non-specific intra- or inter-molecular cross-links with molecules within the radius of the carbon linker region. Circles schematically represent β_2m molecule labelled (black) or unlabelled (white) with the diazirine moiety.

UV cross-linking was then 'scaled-up' by photo-activating multiple 120 μM 100 μl aliquots of fibrils containing diazirine-labelled β_2m monomers as outlined above. The resulting cross-linked fibrils were purified from non-cross-linked material by diluting to 30 μM in pH 7.4 buffer (see Section 2.2.6 for buffer composition) and leaving to incubate overnight at 25°C. Remaining fibrillar material was pelleted by centrifugation at 16300 x *g* at room temperature for 30 min using a sorvall rotor. The concentration of protein within the supernatant was determined using Beer Lambert's law and fibrils were re-suspended to 120 μM in fibril growth buffer by assuming that all pelleted material was fibrillar in origin. The process was then repeated until no soluble material was detected in the supernatant after an overnight incubation. ThT fluorescence of several aliquots were monitored alongside by diluting cross-linked fibrils to 30 μM in pH 7.4 buffer supplemented with 10 μM ThT using a BMG Labtech Optima plate reader operating as described in Section 2.2.4 to show that once no soluble material is detectably released following an overnight incubation that ThT fluorescence had plateaued.

2.2.12 3-(4,5-Dimethylthiazol-2yl)-2,5-diphenyltetrazolium Bromide (MTT) cell viability assay

SH-SY5Y neuroblastoma cells were cultured in Dulbeccos Modified Eagles Medium (DMEM, Life Techonologies) supplemented with 10% (v/v) fetal calf serum, 1% (*w/v*) L-glutamine and 1% (*w/v*) penicillin/streptomycin at 37°C, 5% CO_2. 200 μl aliquots of a cell suspension containing 15,000 cells.ml^{-1} were plated out in 96 well plates (Nunc, Thermo Fisher Scientific, UK) and incubated for 24 h at 37°C 5% CO_2.

After 24 h, cell medium was removed and 1.2 μM fibril samples and controls were added in 200 μl of fresh DMEM (controls; 1.2 μM monomeric β_2m, 1% (*v/v*) fibril buffer, or 0.2% (*w/v*) NaN_3) prior to a further 24 h incubation at 37°C, 5% CO_2. After incubation with fibril and control samples, 20 μl of 5mg.ml^{-1} MTT was added and cells were incubated at 37°C, 5% CO_2 for a final 60 minutes. The cell medium was then removed and the resulting formazan crystals were solubilised in 50 μl dimethyl sulfoxide (DMSO) before measuring the absorbance at 570 nm with background cell debris light scattering at 650 nm subtracted.

For MTT assays performed in the presence of Hsp70 (recombinant Hsp70 was kindly provided by Toral Jakhria, University of Leeds), SH-SY5Y cells were prepared as above. Prior to the addition of samples, 0.3 μM or 3.6 μM Hsp70-1A was incubated with cells for 6 h. Medium was then removed and replaced with 200 μl fresh complete DMEM along with samples. Cells were then incubated and analysed as stated above.

2.2.13 Electrospray ionisation ion mobility spectrometry mass spectrometry of species formed during depolymerisation (ESI-IMS-MS)

The analysis of soluble species that form during depolymerisation of β_2m amyloid fibrils was performed using a Synapt HDMS (Waters, UK), which uses quadrupole-orthogonal acceleration time-of-flight (ToF) geometry and has an built-in travelling wave ion mobility spectrometry device for separating ions of same mass, or m/z ratio, but different cross-sectional areas. The samples were sprayed using the NanoMate Triversa (Advion Biosciences) automated injection and nanoESI interface. The instrument was operated in the positive-ion mode. The ESI conditions were optimized for the highest sensitivity detection of the multimeric complexes in the gas phase: transfer wave velocity = 150 m/s, transfer wave height = 5V, backing pressure (Synapt HDMS source pressure) = 5.5 mbar, sample cone voltage = 40-100V, trap collision energy = 6V, transfer collision energy = 4V and Trap gas flow rate of 5ml.min^{-1}. Chromatograms 2 min in length were combined and smoothed using the Savitzky-Golay method and *m/z* peaks were centered by mass using MassLynx software. For the quantification of soluble material, 1.2 μM bradykinin (Sigma) dissolved in 18 MΩ H_2O was added to the sample prior to ionisation. Peak centres corresponding to the bradykinin, Na^+-adducted and 2xNa^+-adducted ions were summed to provide a means of normalising ionisation efficiencies between independent samples. Peaks corresponding to β_2m 8^+, 7^+ and 6^+ charge states along with the same Na^+-adducted peaks as described above from either 12 μM β_2m controls prepared in 164 mM ammonium bicarbonate buffer, pH 7.4 or soluble material isolated 30 min after the dilution of 120 μM β_2m fibrils to 30 μM in 164 mM ammonium bicarbonate buffer pH 7.4 at 25°C were summed. The relative peak intensities were then normalised according to the difference in summed bradykinin peak intensities between controls and samples. Drift plots were constructed using

Driftplot software (Waters, UK).

2.2.14 Tracking native peak reappearance during fibril depolymerisation by NMR

NMR experiments were performed in collaboration with Dr Theo Karamanos (University of Leeds). In brief, fibrils composed 600 μM of uniformly-labelled ^{15}N *wt* β_2m (kindly provided by Dr Theo Karamanos) were grown quiescently at 25°C for at least 48 h using 0.1% (*w/w*) seeds outlined in Section 2.2.2. ^{15}N *wt* β_2m was prepared by protein expression in HDMI medium enriched with ^{15}N-labelled NH_4Cl (Table 2.2.2) . Expression and purification was carried out as described in Section 2.2.3.

Table 2.2.2 Reagents for the medium used to express ^{15}N-labelled *wt* β_2m.. All salts are made to 1L with 18 MΩ water and autoclaved in 2L flasks (when using the HDMI medium only 500mL of media are included in each flask to achieve better aeration of bacteria). Just before culturing, the HDMI medium was supplemented with the following filter sterilised supplements (added to each litre): 1M $MgCl_2$ (2mL), 1M $CaCl_2$ (100μL), 20% (w/v) D-glucose-$^{12}C_6$ (20mL). *Can be replaced by heavy isotopes.

	HDMI
Bacto-tryptone	
Yeast extract	
NaCl	
Na_2HPO_4-	7.5g
K_2HPO_4-	10g
K_2SO_4-	9g
KH_2PO_4-	10g
NH_4Cl*	1g

To initiate the reaction, samples were diluted *in situ* to 150 μM in either pH 7.4 buffer or pH 6.4 buffer supplemented with 10% D_2O (detailed buffer compositions available in Section 2.2.3). The appearance of NMR-observable species was monitored over time by SOFAST ^1H-^{15}N HSQC spectra (361) at 25°C using a Varian Inova spectrometer (Agilent) performed at a ^1H frequency of 750MHz, equipped with a cryogenic probe. The dead time of the experiment was 3-10 min

while the acquisition time of individual spectra varied between 10 – 15 min (4 and 8 scans per incremental delay, respectively). At least 20 sequential HSQC spectra were acquired under both conditions with a final acquisition performed 24 h after the initial dilution into pH 7.4 or pH 6.4 buffer. Spectra of ^{15}N-labelled native β_2m at a concentration of 50 μM were acquired in both pH 7.4 and pH 6.4 buffers and the assignments of native amide resonances were transferred from previously assigned spectra of native β_2m acquired under similar conditions (157). The same peak mapping technique was used for each HSQC spectrum and relative peak intensities (peak height from native amide resonances) were extracted using NMRview and plotted versus time on a residue-by-residue basis. The build-up of signal corresponding to the amide resonances due to the release of soluble material was fitted to the single exponential equation shown below using in house software written in Python by Dr Karamanos, where A and *k* and the amplitude and rate constant, respectively.

$$y = -A.e^{-kx}$$

Errors associated with the average rate constant for native amide reappearance are the standard deviation of all assigned native amide resonances that appear during fibril depolymerisation

2.2.15 Circular dichroism

120 μM β_2m amyloid fibrils formed as described in Section 2.2.4 were diluted to 30 μM in either pH 6.4 or pH 7.4 buffer at 25°C to initiate depolymerisation. Far-UV CD spectra were acquired after 30 min or 60 min after the initial dilution into pH 7.4 buffer or pH 6.4 buffer respectively using a Chirascan plus (Applied PhotoPhysics) over the wavelength range of 190 – 260 nm using a 1 mm path length Hellma cuvette. Spectra were also acquired for native β_2m samples at the equivalent concentrations as judged by SDS-PAGE under the same solution conditions. Scans were recorded at a rate of 60 nm.min^{-1} with 3 acquired spectra averaged for the final display. Buffer-only control spectra were also acquired and subtracted from the protein spectra.

2.3 Results

2.3.1 Purification and formation of *wt* β_2m amyloid fibrils

The purification of β_2m uses a well-established protocol that involves the refolding of β_2m from insoluble inclusion bodies formed during over-expression in *E.coli* (330). Refolding of β_2m was performed by first solubilising inclusion bodies in 25 mM Tris.HCl, pH 8.0, containing 8 M urea, prior to refolding by dialysis against 25 mM Tric.HCl, pH 8.0. The resulting refolded protein was then purified by anion exchange chromatography (ANEX) to remove contaminants using a self-packed Q-Sepharose column. Refolded β_2m typically elutes over a linear 0 – 400 mM NaCl gradient (Figure 2.3.1a – green line) at an approximate salt concentration of 200 mM. ANEX-purified β_2m was subsequently dialysed against water prior to freeze drying before the final stage of gel filtration purification. Figure 2.3.1b shows the typical elution profile of native β_2m when gel filtrated using a Superdex-75 column, with the peak eluting at an approximate volume of 200 ml corresponding to monomeric β_2m. The identity of protein eluting within the single peak was confirmed using ESI-MS, where the expected mass of β_2m of 11860 kDa was observed (Figure 2.3.1d). From 1 L of bacterial culture about 60 mg of purified native β_2m was routinely obtained. Figure 2.3.1c shows an SDS-PAGE gel

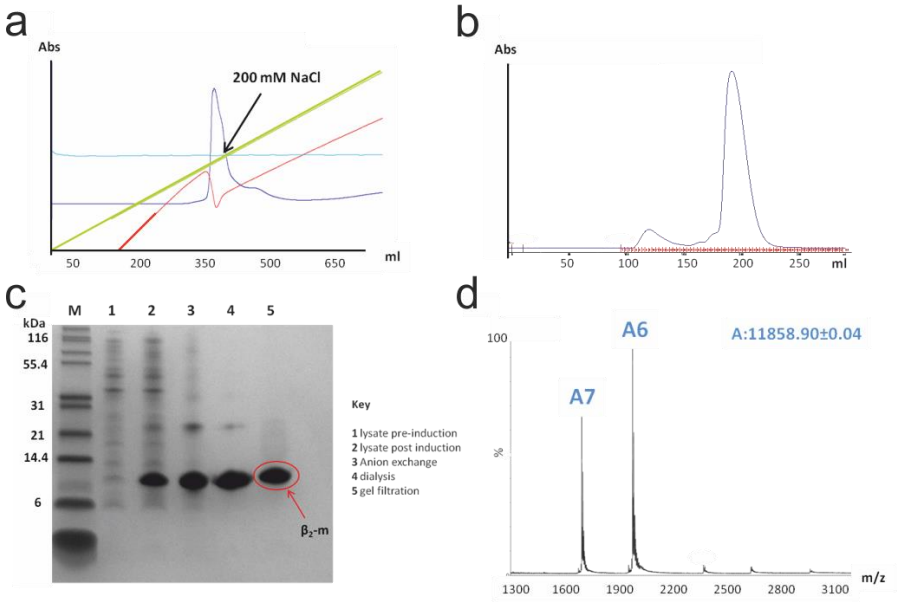

Figure 2.3.1 Expression and purification of *wt* β_2m. (a) Anion exchange chromatography of β_2m refolded from inclusion bodies. Blue trace = Abs_{280nm}, green line - linear increase in [NaCl], red trace - conductivity and cyan – temperature. (b) Elution of β_2m during gel filtration. (c) Enrichment of β_2m at each stage of the purification. (d) ESI-MS spectrum of purified β_2m. Expected mass of β_2m is 11860 Da. A7 and A6 denote the 7^+ and 6^+ charge states of ionised β_2m.

illustrating the sequential purification of β_2m through different stages of the protocol outlined in Section 2.2.3.

The morphology of amyloid fibrils formed from β_2m is ighly dependent upon the solution conditions used to promote aggregation. Different polymorphs can be obtained depending on the ionic strength under which aggregation takes place (155). For the purposes of these experiments, β_2m fibrils with a long-straight morphology were used. These were preferred over competing polymorphs due to the structural homology of these amyloid fibrils formed *in vitro* and fibrils isolated *ex vivo* from patients suffering from DRA (82).

Fibril formation was initiated by re-suspending 120 μM purified β_2m in 10 mM sodium phosphate buffer, pH 2.0, containing 50 mM NaCl (fibril growth buffer). Fibril formation was seeded under quiescent conditions at room temperature for a minimum of 48 h at a seed concentration of 0.1% (*w/w*) (seeds were made as described in Section 2.2.4). Seeding fibril formation means that the same fibril morphology can be propagated between independent samples, thus establishing a degree of consistency between separate experiments that may take place at different times and are performed with different samples. The conformation of β_2m amyloid fibrils formed under these conditions was observed using negative-stain transmission electron microscopy (TEM). Figure 2.3.2 shows a selection of seeded β_2m amyloid fibrils formed as outlined above using protein purified from Figure 2.3.1. Images

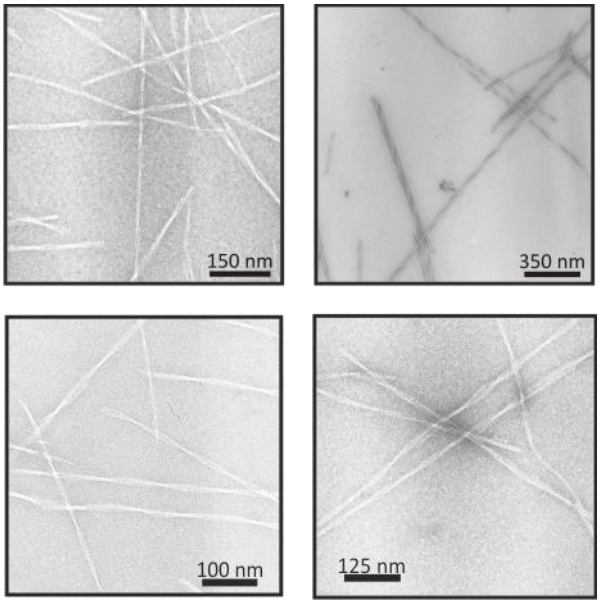

Figure 2.3.2 Negative-stain TEM of seeded β_2m amyloid fibrils.

display fibrils that are formed at various stages from my PhD and highlight the consistency of the morphology obtained from seeding fibril formation.

2.3.2 Characterisation of β_2m amyloid fibril length distributions

One of the fundamental principles elucidated for β_2m amyloid fibril-mediated cellular dysfunction is its length dependence, as outlined in the introduction (Section 2.1) (245). The analysis and biophysical characterisation of the length distribution of β_2m amyloid fibrils enables the description of the disruptive effects of amyloid fibrils on a more quantitative level. Therefore the characterisation of amyloid fibrils is an important process underlying the analysis of mechanisms of cellular disruption and *in vitro* processes, such as fibril-mediated membrane disruption.

In order to perform experiments evaluating differences in fibril activities based on length, seeded amyloid fibrils were fragmented for 48 h at room temperature on a custom-made precision stirrer set to 1,000 rpm. The distribution of fibril lengths was then quantified by imaging β_2m amyloid fibrils using atomic force microscopy ((AFM) Section 2.2.5). The resulting images were analysed and fibrils traced using scripts written in Matlab that extract fibril length distributions (FLD) (360). AFM analysis begins by initially identifying fibrils ends based on boundary differences in fibril height from the surface background. Only fibril ends that satisfy a particular width are taken forward in the analysis of fibril lengths, whereby the distance between two fibril ends that can be unambiguously traced will satisfy the criteria of being a fibril. Therefore, fibrils that overlap one another on the image surface, or are cut-off by image boundaries, will be excluded from analysis. Because fibrils exhibit length dependent surface deposition properties, a bias correction factor must be applied to correct for the underestimation of the population of longer amyloid fibrils in solution. Longer fibrils tend to clump during sample preparation and are more frequently interrupted by image boundaries, thus restricting the number of fibrils that can be unambiguously traced. The bias correction factor is calculated from the difference in the total length of fibrils traced from fragmented and un-fragmented fibril samples analysed by AFM (360). Therefore, the bias correction factor accounts for the differences in surface deposition properties of fibril populations that manifest in a perceived difference in the concentration of protein detectable on the AFM imaging surface.

After the application of the bias correction, FLDs generated from un-fragmented fibrils and 48 h fragmented fibrils have distribution profiles shown in Figure 2.3.3a. Each FLD is the sum of no less than 200 individually traced particles. Representative AFM images of each sample are shown alongside. The reproducibility of fibril fragmentation from seeded fibrils is highlighted in Figure 2.3.3b, by the similarity of FLDs measured from independent samples used in different studies. The average length of fibrils within un-fragmented samples is consistently 1.3 µm, while the average fibril length in fragmented fibril populations is 300 nm.

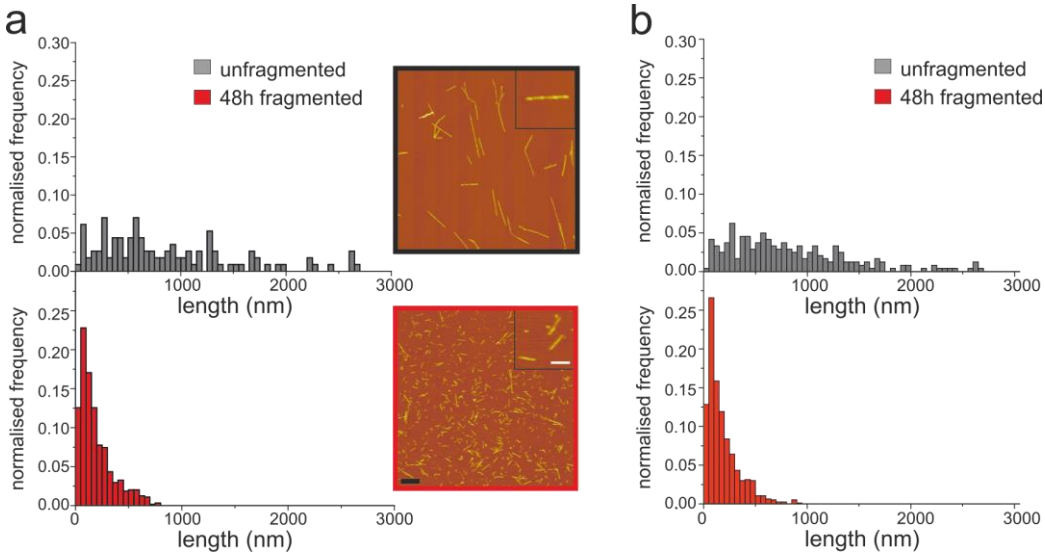

Figure 2.3.3 Fibril length distributions of unfragmented and fragmented β_2m fibrils. (a) Normalised frequency distributions of un-fragmented (grey) and 48 h fragmented (red) β_2m amyloid fibrils analysed by AFM. Representative sample images are shown alongside (black scale bar = 1 µm, white scale bar = 200 nm). (b) AFM fibril length distributions of fibril samples prepared from β_2m on a different day.

These fibril samples were subsequently used in the following investigations (340–342). Data presented in this and the subsequent results chapters do not focus on length dependent phenomena, however samples were prepared and characterised in the same manner as outlined above.

2.3.3 β_2m fibril-mediated membrane disruption is lipid and pH dependent

As detailed within the introduction to this chapter, β_2m amyloid fibrils cause length dependent metabolic dysfunction that is inhibited upon preventing endocytosis (340). This length-dependent behaviour is also observed *in vitro* using a liposome membrane disruption assay (245). The ability to prevent β_2m amyloid fibril toxicity upon restricting endocytosis (Figure 2.1.2) (340), the conservation of length dependent phenomena between *in vitro* and *in vivo* assays (245), and the generally

accepted view of the importance of amyloid-lipid interactions in mediating cellular dysfunction (23, 182, 196, 197, 204, 205, 207–209, 362, 363), inspired a systematic investigation into the effect of lipid composition on the ability of β_2m fibrils to induce liposome disruption, as measured using the carboxyfluorescein dye release (assay outlined in Section 2.2.6) (245, 341). Several complex lipid mixes consisting of 1-palmitoyl-2-oleoyl-sn-glycero-3-phosphocholine (POPC), 1-palmitoyl-2-oleoyl-sn-glycero-3-phosphoethanolamine (POPE), sphingomyelin and cholesterol, in addition to one of the following anionic lipid components, were made (Table 2.3.1). These included, 1-palmitoyl-2-oleoyl-sn-glycero-3-phospho-L-serine (POPS), 1-palmitoyl-2-oleoyl-sn-glycero-3-phospho-(1'-rac-glycerol) (POPG) and, bis(monoacylglycero)phosphate (BMP) (Figure 2.3.4). POPS is most highly enriched within the inner leaflet of the plasma membrane, POPG is a precursor of the mitochondrially enriched lipid cardiolipin, and BMP is a lipid that is found almost exclusively within the bilayer of endocytic compartments. BMP typically comprises ~15% of the total lipid composition of late endosomes (364–366), but can be found to comprise $\geq$ 70% of some lipid bilayers within the endocytic pathway (364–366). It is also a structural isomer of POPG (Figure 2.3.4). The different anionic lipids were incorporated into extruded 400 nm LUVS at 12 mol% or 50 mol% of the total lipid composition. The other components were chosen based on their ubiquity among biological membranes. Detailed compositions of lipid mixtures used in this section can be found in Table 2.3.1.

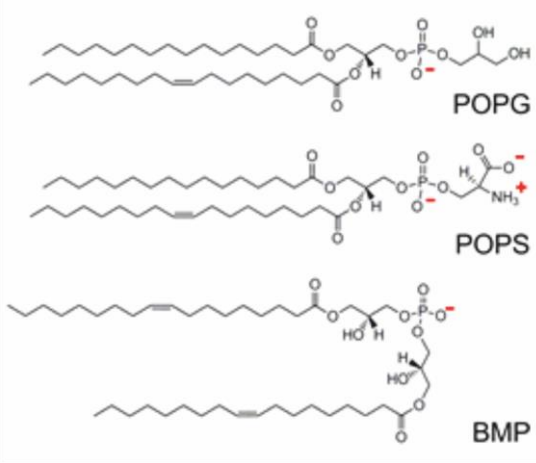

Figure 2.3.4 Structures of varied anionic lipid components

Table 2.3.1 Lipid composition in total mol % for the complex lipid mixes used to form LUVs. . LUVs containing 0 (control), 12 or 50 mol % anionic lipid component with the remaining lipid zwitterionic components in a mol/mol ratio of 36 POPC: 20 POPE: 7 SM: 25 cholesterol

Anionic Lipid[1]	POPC	POPE	sphingomyelin	cholesterol
0	41	23	8	28
12	36	20	7	25
50	21	11	4	14
[1] *Anionic lipid component: POPG, POPS or BMP*				

In addition to monitoring the extent of fibril-induced dye release from liposomes composed of these different lipid mixes, the effect of pH was also examined. Dye release experiments were performed at pH 4.5, 5.5, 6.4 and pH 7.4, which are the cellular pH values likely to be encountered by β_2m amyloid fibrils upon trafficking from the extracellular environment towards lysosomes. 400 nm LUVs were loaded with carboxyfluorescein at concentrations that promote self-quenching (50 mM), and the release of carboxyfluorescein into the surrounding buffer (as a consequence of membrane disruption) upon the addition of fibrils was then measured.

Figure 2.3.5 summarises the results of these experiments. They show that β_2m fibril-mediated membrane disruption is not only lipid specific, but is also pH-dependent. Firstly, LUVs containing 12 mol% (Figure 2.3.5a – dashed blue line) or 50 mol% POPS (solid blue line), display minimal membrane disruption in the presence of β_2m amyloid fibrils. In fact, the extent of membrane disruption is comparable to that of control LUVs lacking an anionic lipid component (Table 2.3.1, Figure 2.3.5a – black line). This can be most clearly observed in the bar graph in Figure 2.3.5a, which shows the extent of dye release at pH 5.5 for all samples. LUVs containing POPG or BMP, however, both display pH-dependent membrane disruption, with a dramatic increase in the extent of dye release from pH 7.4 to pH 6.4 in LUVs containing either 12 mol% or 50 mol% BMP (Figure 2.3.5a red dashed and solid lines, respectively) or 12 mol% or 50 mol% POPG (green dashed and solid lines respectively). The amplitude of dye release in LUVs containing 50 mol% POPG displays an additional small increase upon reducing the pH further to 5.5. The extent of membrane disruption within LUVs containing 50 mol% of either BMP or POPG decreases upon

reducing the pH further to pH 4.5. This pH-dependent trend is less pronounced for LUVs containing only 12 mol% BMP or POPG, where the dye release does not change significantly from that observed at pH 6.4 upon further mild acidifaction (Figure 2.3.5a dashed red and green lines respectively). The greatest extent of dye release is observed in LUVs containing 50 mol% BMP, which exhibit 60% membrane disruption at pH 5.5, approximately 1.5-fold greater than that observed for LUVs containing 50 mol% POPG at the equivalent pH. Controls performed using native β_2m monomer at equivalent concentrations do not display any membrane disruption activity (Figure 2.3.5b), confirming that liposome disruption is mediated by fibrils.

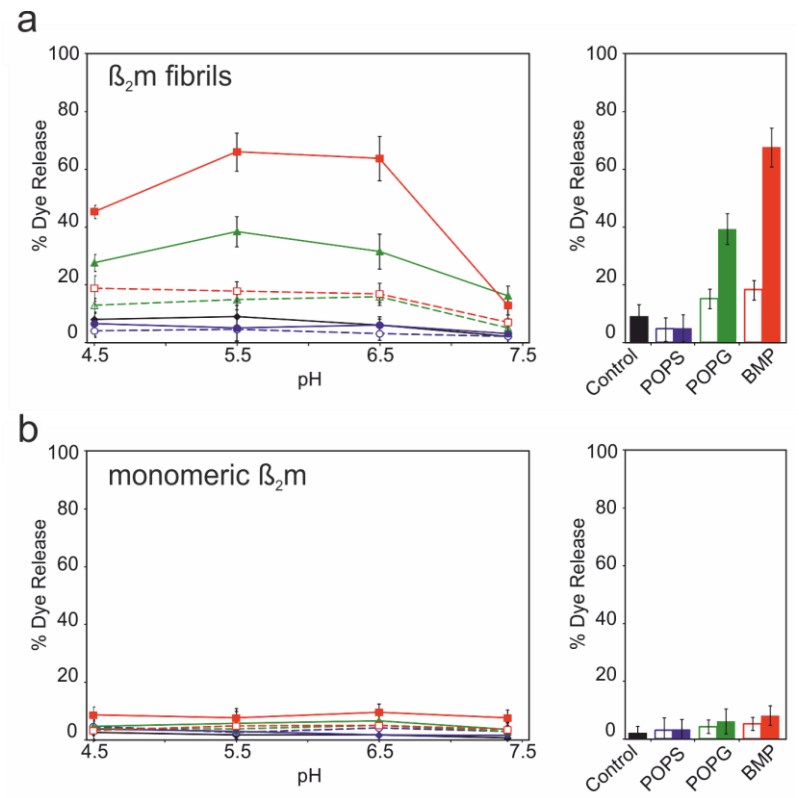

Figure 2.3.5 Lipid-specific and pH dependent β_2m fibril-mediated membrane disruption. Relative dye release induced by β_2m (a) fibrils and (b) native monomer for 400 nm LUVs containing 0 % (control, black), 12% (open symbols, dashed line) or 50% (solid symbol, solid line) POPS (blue), POPG (green) or BMP (red). The corresponding bar graph displays the dye release at pH 5.5 in the control (black), 12% (open bar) and 50% (solid bar) of POPG, POPS or BMP containing LUVs. Error on all values is SE from n=3, each of 3 replicates (341). Experiments performed by Dr Sophie Goodchild.

2.3.4 The role of fibril dynamics in membrane disruption

In parallel with this analysis, a separate study performed by Dr Tania Sheynis (University of Leeds, (342)) investigated the role of small molecules in modulating

the extent of β_2m amyloid fibril liposome disruption. The same carboxyfluorescein dye release assay was employed. These studies showed that in the presence of heparin, a known stabiliser of long-straight β_2m amyloid fibrils formed at low pH (78), the extent of dye release was significantly reduced (342). The reduction of membrane disruption was achieved without affecting the extent of fibril-lipid interactions (342). This raises the possibility that, although β_2m amyloid fibril-lipid interactions are known to take place (358), they may not directly mediate membrane disruption, but instead suggest that membrane disruption could be mediated by a species that forms from the amyloid fibril. Observations similar to this have been made before, such as the formation of 'reverse-generated' oligomers of $A\beta_{40}$ when fibrils interact with cellular membranes (367) (see Section 1.3.7) Therefore, to further probe the mechanism of fibril-mediated membrane disruption, the dynamic behaviour of β_2m amyloid fibrils upon dilution into pH 7.4 and pH 6.4 buffers was analysed – the two conditions in which the greatest difference in membrane disruption potential is observed (Figure 2.3.5).

To explore the role of fibril dynamics in membrane disruption, the response of amyloid fibrils upon dilution into pH 7.4 or pH 6.4 buffers was investigated in the absence of 400 nm LUVs. 120 μM β_2m fibrils formed at pH 2.0, as described in Section 2.2.4, were diluted to 30 μM in either 50 mM sodium phosphate buffer, pH 7.4, containing 35 mM sodium chloride (pH 7.4 buffer) or 50 mM sodium phosphate buffer, pH 6.4, containing 85 mM sodium chloride (pH 6.4 buffer, buffers possess equivalent ionic strength of 164 mM). The effect of diluting the fibrils into these conditions was monitored at 25°C using the fluorescent molecule Thioflavin T (ThT) (79). Upon dilution into either pH 7.4 or 6.4 buffers, β_2m fibrils show significant changes in ThT fluorescence, with an initial increase followed by a slow decrease of fluorescence, after 10 and 25 min respectively (Figure 2.3.6a and b). This biphasic behaviour can be described by a double exponential function, enabling quantitative kinetic information regarding the change in ThT fluorescence over time to be extracted (Figure 2.3.6b). The rate constants relating to both the enhancement and loss of ThT fluorescence are surprisingly similar between both conditions (Figure 2.3.6b), however a larger increase in the amplitude associated with the loss of ThT fluorescence is observed at pH 7.4, corresponding to 60% of the total kinetic amplitude compared with only 30% at pH 6.4, 200 min after dilution (Figure 2.3.6a).

The similarity between kinetic rate constants suggests that the underlying response of the fibrils is similar at both pH values, although the equilibrium has shifted significantly at pH 6.4 in favour of maintaining cross-β architecture.

To show that that the loss of ThT fluorescence does not simply result from fibril dilution, samples were diluted to the same concentration in pH 2.0 fibril growth buffer. Fibrils were then incubated at room temperature for 1 h alongside samples diluted to pH 6.4 or 7.4. After 1 h, the FLDs were determined using AFM to examine (a) how the loss of ThT fluorescence relates to the change in the distribution of fibril lengths and (b) to ensure that the FLD of samples diluted into fibril growth buffer remained unchanged. Figure 2.3.6c and d shows that upon dilution into pH 7.4 buffer or pH 6.4 buffer, the FLD is shifted significantly to shorter particles, indicating that fibril lengths have been globally reduced in comparison with the

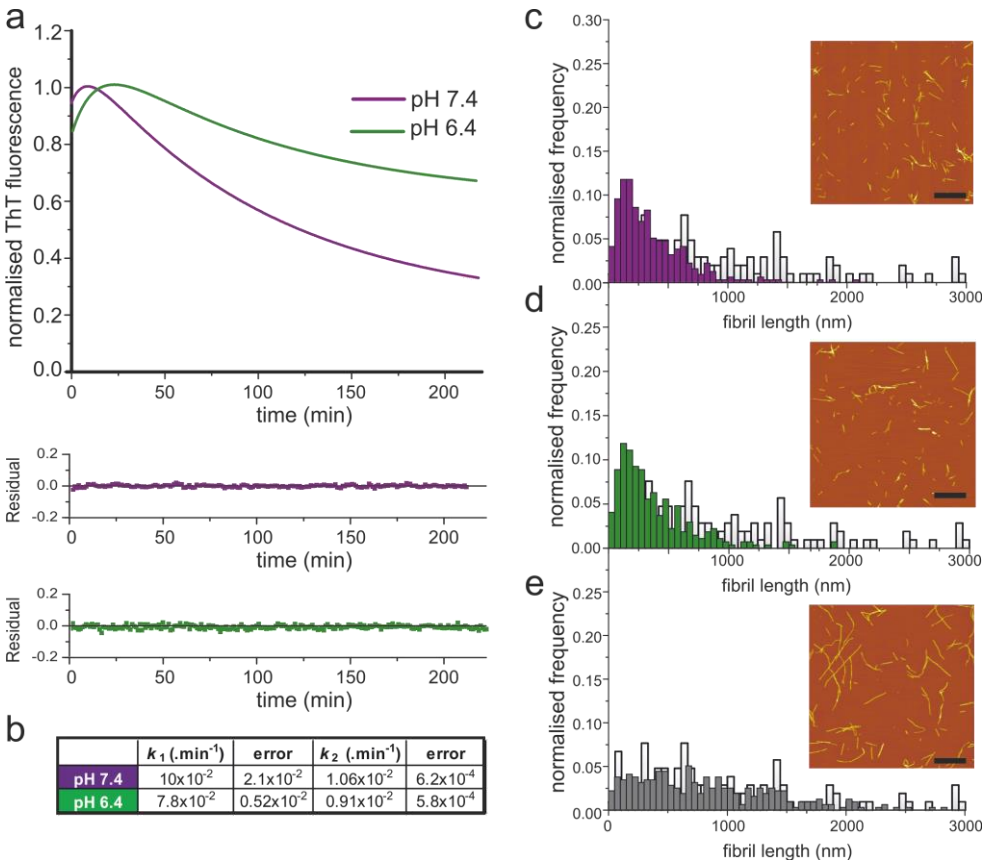

	k_1 (.min^{-1})	error	k_2 (.min^{-1})	error
pH 7.4	10x10^{-2}	2.1x10^{-2}	1.06x10^{-2}	6.2x10^{-4}
pH 6.4	7.8x10^{-2}	0.52x10^{-2}	0.91x10^{-2}	5.8x10^{-4}

Figure 2.3.6 Dynamic β_2m fibril behaviour upon dilution to higher pH. (a) ThT fluorescence kinetics of β_2m amyloid fibrils upon dilution into pH 7.4 buffer (purple) or pH 6.4 buffer (green) fitted by a double exponential function (residuals shown below curve). Curves are normalised to the highest ThT fluorescence reading within each curve Rate constants extracted from the fitting procedure are shown in (b). Errors are the standard deviation from fitting at least 5 independent curves from each condition. (c) AFM FLDs of β_2m 1 h after dilution at pH 7.4 (c), pH 6.4 (d) or pH 2 (e). The FLD of the original fibril sample used is shown plotted behind the FLDs in light grey. Scale bar = 2 μm.

original FLD (grey distribution shown behind in Figure 2.3.6c-e). Conversely, upon dilution and incubation of fibrils with fibril growth buffer, the FLD remains unchanged (Figure 2.3.6e). This indicates that the reduction in ThT fluorescence is specific to the increase in pH and reflects a reduction of fibril length.

Losing fibril mass would be to expected to result in the formation of soluble species. This was confirmed using a filter-trap assay. Fibrils were partitioned from soluble material at different times after the initial dilution at pH 7.4 or 6.4 by passing the solution through a 0.2 µm syringe filter. The amount of soluble material released was then quantified using SDS-PAGE as outlined in Section 2.2.8. After 0 min at pH 7.4 or pH 6.4, no soluble material is detectable in the fibril samples as judged by SDS-PAGE (Figure 2.3.7a and b respectively). This is consistent with previous results showing that ~100% of β_2m is incorporated into amyloid fibrils at low pH (146). The reappearance of soluble material over time is shown in Figure 2.3.7a-b along with the corresponding ThT fluorescence measurements from Figure 2.3.6. The amount of released soluble material has been normalised with respect to the total β_2m assay concentration of 30 µM. Under both conditions, a loss of ThT fluorescence correlates with the reappearance of soluble material (Figure 2.3.7a – pH 7.4 and b – pH 6.4). The greater amount of soluble material reappearing at pH 7.4 corresponds to the greater amplitude of the decrease in ThT fluorescence observed from the kinetic experiments (Figure 2.3.7). Thus, the loss of ThT fluorescence is due to fibril depolymerisation that yields soluble species induced by changes in pH.

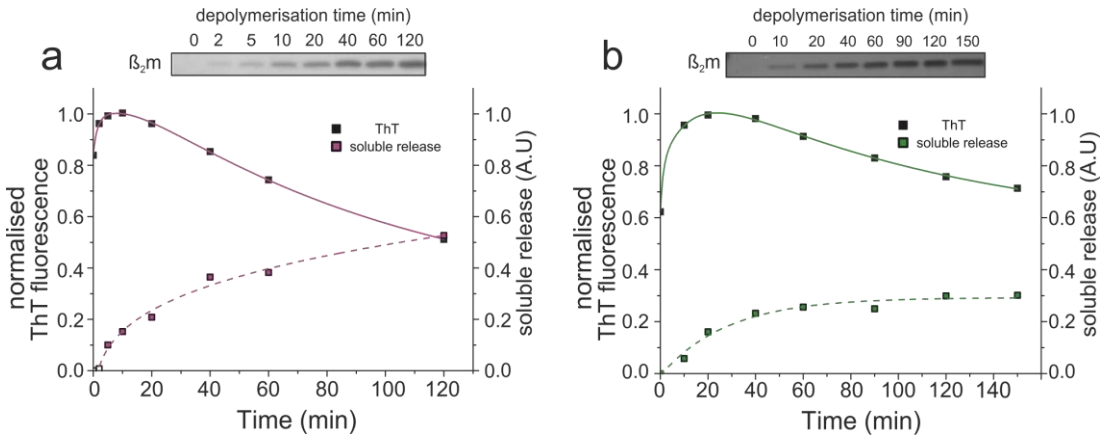

Figure 2.3.7 Soluble material reappears upon loss of ThT fluorescence. Normalised ThT fluorescence kinetics of β_2m amyloid fibrils incubated at pH 7.4 (a) or pH 6.4 (b, solid lines) and the corresponding production of soluble material quantified using SDS-PAGE densitometry (dashed lines, representative gel image shown above).

At present it is unknown why ThT fluorescence increases during the initial stages of depolymerisation. Upon dilution into buffers at near-neutral pH, β_2m amyloid fibrils are known to laterally associate (358). The change in environment may increase the fluorescence yield of ThT. Equally; β_2m fibrils may undergo conformational changes that create architectures with greater ThT binding affinities, or fluorescence quantum yields. Such changes in the fluorescence yield of ThT is known to take place for different amyloidogenic aggregates of β_2m (368). A solution-induced conformational change of the β_2m fibril structure is supported from CD analysis of fibrillar material. The negative λ_{max} shifts from 217 nm under fibril growth conditions (pH 2.0) to 225 nm, 30 min or 60 min after dilution into pH 7.4 or 6.4 buffers, respectively (Figure 2.3.8a and b). The reason for solution-induced conformational change in the fibril architecture is discussed in more detail in Chapter 4.

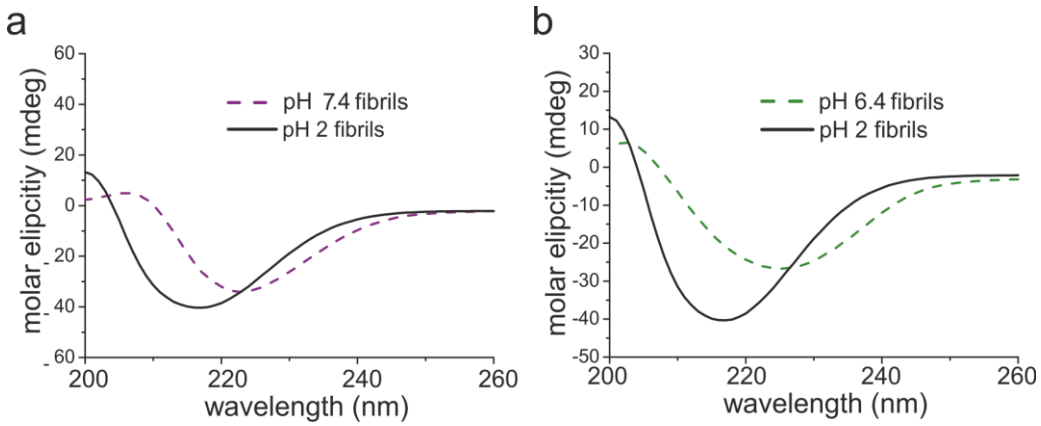

Figure 2.3.8 Conformational changes within β_2m amyloid fibrils upon changes in pH. CD spectra of β_2m amyloid fibrils under fibril growth conditions (black line) and 30 min or 60 min after dilution into pH 7.4 buffer (a – purple dash line) or pH 6.4 buffer (b – green dashed line) respectively.

The consequence of releasing soluble material during depolymerisation was next investigated by employing the carboxyfluorescein dye release assay with vesicles containing 12 mol% BMP and the complex lipid mix defined in Table 2.3.1. 400 nm LUVs containing BMP were used in these assays as they show the greatest amplitude of dye release (Figure 2.3.5a). In order to assay the membrane disruption potential of soluble species released from β_2m fibrils, duplicate samples were diluted to pH 7.4 or pH 6.4 before allowing depolymerisation to proceed for 30 or 60 min respectively. At these time points a similar amount of soluble material (~30%) has been released under both conditions (Figure 2.3.7a-b). Prior to adding LUVs to

samples, one replicate was filtered to remove fibrils from solution, thus allowing a direct comparison between the dye release potential of total protein (filtrate + fibrils) and filtrate (soluble material) to be made. Under both conditions, the dye-release potential of the filtrate accounts for 60 – 80% of the total dye release (Figure 2.3.9a – pH 7.4 and b – pH 6.4). Moreover, the extent of dye release increases ~ 2-fold from pH 7.4 to pH 6.4, consistent with previous observations (Figure 2.3.5).

To compare the membrane disruption potential of fibrils and soluble species, the extent of fibril-induced dye release was calculated by subtracting the % dye release of the filtrate alone from that of the total protein sample. Dye release potential was normalised to the amount of soluble material within each fraction by quantifying the protein concentration in partitioned filtrates using SDS-PAGE (gel inset, Figure 2.3.9a and b). The fibril concentration was calculated by subtracting the filtrate concentration from the total assay concentration. This shows that the filtrate generated at pH 6.4 has 5 times the membrane disruption potential of fibrils at the equivalent pH and is greater than 2-fold more membrane-active than the filtrate generated at pH 7.4 per µM of protein (Figure 2.3.9c). Native monomeric β_2m controls exhibit minimal dye release potential (Figure 2.3.9a - b). This suggests that depolymerisation must produce soluble, non-native, membrane-active species, the stability and concentration of which are significantly enhanced at pH 6.4.

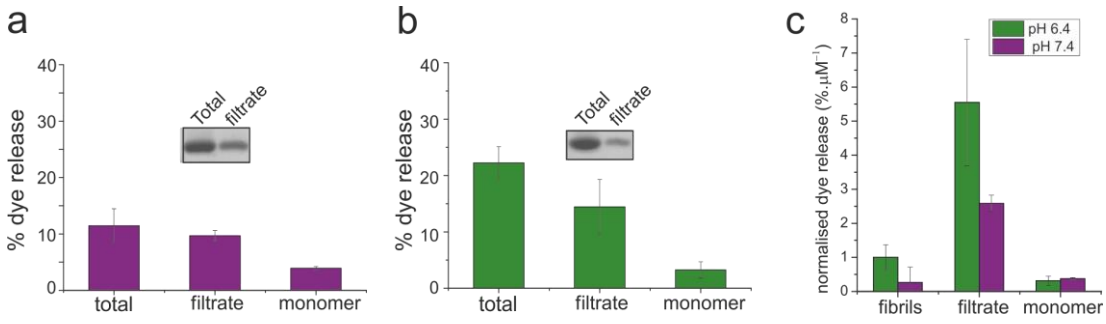

Figure 2.3.9 Soluble material causes membrane disruption. (a) Carboxyfluorescein dye release caused by β_2m amyloid fibrils and soluble material (total) and isolated soluble material (filtrate) 30 min after depolymerisation initiation at pH 7.4. (b) Dye release experiments of filtrate and total protein samples after 1 h of depolymerisation at pH 6.4. Native monomeric β_2m controls were performed at an identical concentration to total protein samples. (c) Dye release potential of fibrils only, filtrate and native β_2m monomers, normalised to protein concentration calculated by SDS-PAGE densitometry.

2.3.5 Reducing molecular shedding via chemical cross-linking alleviates β_2m fibril-mediated toxicity

To examine whether fibrils mediate metabolic dysfunction through the release of membrane-active soluble species, a cross-linking strategy was developed to prevent (at least in part) the depolymerisation of β_2m amyloid fibrils upon dilution into near-neutral pH buffers. The rationale behind the choice of cross-linking moiety was to promote intra- over inter-fibril cross-linking, thus ensuring fibrils remain diffuse, but depolymerisation is disfavoured. To this end, the amine reactive and pH independent photo-activatable cross-linking moiety LC-SDA diazirine was used, to enable cross-linking under fibril-growth conditions (Section 2.2.11). Diazirine-labelled native β_2m was incorporated into β_2m amyloid fibrils at 40% of the total protein without affecting the fibril morphology, or reducing the yield of incorporation of β_2m monomers into amyloid fibrils (Figure 2.3.10a and b). An ESI mass spectrum of

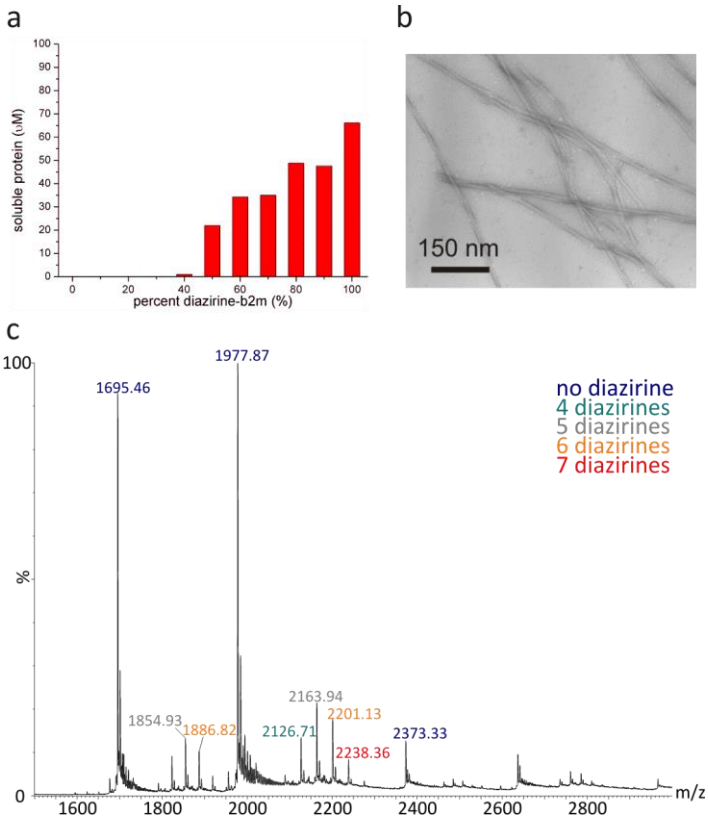

Figure 2.3.10 Incorporation of diazirine-labelled β_2m into β_2m amyloid fibrils. (a) Quantification of remaining soluble material after 48 h fibril growth with increasing % of Diazirine β_2m. (b) Negative-stain TEM of 40% diazirine-labelled β_2m monomer-containing fibrils. (c) ESI mass spectrum of HFIP depolymerised fibrils formed from 60% *wt* β_2m and 40% diazirine-labelled β_2m monomers.

HFIP depolymerised fibrils containing diazirine-labelled β_2m monomers is shown in Figure 2.3.10c. As β_2m contains seven lysine residues (and a reactive N-terminal amine), a range of stoichiometries of diazirine-labelled β_2m monomers are present in the fibrils. While the majority of molecules within the spectrum corresponds to unlabelled β_2m (no diazirine, mass of 11860 Da), peaks corresponding to diazirine-labelled β_2m with 4 (12756 Da), 5 (12980 Da), 6 (13204 Da) or 7 (13428 Da) conjugated diazirine moieties can be observed (Each diazirine label adds 224 Da of mass to β_2m). β_2m molecules with < 3 diazirine moieties are not observed. Thus, diazirine-β_2m can be successfully incorporated into *wt* β_2m fibrils formed at low pH.

To ensure that the stability of fibrils containing 40% diazirine-labelled β_2m monomers (without cross-linking by irradiation) is similar to that of *wt* fibrils under cell culture conditions, the kinetic stability assay was again employed (Section 2.2.7). The kinetics of depolymerisation of 1.2 μM *wt* fibrils and non-irradiated fibrils containing 40% diazirine-labelled β_2m were monitored within DMEM containing 10% (*v/v*) foetal bovine serum (FBS), 1% (*w/v*) L-glutamine, and 1% (*w/v*) penicillin/streptomycin (complete DMEM) at 37°C. The kinetics of depolymerisation were similar for both fibril samples (Figure 2.3.11a). There is also no significant difference in the reduction in metabolic activity in SH-SY5Y cells incubated with non-irradiated fibrils containing 40% diazirine-labelled β_2m monomers or *wt* fibrils, as judged by the MTT assay (Figure 2.3.11b).

Photo-activation of fibrils containing 40% diazirine-labelled β_2m monomers in fibril growth buffer yields a high molecular weight ladder of bands as judged by SDS-PAGE, indicating higher-order cross-linking has taken place (Figure 2.3.11c). Moreover, the degree of cross-linking is independent of fibril concentration, suggesting that cross-linking is predominantly intra-fibrillar (Figure 2.3.11c). UV-stabilised fibrils were then purified from non-cross-linked material through successive rounds of depolymerisation (Section 2.2.11) until a stable ThT fluorescence signal was observed upon dilution into pH 7.4 buffer (Figure 2.3.11d). Stabilised fibrils appeared well dispersed by EM, again supporting intra-fibril cross-linking, but were reduced in length (approximately > 0.5 μm) in comparison to the parent the fibril population (Figure 2.3.10b). UV-stabilised fibrils and *wt* fibrils were then incubated with SH-SY5Y neuroblastoma cells for 24 h at identical monomer-

equivalent concentrations of 1.2 μM. Cellular metabolic activity was measured using the MTT assay (Section 2.2.9). The results revealed that cells incubated with UV-stabilised fibrils experience a modest, but significant, reduction in the metabolic dysfunction caused by the presence of β_2m amyloid fibrils (Figure 2.3.11f). Thus, shedding of soluble material from fibrils appears to contribute towards β_2m fibril-mediated mechanisms of metabolic dysfunction.

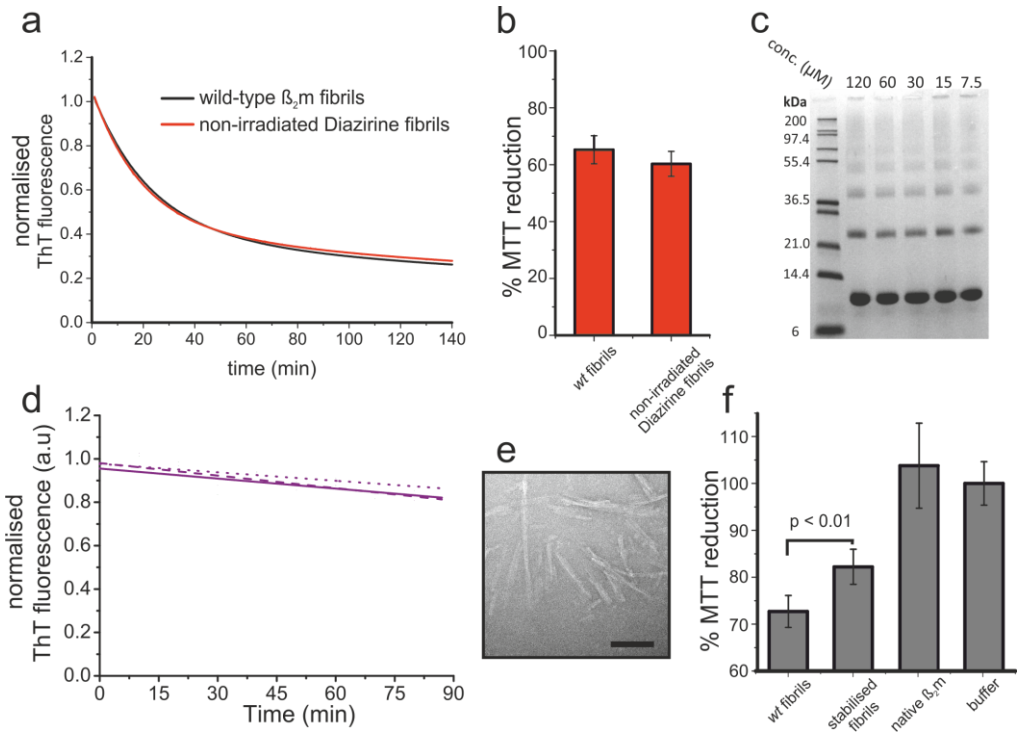

Figure 2.3.11 Diazirine stabilised fibrils display reduced cellular effects. (a) Comparison of kinetic stability of 1.2 μM non-irradiated fibrils containing 40% diazirine-labelled β_2m and *wt* fibrils incubated in complete DMEM at 37°C monitored by ThT fluorescence. (b) MTT reduction in SH-SY5Y cells in the presence of 1.2 μM *wt* or non-irradiated fibrils containing 40% diazirine-labelled monomer. MTT reduction is shown normalised to buffer-only controls (c) The concentration dependence of 40% diazirine-labelled monomer fibril cross-linking assayed by SDS-PAGE. (d) Kinetic stability of purified cross-linked fibrils in pH 7.4 buffer. (e) negative-stain TEM of cross-linked fibrils after purification by depolymerisation in pH 7.4 buffer (Scale bar = 100 nm). (h) % MTT reduction of SH-SY5Y cells treated with either 1.2 μM *wt* fibrils, stabilised fibrils, native β_2m monomer or buffer. Error bars are the standard deviation from 3 x 5 replicates.

2.3.5 Hsp70 reduces fibril depolymerisation and rescues fibril-mediated metabolic disruption

Many recent advances in identifying the mechanisms of toxicity in protein conformational diseases have shown that the aberrant association of aggregates with constitutive parts of the proteostatic network can have damaging consequences (233, 234, 311, 369, 370). As such, modulation of the proteostatic network, in particular

redressing proteostatic imbalance, has been touted as a promising therapeutic avenue for amyloid diseases (8, 51, 250, 310, 311, 371–375). The molecular chaperone, Hsp70, is expressed upon the induction of a wide range of cellular stresses (45). The inducible expression of Hsp70 has made this an attractive target to increase the protein-assisted protein folding capacity of a cell overwhelmed with amyloid aggregates (372). The association of Hsp70 (and its constitutively expressed homologue Hsc70) with aggregates has thus been intensively investigated (236, 239, 376–381). Here, recombinant Hsp70-1A (kindly provided by Toral Jakhria, University of Leeds – purified as detailed in (380) and herein referred to as Hsp70) was incubated with β_2m amyloid fibrils in a 1:0.25 and 1:3 molar ratio to investigate the effect of the chaperone on fibril depolymerisation kinetics monitored by ThT fluorescence (Section 2.2.7). Upon dilution of 120 µM β_2m fibrils to 1.2 µM in either pH 7.4 or 6.4 buffer at 37°C, Hsp70 rescues against the loss of ThT fluorescence in a dose-dependent manner (Figure 2.3.12a-b). More specifically, even at a 1:0.25 β_2m:Hsp70 molar ratio, the kinetic amplitude of the loss of ThT fluorescence after 200 min is reduced by 3-fold or 4-fold at pH 6.4 or pH 7.4 respectively, over fibril-only controls (Figure 2.3.12a and b). Incubating fibrils with a 3-fold molar excess of Hsp70 reduces significantly the decay of ThT fluorescence at pH 6.4 (although the initial increase in amplitude is still observed) and increases the ThT fluorescence at equilibrium to almost 80% of the initial ThT fluorescence intensity at pH 7.4 (Figure 2.3.12b). Therefore at both pH 6.4 and 7.4 Hsp70 is able to restrict β_2m amyloid fibril pH-induced depolymerisation.

To determine whether the stabilisation of β_2m amyloid fibrils upon interacting with Hsp70 reverses the metabolic defects induced by fibrils upon incubation with cells, the MTT assay was again employed. SH-SY5Y neuroblastoma cells were pre-incubated with either 0.3 µM or 3.6 µM Hsp70 for 6 h prior to adding 1.2 µM β_2m and incubating for a further 24 h (Section 2.2.12). Pre-incubating cells with Hsp70 allows the chaperone to localise to endocytic vesicles prior to the addition of β_2m amyloid fibrils. This should allow fibrils to be subsequently trafficked within the cell and promote *in situ* binding of amyloid fibrils and Hsp70 within endocytic compartments. Quantifying metabolic dysfunction 24 h after the addition of fibrils reveals a dose-dependent rescue in apparent cell viability, with 3 molar equivalents of Hsp70 reversing the metabolic dysfunction observed upon addition of β_2m fibrils

(Figure 2.3.12c). This dose-dependent rescue is similar to that observed in the kinetic stability assay (Figure 2.3.12a - b). In addition, recent experiments from our laboratory have shown that β_2m amyloid fibrils disrupt lysosomal function by reducing lysosomal proteolysis (340). Exogenously applied fluorescent ovalbumin localises to the lysosome and acts as a substrate for lysosomal proteolysis (340). Quantifying the fluorescence of ovalbumin 24 h after feeding the substrate to SH-SY5Y cells in the presence or absence of β_2m fibrils reveals that almost twice the amount of fluorescent ovalbumin persists when fibrils are present (Figure 2.3.12d). This indicates that fibrils impede the lysosomal proteolytic machinery. Here, pre-incubating cells for 6 h with Hsp70 before the addition of fibrils restores ovalbumin fluorescence levels after 24 h to those observed for buffer only controls (Figure 2.3.12d). This indicates that preventing the *in situ* depolymerisation of β_2m amyloid fibrils within endocytic vesicles may be responsible for reducing fibril-mediated metabolic dysfunction, further supporting the view that shedding of soluble species from fibrils is an important determinant of β_2m fibril-mediated metabolic dysfunction.

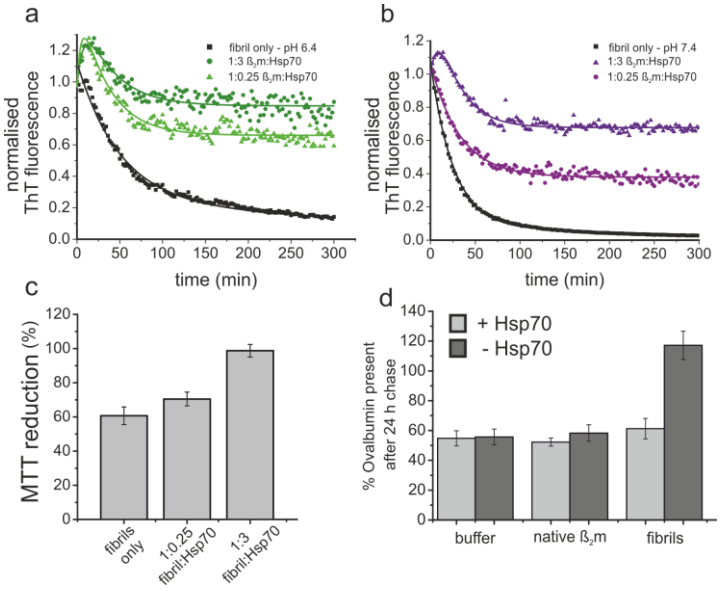

Figure 2.3.12 Hsp70 prevents disassembly and rescues against β_2m fibril-mediated deleterious effects. Kinetic stability of 1.2 μM β_2m amyloid fibrils at 37°C in the presence or absence (black) of 0.25 molar (triangles) or 3 molar (circles) equivalents of Hsp70 at pH 6.4 (a) or pH 7.4 (b). (c) % MTT reduction in cells incubated with 1.2 μM β_2m fibrils after pre-incubating with 0, 0.25 or 3 molar eq. of hsp70 for 6 h. (d) Lysosomal degradation assay performed with labelled Alexa647 labelled ovalbumin. After incubating cells for 6 h with 3 molar equivalents of hsp70, buffer, native β_2m or fibril samples were added to cells and incubated for a further 24 h prior to the addition of fluorescent ovalbumin. Fluorescence was quantified after 0 h 24 h by FACS. % fluorescence is expressed as a change in the levels from 0 to 24 h. Performed in collaboration with Toral Jakhria.

2.3.6 Detection of depolymerisation intermediates using ESI-IMS-MS

Having established that soluble species are responsible for liposome disruption and appear to mediate, at least in-part, the metabolic defects elicited by β_2m fibrils in cells, the next step was to elucidate structural properties of these species. To this end electrospray ionisation ion mobility spectrometry mass spectrometry (ESI-IMS-MS), a technique able to detect assembly intermediates on pathway to amyloid formation, was used (306–308, 382, 383). ESI-IMS-MS provides an even greater resolution than ESI-MS by separating species based on their shape/size in addition to their mass-to-charge ratio (*m/z*). This is performed by accelerating species after ionisation through an ion mobility 'drift' cell filled with an inert buffer gas (Figure 2.3.13). Collisions between molecules and the buffer gas slow the progress of ions in a manner dependent on their collisional cross section as they traverse the drift cell, thus separating species by shape/size. Therefore, ions with identical *m/z* ratio but distinct conformations (e.g. folded and unfolded monomer) can be resolved (Figure 2.3.13b). For higher order assemblies, ESI-IMS-MS can provide structural information by reporting on the size, collisional cross sections, and stoichiometry (384). Combining spatial information with mass measurements allows models to be built to approximate the morphology of oligomers detected within the gas phase (308, 382, 385). The relative success of employing this technique in studying

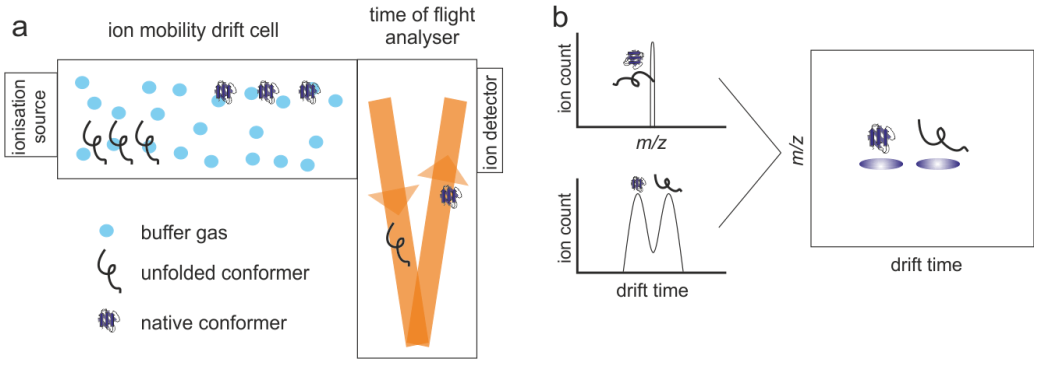

Figure 2.3.13 Schematic of ESI-IMS-MS. (a) Simplified schematic showing the essential features of an ion-mobility spectrometry mass spectrometer. Proteins are ionised at the ionisation source prior to being guided into the ion mobility drift cell where species are separated based on their size and shape. Collisions with an inert buffer gas retard the speed at which ions traverse the cell, with expanded, unfolded conformers exhibiting increased drift times in comparison with their compact natively folded counterparts. From the drift cell ions are separated in a time of flight (ToF) mass analyser based on their *m/z* ratio. (b) Illustration of the power of ion mobility resolve species with the same *m/z*. In the *m/z* graph the expanded and folded conformers appear as a single peak due to having the same *m/z* ratio. The drift time graph indicates the presence of two conformers. Combining the data allows the separation of ion based on *m/z* and drift time.

assembly mechanisms from several distinct amyloidogenic precursors was why ESI-IMS-MS was used to interrogate the species forming during β_2m amyloid fibril depolymerisation.

In order to study fibril depolymerisation using ESI-IMS-MS alternative buffers need to be used. Salts, such as NaCl, form adducts to proteins during the ionisation process, leading to a large spread in ion intensities due to the increase in heterogeneity of mass in the presence of the adduct ions. Therefore, buffers, such as ammonium bicarbonate are more desirable (volatile buffer), as buffer ions evaporate during the ionisation process. To test whether observations made in sodium phosphate buffers are equivalent in volatile buffers of identical pH and ionic strength, the kinetic stability of β_2m fibrils was monitored in 164 mM ammonium bicarbonate buffer (volatile buffer), pH 7.4 at 25°C. The rate of depolymerisation and appearance of soluble material were unaltered by the change to volatile buffer, as indicated by the good correlation between the loss of ThT fluorescence and appearance of soluble material, and the rate constants for the loss of ThT fluorescence calculated under both conditions (Figure 2.3.14a-b). Moreover,

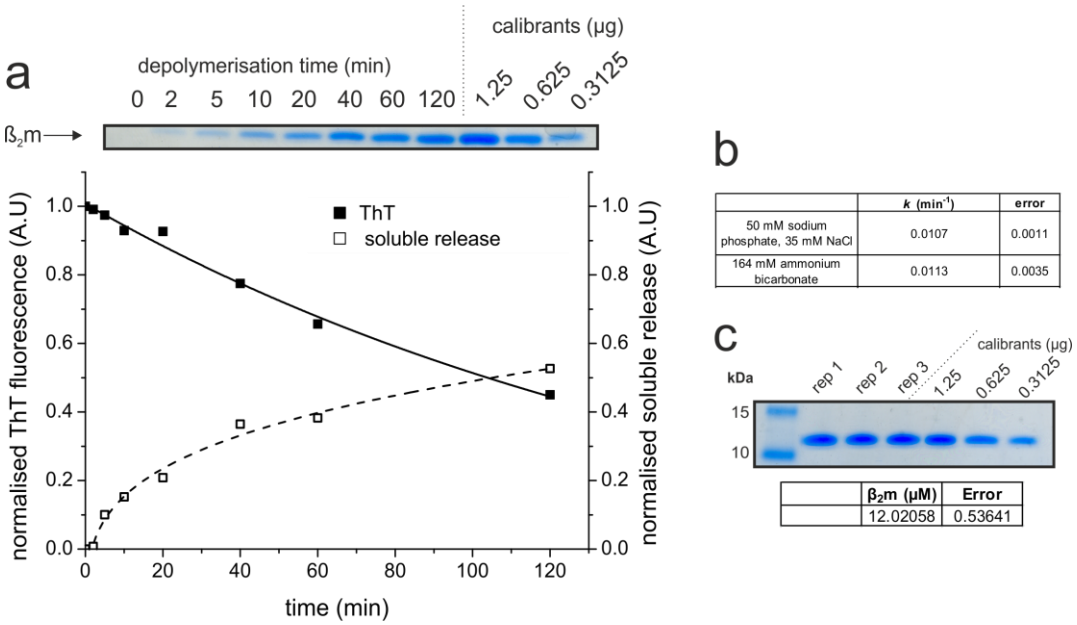

Figure 2.3.14 Fibril depolymerisation in volatile buffer. (a) SDS-PAGE of soluble material and the corresponding ThT fluorescence time points recorded during depolymerisation of β_2m in 164 mM ammonium bicarbonate buffer, pH 7.4. (b) Rate constants for the decay of ThT fluorescence during fibril depolymerisation in 50 mM sodium phosphate buffer, pH 7.4 containing 35 mM NaCl (salty buffer) and in volatile buffer, pH 7.4. Error is the standard deviation from a minimum of three independent replicates. (c) SDS-PAGE quantification of multiple replicates (reps 1-3) of soluble material partitioned 30 min after the initiation of depolymerisation in volatile buffer at pH 7.4. Error is the standard deviation of the three measurements.

partitioning and quantifying soluble material 30 min after the initiation of depolymerisation in pH 7.4 volatile buffer shows that 12 µM of protein is reproducibly released (Figure 2.3.14c). This is consistent with previous results (Figure 2.3.7) and further confirms the conservation of depolymerisation kinetics upon dilution into volatile pH 7.4 buffer. Depolymerisation kinetics were not monitored at pH 6.4 due to difficulties in buffering in volatile buffers at this pH.

To structurally probe soluble species released during depolymerisation using ESI-IMS-MS, spectra of soluble material partitioned after 30 min of fibril depolymerisation in volatile buffer were acquired (Section 2.2.13). Depolymerisation was initiated as previously described (Section 2.2.13) using fibrils formed at pH 2.0. Spectra of native monomeric β_2m under equivalent conditions and identical concentration were also acquired, to allow side-by-side comparison of species

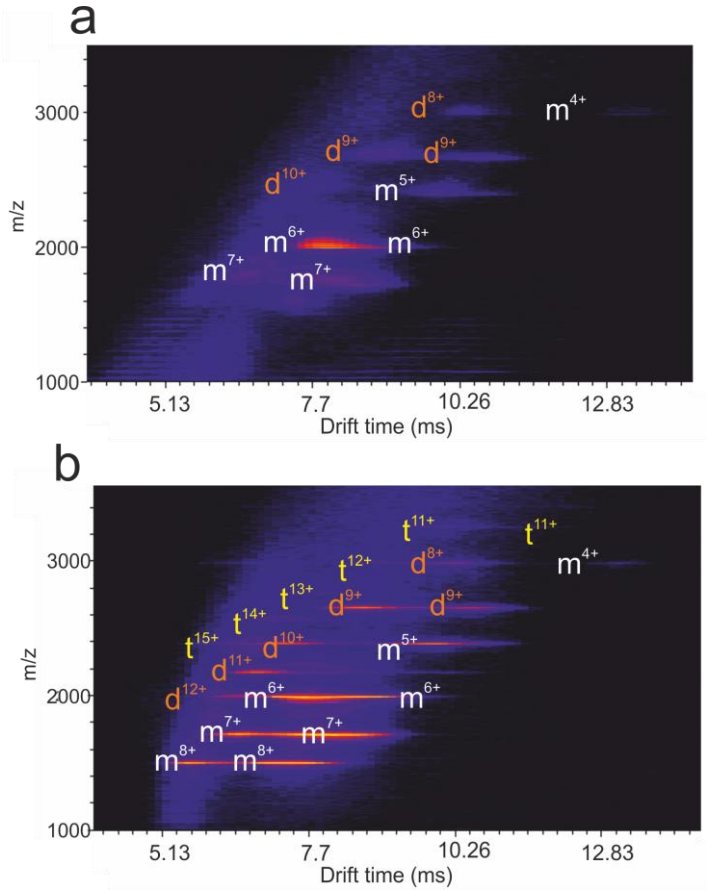

Figure 2.3.15 Drift plots of soluble material and native β_2m controls at pH 7.4. (a) Drift plot acquired 30 minutes after depolymerisation initiation in pH 7.4 volatile buffer and of (b) native β_2m controls performed at equivalent concentrations in the same buffer. Monomer, , dimer and trimer species are indicated by m, d and t respectively. The superscript number indicates the charge state of the ion.

formed during depolymerisation and those observed in native β_2m controls. Figure 2.3.15 shows that ESI-IMS-MS was not able to detect oligomeric species released from fibrils that are distinct from those formed in native β_2m controls. The oligomerisation of native β_2m (Figure 2.3.15b) taking place during ionisation and has been previously documented (383).

Control samples also appeared to possess a significant degree of unfolded monomeric protein as judged by ESI-IMS-MS. This is best observed for the monomer 8+ charge state (Figure 2.3.15b), as two clearly separated conformers are observed, with approximate drift times of 5 and 7.5 ms respectively. Unfolding of native β_2m in control samples is a consequence of the relatively high energy instrument parameters required to detect higher order species. Identical monomer control samples subjected to ESI-MS (section 2.2.1.6) show a different charge state distribution in comparison with the monomer charge state distribution collected under ESI-IMS-MS conditions (Figure 2.3.16). The base peak shifts from the 7+ to

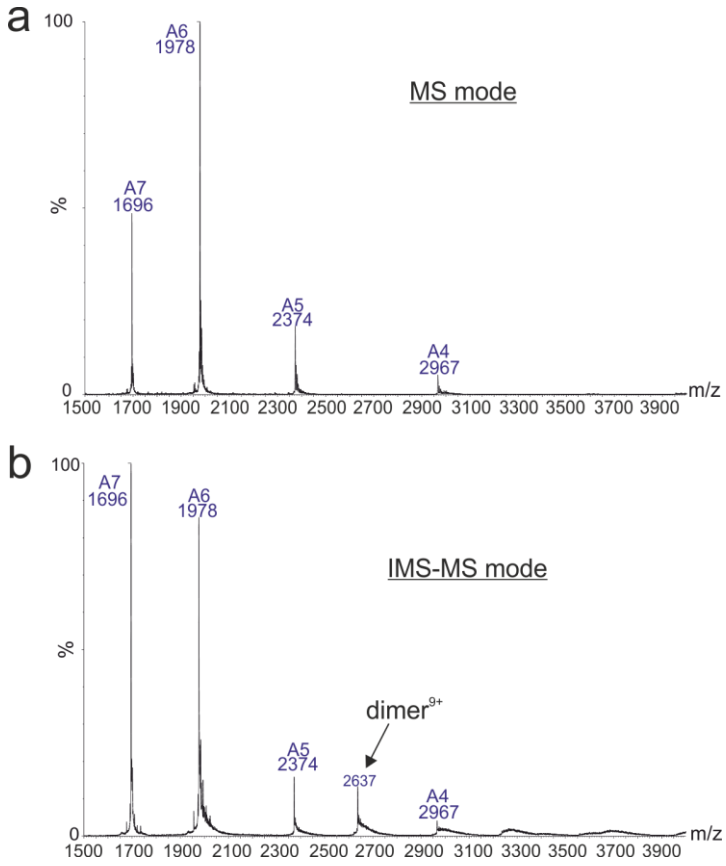

Figure 2.3.16 IMS parameters promote native β_2m gas phase unfolding. (a) *m/z* spectra of native β_2m in 50 mM ammonium acetate pH 7.4 in MS-mode and IMS-MS mode (b). Monomer charge states are labelled, with the charge state indicated by the number.

the 6+ charge state from IMS to MS mode (Figure 2.3.16), indicating ions are more compact when the drift cell is not employed. The acquisition of charge during sample ionisation is related to the fold of a protein, with a more expanded, or unfolded, conformer often displaying an increase in the number of ionisation charges (386).

Although ESI-IMS-MS was unable to detect oligomeric species whose formation is specific to fibril depolymerisation (Figure 2.3.15), comparison of the spectra show that soluble material partitioned during fibril depolymerisation is significantly reduced in peak intensity in comparison with native β_2m controls acquired at equivalent concentrations. (Figure 2.3.15). This suggests that oligomeric species may be present in the soluble material, but are not detected by ESI-IMS-MS. This may be because either higher order species released during depolymerisation are too heterogeneous to detect, or are not ionised under the conditions employed. The amount of detectable monomer within the soluble material was therefore measured quantitatively using ESI-MS so as to demonstrate whether oligomeric species may be present but undetected in samples analysed by ESI-IMS-MS. Quantitative ESI-MS was performed by incorporating bradykinin as an internal standard into soluble material and native controls prior to ionisation (Section 2.2.13, (387)). Normalising the ion intensity to the bradykinin internal standard shows that of the 12 μM soluble material determined to be in solution after 30 min of depolymerisation at pH 7.4 (Figure2.3.14b), only 25% was detectable in comparison with native monomeric β_2m controls acquired at equivalent concentration (Figure 2.3.17a-c).

To show that the loss of β_2m monomer peak intensities in spectra acquired from soluble material is due to the sequestration of β_2m into MS-unobservable species and not due to the incorrect calculation of the concentration of soluble material isolated during depolymerisation, samples and controls were lyophilised and re-suspended in the equivalent volume of acid denaturing buffer (H_2O containing 50% (*v*/v) acetonitrile and 0.1% (*v*/v) formic acid) (Figure 2.3.17d-e). Re-quantification of peaks under these conditions resulted in the detection 100% of monomer in the soluble material samples, with the overall ion intensity in good agreement with monomer controls (Figure 2.3.17a). This confirms that the lower ion intensity of

monomer in samples generated during fibril depolymerisation at pH 7.4 is not due to the incorrect calculation of the concentration (Figure 2.3.17a).

There are several possible reasons why higher order or, more specifically non-native species are not detectable by ESI-IMS-MS. Firstly, the lack of detection of higher order species could be due to the heterogeneous nature of amyloidogenic aggregates, with no one oligomeric state populated to a high enough concentration for detection by ESI-IMS-MS. Secondly, the presence of higher order aggregates may also affect

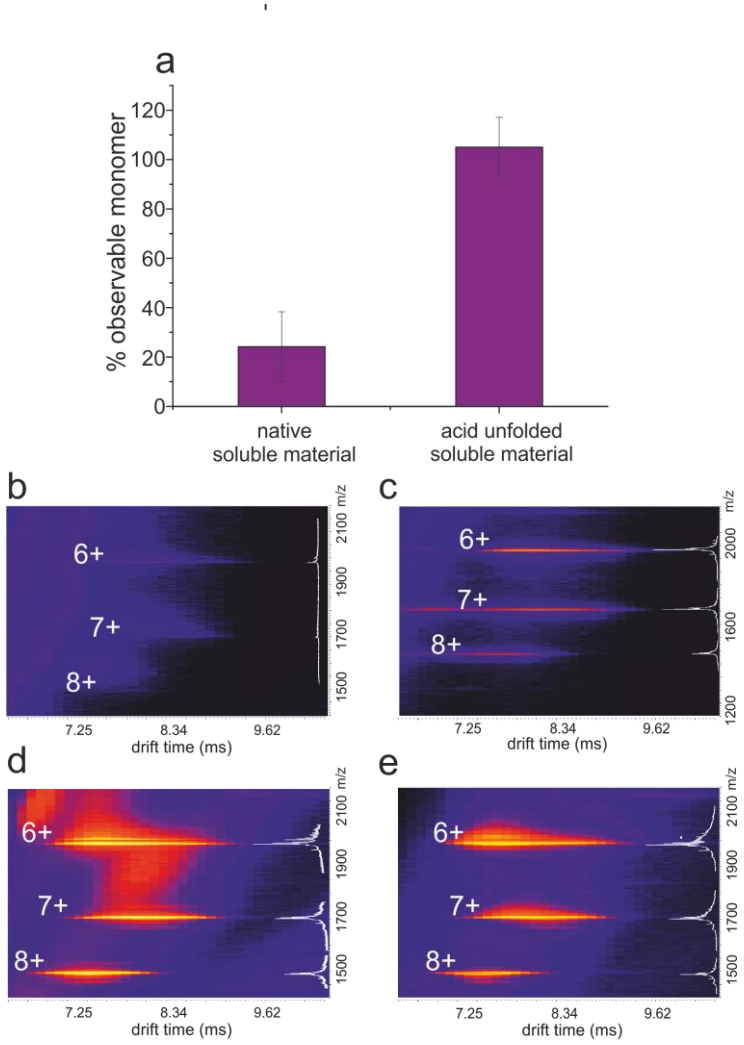

Figure 2.3.17 Quantification of monomer peak intensity during fibril depolymerisation. (a) The relative monomer intensity of soluble material ionised under native (pH 7.4 volatile buffer) and in acid unfolded conditions expressed with respect to the ion intensity of native β_2m controls acquired at equivalent concentrations. Example drift plots of soluble material and native β_2m controls acquired in native conditions (b and c respectively) and in acid denaturing conditions (d and e respectively). The $6 - 8^+$ monomer charge states used for quantification are labelled with the corresponding *m/z* spectra shown on the right-hand y –axis.

the ionisation of native monomer in solution, therefore generating artificially low detectable concentrations of native β_2m with respect to the total amount of protein present in the soluble material. Nevertheless, ESI-IMS-MS has illustrated the presence of non-native species accumulating during fibril depolymerisation at pH 7.4, as demonstrated by the reduced native β_2m ion intensity in comparison with native β_2m controls (Figure 2.3.17a).

2.3.7 Using NMR to probe differences in species formed during fibril disassembly

The experiments performed so far have indicated that the pH-dependent differences in liposome disruption potential of β_2m amyloid fibrils cannot be rationalised simply through the extent of the loss of cross-β structure (or ThT fluorescence). If anything, the loss of ThT fluorescence is inversely proportional to the membrane disruption potential of soluble material generated during depolymerisation, as soluble material at pH 6.4 has more than twice the membrane disruption potential than that generated at pH 7.4 per μM of protein (Figure 2.3.9c). As non-native species must populate during depolymerisation (since native monomeric β_2m is unable to cause membrane disruption (Figure 2.3.9) the species generated during depolymerisation at pH 6.4 are either distinct to those which form at pH 7.4, or are present in higher concentrations. As shown in the previous section, ESI-IMS-MS was not able to detect non-native species that form during fibril depolymerisation at pH 7.4. Therefore, in order to interrogate the formation and structure of soluble species generated during depolymerisation further, fibril depolymerisation was monitored in all-atom-detail using heteronuclear NMR (Section 2.2.12). NMR was chosen due to its ability not only to inform as to the reappearance of native monomer during fibril depolymerisation, but also because it enables the interrogation of the rate of production of native molecules during the fibril depolymerisation process. In addition, NMR may be able to detect i) small, non-native species that are significantly populated during depolymerisation, ii) identify residues within β_2m that may be important for the formation of non-native species and iii) allow the kinetics of depolymerisation to be probed in greater detail in the sodium phosphate buffers used thus far.

Under the current experimental conditions, the monomer equivalent concentration of β_2m used in depolymerisation experiments is likely to be too low in order to interrogate fibril depolymerisation. Fibril depolymerisation control experiments performed at pH 6.4 at significantly elevated concentrations show that the kinetics of fibril depolymerisation do not depend on the initial fibril concentration (Figure 2.3.18). Therefore, the initial monomer equivalent fibril concentration can be enhanced significantly to enable detection of species that form during depolymerisation using NMR.

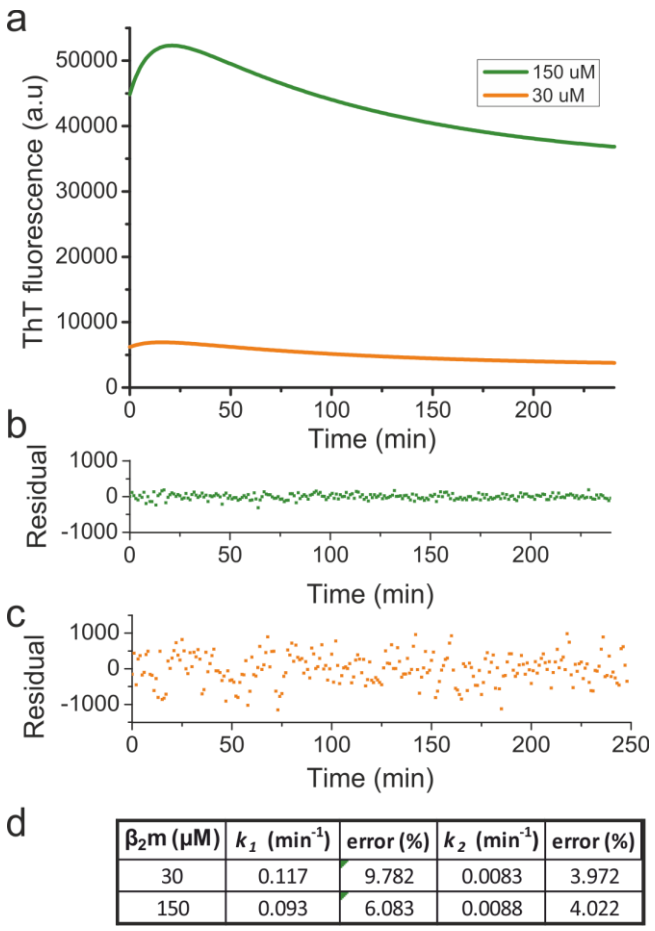

β_2m (μM)	k_1 (min^{-1})	error (%)	k_2 (min^{-1})	error (%)
30	0.117	9.782	0.0083	3.972
150	0.093	6.083	0.0088	4.022

Figure 2.3.18 The rate of fibril depolymerisation at a different initial fibril concentration. (a) Depolymerisation kinetics of β_2m amyloid fibrils monitored by ThT fluorescence. 600 μM or 120 μM β_2m fibrils were diluted 4-fold to 150 μM and 30 μM into pH 6.4 buffer at 25°C. The Traces show the fitted curve, with residuals shown in (b) for the 150 μM sample and (c) for the 30 μM sample. (d) Comparison of the two kinetic rate constants for the different fibril concentrations.

Measurement of the depolymerisation of β_2m fibrils using real-time NMR was performed by diluting 600 μM ^{15}N-labelled β_2m fibrils formed at pH 2.0 to 150 μM

in pH 7.4 or 6.4 buffer. ^{15}N – ^{1}H HSQC spectra were acquired at evenly spaced time intervals after depolymerisation was initiated (see Section 2.3.12). During early time points at pH 6.4, significant chemical shift differences are seen for a number of residues as compared with native-β_2m controls, including H84, K75 and R45 (Figure 2.3.19). These non-native peaks are not observed at later time points, presumably due to the accumulation of native β_2m amide resonances (black crosspeaks in Figure 2.3.19 – collected 3 h after depolymerisation was initiated in either condition). Notably, non-native chemical shifts are not observed during the initial stages of fibril depolymerisation at pH 7.4 (Figure 2.3.19 and Figure 2.3.20 – purple cross peaks). The acquisition time of individual spectra could not be significantly reduced in order to determine whether similar peaks populate during the initial stages of fibril depolymerisation at pH 7.4 (see Section 2.2.14).

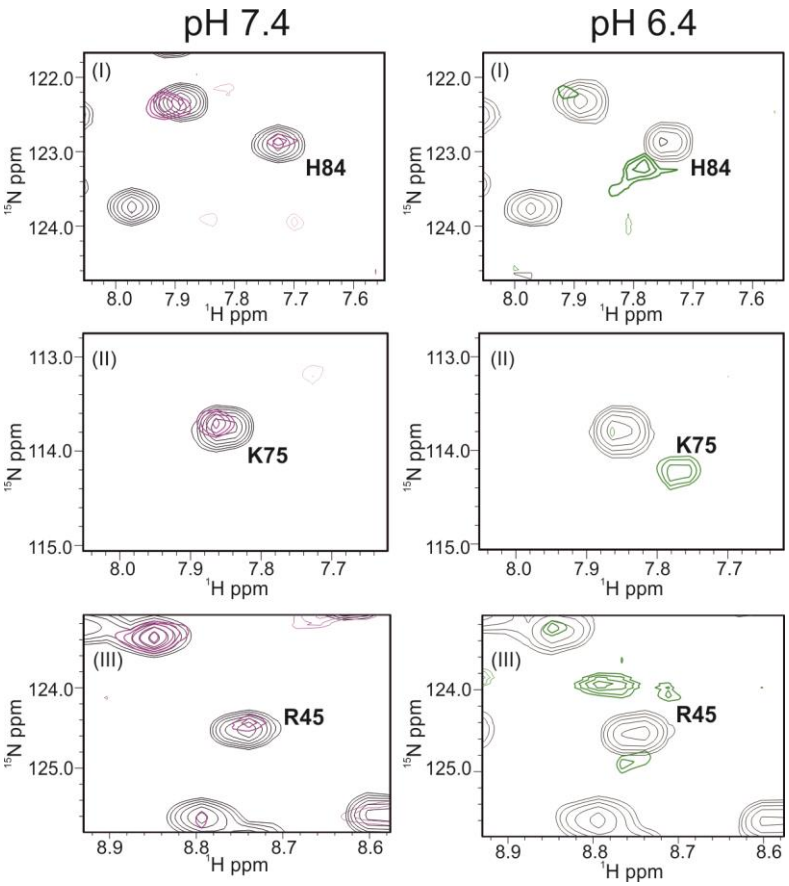

Figure 2.3.19 ^{15}N-^{1}H chemical shifts of resonances observed during the initial stages of fibril depolymerisation. Select regions of ^{15}N-^{1}H HSQC spectra collected 15 min after initiating depolymerisation at pH 7.4 (a) and pH 6.4 (b). Plots are overlayed with chemical shifts from the same region collected 3 h after depolymerisation was initiated (black). The identity of residues are labelled in the spectra

During the depolymerisation time course, the extent to which native amide resonances reappear is much greater at pH 7.4 than pH 6.4 (Figure 2.3.20). This observation is consistent with the increased amplitude of soluble material released during depolymerisation at pH 7.4, as monitored by SDS-PAGE (Figure 2.3.7). In addition, the detection by NMR of large amplitude of native monomeric β_2m

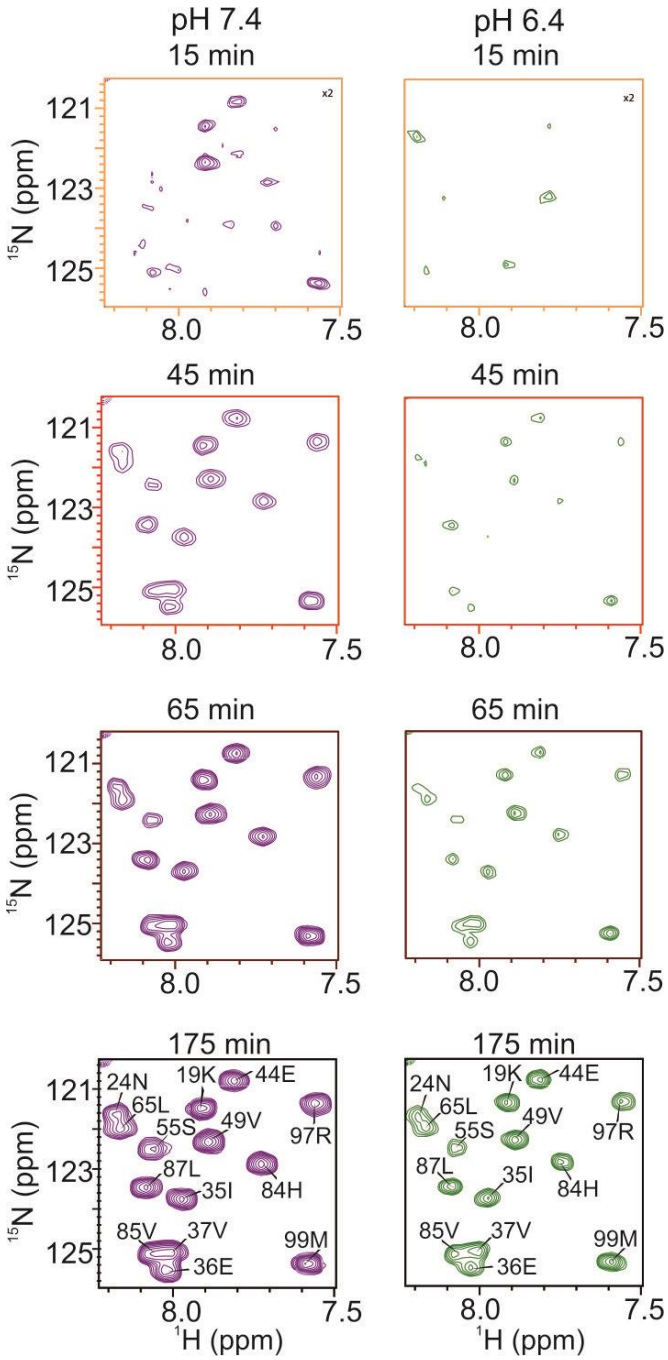

Figure 2.3.20 Reappearance of native amide resonances during depolymerisation of β_2m amyloid fibrils. Select region of ^{15}N-^{1}H HSQC spectra acquired during depolymerisation of 150 µM ^{15}N-labelled β_2m fibrils at pH 6.4 (green) or pH 7.4 (purple). Equivalent time points from each experiment are displayed with the identity of native amide resonances labelled on the t = 175 min spectrum.

reappearing during depolymerisation at pH 7.4 suggests that the presence of a small population of non-native species must prevent the ionisation of monomer during ESI-IMS-MS (Figure 2.3.15). This is as opposed to a large concentration of non-native species accounting for the reduced ion intensities of native β_2m charge states observed in comparison with monomeric β_2m controls.

Additional information can be extracted from NMR by calculating the rate at which native amide resonances reappear during fibril depolymerisation, by plotting peak intensity vs. time (Figure 2.3.20 and Figure 2.3.21). Native amide resonances in each spectrum were identified by peak mapping to spectra obtained of native β_2m controls assigned in identical solution conditions. Peak intensities for each amide resonance were then extracted and plotted vs. time (Figure 2.3.21) (Section 2.2.14) (157). Time constants for the reappearance of all assigned native amide resonances were then calculated by fitting the curves to a single exponential function (Figure 2.3.21) Plotting the resulting time constant on a per residue basis reveals that every residue of β_2m appears in the spectrum at a similar apparent rate (Figure 2.3.22). This is consistent with a global cooperative process for the formation of native β_2m during fibril depolymerisation. Native monomer reappears more rapidly during depolymerisation at pH 7.4 compared with pH 6.4 (average time constant of 101 min and 156 min respectively). Comparison of these time constants with those determined using ThT fluorescence shows the two rates are in excellent agreement at pH 7.4 (ThT – 91 ± 7.min, NMR – 101 ± 10.min; inter-experiment error calculated

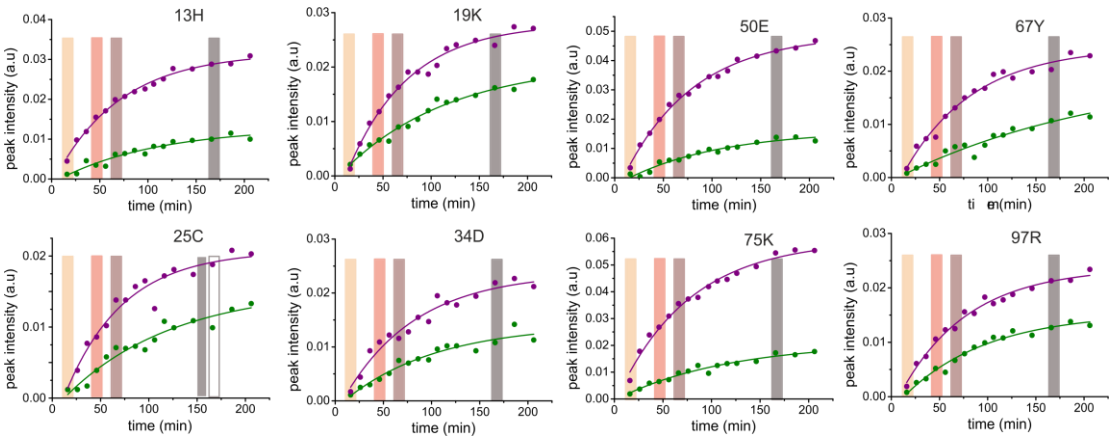

Figure 2.3.21 Extracting rates for the reappearance of native amide resonances during fibril depolymerisation. Peak intensities of native amide resonances identified by peak mapping (see section 2.2.12) were extracted from each HSQC spectrum collected during the depolymerisation time course at pH 6.4 (green) and pH 7.4 (purple). Coloured blocks indicate time points equivalent to sections of the spectra displayed in Fig. 2.3.20.

from two independent experiments). This suggests that the loss of fibrillar material after dilution at pH 7.4 results in the rapid formation of membrane-inactive, native β_2m. Non-native membrane-active soluble species must therefore exist transiently at low populations to explain why membrane disruption occurs for soluble material generated during depolymerisation at this pH (Figure 2.3.9). The presence of non-native species populating during depolymerisation at pH 7.4 is supported by the reduced ionisation during ESI-IMS-MS of native β_2m in soluble material generated during depolymerisation at pH 7.4 (Figure 2.3.15).

Comparison of the two rates at pH 6.4 however, reveals a significant difference between the loss of ThT fluorescence and the average rate of native amide resonance reappearance as judged by NMR (ThT – 110 ± 10 min, NMR – 158 ± 8.5 min; p < 0.001, student's t-test of unequal variance). This confirms that a non-native NMR-invisible, ThT-negative species, whose formation precedes that of native β_2m, must be significantly stabilised and persistent during fibril depolymerisation at pH 6.4. The enhanced stability and accumulation of non-native soluble species at pH 6.4 may explain why this filtrate is more than 2-fold more membrane-active per µM of soluble material than that generated during depolymerisation at pH 7.4 (Figure 2.3.9c).

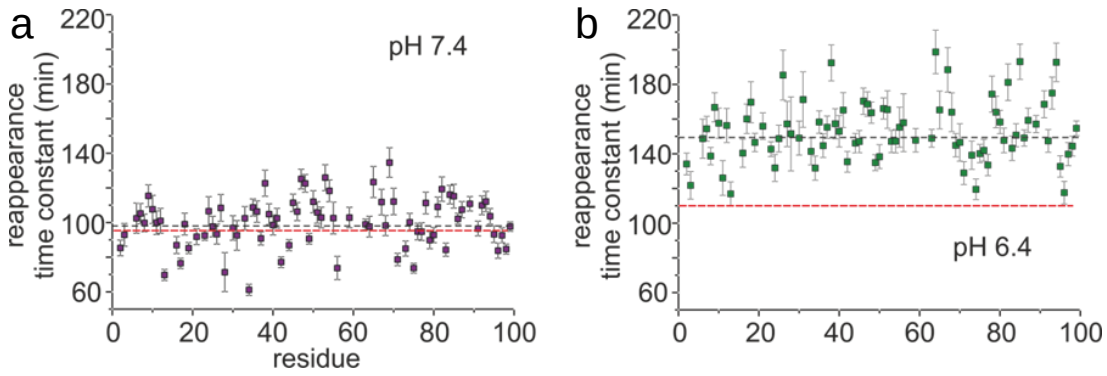

Figure 2.3.22 Per residue reappearance time constant extracted from NMR. (a) Native amide resonance peak intensities were extracted from ^{1}H-^{15}N HSQC spectra collected during the depolymerisation of 150 µM ^{15}N-labelled β_2m amyloid fibrils in pH 7.4 (a) or pH 6.4 (b) buffer. Black dashed lines represent the average amide resonance time constant for reappearance calculated by NMR. Red dashed lines represent the average time constant for the loss of ThT fluorescence.

2.4 Discussion

The results presented in this chapter establish the importance of β_2m amyloid fibrils in mediating liposome disruption and metabolic dysfunction through the molecular

shedding of membrane-active non-native species. Amyloid fibrils have previously been shown to recycle soluble species (188, 238, 242, 243) (as outlined in Section 1.3.7). However these examples show that the exchange of soluble species with amyloid fibrils takes place over long timescales under conditions which promote fibril formation (e.g. fibrils formed from the PI3 kinase SH3 domain exchange about half their molecules over a period of weeks (242)). In addition, not all of these were shown to recycle soluble species which demonstrate toxicity (238, 242, 243). There is evidence to support that recycling of soluble species from amyloid fibrils is a contributing factor to amyloid toxicity in living systems, as evidenced by the oligomeric halo of cytotoxic $A\beta_{1-42}$ oligomers radiating from fibril plaques in mice models of Alzheimer's disease (343, 388). In addition, membrane-induced amyloid fibril depolymerisation has also been shown to promote the release of 'reverse-generated' oligomers of $A\beta_{1-42}$, identical to those that form in the lag phase of amyloid assembly that are cytotoxic (249). The work presented here, however, is the first demonstration that amyloid fibril stability can be dramatically altered by subtle changes in pH to enhance/supress the formation of species that interact with, and damage, liposomes and contribute towards the onset of metabolic dysfunction. The surprising sensitivity of the fibril-intermediate-monomer equilibrium to subtle changes in pH suggests the latent cytotoxic capacity of an amyloid fibril can be fine-tuned by the cellular environment into which amyloid may be deposited (Figure 2.4.1). This phenomenon is likely to have important consequences for a number of amyloid diseases, as fibrils are trafficked to environments which are physiologically distinct from those in which they are initially formed (216–219, 268, 351).

More specifically to β_2m, the modest reversal in metabolic dysfunction in the presence of cross-linked fibrils is mirrored by a reduction in carboxyfluorescein dye release assay from BMP containing liposomes. In addition, the total membrane disruption potential is not fully accounted for by soluble species generated during the depolymerisation process (Figure 2.3.9). Therefore the fibril-membrane interaction previously characterised is likely to mediate a proportion of the membrane disruption from LUVs, and additionally facilitate toxicity in cells (358). This may also be why Hsp70-1A inhibits the metabolic dysfunction associated with β_2m amyloid fibril incubation; as not only does it prevent the molecular shedding of cytotoxic oligomers, but it may also mask the fibril surface which could contribute to the onset

of metabolic dysfunction. This illustrates the likely multiplicative toxic mechanisms exhibited in the presence of an ensemble of amyloidogenic structures.

By combining the results presented here with the known biological processes leading to β_2m amyloid fibril-mediated metabolic dysfunction (outlined in Section 2.1), a model of β_2m amyloid fibril-mediated cellular disruption can be constructed (Figure 2.4.1). This shows that, within the extracellular matrix or cell growth medium at ~pH 7.4, fibril depolymerisation/molecular shedding is rapid and results in the formation of native non-toxic β_2m. Coupled with a potentially unfavourable lipid composition low in BMP (indicated by the green bilayer. BMP is preferentially enriched within endocytic membranes), this could explain why β_2m fibrils do not disrupt the plasma membrane (340) or must be internalised in order to effect metabolic dysfunction (340). Upon internalisation, endosome maturation combines a lowering of the pH, which may increase the stability of membrane-active soluble species formed during depolymerisation, with an increase in the concentration of BMP within the bilayer (green to red bilayer). This would create a hotspot from which cellular dysfunction could manifest (red organelle). So far, however, there is no evidence to suggest that amyloid toxicity is mediated through the disruption of membranes in cells (245, 340, 349). The complexity of biological membranes however, means that the

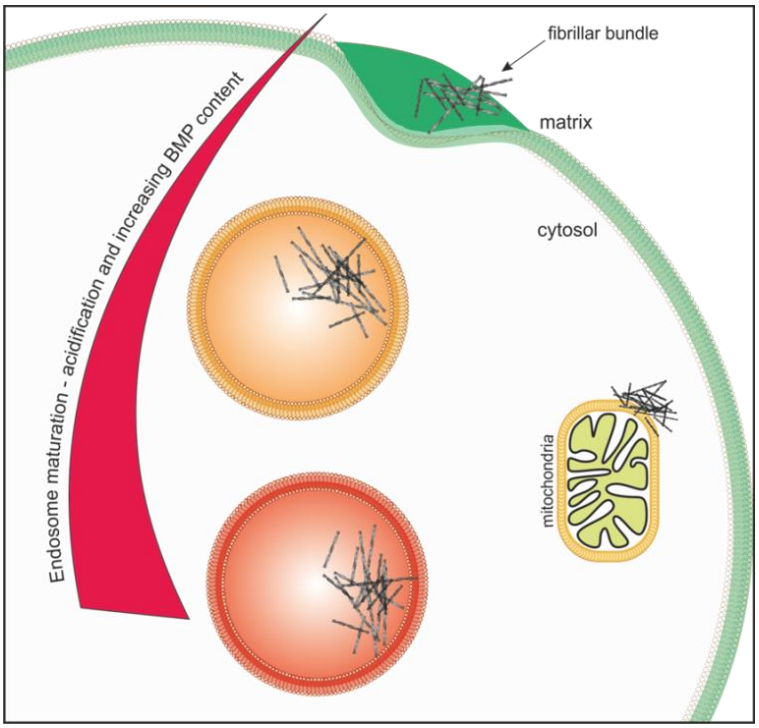

Figure 2.4.1 Hypothetical model of β_2m fibril-mediated toxicity.

consequences of amyloid-lipid interactions may manifest itself in entirely different consequences than simply the disruption observed in the carboxyfluorescein dye release assay.

Overall, the results presented in this chapter establish the pH–dependent formation of non-native soluble species that are responsible for the majority of fibril-mediated *in vitro* membrane disruption, and contribute to fibril-mediated metabolic defects. The next chapter will aim to elucidate the structural properties of soluble species generated during fibril depolymerisation by using fluorescence correlation spectroscopy, electron microscopy and a range of biochemical assays.

CHAPTER 3

Structural analysis of molecular shedded species

3.1 Introduction

3.1.1 Introduction to FCS and its advantages for the study of amyloidogenic systems

As evidenced from results presented in the Chapter 2, despite identifying chemical shift perturbations in early time point spectra acquired during fibril depolymerisation at pH 6.4, NMR was not able to provide structural information as to the identity of species formed through molecular shedding from β_2m amyloid fibrils. Equally, although ESI-IMS-MS is a powerful technique for analysing the stoichiometries and structural properties of oligomers that form in the lag phase of amyloid assembly (286, 306–308, 382), it could not detect non-native species that form during the depolymerisation of β_2m amyloid fibrils. Therefore another strategy was required to identify soluble species shed from β_2m fibrils that cause membrane disruption.

Assuming a high level of heterogeneity and low abundance of species that form during fibril depolymerisation, single molecule fluorescence correlation spectroscopy (FCS) was employed. FCS is a correlation based method which exploits fluctuations in fluorescent signals as molecules diffuse through a confocal volume (typically 0.1 fL) of known size (389). Due to the increased sensitivity of FCS over other diffusion based techniques (when properly optimised, picomolar concentrations can be detected) such as dynamic light scattering, and the ability to simultaneously correlate species that differ in size over several orders of magnitude, FCS is an ideal technique for studying and comparing the lowly abundant populations of highly heterogeneous species that form during fibril depolymerisation under different sets of conditions.

3.1.2 Single molecule fluorescence techniques for studying amyloid aggregation

Many single molecule fluorescence techniques are capable of analysing the complex ensembles formed during amyloid assembly. Although each technique is distinct, most provide similar information, such as oligomer stoichiometry, concentrations, and/or apparent hydrodynamic radii. One of the most powerful fluorescence methods currently in use is Two Colour Coincidence Detection (TCCD) (390, 391). TCCD is

a true single molecule fluorescence technique, as rather than relying upon the correlation of fluorescence signals within the residence volume, it instead relies upon coincident counting of fluorescence emission at different wavelengths after excitation by two different, spatially overlapping lasers (Figure 3.1.1a) (390). Equimolar concentrations of an amyloidogenic precursor labelled with either of two distinct fluorophores are incubated and then detected within the confocal volume. As aggregation proceeds, differentially labelled precursors will coalesce, resulting in a coincident fluorescent burst event (Figure 3.1.1b) (188, 238, 392). If the quantum yields of the dyes are known, then the amplitude of the dual emission can provide insights into the molecular weight of assembly intermediates. The frequency of signatory fluorescence emissions can also provide quantitative information regarding

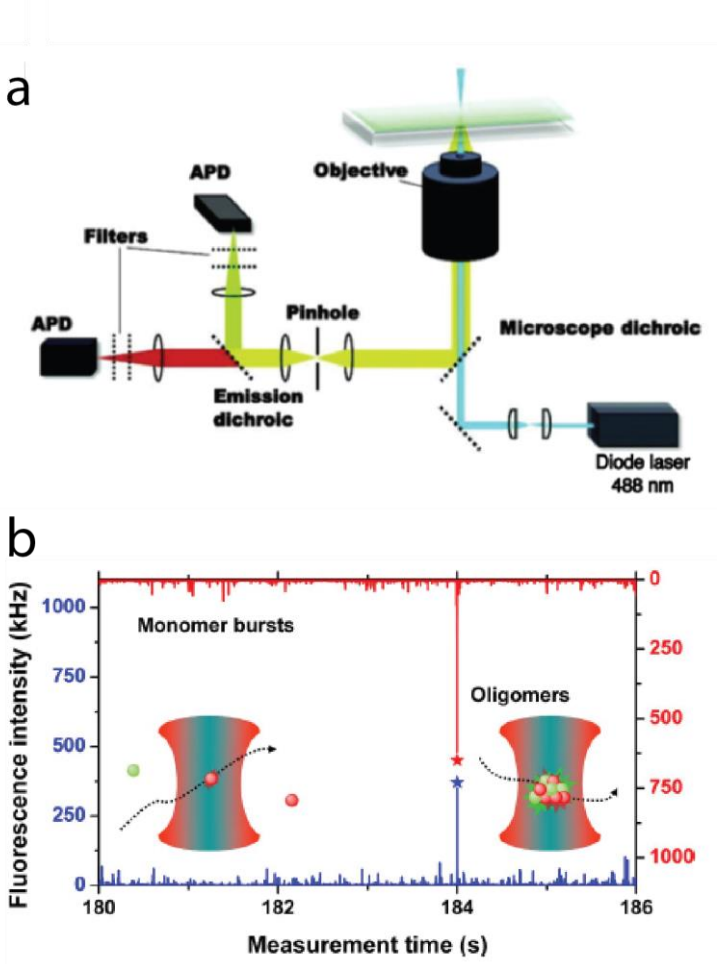

Figure 3.1.1 Schematic of TCCD. (a) Experimental set-up of TCCD showing excitation laser, confocal objectives and separation of emission wavelengths prior to detection by avalanche photodiode detectors. This set up has been modified for using smFRET in (188), hence only single wavelength excitation at 488 nm. (b) Typical data output from TCCD showing predominantly monomer-derived fluorescent bursts detected within the confocal volume. Occasionally large fluorescent bursts are seen coincidently within both channels, indicating oligomerisation (392).

oligomer-specific concentrations. Monitoring these populations over time therefore provides accurate information regarding the evolution of assembly intermediates over the aggregation time course (238). By using dye labels that have overlapping emission and excitation spectra, TCCD can also provide insights into the conformational rearrangement of oligomeric species. This can be achieved by quantifying changes in Forster resonance energy transfer (FRET) between the two dyes during the lag phase of assembly (188). smFRET-TCCD was used to highlight conformational conversion of oligomeric species formed during the lag phase of α-synuclein amyloid formation (188). In addition, TCCD has also been used to study bimolecular interactions between chaperones and oligomeric species by monitoring which aggregates are depleted from solution upon incubation with unlabelled chaperones (237, 238). One significant drawback to using TCCD, however, is the requirement for 100% labelled protein samples. This means that experiments have to be conducted within the low nM range, and as the aggregation of amyloid is highly dependent upon concentration (148), it may not be suitable for the study of all amyloidogenic systems.

Other fluorescence-based techniques, such as fluorescence cross-correlative spectroscopy (FCCS) have also been used to study these types of amyloidogenic phenomena. FCCS in principle is performed analogously to TCCD, although dual fluorescence fluctuations are correlated as opposed to counted (393, 394). A high correlation of fluorescence signals of differentially labelled species is diagnostic of an intermolecular interaction. The technique has proved highly successful in studying *in vitro* protein-protein interactions and also those within living cells (395, 396). Because of the ability to cross-correlate fluorescent signals within the low pM range, FCCS has been proposed as a diagnostic tool for some amyloid disorders (397, 398). For instance, PrP fluorescent probes can be incubated in isolated cerebrospinal fluid of suspected Creutzfeldt Jakob disease patients and can co-aggregate with scrapie isoforms of PrP (PrP^{SC}). A second PrP^{sc}-specific fluorescently labelled antibody probe can then be added and cross-correlation events detected at aggregate concentrations in the femtomolar concentration range. Therefore FCCS is well suited to studying lowly populated, transient bimolecular interactions, although the inferior resolution of correlative measurements (in terms of defining particle stoichiometry), coupled with the heterogeneity of amyloid systems, means that less

detailed information is obtained in comparison with fluorescence counting experiments (399). One advantage, however, is that the limited concentration range in which fluorescence counting methods can be performed is not a problem for correlative experiments, as the latter can be carried out at concentrations identical to those used in standard biochemical ensemble assays. This means that, unlike TCCD, FCS and FCCS are not subject to potentially adverse concentration dependence effects of amyloid aggregation (148). A high signal to noise ratio in fluorescence correlative spectroscopy is instead maintained by doping in low concentrations (typically nM) of fluorescently labelled samples with unlabelled samples within the reaction.

These are only two of a plethora of fluorescence spectroscopy techniques that have been developed for the study of amyloid aggregation. Other methods can be found here (400–402). These techniques generally rely upon the continual advances made towards the analysis of fluorescence fluctuation traces. The application of mathematical functions capable of de-convoluting complex ensembles within standard FCS autocorrelation curves (ACs), or fluorescent fluctuation traces, such as photon counting histograms or number and brightness analysis (400, 401), makes FCS an accessible analytical tool for the study of these systems. With correct calibration of the confocal volume, FCS-based experiments can also provide information such as the apparent hydrodynamic radius (R_H). For the investigations described here, maximum entropy method (MEM) (403), a well-used method for the analysis of heterogeneous samples with providence in the study of amyloidogenic proteins (404–406), was used to extract population ensembles from ACs collected during fibril depolymerisation.

3.1.3 General principles of fluorescent spectroscopy

Fluorescence spectroscopy techniques rely on the ability of compounds to emit fluorescence once excited from the ground state by the absorption of light of specific wavelengths. Fluorescence emission is most usually described by the Jablonski diagram, which shows the excitation of a fluorophore to higher energy singlet states by the absorption of light (Figure 3.1.2). Fluorophores can be excited to multiple energy orbitals, but prior to emission, vibrational relaxations and internal conversions ($1x10^{-11}$ to 10^{-14} sec) means that molecules typically relax back to the

ground state (S_0) from the lowest energy singlet state (non-radiative decay, or fluorescence emission - timescale typically $1x10^{-9}$sec). The relaxation from S_1 to S_0 is accompanied by the emission of a photon which is the cause of fluorescence emission (Figure 3.1.2). As the energy level from which relaxation to S_0 occurs is typically lower than the original excited state (due to vibration relaxations - Figure 3.1.2), the wavelength of emitted fluorescence is longer than that used for excitation. This property, known as the Stokes shift, is taken advantage of in commercially available fluorophores to reduce spectral overlap between excitation and emission wavelengths. There are additional pathways for the relaxation to the ground state (Figure 3.1.2), including intersystem crossing to the lower energy triplet excitation state (T_1). Non-radiative decay (fluorescence emission) from T_1 is typically forbidden, so relaxation to the ground state takes place through phosphorescence (comparatively long time scale ~10^1sec). Both phosphorescence and intersystem

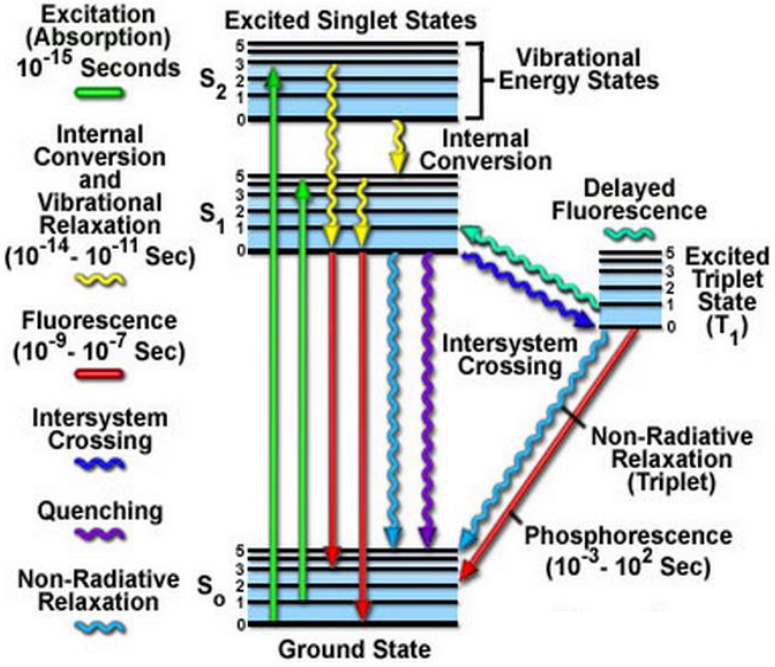

Figure 3.1.2 Jablonski diagram The ground state and the S1 and S2 excited singlet states are depicted by S_0, S_1 and S_2. Absorption promotes the ground state to excited singlet states (green arrows), which undergo vibrational relaxation and internal conversion from the S_2 to S_1 singlet states. Non-radiative relaxation takes place from the S_1 state to the ground state, involving the emission of a photon (fluorescence – light blue arrow). Alternative relaxation pathways, such as quenching (relaxation via heat loss – purple arrow), or transition to the excited triplet state via intersystem crossing are also shown (blue arrow). Typical relaxation from the excited triplet state takes place either through phosphorescence (red arrow), or through photon emission (light blue arrow). Relation through non-radiative decay however from the excited triplet state is at longer wavelengths than from the S_1 singlet state so therefore does not interfere with fluorescence measurements. Figure taken from (435)

crossing takes place on timescales that are distinct from diffusion times of biological molecules and therefore do not often impinge upon the measurements within FCS experiments of the biologically relevant molecules under investigation.

Commercial dyes can be used to label biological molecules and thus fluorophores can be exploited to study a range of biological phenomena in a variety of fluorescence spectroscopy methods, several of which have been described (188, 238, 392, 395, 397, 401, 405). In general, fluorescence spectroscopy techniques hold significant advantages over other methods in that it allows the analysis of single molecules. Although FCS can observe fluorescent fluctuations from single molecules, fluctuations from many thousands of molecules are analysed and averaged in a process known as autocorrelation. Therefore, strictly speaking, FCS is not a true single molecule technique.

In order to utilise fluorescence for correlative measurements, fluorescence fluctuation traces must be obtained over a time-course. This is most commonly performed by illuminating a sample volume using confocal optics (Figure 3.1.3a). A collimated laser beam is typically focused into a sample using a high numerical aperture objective lens to create a diffraction-limited focal spot within the sample chamber. A pinhole aperture of 50 µm is placed in the pathway of the collected emitted light. The role of the pinhole aperture is to reduce the transmission of emission photons excited outside of the focal plane, thus only fluorescently-labelled

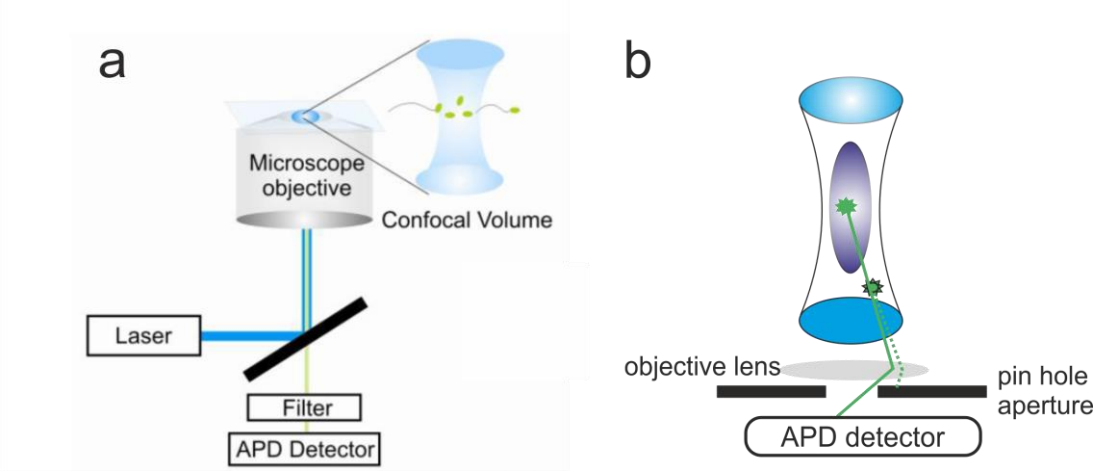

Figure 3.1.3 Confocal configuration used in FCS. (a) A collimated laser is focused into a sample chamber through a high numerical aperture objective lens. A schematic zoom of the confocal volume is shown in (b) – with the femtolitre focal volume shown in dark blue. The in-focus correlated fluorescent species are shown in green, where the objective lens has focused the emitted fluorescence through the pin-hole aperture to the detector (solid green line). Fluorescence from out-of-focus species (black outline) is blocked by the pin-hole aperture (dashed line), thus increasing the signal-to-noise of the experiment.

species which diffuse through the confocal volume are recorded (Figure 3.1.3b). The combination of the objective lens and pinhole aperture effectively create a confocal volume less than a femtolitre in size. The reduced volume obtained using confocal objectives greatly improves the signal-to-noise ratio within fluorescence spectroscopy measurements, allowing detection of molecules in the low nM to pM range.

3.1.4 The autocorrelation function

The fluctuations of fluorescence signals can be quantified by temporal autocorrelation defined as thus:

$$G(\tau) = \frac{\langle \delta F(t) \delta F(t+\tau) \rangle}{\langle F(t) \rangle^2} \quad (1)$$

where δF(t) is the fluorescence signal at time t from the mean fluorescence <F(t)>, and δF(t + τ) is the fluctuation of fluorescence at time t plus the lag time τ (Figure 3.1.4a). Essentially, molecules with a longer residence time within the confocal volume will have a correlation score (G) > 0 at longer lag times (t+τ). The time it takes for a fluorescent molecule to traverse the confocal volume (diffusion time $-\tau_D$) is directly related to the size of the molecule, and can be calculated by expressing the autocorrelation function as such:

$$G(t) = \frac{1}{N}\left(1 + \frac{\tau}{\tau_D}\right)^{-1}\left(1 + \frac{\tau}{K^2.\tau_D}\right)^{-0.5}\left[F_T exp\left(-\frac{\tau}{\tau_T}\right) + (1 - F_T)\right] \quad (2)$$

where N is the number of molecules within the confocal volume at any given time, τ is the delay time associated with correlating the fluorescence signal, K is the shape parameter approximating the size of the three-dimensional Gaussian confocal volume, and τ_D is as previously defined. F_τ and τ_t are photophysical phenomena related to the excited triplet state of the fluorescent probe used as a label (the amplitude and decay constant respectively). Triplet state parameters are not always defined within the autocorrelation function due to the rapid intersystem conversion time as illustrated by the Jablonski diagram (S_1 – T_1, Figure 3.1.2). However, experimental ACs almost always exhibit some degree of decay from the excited triplet state and therefore is usually included as an exponential function. The

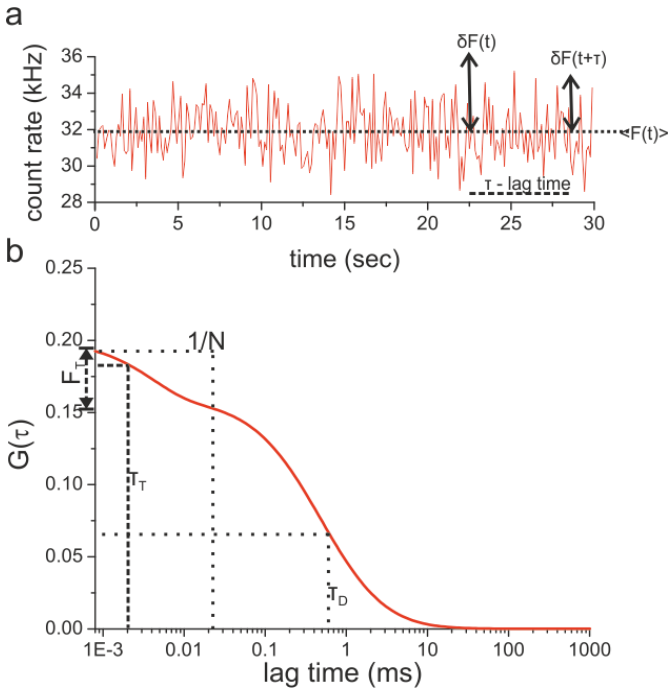

Figure 3.1.4 Typical output obtained from FCS. (a) Generalised fluorescence fluctuations parameters used to generate ACs (b) A typical AC derived from a single component solution displaying features related to triplet state phenomena (F_τ and τ_T), the amplitude of the signal (1/N) and τ_D.

relationship of the parameters to the shape of the AC is shown in Figure 3.1.4b and a full derivation of the autocorrelation function is available in (389).

As τ_D is inversely proportional to the diffusion coefficient (D_0 – Equation 3) small molecules will have large D_0 and small τ_D within the confocal volume, while the opposite is true for large molecules. With knowledge of the dimensions of the confocal volume (K), D_0 can be calculated from experimentally derived τ_D, and the apparent hydrodynamic radii (R_H) subsequently calculated using the following equations:

$$\tau_D = \frac{\omega_0^2}{4D_0} \tag{3}$$

where ω_o describes the $1/e^2$ decay of the 3D Gaussian confocal volume in the plane radial to the path of travelling light, and Stokes Einstein Equation:

$$D_0 = \frac{K_B T}{6\pi\eta R_H} \tag{4}$$

Where K_B is the Boltzmann constant, T is the absolute temperature, η is viscosity and R_H is the apparent hydrodynamic radius. Therefore, through the correct calibration of the confocal volume, one can estimate the apparent size of species undergoing diffusion. The confocal volume is usually calculated using a calibration standard, such as fluorescein, which has a known D_o under particular solution conditions. Using the experimentally derived calibrant τ_D with the known D_o means that ω_o can be calculated. This parameter (ω_o) can then be used to calculate D_o from measured values of τ_D for the sample of interest. This can subsequently be used in Stokes-Einstein equation to calculate apparent R_H values. Excellent reviews that further describe the principles and practise of FCS can be found in (389, 407, 408).

The remainder of this chapter describes the collection of ACs during fibril depolymerisation and analysis of the ACs using MEM, in order to identify the nature of the species released during fibril depolymerisation. This chapter also outlines additional structural characterisations of the species generated during molecular shedding.

3.2 Materials and Methods

3.2.1 Purification and labelling of β2m R3C for FCS experiments

In general, β_2m R3C (R3C – mutation of R at residue 3 of β_2m to C so the protein can be labelled) was expressed and purified as previously outline for *wt* β_2m **(**see section 2.2.3**)**. The only differences were made in the step to initially refold β_2m by dilution after inclusion body re-solubilisation in 8 M urea. Re-solubilised R3C was refolded by dilution into 10 mM Tris-HCl pH 7.5 supplemented with 400 mM arginine, to a urea concentration < 2 M (4-fold dilution). Samples were then dialysed and purified by anion exchange chromatography as previously detailed (section 2.2.3). Fractions containing R3C were confirmed using SDS-PAGE and pooled and placed in dialysis tubing (Thermo Scientific). R3C was then dialysed against 5 L of 18 MΩ H_2O at 4°C for 24 h with changes to the water made at least three times. Dialysed R3C was then frozen in a 200 ml round-bottom flask using dry ice and ethanol prior to being freeze-dried and stored at -20^{O}C. No gel filtration was performed prior to R3C labelling.

R3C was labelled with Alexa488-maleimide (Invitrogen) via the free thiol moiety by re-suspending the lyophilised protein in 25 mM Tris-HCl pH 8.0 supplemented with 5 mM DTT. Addition of 5 mM DTT reduces the newly introduced thiol without reducing the native disulphide bond (409). Re-suspended R3C was incubated at room temperature for 10 min prior to desalting using a gravity-flow Nap-10 column (GE Healthcare) previously equilibrated with 25 mM sodium phosphate buffer, pH 7.2. Once desalted, the concentration of R3C was adjusted to 100 µM by checking the eluent concentration using Beer-Lambert's law (R3C ε = 20065.M^{-1}.cm^{-1}). R3C was then placed into a brown 1.5 ml chromacol glass vial with a 3 x 8 mm magnetic stirring bar. Alexa488-maleimide was re-suspended to 10 mM in 100% DMSO and added in drop wise fashion to R3C using a glass Pasteur pipette until a 10-fold molar excess of the dye over protein was reached. The solution was gently agitated at room temperature on a magnetic stirring plate for 2 hours. Alexa488 labelled R3C (R3C488) was then separated from free dye by desalting on a Nap-5 column equilibrated with 25 mM sodium phosphate pH 7.2 prior to gel filtering R3C on an analytical Sup75 column (GE healthcare) equilibrated with the same buffer, at a flow rate of 0.5 ml.min^{-1} and backing pressure of 1.0 mPa (Figure 3.2.1a). Fractions of 0.5 ml were collected and those that eluted at approximately 10 ml were pooled and stored at 4°C (Figure 3.2.1a). A 30 µM samples was prepared for ESI-MS to confirm labelling efficiency by buffer exchanging into 50 mM ammonium biocarbonate pH 7.4 buffer using a Zeba Spin 7kDa 2 ml desalting column (Thermo Scientific). Labelling (100%) was confirmed (Figure 3.2.1b, expected mass of conjugated R3C488 = 12506 Da) prior to concentrating using a Centricon centrifugal filter with 3 kDa cut-off by centrifuging at 4,000 x *g* for 10 min intervals at 4°C. Aliquots of

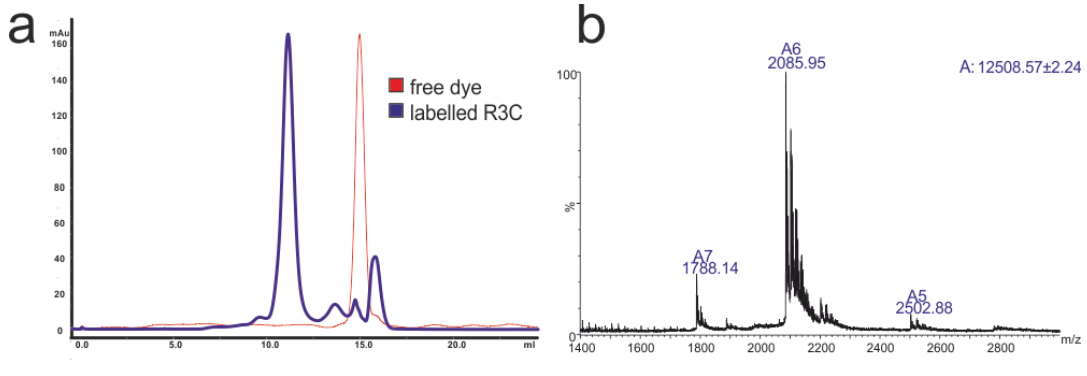

Figure 3.2.1 Purification of R3C488. (a) Labelled R3C (blue) was purified from free dye (red) using analytical gel filtration. (b) Labelling was confirmed using mass spectrometry, with the expected mass of R3C488 being 12,506 Da.

R3C488 at a final concentration of 75 µM sufficient for fibril growth experiments were snap-frozen in liquid N_2 and stored at -80^{0}C.

3.2.2 FCS set-up

FCS experiments were performed using a custom-built fluorescence microscope equipped with a collimated laser beam (max power 5 mW) working at an approximate power output of 40 µW. A simplified schematic outlining the general features of the instrument is shown in Figure 3.2.2. The beam (488 nm, Sapphire OPSL, Coherent Inc., UK) was spatially filtered and collimated to obtain a TEM_{oo} Gaussian beam, prior to being guided via a series of mirrors through a shortpass dichroic beam splitter (488DSCX, Chroma Tech., USA) to a microscope objective (63 x magnification, 1.4 NA, Zeiss, Germany), where it was focused into the sample at a depth of 30 µm from the inner surface of the coverslip chamber of 200 µl volume (Labtech, Nagle Nunc). The focal depth was precisely maintained by a piezoelectric feedback loop (Piezosystmes Jena, Germany). Contact between the objective lens and the coverslip chamber was maintained with low autofluorescence immersion oil (refractive index 1.515, type DF, Cargille Laboratories, USA) and

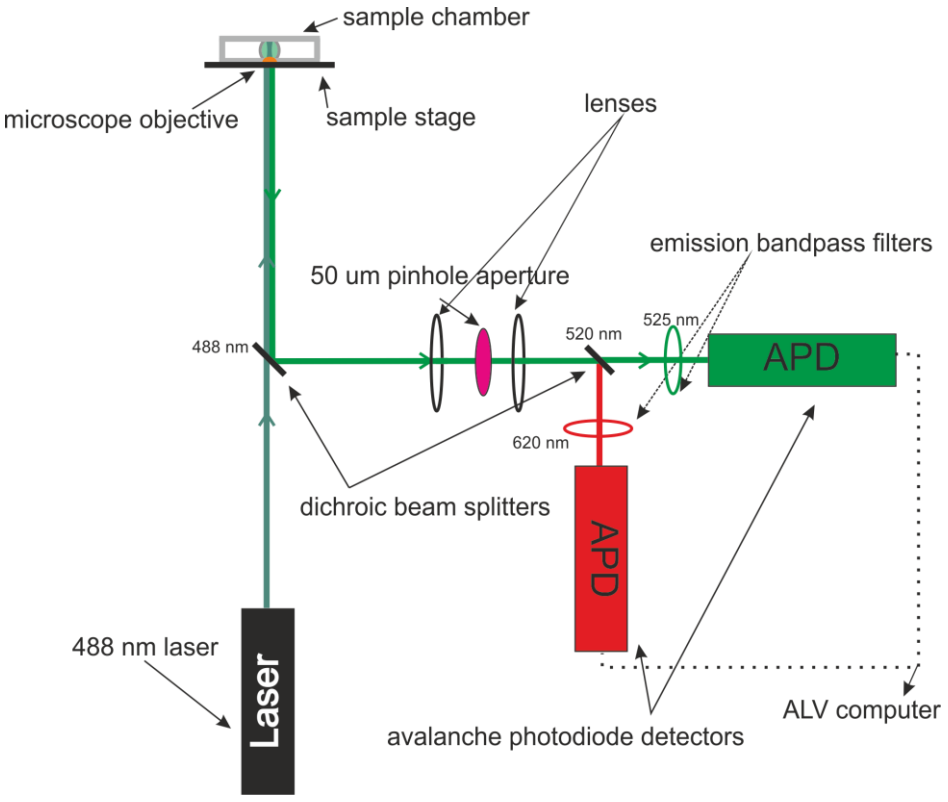

Figure 3.2.2 Schematic of FCS set-up. Parts are described in Section 3.2.2.

samples thermo-regulated by re-circulating water around the sample holder and objective lens, set to 25°C. Emitted fluorescence collected by the objective lens was focused through an aperture (50 µm pinhole), prior to passing through a dichroic beam splitter (565DCLP, Chroma Tech., USA) and detected and analysed by an ALV-5000 multiple tau digital correlator used in a single channel mode (Perkin Elmer, Optoelectronics, USA).

3.2.3 Confocal volume calibration

Calibration of the confocal volume was performed using 1 nM Alexa488 in deionised 1 x PBS containing 0.001% (*v/v*) Tween, by calculating the diffusion time from multiple 30 sec acquisitions before and after each experiment. Control experiments were analysed by non-linear least-squares fitting with a single diffusion component and triplet state autocorrelation function (Equation 2) using scripts written in Matlab and provided by Dr Roman Tuma, University of Leeds (version 7.11, Mathworks). Apparent Rh values for free dye were calculated from the measured τ_D and the diffusion coefficient of free Alexa488 in H_2O of $3x10^{-10}m^2.sec^{-1}$ (410), using equations 3 and 4 described in Section 3.1.4.

3.2.4 Monitoring molecular shedding using FCS

To detect oligomeric species during fibril depolymerisation, fibril growth was seeded with 1% (*w/w*) *wt* β_2m fibril formed at pH 2 (Section 2.2.4) mixed with 120 µM *wt* β_2m and 120 nM R3C488 at pH 2 as previously described (section 2.2.4) Solutions were left at room temperature for no more than 12 h. Fibrils were diluted to 30 µM (assay concentration of R3C488 therefore 30 nM) in either pH 6.4 or pH 7.4 buffer (see section 2.2.6 for buffer compositions) supplemented with 0.001% (*v/v*) Tween at 25°C and placed within a sealed 200 µl volume glass coverslip chambers (Nunc). Multiple 20 x 30 second acquisitions were collected to provide 10 minute windows during the depolymerisation process. Times quoted in figures displaying ACs represent the median time point of the spectral window, with the average of up to 100 ACs correlated from 30 sec acquisitions providing the raw data for MEM fitting. The standard deviation of the combined ACs provides the associated error for each time-point curve.

3.2.5 Maximum entropy method

In order to de-convolute heterogeneous ensembles of species represented within the ACs collected during depolymerisation, MEM was employed. This technique allows the measured AC to be best fit by a non-continuous distribution of diffusing species separated over several orders of magnitude in size. The algorithm is reported to provide a greater degree of robustness in comparison with conventional multicomponent fitting regimes (403). The relationship between the multicomponent fitting regime and the standard AC is represented below,

$$G(\tau) = \frac{1}{N}\sum_{i=1}^{n}\frac{a_i}{\left(1+\frac{\tau}{\tau_{Di}}\right)\left(\sqrt{1+.\frac{\tau}{K^2.\tau_{Di}}}\right)} \quad (5)$$

whereby a_i represents the amplitude associated with each individual τ_{Di}, which are logarithmically spaced in the time domain. Summation of the individual ACs describing each τ_{Di} should provide a good approximation of the raw AC. N, τ and K are as described for Equation 2. Triplet state parameters (see Equation 2) calculated from ACs of dye-only controls by SCA were used as initial estimates for triplet state parameters during MEM fitting (see Section 3.2.3). A full description of the MEM algorithm can be found here (403).

The sum of individual diffusing species have to satisfy the raw experimental data, therefore the goodness of fit must be assessed. Qualitatively, a random distribution of residuals (r_i) about a mean value of zero is a good estimation of the quality of the fit, when r_i is defined as:

$$r_i = \frac{G^c(t_i) - G^e(t_i)}{\sigma_i} \quad (6)$$

In this equation G^C is the calculated correlation value at time t and G^e is the raw experimental value and σ_i is the inverse of the weight of the i^{th} datum. The goodness of fit is quantitatively assessed through the chi square parameter χ^2:

$$\chi^2 = \frac{1}{M}\sum_{i=1}^{M} r_i^2 \quad (7)$$

$$S = -\sum p_i ln p_i \quad (8)$$

where M is the number of data points within the autocorrelation curve. However, the inherent noise of FCS data can lead to multiple distributions being able to satisfy the raw data according to χ^2. Therefore a second parameter, known as the entropy score, S, is used to ensure the least discrete (narrow) and most uniform distribution is chosen at a given χ^2 value. S is defined as thus:

where p_i is:

$$p_i = {}^{\alpha_i}/_{\sum \alpha_i} \quad (9)$$

According to MEM, a discrete population of τ_D would give the lowest value of S and is therefore the least acceptable solution for noisy data. S increases as the width of the distribution increases; therefore, the distribution providing the maximal value of S at a given χ^2 is put forward. MEMFCS thus ensures that χ^2 is minimised as S is maximised.

MEMFCS begins with an equal weighting (α_i) for all specified τ_{Di}, with the distribution altered through successive iterations to satisfy the raw data. The fitting regime is terminated when χ^2 remains unchanged in successive iterations. The MEMFCS algorithm used in this study was kindly provided by Professor Sudipta Maiti *et al* at the Tata Institute for Fundamental Research (403). Errors associated with species identified using MEM are the full width half maximum (FWHM) from Gaussian-like peaks observed in the final distribution.

3.2.6 ThT seeding assay

ThT assays were performed on a BMG LabTech Optima plate reader as described in Section 2.2.7. In brief, 120 μM (*w/w*) 0.1% seeded β_2m amyloid fibrils formed at pH 2 were diluted 4-fold into pH 7.4 or 6.4 buffer (see section 2.2.6 for buffer compositions) and depolymerised at 25°C for 30 or 60 min respectively. These solutions were then used in seeding assays with 120 μM native β_2m or ΔN6 (kindly provided by Dr Theo Karamanos, University of Leeds) incubated in either pH 7.4 or pH 6.4 buffer, with a seed concentration of 10% (*w/w*) (12 μM seeds). Buffers were supplemented with 40 μM ThT, the fluorescence emission of which was recorded for

4 h at 25°C. Curves shown are a smoothed line from the average of at least three independent replicates.

3.2.7 Negative stain-transmission and cryo-electron microscopy

3µl of sample was deposited onto colloidion-copper coated EM grids (prepared by Martin Fuller, University of Leeds) and incubated for 30 sec at room temperature. The sample was subsequently removed by blotting the grid onto filter paper (Whatmann), prior to washing with 2 x 10 µl of 18 MΩ H_2O and 1 x 10 µl 2% (*w/v*) uranyl acetate before staining with 10 µl 2% (*w/v*) uranyl acetate for 30 sec. Excess dye was removed and grids dried at room temperature. Images were recorded using a BM Ultrascan 2k x 2k CCD (Gatan) on a Technai T12 TEM (FEI) operating at 120 keV For cryoEM, samples were deposited on a Quantifiol 2/1 holey carbon grid (Electron Microscopy Sciences) and vitrified by plunging into liquid ethane using a Vitribot (FEI). Samples were examined at cryogenic temperature on a F20 TEM (FEI) operating at 200 keV and images recorded using a BM Ultrascan 4k x 4k CCD (Gatan). Individual particles were picked and class averages calculated using EMAN2 (411) and RELION (412). Dr Matt Iadanza, University of Leeds, performed the cryoEM experiments.

3.2.8 Dot blots

Samples were prepared for dot blots by initiating depolymerisation of 600 µM (0.1% seeded (*w/w*)) β_2m amyloid fibrils by diluting 4-fold into either pH 7.4 and 6.4 buffers at a final volume of 100 µl (see section 2.2.6 for buffers). Depolymerisation was allowed to proceed for 30 and 60 min respectively. Prior to dot blotting, 40 µl of samples (total protein) under each condition were filtered using a 0.2 µm syringe filter (Millipore) to partition fibrils from soluble material (filtrate). Total protein and filtrate samples (2 µl, 2 µl x 2 for filtrate) were then 'dotted' onto a nitrocellulose membrane and allowed to dry before the membrane was blocked using 1 x PBS containing 0.2% (*v/v*) Tween-20 (dot blot buffer) supplemented with 10% (*w/v*) Marvel Milk for one hour at room temperature by gently rocking on a rocking platform. Membranes were then washed 3 x 5 min in dot blot buffer before incubating with dot blot buffer containing 3% (*w/v*) bovine serum albumin and 1:5,000 dilution of the W01 primary antibody (kindly provided by Prof. Ronal Wetzel, Univeristy of Pittsburgh) overnight at 4^{o}C. Membranes were then washed 3

x 5 min in dot blot buffer prior to incubating with 1:5,000 horse raddish peroxidase-conjugated rabbit α-mouse IgG antibodies in the same buffer for 1 h at room temperature. Membranes were then washed 3 x 5 min in dot blot buffer before antibody binding was visualised using Supersignal West Pico chemiluminescent susbtrate (Perco) and Amersham Hyperfilm ECL. For β_2m control blots, samples were prepared in the same way and blocked overnight in dot blot buffer containing 10% (*w/v*) Marvel Milk at 4°C. Membranes were then washed as described prior to incubating for one hour at room temperature in dot blot buffer containing 5 % (*w/v*) Marvel Milk and 1:5000 dilution of α-β_2m antibody for one hour at room temperature on a rocking platform. Membranes were then washed and probed with secondary antibodies and visualised as described for the W01 antibody. Secondary antibody only controls were also performed to ensure binding was not non-specific.

3.2.9 Circular dichroism

Filtrate and total protein samples were prepared for CD by diluting 120 μM fibrils 4-fold into pH 7.4 or 6.4 buffer respectively (see Section 2.2.6 for buffer compositions). Samples were incubated at 25^{o}C for 30 or 60 minutes, respectively. Prior to analysis, samples were filtered through a small volume 0.2 μm syringe filter (Millipore) and quantified using SDS-PAGE densitometry as previously described (Section 2.2.8). Far-UV CD spectra were acquired using a Chirascan plus (Applied PhotoPhysics) over the wavelength range of 190 – 260 nm using a 1 mm path length Hellma cuvette. Spectra were also acquired for native β_2m samples at the equivalent concentrations as judged by SDS-PAGE under the same solution conditions. Scans were recorded at a rate of 60 nm.min^{-1} with 3 acquired spectra averaged for the final display. Buffer-only control spectra were also acquired and subtracted from the protein spectra.

3.2.10 8-Anilinonaphthalene-1-sulphonate (ANS) binding assays

Filtrate samples were prepared and quantified as stated above (Section 3.2.9). Immediately after partitioning through a 0.2 μm filter (Millipore), filtrates were diluted 6-fold into pH 6.4 or pH 7.4 buffer (section 2.2.6) containing 250 μM ANS, previously equilibrated to 25°C. Samples were then left to incubate for 2 min prior to the acquisition of a fluorescence emission scan ranging from 400 – 600 nm after

excitation at 389 nm, using a spectrofluorometer (PTI). The instrument was set up with excitation and emission slit widths of approximately 5 nm, and acquired an average of two scans, using a step size of 1 nm and an integration time of $0.1.sec^{-1}$. Native β_2m and acid unfolded β_2m controls at equivalent concentrations were also acquired, with data normalised to the highest fluorescence emission of acid unfolded β_2m samples.

3.3 Results

3.3.1 Benchmarking MEM

Prior to analysing experimental data, MEM was benchmarked to ensure it could reliably detect the correct τ_D and amplitudes of distinct species in mixed samples from simulated data. ACs were simulated in Excel using Equation 5 with an additional triplet component. For the two examples shown, the following parameters of the autocorrelation function were fixed; $F_t = 0.2$, $\tau_t = 0.004$ ms and $K^2 = 100$ nm^2, while 1/N (amplitude) and the τ_{Ds} of the simulated species are shown in Figure 3.1.1. Each data point was assigned a random error value of up to 10% of 1/N.

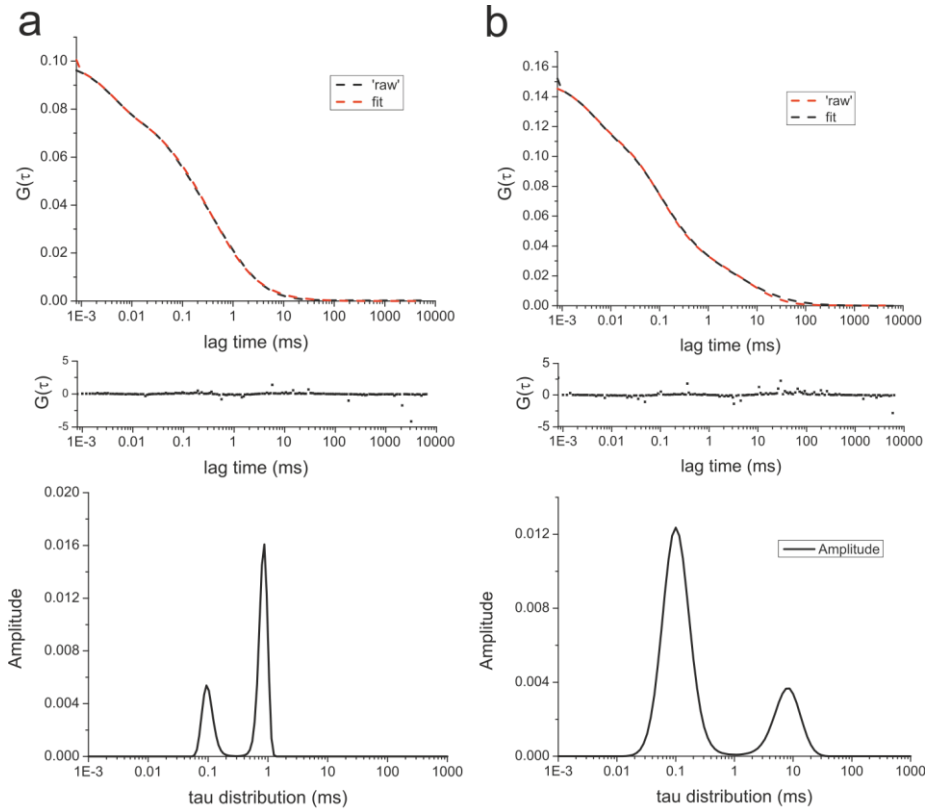

Input		MEM output	
τ_{Ds} (ms)	% amplitude	τ_{De} (ms)	% amplitude
0.1	25	0.099	27.8
1	75	0.856	72.2

Input		MEM output	
τ_{Ds} (ms)	% amplitude	τ_{De} (ms)	% amplitude
0.1	75	0.117	73.1
10	25	9.28	26.9

Figure 3.3.1 Benchmarking MEM with multicomponent simulated curves. (a and b) Examples of simulated ACs ('raw') containing two distinct populations of species and the subsequent MEM-derived AC (fit), with residuals. Tau distributions and input and MEM derived parameters related to simulated species are shown below (τ_{Ds} and τ_{De} respectively).

In the first example (Figure 3.3.1a), the two species have τ_D of 0.1 and 1 ms, respectively, with the second species contributing 75% of the overall amplitude of the simulated curve. In the second example (Figure 3.3.1b), the τ_D of the longer

diffusion component is increased by an order of magnitude to 10 ms and the amplitudes between the two species are inversed (see Tables in Figure 3.3.1 for inputs). The simulated and MEM-derived ACs are shown in Figure 3.1.1a and b with residuals for the fits shown below. Comparison of τ_D (peak centre position) and amplitudes (summed amplitudes of all non-continuous τ_D associated with the corresponding peak) between experimentally derived values (τ_{De}) and those originally used to simulate curves (τ_{Ds}) shows that MEM is able to accurately describe the τ_D and amplitude associated with each species (Figure 3.3.1a and b). MEM could not reproducibly resolve two species whose τ_D values were within an order of magnitude of one another (data not shown). Therefore MEM can be used to separate species that differ in τ_D by at least an order of magnitude and can also reliably describe the relative amplitude associated to each species.

3.3.2 Using MEM to fit experimental data – comparison with other methods of analyses

Typical ACs of homogeneous samples can be accurately described using single component analysis (SCA) as opposed to using a complex fitting algorithm such as MEM. Therefore, dye-only control ACs were fit using both SCA or MEM to see whether both methods provide comparative information. SCA was performed on control solutions of 1nM Alexa488 collected before and after acquisitions of sample ACs under conditions described in Section 3.2.3. Figure 3.3.2a shows the average AC from a minimum of 20 x 30 sec individual ACs collected from control solutions of 1 nM Alexa488 (black line). The overlayed fit from SCA is shown in red (red line). From an unconstrained fit (no parameter within the autocorrelation function was fixed during SCA of control curves), the triplet state parameters, F_t and τ_t, and the shape parameter K^2 were derived (see Section 3.1.4 and 3.2.3) and subsequently used to fit the same control AC using MEM (Figure 3.3.2b). MEM was as accurate in describing the shape of the AC (Figure 3.3.2b – purple line), and describes a single, discrete (high signal to noise ratio due to sample homogeneity, therefore tau distribution is better defined and more discrete) population of species present within solution (Figure 3.3.3).

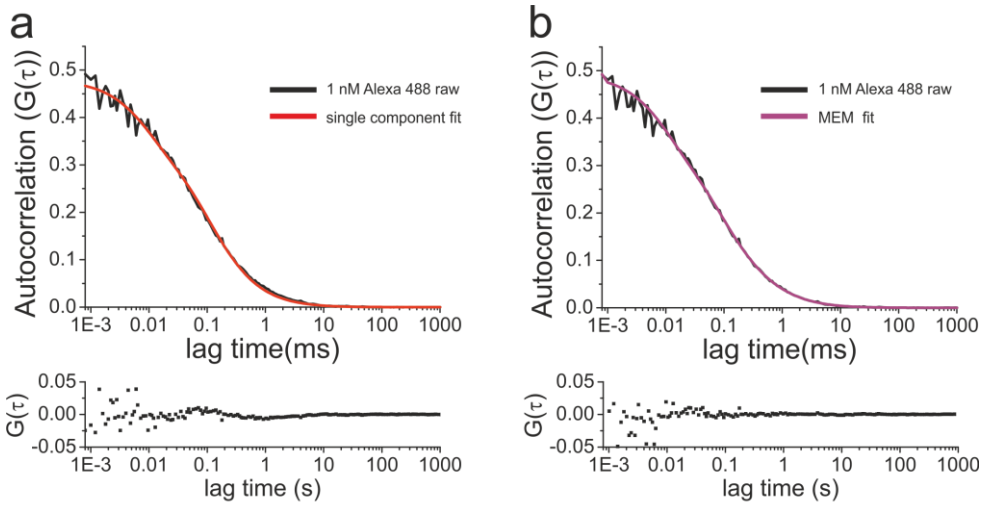

Figure 3.3.3 Comparison of the goodness of fit of calibrant ACs using MEM and SCA. Raw ACs (black curves) of 1 nM Alexa488 solutions in 1 x PBS 0.001% (*v/v*) Tween at 25 °C are the average of at least 20 x 30 sec acquisitions. The triplet state parameters and shape parameter derived from unconstrained SCA (a – red curve) of the controls curves were subsequently used to fit the same data using MEM (b – purple curve).

Comparison of τ_D values calculated using MEM and SCA from the same AC showed these to be roughly equivalent (SCA – 91±3.3 µs, vs. MEM – 85±5 µs). Therefore, MEM can be used to reliably fit ACs obtained from mono-dispersed, highly homogeneous solutions to a high degree of accuracy, when F_t, τ_t and K^2 can be estimated.

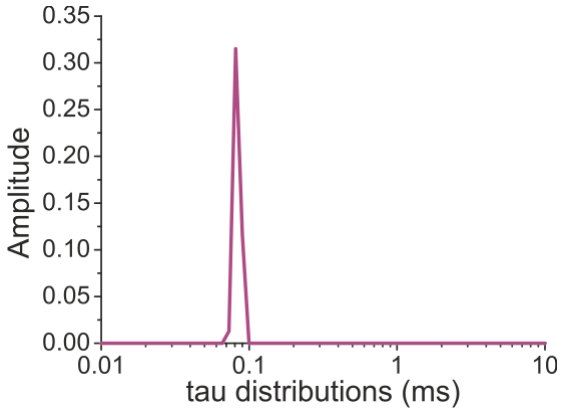

Figure 3.3.2 Tau distribution of species extracted using MEM to fit an Alexa488 AC. Representation of the distribution of species extracted from 1 nM Alexa488 control samples described in Figure 3.3.2 using MEM.

Although MEM is able to describe the population of species within ACs for which the triplet state parameters can be accurately estimated using SCA, it is not possible to calculate F_t and τ_t from ACs that are the product of highly heterogeneous systems. In most instances, attempting to fit ACs by SCA that are the product of a

multicomponent system leads to the gross overestimation of triplet state parameters. This is due to the fitting regime overcompensating for the presence of longer diffusion components. Therefore, ACs with varying degrees of heterogeneity and under different solution conditions were fitted using MEM with SCA-calculated F_t, τ_t, and K^2 from mono-dispersed, Alexa-488 control solutions collected on the same day. Figure 3.3.4 shows that, in addition to dye-only controls being accurately fit using MEM when combined with SCA-calculated F_t, τ_t and K^2 values (Figure 3.3.2), so are ACs corresponding to 30 µM *wt* β_2m with 18 nM R3C488 monomer in pH 6.4 buffer or fibrils formed at low pH from 30 µM *wt* β_2m with 30 nM R3C488 (Figure 3.3.4). Both raw ACs for these samples are the average of at least 20 x 30 sec individual ACs. Therefore, triplet state parameters calculated by SCA from ACs of dye-only controls can be used to estimate the triplet state parameters of subsequent multicomponent samples, even when collected under different solution conditions.

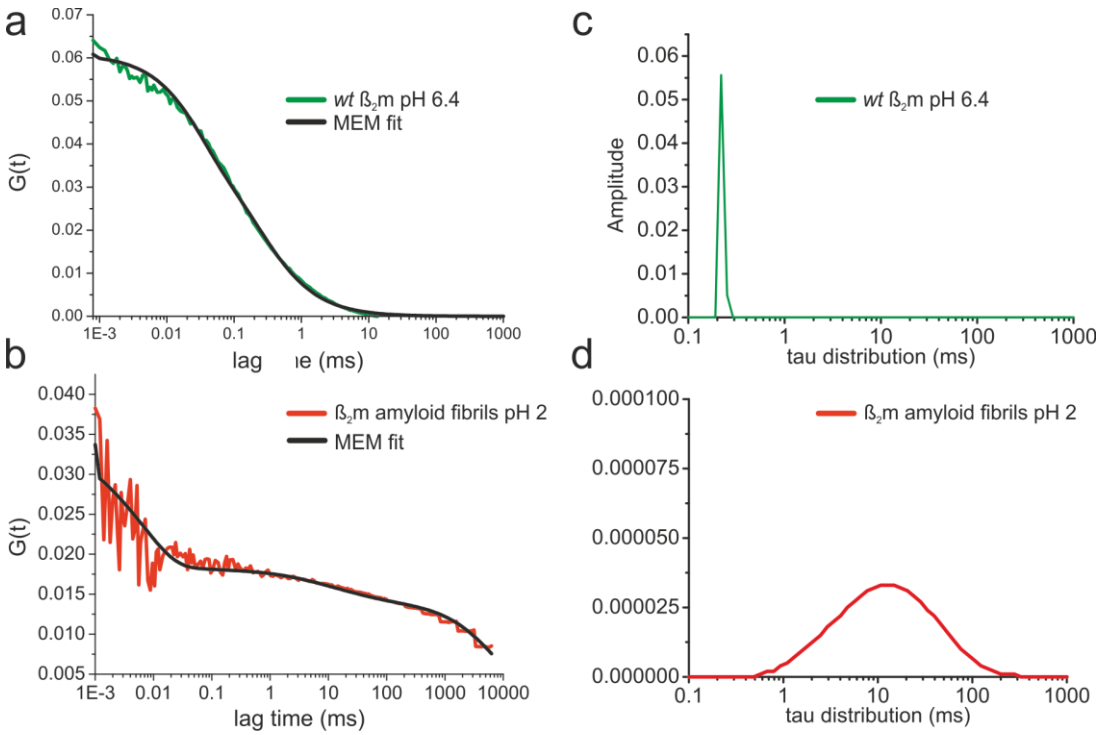

Figure 3.3.4 SCA-derived F_T, τ_t and K^2 calculated from Alexa488 controls used for MEM fitting of more complex solutions. Raw ACs and overlayed MEM fits of 30 µM native β_2m with 18 nM R3C488 in pH 6.4 buffer (a) and 1% (*w/w*) seeded 30 µM *wt* β_2m with 30 nM R3C488 amyloid fibrils at pH 2 (b). MEM fits were performed using F_t τ_t and K^2 calculated from SCA analysis of 1 nM Alexa488 control solutions collected on the same day. (c) and (d) show the tau distribution of species extracted from ACs described in (a) and (b) respectively using MEM.

3.3.3 FCS during fibril depolymerisation – data collection

To detect species populating as fibril depolymerisation proceeds, 120 µM *wt* β_2m fibrils containing 120 nM R3C488 were diluted four-fold into either pH 6.4 or 7.4 buffer containing 0.001% (*v/v*) Tween-20, and were immediately analysed as described in Section 3.2.4. The final concentration of dye-labelled protein had to be increased to 30 nM as the majority of R3C488, at least initially, remains sequestered within the fibrils, therefore lowering the effective concentration of soluble species being detected. Fibrils were infrequently encountered during the depolymerisation process. This is most likely due to the self-association of β_2m fibrils formed at pH 2 that takes place upon diluting into near-neutral pH buffers (92). As such, fibrillar bundles are sufficiently large to be encountered only rarely within the confocal volume. Figure 3.3.5 shows the raw ACs collected during β_2m fibril depolymerisation at pH 7.4 (a) and pH 6.4 (b). Each curve is the average of up to 60 individual ACs collected from three individual experiments performed on the same day. Each experiment consists of 20 x 30 sec ACs, where the depolymerisation time stated is the median within the time window in which the acquisition occurred. ACs are displayed normalised to G(0) of the earliest time point within each depolymerisation data series. This was performed to correct for differences in the relative amplitude of each individual experiment due to the stochastic incorporation of R3C488 into β_2m amyloid fibrils at low pH. Prior to these time points at pH 6.4, the concentration of diffusible dye-labelled species was too low to reproducibly

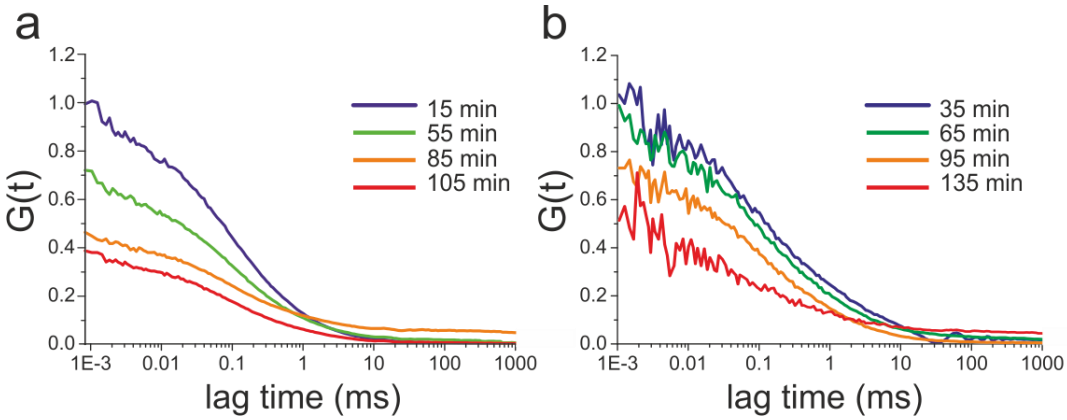

Figure 3.3.5 ACs collected during β_2m amyloid fibril depolymerisation. 1% (*w/w*) seeded 120 µM β_2m 120 nM R3C488 amyloid fibrils grown at pH 2 were depolymerised by diluting 4-fold into pH 7.4 (a) or pH 6.4 (b) buffer at 25°C. Up to five 20 x 30 sec acquisitions were made to produce the average AC displayed. The time indicates the median point of the collection window. ACs within each data set are normalised to the G(0) of the corresponding initial time point to remove the inherent differences of the amplitude of individual repeats.

detect.

The decrease in G(0) of each AC as the depolymerisation time course proceeds is indicative of soluble species becoming increasingly populated over time within both conditions. This is because the amplitude of the AC is inversely proportional to the number of molecules present during the acquisition of the fluorescence fluctuation trace (1/N in the autocorrelation function, see Equation 2, Section 3.1.4). The 85 min and 135 min time points collected at pH 7.4 and pH 6.4, respectively, appear to exhibit increased baselines in comparison with other samples. This could be due to the presence of fibrils diffusing through the residence volume, the signal of which eventually decays at lag times not plotted upon these curves (approximate τ_D of 10,000 ms, see Figure 3.3.4b as an example). It may also be due to mechanical instability of the sample stage during data acquisition. In addition, data collected at pH 6.4 is inherently noisier than that collected at pH 7.4. This is because less soluble material is released during depolymerisation at pH 6.4. As the overall amplitude of soluble species generated during depolymerisation is lower at pH 6.4, the signal to noise ratio is also lower.

These ACs were subsequently fitted using MEM to extract population distributions that form during molecular shedding from β_2m fibrils at pH 6.4 and pH 7.4. The normalised ACs, overlayed MEM fits and residuals to each of the curves are shown in Figure 3.3.6. In general there is a good agreement between the raw data and MEM-derived curves, with a qualitative observation of the distribution of residuals confirming all ACs are satisfactorily fitted. Deviations of residual values from a random distribution about zero typically take place below 50 μs. Fluorescent events taking place on this time scale are most likely to be due to differences between the estimated F_T and t_τ values and those of the experimental AC. This is a caveat of MEM, however, it does not impinge on the ability to further analyse these results.

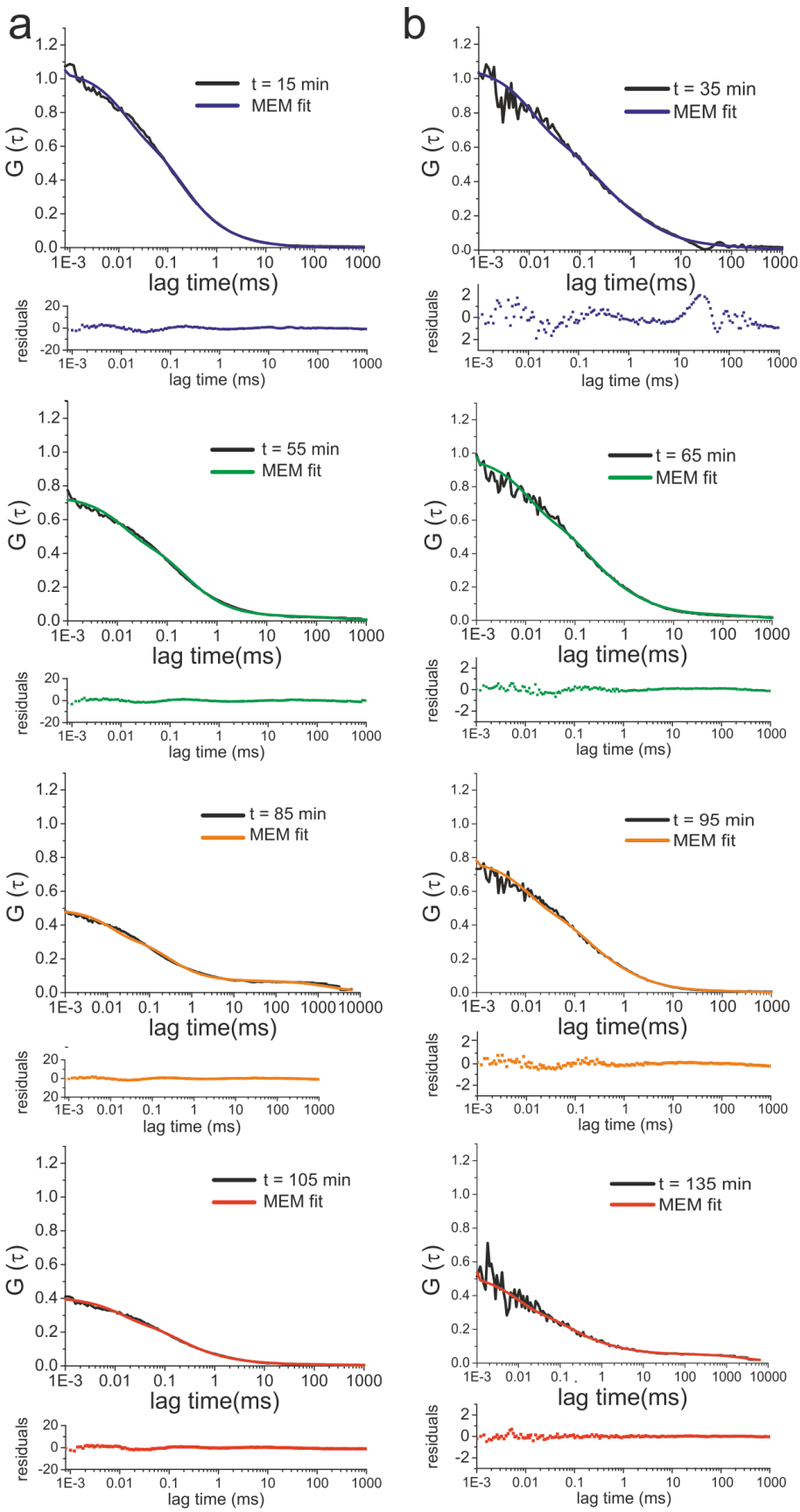

Figure 3.3.6 ACs with MEM fits collected during β_2m fibril depolymerisation. (a) Raw ACs collected 15, 55, 85 and 105 min after initiation of depolymerisation at pH 7.4 are shown in black with the MEM-derived AC shown overlayed. Residuals for the fit are shown below the curve. (b) As above, but for data collected at pH 6.4 35, 65, 95 and 135 min after was initiated.

3.3.4 Comparison of molecular shedding at pH 6.4 and pH 7.4

The normalised ACs collected during the initial stages of β_2m fibril depolymerisation at pH 6.4 (Figure 3.3.6b, 35 min) show a significant, 2-fold, increase at G(τ)= 1 ms in comparison with data obtained at the most equivalent time point during fibril depolymerisation at pH 7.4 (Figure 3.3.6a , 15 min). It is likely that this increase is due to an elevated concentration of a high molecular weight (HMW) species present during depolymerisation under these conditions. By calibrating the confocal volume with the fluorescent dye Alexa 488, the tau distribution extracted from the raw data using MEM (e.g. Figure 3.3.4c-d) can be converted to an apparent R_H scale. The calibration requires the experimentally derived τ_D, and the known D_o of Alexa488 under specific conditions in order to calculate the ω_o (see Section 3.1.4, Equation 3, and Section 3.2.3). Once ω_o is known, it can subsequently be used to determine D_o from τ_D of unknown species, which in turn can then be used to determine an apparent R_H using the Stokes-Einstein equation (Equation 4, Section 3.1.4). Typically, the τ_D of Alexa488 in 1 x PBS pH 7.4 at 25°C calculated from the average of a minimum of 20 x 30 sec ACs gave an approximate ω_o value of 350 nm. The calibration of the confocal volume was validated using native β_2m control solutions (30 μM β_2m 18 nM R3C488 in 1 x PBS pH 7.4 at 25°C, minimum of 20 x 30 sec acquisitions), which gave an apparent R_H of approximately 1.9 nm (Figure 3.3.7). This is consistent with previous measurements calculated from using different techniques and therefore validates the calibration (413).

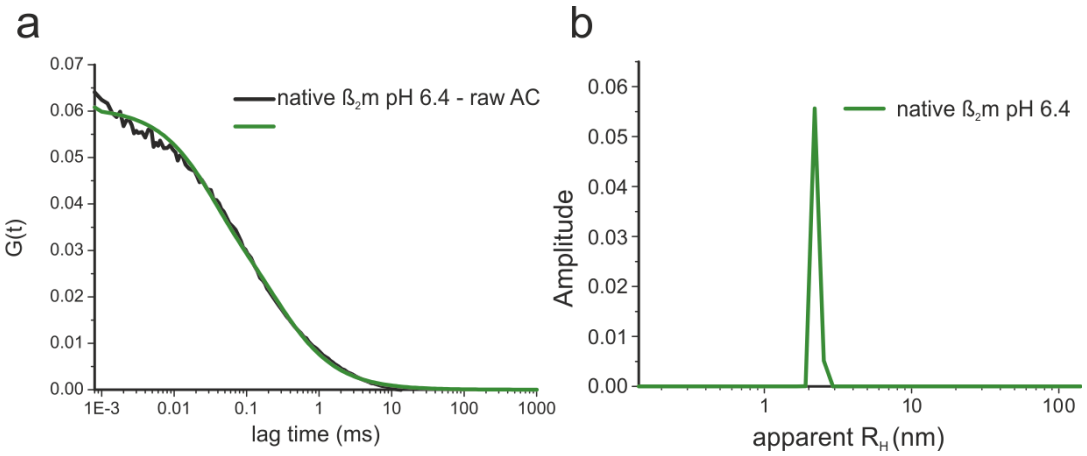

Figure 3.3.7 Conversion of tau distribution to apparent R_H scale after confocal volume calibration. AC of 30 μM *wt* β_2m and 18 nM native R3C488in pH 6.4 buffer with MEM-derived fit overlayed (green). The apparent R_H distribution observed after calibrating the confocal volume using dye-only controls is shown in (b).

The apparent R_H distributions of species that populate during fibril depolymerisation are shown in Figure 3.3.8. At pH 7.4, soluble species are dominated by the presence of a low molecular weight (LMW) peak with an apparent R_H of 2±0.4 nm (Figure 3.3.8a). This value is consistent with that calculated for β_2m monomer controls (Figure 3.3.7), and therefore corroborates previous experiments, such as the NMR analysis described in Section 2.3.7, suggesting that depolymerisation at pH 7.4 results in the rapid formation of non-toxic, native monomer, (larger species are infrequently observed and are lowly populated - peak between 10 – 100 nm observed at 15 and 105 min). The size distribution of species that appear during fibril depolymerisation at pH 6.4 however is significantly different. In addition to the LMW peak at ~1.8±0.5 nm, a second, larger peak is observed to be significantly populated at all recorded time points (Figure 3.3.8b). This species has an apparent R_H of 20±10 nm between 35 – 95 min, with an increase in apparent R_H to 31±20 nm 135 min after the initiation of depolymerisation. The increase in apparent R_H is accompanied by an increased broadness (Figure 3.3.8b – 135 min). This is not

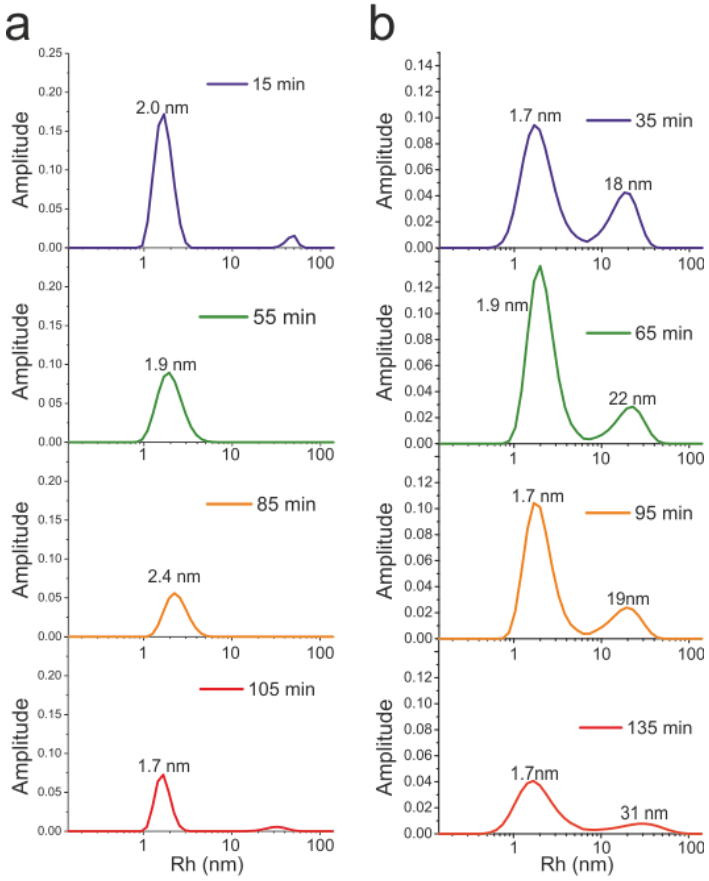

Figure 3.3.8 Apparent R_H distributions of species formed during fibril depolymerisation. Apparent R_H scales were calculated at pH 7.4 (a) and 6.4 (b) from MEM-derived tau distributions extracted from the ACs shown in Figure 3.3.6.

accompanied by a similar increase in LMW peak width, indicating that HMW species may exhibit increased heterogeneity as fibril depolymerisation proceeds.

The sustained presence of HMW species that accumulate during fibril depolymerisation at pH 6.4 is likely to be responsible for the delayed reappearance of native β_2m amide resonances as monitored by NMR, with respect to the loss of ThT fluorescence (discussed in Section 2.3.7). In other words, HMW species may be an intermediate of fibril depolymerisation that form prior to the refolding of native β_2m monomer. Comparison of peak heights of LMW and HMW species detected by FCS during fibril depolymerisation at pH 6.4 shows that at the earliest time point, the relative ratio of LMW to HMW species is most equivalent (Table 3.3.1) At time points thereafter the relative LMW:HMW species peak height ratio increases from 2 – 5 for species observed 135 min after the initiation of depolymerisation (Table 3.3.1). The increase of LMW species with respect to HMW species over time supports the view that HMW species form prior to the formation of LMW species.

Due to the broadening of the HMW peak detected 135 min after the initiation of fibril depolymerisation (Figure 3.3.8b), peak area, as opposed to peak height, was also calculated and used to compare the relative populations of both species. Peak area was calculated by summing all τ_D amplitudes that are ≥ 50% of the amplitude of the peak height (FWHM) (Table 3.3.1). This comparison shows that a similar increase in relative LMW:HMW species ratio is observed between 35 – 65 min, but then stabilises, with no further increase between 95 – 135 min as observed when comparing peak height. This shows, therefore, that the relative ratio of LMW to HMW species equilibrates between 35 – 65 min after the initiation of depolymerisation at pH 6.4, with a greater proportion of HMW species only apparent with respect to LMW species at the earliest recorded time point (35 min).

Table 3.3.1 The formation of HMW species precedes that of LMW species. Comparison of peak height (the amplitude of τ_D at the peak centre position) and peak areas (summed τ_D ≥ 50% of the amplitude of the peak centre), of HMW and LMW species formed during depolymerisation at pH 6.4.

	peak height			**peak volume**		
time (min)	**LMW**	**HMW**	**ratio**	**LMW**	**HMW**	**ratio**
35	2.37E-03	1.07E-03	2.2	1.32E-02	5.71E-03	2.3
65	3.43E-03	7.15E-04	4.8	1.37E-02	3.33E-03	4.1
95	2.62E-03	6.01E-04	4.3	1.20E-02	3.16E-03	3.8
135	1.02E-03	1.95E-04	5.2	6.13E-03	1.50E-03	4.1

The persistence of HMW species at all recorded time points during depolymerisation at pH 6.4 indicates an increased stability of these species in comparison with those that form during fibril depolymerisation at pH 7.4. This is likely to explain the increased dye release potential of soluble material at pH 6.4 (Section 2.3.4), despite the overall lower amplitude of fibril depolymerisation vs. time at this pH (Section 2.3.4). As the filtrate at pH 7.4 also exhibits dye release potential, membrane-active species must also be present at this pH (as evidenced by time points 15 min and 105 min at pH 7.4, Figure 3.3.8a), but the rapid equilibration of HMW species to membrane-inactive LMW species, means they must be highly transient, lowly populated and rarely encountered during these FCS experiments. The transient existence of HMW species at pH 7.4 is supported by the good agreement between the rate of loss of fibrils as monitored by ThT fluorescence and the reappearance of native β_2m during depolymerisation at pH 7.4 (Section 2.3.7).

Despite the increased persistence of HMW species forming during fibril depolymerisation at pH 6.4 explaining differences in membrane disruption potential between the two conditions, the broadness of the LMW peak under both conditions (in comparison with native β_2m controls (Figure 3.3.7)) means that the presence of non-native LMW species cannot be ruled out. However, as the broadness of the peak is related to the signal to noise ratio of the ACs (greater error, less discrete distribution of species according to MEM – Section 3.2.5), it is difficult to comment with any degree of confidence about the potential heterogeneity of LMW species from this parameter alone. Nevertheless, as different species with τ_D within an order of magnitude of one another cannot be resolved by MEM (Section 3.3.1), the position of the peak centre can be informative as to the heterogeneity of LMW species in solution. A significant population of LMW oligomers would manifest in a shift of the peak centre away from that obtained for native β_2m controls. As the LMW peak centre falls within range of that for native monomer controls (Figure 3.3.7) it is most likely that the LMW peak is predominantly monomeric. This is supported by the previous NMR experiments, as significantly populated LMW non-native species would lead to observable non-native chemical shifts at various time points during the acquisition of ^{1}H-^{15}N HSQC spectra as depolymerisation proceeds. Chemical shift differences are only observed during the earliest time point collected during fibril depolymerisation at pH 6.4 (Figure 2.3.19).

As the LMW peak is completely resolved from the small amount of higher order species observed during fibril depolymerisation at pH 7.4, the relative number of molecules contributing to this peak can be calculated and plotted vs. time. If the rate of LMW peak appearance is consistent with native β_2m reappearance calculated by NMR, then this will confirm that the LMW peak is predominantly native, non-toxic β_2m.

The number of molecules within the LMW peak can be calculated by scaling the summed amplitudes associated with all τ_D values that fall within the LMW peak, by the overall amplitude of all species extracted from the entire AC (1/N in equation 10) and the proportion (or fraction) of the overall amplitude attributed to the LMW peak (α_i).

$$G(\tau) = \frac{1}{N}\sum_{i=1}^{n}\frac{a_i}{\left(1+\frac{\tau}{\tau_{Di}}\right)\left(\sqrt{1+.\frac{\tau}{K^2.\tau_{Di}}}\right)} \qquad (10)$$

The way that peak area scales as a function of multicomponency is best illustrated in Figure 3.3.9. An AC derived from a homogenous solution containing on average 5 fluorescent molecules within the confocal volume is shown in Figure 3.3.9a. When the number of molecules (N, Equation 10) is increased two fold, the initial amplitude of the AC, is decreased by half (0.2 to 0.1, G(0), Figure 3.3.9a and b). The AC in Figure 3.3.9b indicates that an additional species (HMW species) of increased τ_D is now observable in solution in addition to the original species (LMW species) from Figure 3.3.9a. Each species comprise half of the molecules detected at any one time (5 each) so the number of LMW species is unchanged from Figure 3.3.9a. However, for multicomponent systems, each species contributes only the fraction of signal derived from that species as a function of the total amplitude of the AC (α_i in the above equation). Therefore each species in Figure 3.3.9b contributes only half of the overall amplitude (Figure 3.3.9c LMW species green – HMW species orange). So despite the same number of LMW species present within each sample from Figure 3.3.9a and b, the relative signal has been reduced 4 fold (G(0) from Figure 3.3.9a – c reduced from 0.2 to 0.05). This is also seen in the MEM distribution (Figure 3.3.9d), where the area of the LMW peak has been reduced four-fold due to the increased number of species detected (signal decrease by half) and the heterogeneity of the

system (by half again) (Figure 3.3.9d). In order to calculate the number of LMW species populating during depolymerisation at pH 7.4, the LMW peak volume (or summed amplitudes from τ_D within the LMW peak) must be scaled by the overall amplitude (1/N) and the fraction to which LMW species contribute to the overall amplitude of the AC (α_i).

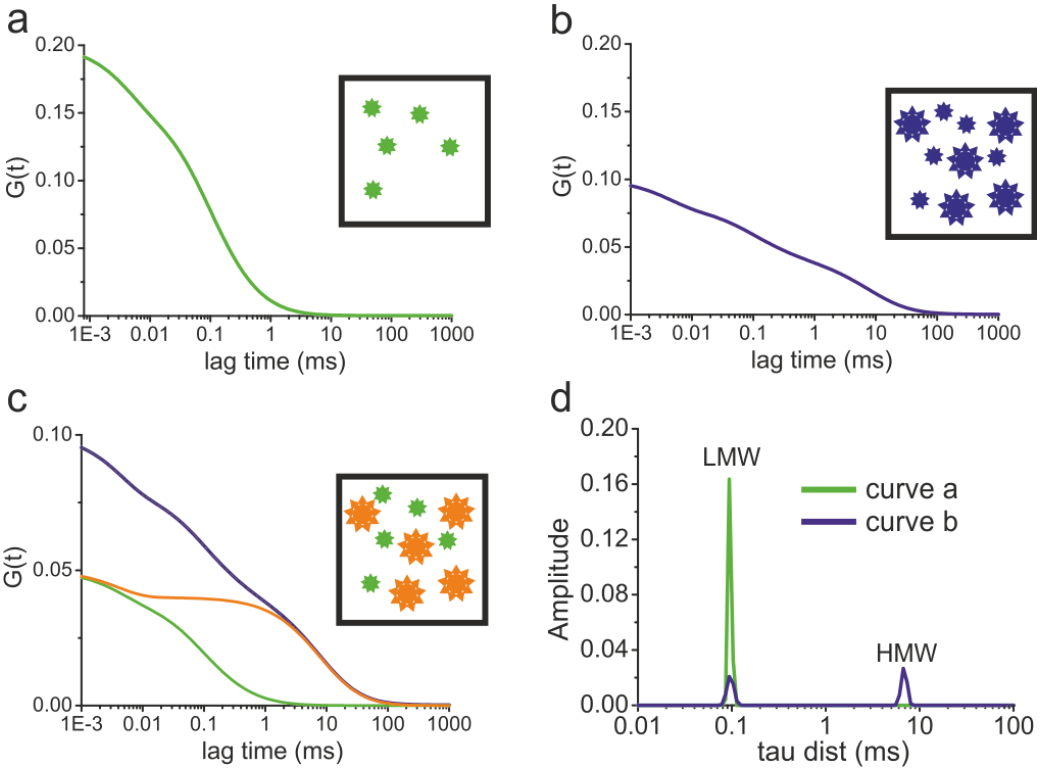

Figure 3.3.9 Simulation to illustrate how peaks scale in multicomponent ACs. (a) AC derived from 5 molecules with τ_D = 100 µs. (b) Multicomponent AC derived from species in (a) plus 5 additional molecules with τ_D = 10 ms. (c) Breakdown of the contribution of both species (species a – LMW species –green, HMW species in orange) to the overall AC (blue). (d) MEM distributions of (a) and (b).

This analysis was performed for the time points shown in Figure 3.3.8a, with two additional time points acquired 5 min and 1440 min after depolymerisation initiation at pH 7.4. The resulting ACs are shown in Figure 3.3.10a, normalised to the 5 min time point.

Figure 3.3.10b shows that after plotting the relative number of molecules associated with the LMW peak vs. time, the appearance of LMW species is best described by a mono-exponential function with an apparent rate constant of 1.4×10^{-2}.min^{-1}. Although slightly faster than that calculated for the rate of appearance of native β_2m resonances by NMR (1.06×10^{-2}.min^{-1}), fibrils used in FCS experiments were seeded with a ten-fold higher concentration to ensure polymerisation was completed on a

time scale that preceded the hydrolysis of Alexa488 at low pH (maleimide ring cleavage occurs under acidic conditions leading to the liberation of free dye). A higher seed concentration will generate a fibril population in which the average length of fibrils is reduced. The reduction of fibril length (while maintaining fibril monomer equivalent concentration) will generate more sites from which depolymerisation can proceed, if fibril depolymerisation is mediated from fibril ends (as suggested by the length-dependency associated with membrane disruption and cellular toxicity caused by β2m fibrils – Section 2.1). Therefore, the difference in the rate at which native β_2m reappears by NMR and the rate at which LMW species populate during depolymerisation as monitored by FCS is likely to be due to differences in fibril lengths of the initial fibril population used in each experiment.

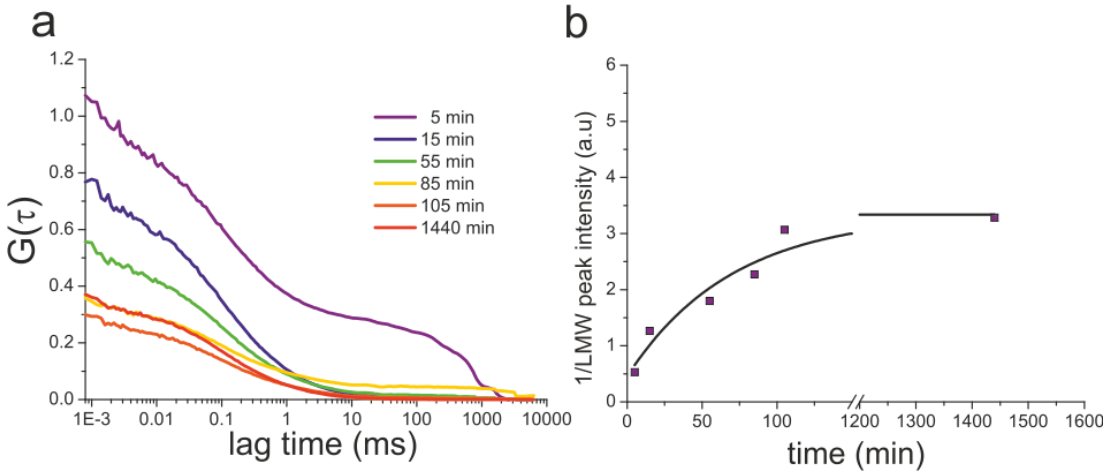

Figure 3.3.10 The rate of LMW peak intensity reappearance at pH 7.4. (a) Normalised raw ACs collected during fibril depolymerisation at pH 7.4. Curves are shown normalised to G(0) of the AC collected 5 min after the initiation of fibril depolymersation. Curves were fitted by MEM and 1/N (see equation 10) corresponding to LMW species were calculated as described in Figure 3.3.9. The reciprocal of 1/N (peak intensity – y axis in b) is plotted vs. time in (b).

The same analysis cannot be performed at pH 6.4 due to difficulties in calculating the relative amplitude of LMW species as they are not exclusively resolved from HMW species (due of the larger error associated with ACs collected during depolymerisation at this pH (Figure 3.3.6b)). However, the consistency of the apparent R_H of the LMW peak centre for native β_2m controls and species observed during depolymerisation at both pH 7.4 and pH 6.4 suggests the LMW peak is likely to be predominantly composed of native β_2m monomer, as detected by NMR (Section 2.3.7). Therefore the LMW species observed during FCS are native, non-toxic β_2m, suggesting that the soluble HMW species, which are most frequently

observed during depolymerisation at pH 6.4, must be the primary source of *in vitro* liposome disruption activity and contribute cellular metabolic dysfunction.

3.3.5 HMW oligomers interact with native β_2m at pH 6.4

The apparent R_H of HMW species increases by approximately 10 nm from ~20 to 31 nm (Figure 3.3.8b) 135 min after the initiation of depolymerisation at pH 6.4. A similar increase in apparent R_H is not observed for LMW species. This suggests that HMW species may coalesce post-formation, sequester refolded native β_2m monomer, or both, between 95 – 135 min after the initiation of depolymerisation. The increase in apparent R_H may also be due to baseline fluctuations within the measurement recorded at the 135 min time point. To test whether HMW species re-interacting with native β_2m could be responsible for the increase in apparent R_H of HMW species 135 min after fibril depolymerisation was initiated, FCS experiments were performed in the presence or absence of unlabelled fibrils and native 18 nM R3C488 at pH 7.4 and pH 6.4. Depolymerisation of 120 μM unlabelled β_2m fibrils was induced by diluting 4-fold into pH 7.4 or pH 6.4 buffer at 25°C. Solutions were left for 30 and 60 min respectively before the addition of native 18 nM R3C488. At pH 7.4, ACs of R3C488 are identical in the presence and absence of unlabelled fibrils, indicating no interaction, or no detectable exchange, between native β_2m and aggregate species (Figure 3.3.11a). However, at pH 6.4, a significant difference in the profile of the AC is observed in the presence of β_2m amyloid fibrils (Figure 3.3.11b). The apparent R_H distributions of species within each AC were extracted using MEM (Figure 3.3.11c and d). At pH 7.4, a single peak equivalent in apparent R_H (1.7±0.1 nm) to that observed for native β_2m monomer controls (Figure 3.3.7) is populated, suggesting that, at least by FCS, native β_2m is not capable of re-interacting with HMW species. The lack of detectable interaction between native β_2m and HMW species may also be due to the low abundance of HMW species populating during depolymerisation at this pH (Figure 3.3.8). At pH 6.4, however, the apparent R_H distribution shows that, in addition to LMW species, a second, HMW species is present with an apparent R_H (Figure 3.3.11d 18±8 nm) equivalent to those detected during fibril depolymerisation experiments outlined in Section 3.3.4. This suggests that β_2m fibrils are able to contribute to *in vitro* membrane disruption and the disruption of cellular metabolic activity via a bipartite mechanism at pH 6.4;

by initial shedding of persistent, membrane-active HMW oligomers that in turn deplete the local pool of native monomeric species.

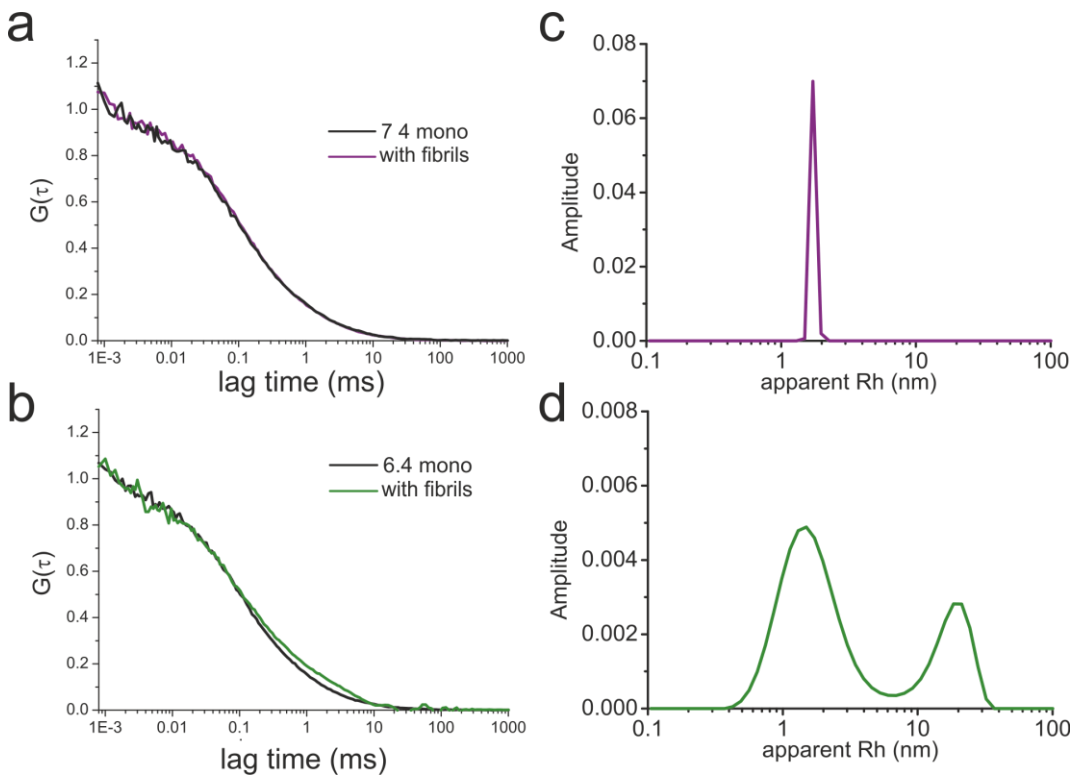

Figure 3.3.11 HMW species interact with native β_2m at pH 6.4. Raw ACs of 18 nM native R3C488 at pH 7.4 (a) and pH 6.4 (b) in the presence and absence of unlabelled β_2m amyloid fibrils acquired 30 and 60 min after depolymerisation initiation respectively. (c) Apparent R_H distribution of species extracted from the AC corresponding to 18 nM R3C488 in the presence of 30 µM *wt* β_2m fibrils 30 min after depolymerisation initiation at pH 7.4. (d) As above, but for fibrils undergoing going depolymerisation at pH 6.4 for 60 min.

3.3.6 Limitations of MEM in quantifying molecular shedded species

As shown in Section 3.3.1, when different species are adequately separated in the time domain, MEM can accurately describe the τ_D and population of each species. This raises the prospect of using MEM to calculate absolute concentrations of the HMW species that are formed at pH 6.4. In experimental ACs, however, the amplitude associated with each τ_D is related not only to the relevant concentration of the species, but also the brightness, or quantum yield, of the fluorescent moiety when incorporated into a higher order species. Neither the quantum yield of dye incorporated into labelled oligomers, or the labelling stoichiometry of the higher order species, which is also required for calculating particle molarity (how many labelled monomers per oligomer), is known, therefore it is not possible to accurately quantify the concentration of HMW species relative to native β_2m (LMW species)

that populate during fibril depolymerisation. However, if species of comparative size populate under both conditions, then MEM distributions can provide semi-quantitative observations of how the population of species differ between the two conditions. What MEM therefore shows us is that at pH 6.4, HMW species are significantly populated and persistent and can presumably participate in liposome disruption and affect cellular metabolic activity. In comparison, fibril depolymerisation at pH 7.4 results in the rapid formation of native, non-toxic β_2m, where HMW species are transient and lowly populated, leading to a lower membrane disruption potential, in spite of an increased amplitude of fibril depolymerisation.

3.3.7 Structural interrogation of molecular shedded species

Although FCS has confirmed the existence of HMW species presumably responsible for fibril-mediated membrane disruption, little has been revealed thus far about their structural properties. Therefore the structural properties of these oligomers were assessed using several techniques. Initially, fibrils were depolymerised at pH 6.4 for 30 min and samples prepared for negative-stain TEM. Figure 3.3.12b shows that spherical aggregates are observed populating at pH 6.4, with species appearing heterogeneous in size and typically ranging from 20 – 50 nm in diameter. No oligomers were detected at pH 7.4 (a). This is consistent with the broadness associated with HMW species described by MEMFCS during fibril depolymerisation at pH 6.4 (Figure 3.3.8). In order to determine whether the size of species in TEM experiments is consistent with those observed in FCS, 850 particles were traced from electron micrographs. The frequencies of end-to-end distances were sorted into 10 nm bins and are shown in Figure 3.3.12c. The most common size observed in TEM is 50 nm. Apparent R_H measurements are typically different from comparative end-to-end distance measurements obtained using other techniques (such as negative-stain TEM) due to the additional presence of a hydration sphere (414). The presence of a heavy metal stain can also make species appear larger in negative-stain TEM, due to the presence of a pool of electron-dense stain about the particles under observation. This is likely to account for the differences between apparent R_H measurements (~20 nm, diameter 40 nm) made using FCS and the distribution of end-to-end distances calculated from particle tracing from electron micrographs. Nevertheless, there is a good overall agreement between size measurements and size distributions of species observed using either technique.

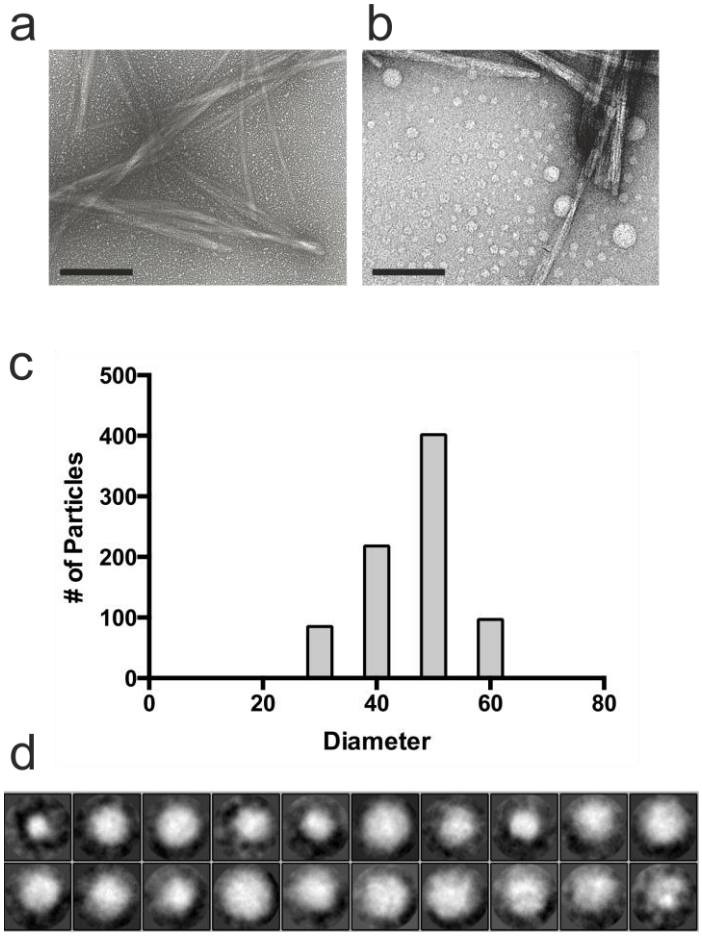

Figure 3.3.12 Detection of molecular shedded oligomers using negative-stain TEM and cryo-EM. Negative-stain EM micrographs of samples at (a) pH 7.4 or (b) pH 6.4, 30 or 60 min after the initiation of fibril disassembly. Scale bar is 150 nm. (c) Distribution of longest end-to-end distances of 850 traced oligomers formed during depolymerisation at pH 6.4. Bin size is 10 nm. (d) Particle class averages from cryoEM of products of depolymerisation formed in pH 6.4 buffer. (c) and (d) kindly performed by Dr Matt Iadanza (University of Leeds)

Oligomers could also been seen embedded within vitreous ice in samples prepared for cryoEM. CryoEM can obtain higher resolution detail (near-atomic) than negative stain EM as samples are not contaminated with heavy metal isotopes and remain hydrated. Despite this, class averaging of particles could not generate any high-resolution structures, presumably due to the high degree of heterogeneity within oligomers (Figure 3.3.12d). The inability of particle averaging to generate high-resolution reconstructions of oligomers suggests that they contain little or no fixed elements of structure.

The suggestion from cryoEM that oligomers are unstructured prompted the structure of oligomers to be probed with the W01 antibody, which recognises the generic cross-β core formed from a range of different amyloid fibrils (80, 81). Dot blots were

performed on total protein samples and partitioned filtrates of fibril solutions that were allowed to undergo depolymerisation at pH 7.4 or 6.4 for 30 or 60 min respectively. Samples of the filtrate were repeatedly administered to the membrane to ensure that comparable protein concentrations of β_2m were present in filtrate and total protein samples (α-β_2m blot, Figure 3.3.13). Figure 3.3.13 shows that the filtrate at both pH 7.4 and 6.4 do not possess the W01 binding epitope, by contrast with fibrils.

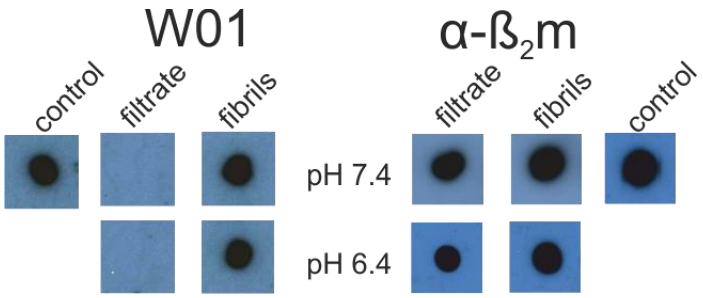

Figure 3.3.13 Dot blot analysis of molecular shedded material. Filtrates generated after depolymerisation at pH 7.4 and 6.4 and total protein samples (fibrils) were blotted with the W01 and α-β_2m antibodies. Control blots were performed with fibrils at pH 2.0

To further probe oligomer structure, filtrates generated during fibril depolymerisation were analysed using far-UV CD spectroscopy. Filtrates were generated as described in Section 3.3.7 and soluble material quantified using densitometry of SDS-PAGE gels (Figure 3.3.14). Filtrates were quantified to facilitate the direct comparison of CD spectra of molecular shedded material with native β_2m controls acquired at equivalent concentrations in the respective buffers. Figure 3.3.14 confirms the accuracy of using SDS-PAGE densitometry to calculate relatively low concentrations of protein (low μM range – absorbance at 280 nm unreliable at this concentration). Samples generated during fibril depolymerisation were loaded alongside three calibrants of known protein concentration and two control samples of β_2m previously quantified using Beer-Lambert's law in order to confirm the accuracy of the method. A calibration curve was constructed from the absorbance of the three calibrant bands against the known concentrations and the corresponding equation used to calculate the concentration for unknown samples. The 30 μM (1.75 μg of protein) and 25 μM (1.45 μg) loading controls were

calculated to a high degree of accuracy using the calibration curve, providing confidence for the concentrations calculated for soluble material generated during depolymerisation.

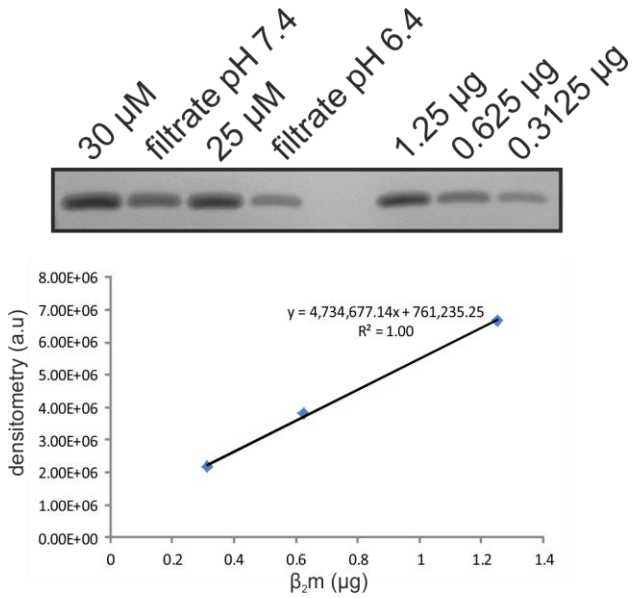

sample	abs (a.u)	β_2M (µg)	[β_2M] (µM)
control 1	9001670	1.74	29.35
filtrate pH 7.4	5216221.5	0.94	15.87
control 2	7673639.5	1.46	24.62
filtrate pH 6.4	3582556.5	0.60	10.05

Figure 3.3.14 Quantification of filtrates partitioned during fibril depolymerisation.. Filtrates generated 30 min or 60 min after depolymerisation initiation were electrophoresed with β_2m calibrants consisting of 1.25, 0.625 and 0.3125 µg. The absorption of bands was calculated and plotted against µg of protein to construct a calibration curve. Filtrate concentrations were then calculated from the in-gel calibration. Two additional controls of 25 and 30 µM β_2m were also loaded onto the gel and quantified by this method.

Far-UV spectra of filtrates partitioned during depolymerisation along with spectra of native β_2m controls collected under identical solution conditions are shown in Figure 3.3.15a and b (pH 6.4 and 7.4 respectively). For both spectra, a reduction in the positive λ_{max} at approximately 200 nm is apparent compared with native monomeric β_2m controls. The difference is more pronounced at pH 6.4, consistent with a higher concentration of non-native species accumulating during depolymerisation at this pH. Under both conditions, the negative λ_{max} value of 217 nm is similar to that of native β_2m controls. This suggests that a significant proportion of soluble material contains β-sheet structure, corroborating with NMR (and FCS) showing that native, monomeric β_2m reappears during depolymerisation. There is also a reduction in mean residue elipicity at approximately 230 nm at pH 6.4. For native β_2m, the

absorption in this region of the far UV CD spectra is thought to arise from aromatic-aromatic π stacking. The loss of signal from this region may be due to higher incidence of non-native oligomers populating at pH 6.4. In order to highlight regions of the spectra where the greatest changes are observed, the difference spectra were calculated by subtracting the native β_2m spectra from that of the partitioned soluble material (Figure 3.3.15a and b, dashed lines). This confirms that the greatest differences are seen between 190 – 210 nm, which is the region of CD absorption for intrinsically disordered proteins (415).

As partially or fully unfolded proteins can display increased solvent-exposed hydrophobic surface area, soluble material generated at pH 6.4 and 7.4 was tested as to its ability to interact with 8-anilinonaphthalene-1-sulphonate (ANS). ANS is a

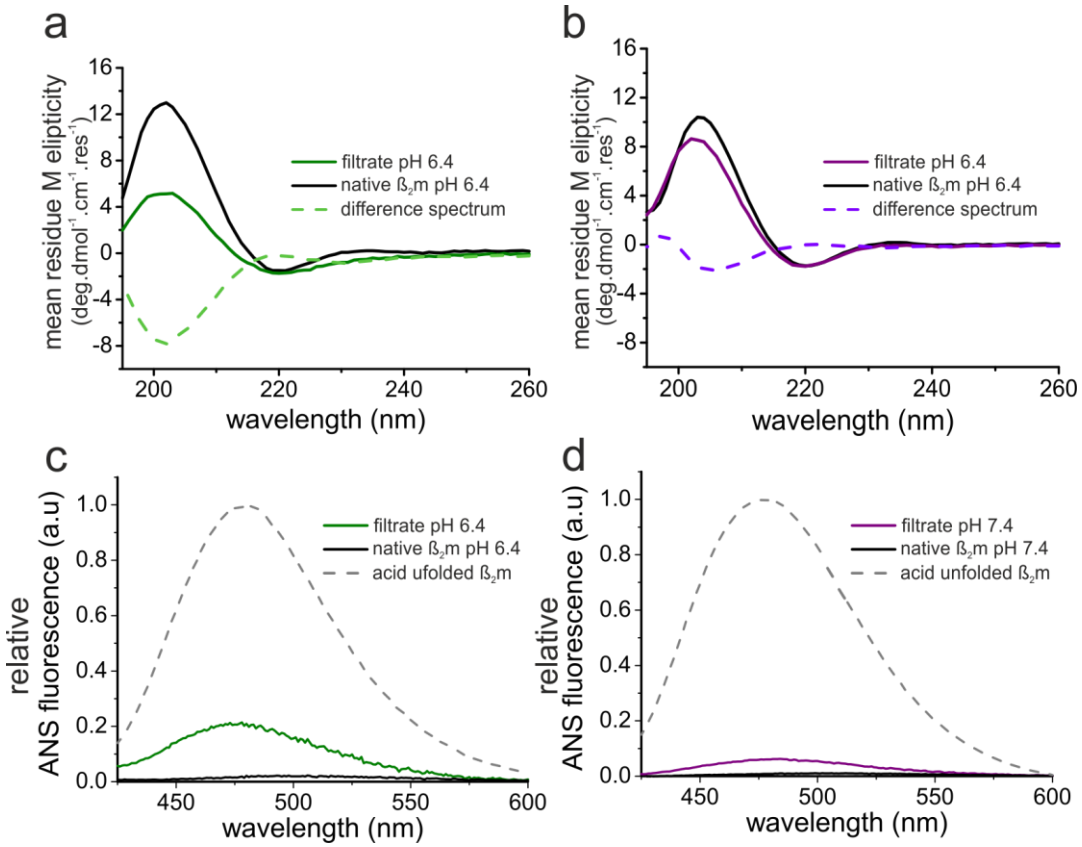

Figure 3.3.15 Far-UV CD and ANS binding studies of molecular shedded species. Mean residue ellipticity of the filtrate isolated 30 or 60 min after the initiation of fibril disassembly at (b) pH 6.4 or (b) pH 7.4,respectively, measured using far-UV CD. Spectra of native β_2m (black) were acquired at the same protein concentration. Difference spectra are shown in dashed lines. ANS fluorescence emission spectra of the filtrate isolated as stated in Section 3.2.10, at (c) pH 6.4 or (d) pH 7.4 and of native β_2m at equivalent concentrations. Curves are normalised to the maximum amplitude of the spectrum of acid unfolded β_2m at pH 2.0 (grey dashed line) acquired at the same protein concentration. Native β_2m monomer controls are shown in black.

fluorescent probe known to bind to surface-displayed hydrophobic patches which generates a marked increase in fluorescence emission intensity and a blue shift in λ_{max} emission wavelength of ANS (416). ANS spectra are shown normalised to the equivalent concentration of acid unfolded β_2m in Figure 3.3.15c - d. At saturating ANS concentrations, the fluorescence intensity of soluble material is approximately 10 or 6 times greater than the equivalent concentration of native β_2m at pH 6.4 (Figure 3.3.15c) or 7.4 (Figure 3.3.15d) respectively. Both ANS spectra of soluble material experience similar λ_{max} blue shifts of approximately 30 nm compared with native β_2m, indicating a significant enhancement in surface exposed hydrophobicity within non-native species shed from fibrils. The similarity of the λ_{max} blue shift suggests that non-native species generated at both pH are equivalently hydrophobic, although the magnitude of the increase in fluorescence intensity in comparison with native control spectra confirms a higher concentration of non-native species populate during fibril depolymerisation at pH 6.4.

3.4 Discussion

Here, the demonstration of the effect of subtle changes to solution conditions on the dynamics and the associated changes to pathological capacity of a disease-associated amyloid assembly are described. The rapid assembly and disassembly of functional amyloids has been shown to be an important facet of tuning rapid metabolic responses in response to the environment within the cell (136–138, 241), but whether amyloid fibrils known to cause cellular dysfunction undergo similar condition-dependent dynamics had not previously been established.

For β_2m, our *in vitro* characterisation of soluble species forming during depolymerisation has shown a remarkable pH dependence; reducing the pH by a single unit, from pH 7.4 to 6.4, results in a large increase in the relative concentration of HMW species in comparison with native β_2m monomer. These species are likely to be responsible for membrane disruption displayed by soluble material generated during fibril depolymerisation, as the identity of the LMW species is predominantly membrane-inactive native β_2m monomer. Evidence for this is provided from experiments performed in Chapters 2 and 3, including i) NMR, which shows the rapid reappearance of native β_2m chemical shifts upon depolymerisation at pH 7.4, ii) the agreement between ThT kinetic rate constants and

the global reappearance of native β_2m resonances, iii) the good agreement between apparent R_H of native β_2m monomer controls and LMW species observed during fibril depolymerisation and iv) the similarity of the apparent rate which LMW species and native β_2m resonances reappear by FCS and NMR respectively. Thus HMW species formed during depolymerisation can be strongly linked to *in vitro* membrane disruption activity exhibited by soluble material.

The greater stability of HMW species formed during depolymerisation at pH 6.4 explains i) the delay between the loss of ThT fluorescence (oligomer formation) and the rate of monomer reappearance as studied by NMR; ii) their increased accumulation during depolymerisation (Figure 3.3.8); and iii) the increased amplitude of membrane disruption (Section 2.3.4). This is in spite of the decreased amplitude of total soluble material generated at pH 6.4 in comparison with

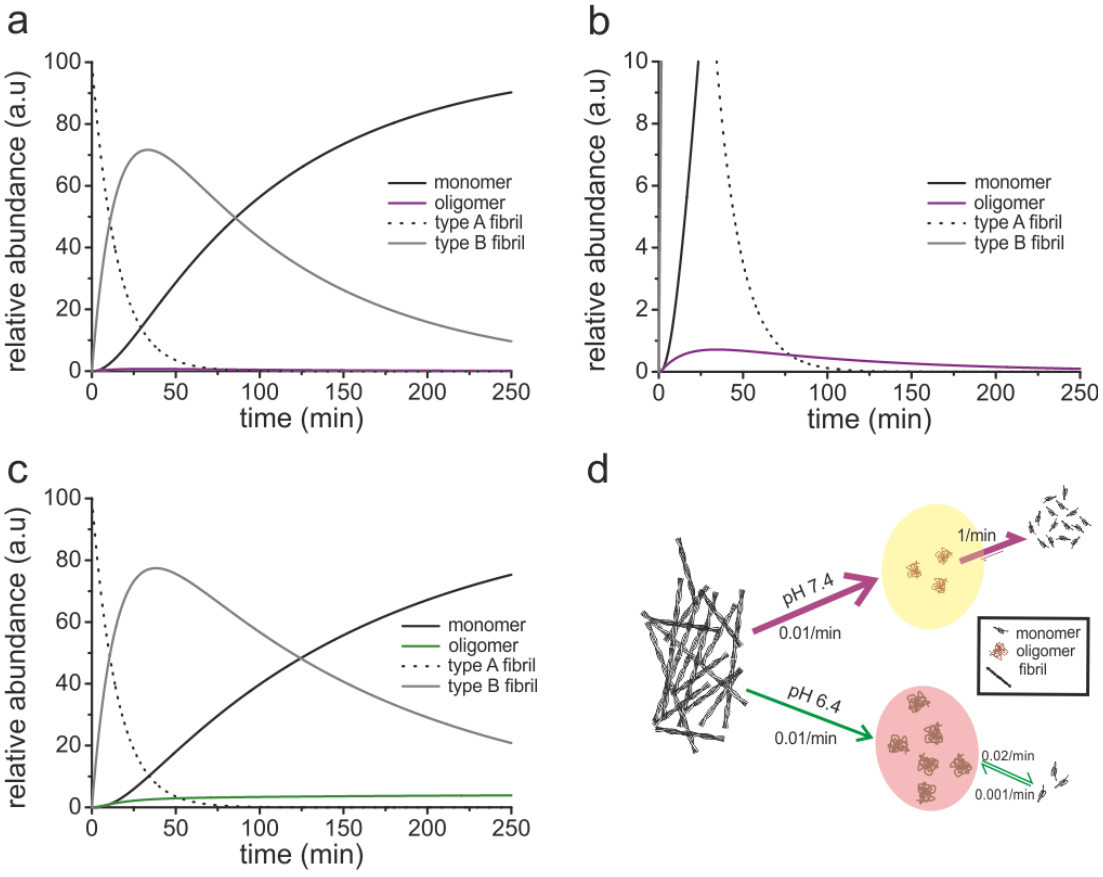

Figure 3.4.1 Modelling the molecular shedding phenomenon. (a) Disassembly of fibrils at pH 7.4 via a 4-state linear model. Species are indicated in the key. (Type A to Type B fibril is the initial increase in ThT fluorescence observed in Figure 2.3.6. (b) provides a zoom of the initial stages of depolymerisation at pH 7.4. (b) Depolymerisation modelled at pH 6.4. (d) Schematic representation of the differences of molecular shedding at the two pH. For simplicity, the initial transition between the possible transition of fibril architecture is not shown.

depolymerisation at pH 7.4 (Figure 2.3.7). The rates calculated from ThT fluorescence measurements and NMR, as well as insights provided by FCS, were used to model the kinetic response of fibrils under the two sets of conditions. This shows that, at pH 7.4, very low populations of oligomers are present throughout fibril depolymerisation, as the equilibrium is driven rapidly to native β_2m (Figure 3.4.2a-b, purple line). Conversely, at pH 6.4, the delay between fibril loss (ThT fluorescence) and monomer reappearance (NMR), and the observed back-exchange between native β_2m and HMW species at pH 6.4 (as seen by FCS – Figure 3.3.11), means that a pool of oligomers persists throughout depolymerisation (Figure 3.4.2c), confirming observations made by MEMFCS (Figure 3.3.8b).

Why HMW species show such pH dependent stability has not been established in this thesis, but one could speculate that it is likely to be to due changes in electrostatic charges upon β_2m caused by the reduction in pH. This may provide some indication as to which residues are important in facilitating oligomer stability and would be an interesting avenue in which to further investigate. This is discussed in more detail in Chapter 4.

The latter part of this chapter has attempted to structurally characterise HMW species formed during molecular shedding. This characterisation has established that oligomers i) lose their cross-β core upon formation, ii) exhibit increased hydrophobic surface exposure in comparison to native β_2m controls under the same conditions, and iii) appear to contain an increase in intrinsically disordered secondary structure in comparison with native β_2m controls. Importantly, soluble species generated at pH 7.4 and pH 6.4 exhibit similar structural characteristics, although the incidence is more pronounced at pH 6.4. This suggests that a low concentration of HMW species must exist at pH 7.4, but are either below the detection threshold of the current FCS set up (Figure 3.3.8a) or are too transient to detect. The presence of HMW species may also explain the low ionisation efficiency of native β_2m during ESI-IMS-MS experiments performed in Chapter 2. This explains the small but significant amplitude of membrane disruption seen from soluble material generated at pH 7.4.

In a cellular context, the subtle changes in pH could have significant consequences on the monomer-oligomer-fibril equilibria. As previously mentioned, fibrils deposited extracellularly, or even cytoplasmically, are often trafficked through

endosomal compartments as they seed amyloid aggregation throughout entire tissue systems. This trafficking may facilitate fibrils from a variety of diseases entering an environment that tunes the equilibrium in favour of generating a large and localised pool of membrane-active oligomers. For β_2m, endosome maturation after fibril internalisation may not only lead to an environment for the optimum generation of HMW oligomers (Figure 3.4.3), but also includes the formation of a lipid

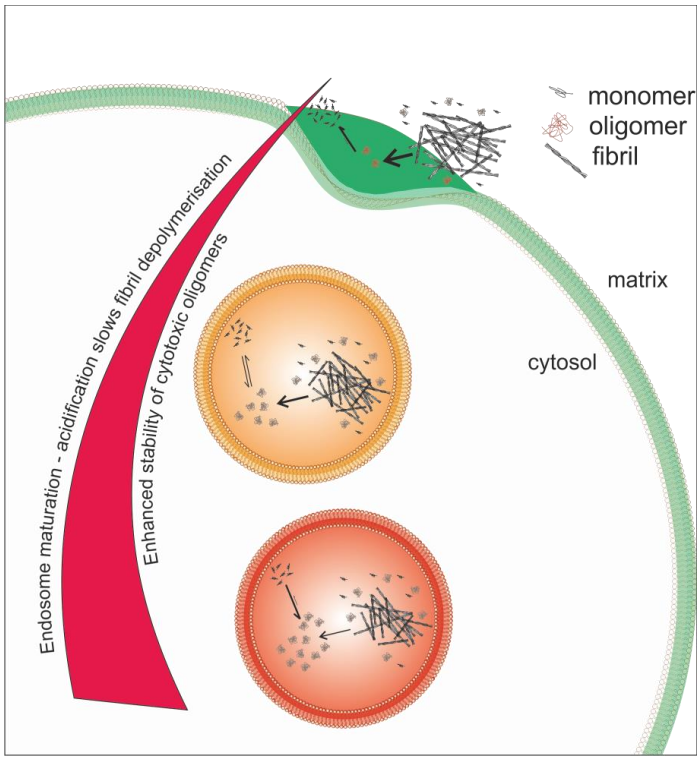

Figure 3.4.2 A potential hot-spot for β_2m amyloid-mediate cellular disruption?

composition enriched in BMP. As shown in Chapter 2, the presence of BMP makes LUVs more susceptible to fibril-mediated membrane disruption (Figure 3.4.3). Thus, β_2m fibril-mediated toxicity may be localised to specific endocytic compartments that favourably stabilise molecular shedded oligomers in the presence of preferential lipid compositions for membrane disruption (Figure 3.4.3).

Another interesting question this discovery poses is whether these oligomers are equivalent to those that form during the lag phase of fibril assembly at low pH. To date, no evidence is available to support their existence during fibril formation, raising the possibility of the discovery of a new, previously uncharacterised oligomer ensemble. The final chapter in this thesis aims to determine whether the processes of polymerisation and depolymerisation are equivalent and opposite or entirely distinct, and whether oligomers formed during each process are structurally homologous.

CHAPTER 4

Comparing the mechanisms of fibril polymerisation and depolymerisation

4.1 Introduction

As discussed in Section 1.3.4, fibril polymerisation is preceded by the formation of a variety of oligomeric species that are required for the initiation of fibril growth (146, 151, 188, 238, 387, 392, 417, 418). These species are typically thought to be responsible for toxicity (2, 20, 21, 25, 184). After the formation of a nucleating particle, fibril polymerisation proceeds by an end-dependent process involving the templated conversion and incorporation of precursors into the elongating amyloid fibril. The morphology of species incorporated during fibril elongation are not widely known (419), however, once fibril growth has reached equilibrium, soluble species that exchange with fibrils have been shown to be structurally homologous to particles that form in the lag phase (188, 238, 392). The structural homology between these two types of oligomers, coupled with the fact that soluble species are consumed at fibril ends during fibril elongation, suggests that the recycling of oligomers from mature amyloid fibrils may be similarly end-dependent. Based on this, it may be reasonable to assume that the release of membrane-active soluble species upon β_2m fibril depolymerisation at near-neutral pH is also end-dependent.

Previous studies performed in the Radford group have highlighted a β_2m fibril length-dependent relationship between the extent of membrane disruption and the disruption of cellular metabolic activity (245, 341). Briefly, fibrils fragmented in order to reduce fibril length display enhanced membrane disruption activity in comparison with their longer counterparts. This length dependent phenomenon was further shown to be conserved for a range of other fibril types, including fibrils formed from α-synuclein, Aβ_{42} and lysozyme (420). For β_2m fibrils at least, the fact that membrane disruption is length-dependent and is mediated by the release of soluble species suggests that β_2m fibril depolymerisation at near-neutral pH is likely to proceed from fibril ends; shorter FLDs at monomer equivalent concentrations possess a greater number of ends from which membrane-active oligomers can be released. Nevertheless, the comparison between the number of fibril ends and the extent of membrane disruption does not correlate exactly. For example, fibrils

fragmented for 48 h cause less than twice the extent of membrane disruption than their longer counterparts. This is despite the average fibril length being approximately four times shorter (245, 341). Work in this chapter therefore aims to investigate the mechanism by which molecular shedding of membrane-active species during fibril depolymerisation takes place, in order to rationalise why membrane disruption potential does not increase in accordance to the number of fibril ends within a fibril population. The end-dependency of seeded fibril polymerisation will also be investigated to establish whether polymerisation at low pH and β_2m fibril depolymerisation at pH 6.4 are equivalent but opposite processes. Finally, the structure of oligomeric species that form within the lag phase of β_2m amyloid assembly will be investigated to probe whether soluble species that form during each process are structurally homologous or distinct.

4.2 Material and Methods

4.2.1 Tapping mode atomic force microscopy

AFM analysis of fibril samples and characterisation of fibril length distributions was performed as previously described in Section 2.2.5. Fibril samples fragmented for different times were generated by first incubating 120 μM β_2m in fibril growth buffer and seeding fibril formation with 0.1% (*w/w*) β_2m fibril seeds (see section 2.2.4) and incubating at room temperature under quiescent conditions for a minimum of 48 h. 500 μl aliquots were then placed on a custom made precision stirrer in 1.5 ml chromacol glass vials and fragmented as previously described at 1000 rpm (section 2.2.4). Aliquots of 100 μl were removed at 0.5, 6.5, 18 and 48 h after the initiation of fibril fragmentation. A maximum of 200 μl was removed from any individual aliquot so duplicate samples were prepared.

4.2.2 Fibril seeding assay

The fibril samples generated above were used in a fibril seeding assay to determine the end-dependency of fibril polymerisation. To do this, 120 μM β_2m monomer in fibril growth buffer (Section 2.2.4) was seeded with 10% (*w/w*) (monomer equivalent concentration) of each of the fibril samples generated above. Fibril formation was monitored on a Fluostar Omega plate reader (BMG Labtech) by supplementing fibril growth buffer with 10 μM ThT. The instrument was operated as previously described and samples prepared as previously described (section 2.2.7), with the only differences being the gain control was set to 75% of the fluorescence emission value of 120 μM pre-formed β_2m amyloid fibril control in the presence of 10 μM ThT. Each seeding assay was performed with a minimum of five repeats. To calculate the initial rate of fibril elongation, the initial 10 data points (one time point per minute) were fitted using a linear equation with the gradient used as the rate. The average of the repeat measurements is displayed as the rate with the standard deviation from repeat measurements the error.

4.2.3 Fibril depolymerisation assay

Depolymerisation assays at pH 6.4 were performed with a minimum of six repeats (except 48 h fragmented fibrils – only four repeats were performed). Fibrils were pre-bound by ThT in fibril growth buffer (Section 2.2.4) by incubating 25 μl aliquots

of 120 µM fibrils with 40 µM ThT in 96 well plates for 30 min prior to diluting samples 4-fold with pH 6.4 buffer (see Section 2.2.6 for buffer composition) pre-incubated at 25°C for at least 1 h before use. Fibril depolymerisation was then immediately monitored exactly as described in Section 2.2.7. Individual repeats of ThT fluorescence curves were fit with the following double exponential function using Origin Pro v.8.6:

$$y = -A^{k_1 t} + B^{k_2 t} + C \quad (1)$$

Where A and B are the amplitudes and k_1 and k_2 are the rate constants for the 1st and 2nd exponential phases, respectively. The rate constants shown in the results section are the average of the repeat measurements and the error is the standard deviation The significance is the difference between calculated rates was performed by comparing the rates calculated for each replicate measurement of fibril samples using a two-tailed student's t-test of equal variance in Microsoft Excel.

4.2.4 Fibril formation assay

120 µM β_2m was incubated in a black, clear-bottomed 96 well plates (Costar) in a Fluostar Omega plate reader at 25°C in fibril growth buffer in the presence and absence of 0.001% (*v/v*) Tween-20 and supplemented with 10 µM ThT. Fibril formation was monitored using instrument parameters outlined in Section 2.2.7. Aggregation was performed by shaking plates at 600 rpm in ortibal mode for 50 sec prior to recording ThT fluorescence emission every minute (10 sec per read). The gain control was set as described in Section 4.2.2. Each aggregation assay was performed with a minimum of four repeats.

4.2.5 Comparison of fibril yield in the presence and absence of Tween-20

The yield of fibril formation in the presence or absence of 0.001% (*v/v*) Tween-20 was compared by quantifying the soluble material remaining within the stationary phase using calibrated SDS-PAGE densitometry (Section 2.2.8). Samples were prepared for SDS-PAGE by centrifuging 100 µl aliquots of β_2m fibrils formed in the presence or absence of 0.001% (*v/v*) Tween-20 by centrifuging at 16300 x *g* on a bench top microfuge for 1 h. 10 µl of the supernatant was then removed, prepared for SDS-PAGE and analysed as previously described (Section 2.2.8)

4.2.6 Negative stain TEM

Samples were prepared and analysed as previously described (Section 2.2.1.5)

4.2.7 FCS of β_2m amyloid formation

FCS data acquisition and analysis by MEM was performed as previously described in Chapter 3. Samples were prepared for FCS by diluting native β_2m to 120 µM in fibril growth buffer supplemented with 0.001% (*v/v*) Tween-20 with the addition of 18 nM R3C488 (see Section 3.2.1 for purification and labelling of β_2m variant). Fibril formation was performed on a Fluostar Omega plate reader as described in Section 4.2.4. Aggregation was stopped after 30, 60, 120, 180, 240, 300, 360, 420, 480 and 540 min so that 50 µl aliquots could be removed from a well and immediately analysed by FCS. Samples were analysed by placing them on glass coverslips on the sample platform before 20 x 30 sec ACs were recorded for each time point. Glass coverslips were cleaned before use by sonicating for 10 min in H_2O in a water bath, followed by 10 min sonication in 2% (*v/v*) Hellmanex solution (Hellma), then 10 min sonication in H_2O and finally sonicating for 10 min in 70% (*v/v*) ethanol. Glass coverslips were then aspirated using a gentle stream of N_2 gas before storing in sealed beakers.

4.3 Results

4.3.1 Calculating fibril concentrations from FLDs

In order to explore differences in the mechanism of fibril polymerisation and depolymerisation, populations of β_2m fibrils with different FLDs were generated. This was done to enable the end-dependency of templated fibril elongation and depolymerisation to be investigated by using fibril seeds with identical monomer equivalent concentrations, but progressively shorter FLDs. FLDs that contain significantly shorter fibrils will contain more ends (for the same monomer equivalent concentration) that should, in theory, accelerate seeded fibril elongation (providing seeded polymerisation is end-dependent) (150). To generate fibril seeds with different FLDs, 120 µM of 0.1% (*w/w*) seeded β_2m fibrils were fragmented for 0, 0.5, 6.5, 18 or 48 h (Section 4.2.1). The corresponding FLDs for these fibril samples fragmented for different times were calculated using AFM as previously described (Section 2.2.5). Figure 4.3.1 shows that, as fragmentation time proceeds, fibrils globally decrease in length, with the weight average length decreasing from 1300±50 nm within the unfragmented fibril population to 286±10 nm for fibrils fragmented for 48 h. These average lengths are consistent with those previously described (245, 341).

To study the effect of varying the number of fibril ends on both polymerisation and depolymerisation, FLDs were converted to fibril concentrations. This enables the accurate determination of the number of fibrils ends in solution as opposed to comparing the weight average length determined from AFM analysis (360). To convert FLDs into fibril concentrations, the following equation was derived (150):

$$C_f = \sum^{i} \left(\frac{MEC}{4.65 * l_{fi}} \right) . f_{fi} \qquad (2)$$

where C_f is the fibril concentration, MEC is the monomer equivalent concentration of β_2m within samples, l_{fi} is the length in nm of fibril *i* within the FLD, and f_{fi} is the frequency of l_{fi} as a function of the overall distribution. 4.65 is a constant related to the number of β_2m monomers per nm of fibril length as calculated from STEM analysis of β_2m amyloid fibrils formed at low pH (92). This analysis showed that the most common density of β_2m fibrils was 52 kDa.nm^{-1} (MW of β_2m is 11860 Da). To

simplify the calculation of fibril concentrations, fibrils were sorted into bin sizes of length 50 nm, with the median point within each bin used as l_f. The frequency of the occurrence of fibrils within each bin was then calculated as a function of the overall FLD.

Table 4.3.1 shows the C_f corresponding to each of the differentially fragmented fibril

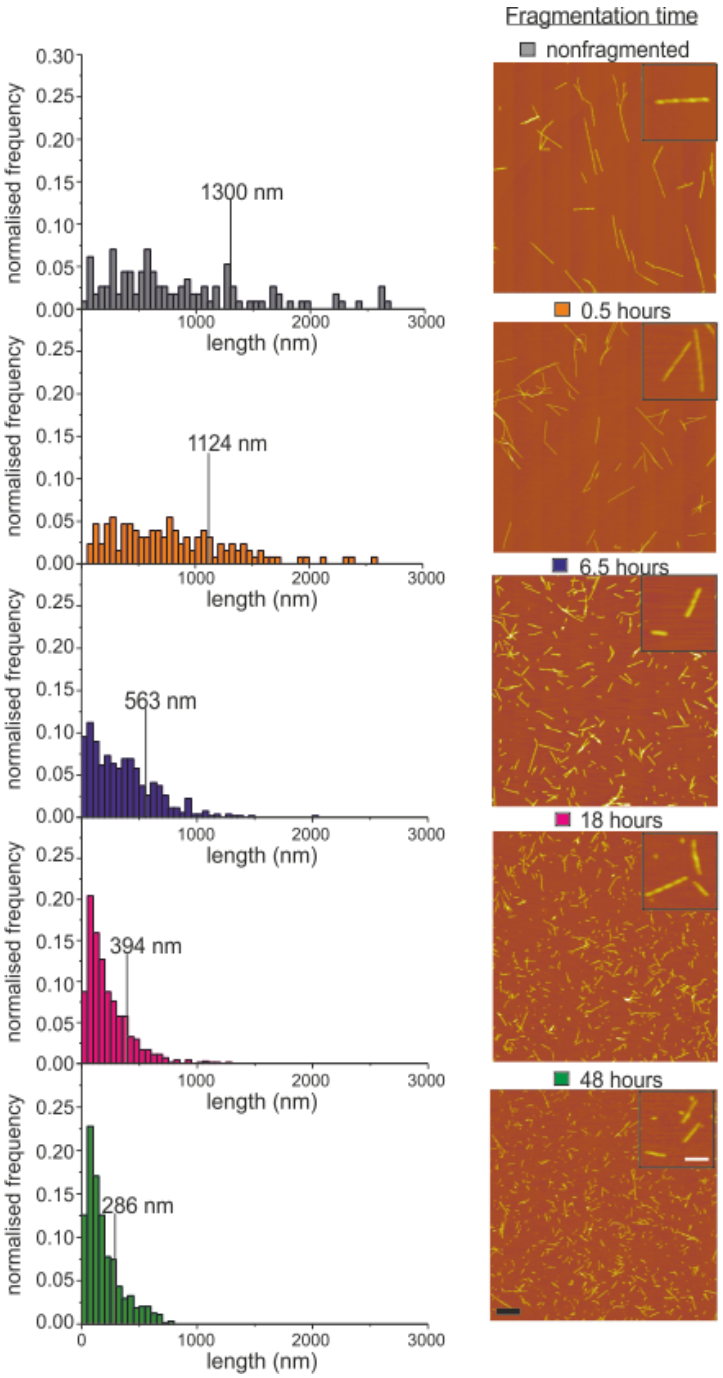

Figure 4.3.1 FLDs of β_2m amyloid fibrils fragmented for different amounts of time. 120 µM pre-formed fibrils were fragmented for 0, 0.5, 6.5, 18 and 48 h using a custom made precision stirrer set to 1000 rpm. Fibril length distributions calculated using AFM are shown normalised to the total number of fibrils traced within each sample.

samples displayed in Figure 4.3.1 when the monomer equivalent concentration is 30 μM. This should be a useful tool for determining C_f in any assay in which β_2m fibrils are used and the monomer equivalent starting concentration is known.

Table 4.3.1 Fibril concentrations calculated from FLDs displayed in figure 4.3.1.

frag time (h)	C_f (nM)
0 h	19.01
0.5 h	15.37
6.5 h	40.73
18 h	63.16
48 h	74.68

4.3.2 Calculating the end-dependency of fibril polymerisation

To determine whether β_2m fibril polymerisation proceeds from fibril ends, the fibril samples characterised above were used in a fibril seeding assay. Fibrils from each sample were used to seed amyloid formation of 120 μM β_2m in fibril growth buffer supplemented with 10 μM ThT (10 % (*w/w*) seed concentration) (Section 4.2.2).

The rate constant of the seeding assay should be dependent on the number of fibril ends in solution, providing that polymerisation is an end-dependent process. The increase in ThT fluorescence over time is a manifestation of the following reaction mechanism;

$$aXn+n \underset{k_r}{\overset{k_f}{\rightleftharpoons}} aX(n+1)$$

Whereby *aX* is the number of available ends (or templating surfaces) and is directly related to C_f, and *n* is the number of subunits. During the seeding assay, the increase in ThT fluorescence is indicative of the conversion of subunits into the fibrillar form and therefore is directly related to k_f (forward rate constant). If there is an increase in the number of fibril ends (such as is the case upon prolonged fibril fragmentation, Figure 4.3.1), k_f should increase proportionately as subunits (*n*) are more rapidly consumed.

As secondary nucleation processes, such as fibril fragmentation and fibril surface-induced catalysis of precursors into amyloid-competent structures (73, 146), can contribute significantly towards modulating the kinetics of fibril elongation, only the most initial data points were used to calculate the initial rate (v_0) of seeded fibril elongation, as opposed to k_f. V_0 was calculated by fitting a linear function to the ten most initial data points from the seeding assay for all fibrils used as seeds, apart from when using fibrils fragmented for 48 h as seeds – only the 7 most initial data points were used. This is because upon seeding with fibrils fragmented for 48 h, within the first 10 min of the reaction the non-linear phase of elongation has already been reached (Figure 4.3.2 – green data series).

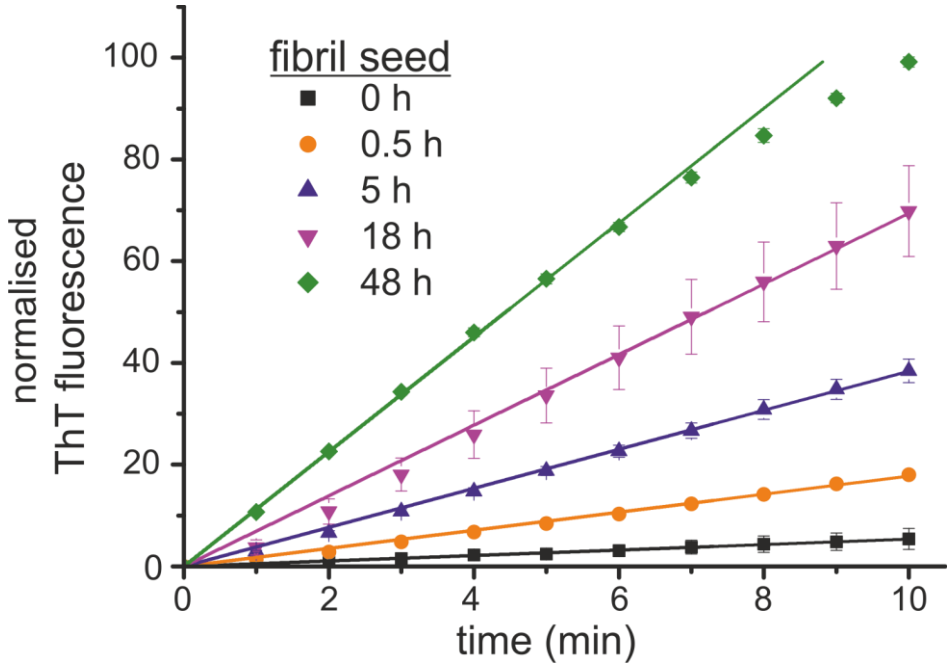

Figure 4.3.2 The dependence upon fibril ends for the initial fibril elongation rate. Fibril elongation rates were calculated by monitoring ThT fluorescence of 120 μM β_2m monomer at pH 2.0 using 10% (*w/w*) seeds of the fibril samples generated in figure 4.3.1. Curves were normalised from 0 – 100 using the initial ThT fluorescence (0) value and the ThT fluorescence post fibril elongation (100). The standard deviation from five replicates is the error

Table 4.3.2 shows that as fibril fragmentation proceeds (C_f increases), v_0 increases too. To check the linear dependence of the increase between v_0 and C_f, both parameters were normalised to those calculated for unfragmented fibril samples. This allows the proportionality coefficient between the increase in v_0 as a function of the increase in the number of fibril ends available for seeding to be calculated.

Table 4.3.2 Fibril fragmentation enhances seeding capacity V_0 of fibril seeding experiments performed as described in Figure 4.3.2. Error is the standard deviation of five replicate measurements. Au is the arbitrary unit of ThT fluorescence used to monitor fibril elongation.

frag time	V_0 (au/min)	error
0 h	0.54	4.83E-03
0.5 h	1.78	1.38E-02
6.5 h	3.84	1.66E-02
18 h	6.94	6.06E-02
48 h	10.12	6.81E-02

Table 4.3.3 shows that the increase in v_0 between using unfragmented (0 h) and 48 h fragmented fibrils as seeds (~19-fold increase) is almost five times as great as the corresponding increase in normalised C_f (~4-fold increase). Despite the apparent decrease in fibril concentration upon fragmenting fibrils for 0.5 h (20% reduction in C_f in comparison with unfragmented samples - Table 4.3.3) v_0 exhibits a 3-fold increase. This difference may be due to errors in calculating the FLD from unfragmented fibril populations due to the previously described difficulties of unambiguously tracing longer fibrils using AFM (360). These arise due to the limited surface deposition of long fibrils onto imaging surfaces and their more frequent cut-off by image boundaries and other fibrils (360).

Table 4.3.3 Normalised fibril elongation rates and C_f. Fibril elongation rates and C_f of the corresponding fibril seeds generated in Figure 4.3.1 are displayed. Each parameter is normalised with respect to that generated for unfragmented fibrils.

frag time	normalised elongation rate	normalised C_f
0 h	1.00	1.00
0.5 h	3.31	0.81
6.5 h	7.15	2.14
18 h	12.92	3.32
48 h	18.84	3.92

To check whether the C_f calculated by AFM for 0 h fragmented fibrils used in these assays was accurate, 0 h fragmented fibrils were qualitatively checked by negative stain TEM. For the 0 h fragmented fibrils FLD shown in Figure 4.3.1, out of >300 fibrils whose lengths were quantified, none exceeded 3 µm in length. Figure 4.3.3 shows that from a single negative stain electron micrograph of 0 h fragmented fibrils, at least four individual particles could be identified that were in excess of 3 µm

(dotted red lines). None of these would have been analysed by AFM as they cannot be traced unambiguously due to their frequent overlap with other fibrils. These long fibrils were also not subsequently accounted for upon application of the bias correction factor to the observed FLD (Figure 4.3.1, see Section 4.2.1). Because of these differences between 0 h fragmented fibril lengths analysed by AFM and EM, 0 h fragmented fibrils were not used to determine the relationship between fibril ends and polymerisation or depolymerisation. V_0 and C_f were instead normalised with respect to those calculated for 0.5 h fragmented fibrils and are shown in Table 4.3.4.

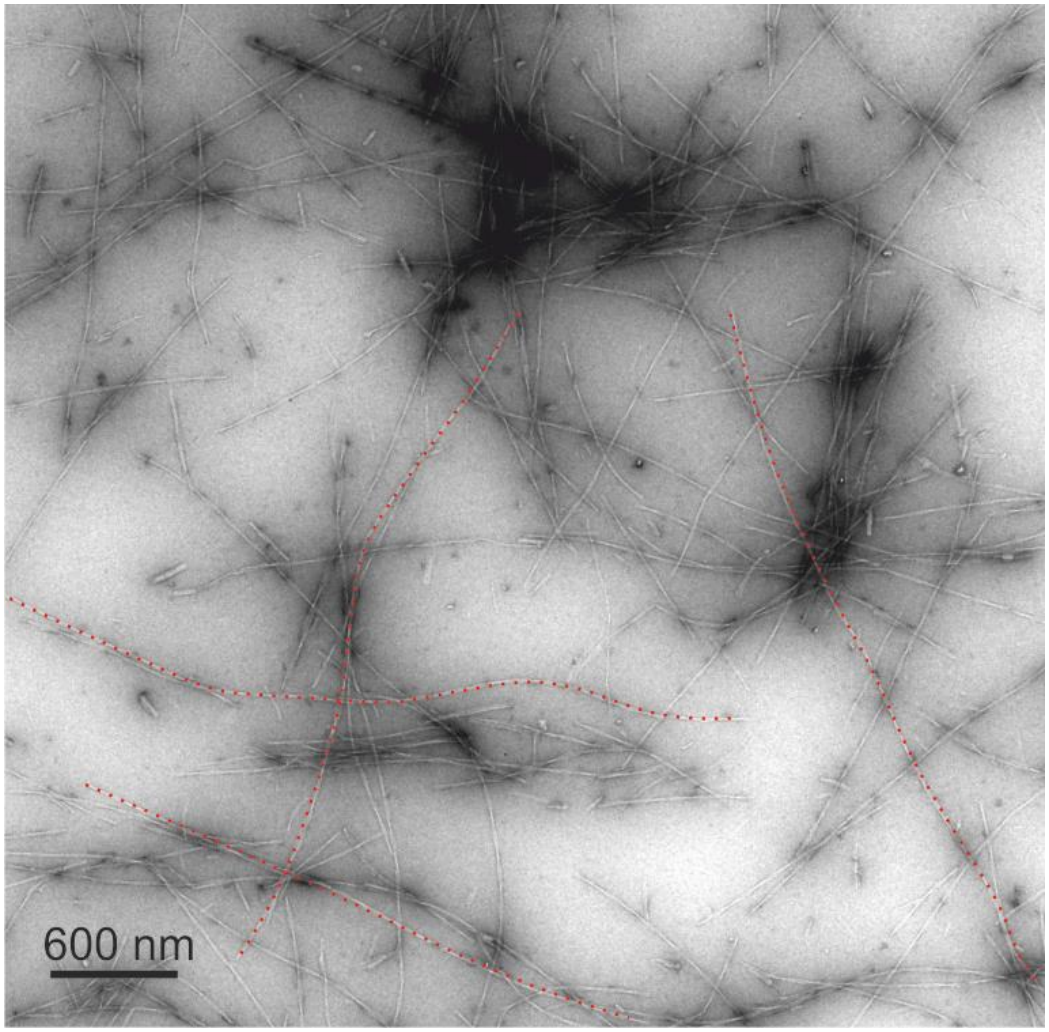

Figure 4.3.3 Representative negative stain TEM of unfragmented β_2m fibrils. Fibril samples exceeding 3µm in length are highlighted by red dashed lines. Red dotted lines directly trace over fibrils to illustrate the end-to-end distances

Table 4.3.4 Initial elongation rate and C_f of fibril samples normalised to fibrils fragmented for 0.5 h.

frag time	normalised v_0	normalised Cf
0.5 h	1.00	1.00
6.5 h	2.16	2.65
18 h	3.91	4.11
48 h	5.70	4.86

Plotting the normalised parameters displayed in Table 4.3.4 indicates a good linear correlation exists between v_0 and C_f (Figure 4.3.4, m value 1.1). The agreement infers that, as expected, fibril elongation is a predominantly end-dependent process. There does, however, appear to be a larger than expected increase in v_0 upon using 48 h fragmented fibrils as seeds (Figure 4.3.4). This may be due to the contribution of as yet unidentified secondary nucleation mechanisms, or those that have been previously described (146, 152). A similar correlation is observed upon seeding fibril elongation with 1% (*w/w*) fibril seeds as opposed 10% (*w/w*) (Table 4.3.5 and Figure 4.3.5), with a similar larger than expected increase in v_0 observed when using fibril seeds fragmented for 48 h. The good correlation therefore suggests that fibril elongation is a predominantly end-dependent process.

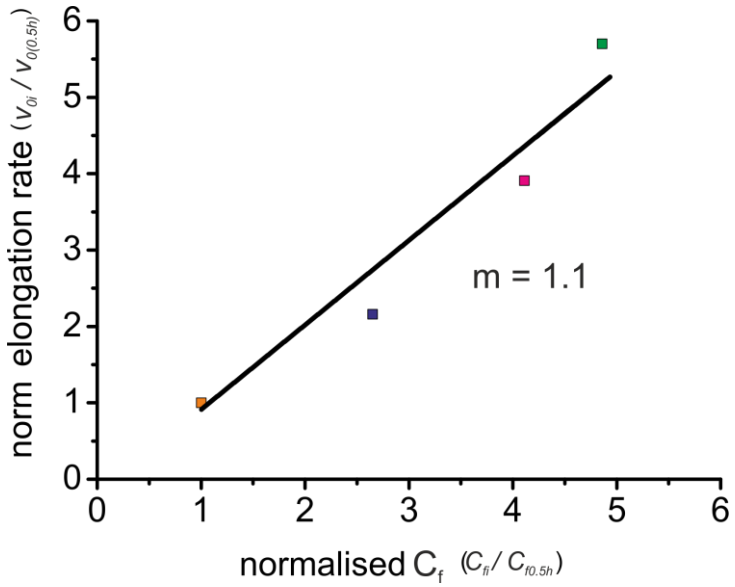

Figure 4.3.4 The correlation between C_f and the initial rate of elongation. C_f and the initial elongation rate (k) were normalised by dividing each by the corresponding value calculated for fibrils fragmented for 0.5 h ($C_{f0.5h}$ and k_i).The resulting plot was fit by a linear function and the gradient of the line (m) used to infer the relationship between fibril ends and elongation.

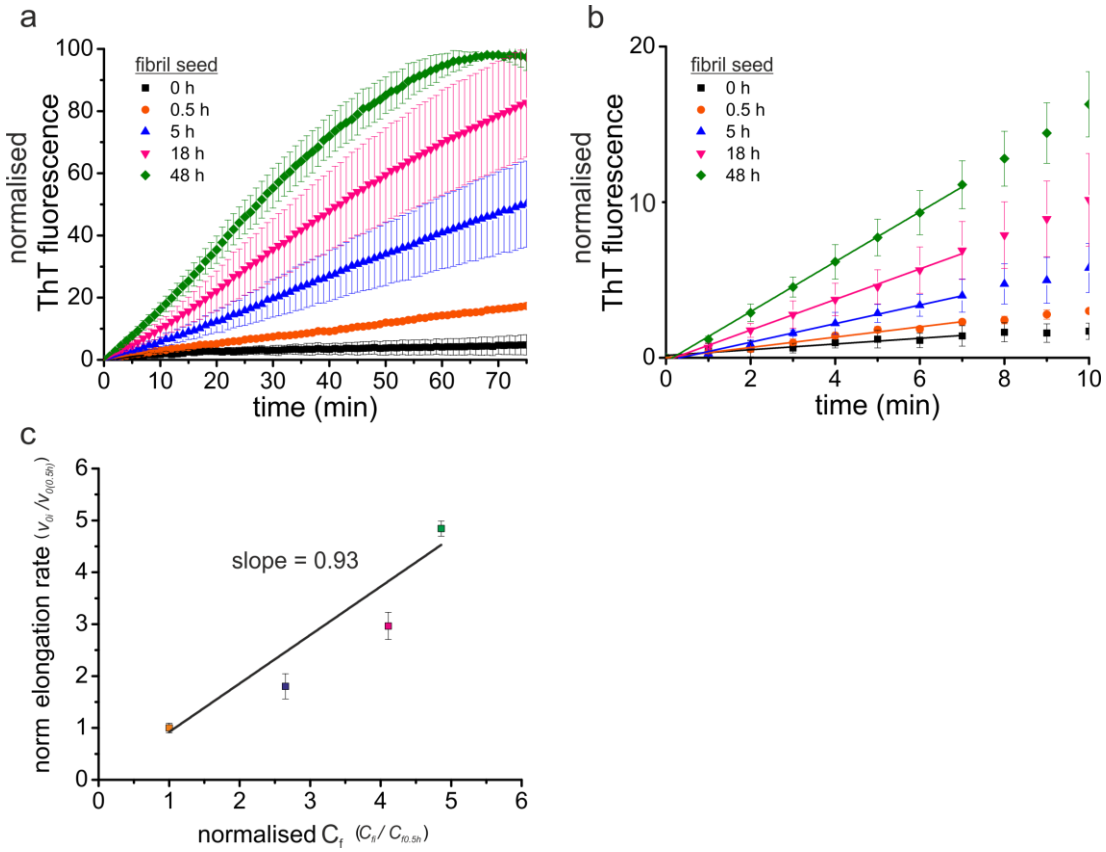

Figure 4.3.5 β_2m fibril elongation is an end-dependent process. (a) 120 µM β_2m monomer was seeded with 1% (*w/w*) β_2m fibrils fragmented for the time specified in the key. Reaction progress curves were monitored by ThT fluorescence (final concentration 10 µM).Curves are shown normalised to the highest ThT fluorescence value recorded with each sample. Errors represent the standard deviation from three independent repeats. (b) Zoom of the curves shown in (a) to show the region from which the initial elongate rate was calculated using a linear function. (c) The normalised rate of 1% (*w/w*) seeded fibril elongation vs. normalised C_f. Each parameter was normalised to that calculated for 0.5 h fragmented fibrils. Errors are expressed as decimals of the normalised elongation rate.

Table 4.3.5 The initial rate of β_2m seeded fibril elongation using 1% (*w/w*) seed. Fibril samples fragmented for different amounts of time (0.5, 5, 18 or 48 h) were used in fibril seeding assays as described in Section 4.2.2. The error is the standard deviation from three individual repeats. The normalised elongation rate (dividing each rate by that obtained for fibril elongation when using 0.5 h fragmented fibril seeds) and the normalised error (expressed as a decimal of the normalised rate) are also shown.

frag time	V_0 (.min^{-1})	error	normalised elongation rate	error
0.5 h	3.31E-03	3.11E-04	1.00	0.09
6.5 h	5.96E-03	1.45E-03	1.80	0.24
18 h	9.82E-03	2.57E-03	2.97	0.26
48 h	1.60E-02	2.33E-03	4.84	0.15

4.3.3 Establishing the end-dependency of molecular shedding

In order to discover whether fibril depolymerisation (molecular shedding), like seeded elongation, also occurs only, or predominantly, from fibril ends, depolymerisation kinetics of fibril samples used as fibril seeds in Section 4.3.2 were assayed at pH 6.4 (see Section 2.2.6 for buffer details).The relationship between the number of fibril ends and the rate of depolymerisation can then be calculated (as described above for fibril elongation) to determine the role of fibril ends in the release of membrane-active soluble species (Chapter 2). Depolymerisation was initiated by diluting 120 μM β_2m amyloid fibrils described in Section 4.3.1 to 30 μM (monomer equivalent concentration) in pH 6.4 buffer. The kinetics of fibril depolymerisation were then monitored using ThT fluorescence (Figure 4.3.6). The amplitude of ThT fluorescence is shown normalised to the highest ThT fluorescence signal across all four samples (Figure 4.3.6). Interestingly, the intrinsic ThT fluorescence is greater for fibril samples with longer FLDs, as shown by the starting amplitude, which decreases upon prolonged fragmentation of fibril samples (t = 0 min in Figure 4.3.6). Why longer fibrils exhibit greater ThT fluorescence is unknown, although it may be that fibril ends exhibit structural differences from the

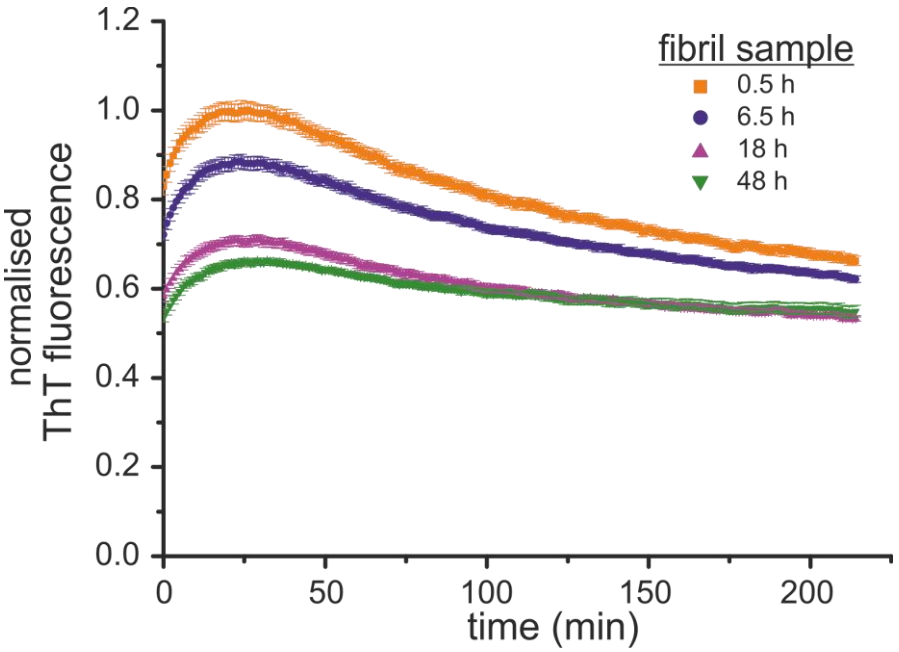

Figure 4.3.6 Depolymerisation kinetics of fibrils fragmented for different times in pH 6.4 buffer. Depolymerisation of fibrils fragmented for 0.5, 6.5, 18 or 48 h was monitored by diluting 120 μM β_2m fibrils 4-fold into pH 6.4 buffer supplemented with ThT. Curves are shown normalised to the highest ThT fluorescence amplitude observed across the series of samples. Error bars represent the standard deviation of up to six individual replicate measurements.

cross-β core that is known to bind and increase the fluorescence of ThT. The inability of fibril ends to bind ThT and increase its fluorescence would explain why fragmented fibril samples exhibit decreased ThT fluorescence, even at monomer equivalent concentrations (as is the case here). In addition, the depolymerisation of fibrils fragmented for 48 h appears to reach equilibrium at an approximate ThT fluorescence value of 0.6. This suggests that depolymerisation is not driven entirely toward native β_2m monomer, but instead reaches a fibril: soluble material equilibrium in which a significant proportion of fibrillar material remains. This is consistent with observations made in Chapter 2, which shows that the yield of soluble material released during fibril depolymerisation at pH 6.4 is significantly lower than that at pH 7.4, as assayed by SDS-PAGE (Figure 2.3.7) and NMR (Section 2.3.7). Therefore soluble species must be in equilibrium with fibrils during depolymerisation at pH 6.4, although this wasn't detected in FCS experiments designed to probe whether native β_2m can back-exchange with higher order species (Section 3.3.5).

The change is ThT fluorescence during fibril disassembly at pH 6.4 is biphasic, with an initial increase followed by a slower decay in fluorescence. The rate constants associated with the increase and decrease in ThT fluorescence were calculated by fitting each curve using the double exponential function described in Section 4.2.3 (Equation 1). The resulting rate constants (k_1 and k_2) are shown in Table 4.3.6. The error associated with each rate constant is the standard deviation from the six replicate measurements. Table 4.3.6 shows that k_1 (initial increase in ThT fluorescence) is independent of C_f. As such, this suggests that the increase in ThT fluorescence is a global phenomenon extending to all ThT binding sites, supporting the idea of conformational change of the β_2m fibril architecture upon changes to solution conditions (Figure 2.3.8).

Table 4.3.6 Length-dependent fibril depolymerisation rate constants. Fibril depolymerisation curves were collected at pH 6.4 by monitoring ThT fluorescence.

frag time	k_1 (.min^{-1})	error	k_2 (.min^{-1})	error
0.5 h	7.98E-02	6.64E-03	9.85E-03	7.18E-04
6.5 h	8.51E-02	4.06E-03	9.57E-03	8.42E-04
18 h	8.04E-02	4.05E-03	1.21E-02	4.47E-04
48 h	7.13E-02	6.73E-03	1.62E-02	3.07E-03

In order to determine the role of fibril ends in the loss of ThT fluorescence, the rate constant for the decay of ThT fluorescence was used (k_2). This can be used, as opposed to v_0 used to elucidate the role of fibril ends in elongation, because; i) the curves shown in Figure 4.3.6 are well described by the double exponential function, thus suggesting that secondary mechanisms contribute minimally to the loss of ThT fluorescence during fibril disassembly, and ii) k_2 is reversible to k_f (see reaction mechanism in Section 4.3.2 – k_r), providing that fibril disassembly proceeds predominantly for fibril ends.

Comparison of k_2 between fibril samples fragmented for 0.5 h or 48 h reveals a small (<2-fold), but significant (p <0.005) increase in the decay of ThT fluorescence as a result of prolonged fibril fragmentation. The comparison of k_2 between sequential fibril samples as fragmentation proceeds shows that the difference in k_2 for fibrils fragmented for 0.5 or 6.5 h is insignificant (p value = 0.57), while the differences in k_2 for fibril samples fragmented for 6.5 or 18 h and 18 or 48 h are small but significant (p = 0.013 and < 0.005 respectively). Despite the statistically significant increase in k_2 between fibril samples fragmented for either 0.5 or 48 h, the loss of ThT fluorescence does not show the same degree of end-dependency as seeded fibril polymerisation, as k_2 exhibits a less than 2-fold increase in comparison with a 5-fold increase in v_0 when the same fibril samples are used as seeds (Tables 4.3.4 and 4.3.5). Figure 4.3.7 illustrates this best by plotting normalised k_2 vs. normalised C_f.

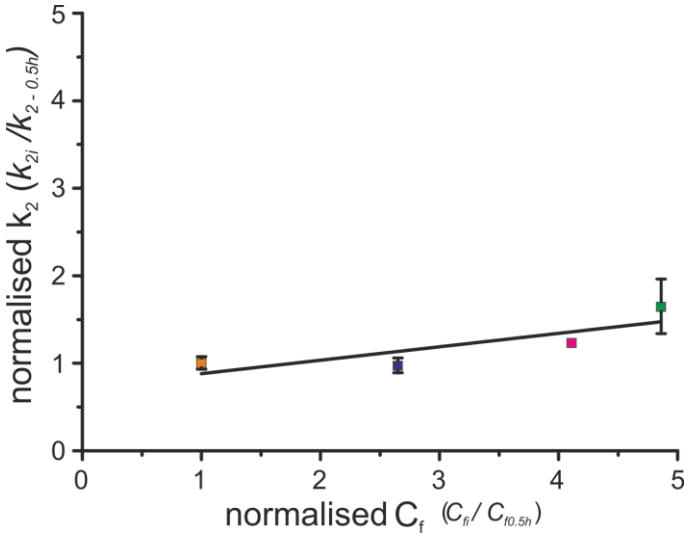

Figure 4.3.7 The end-dependency of fibril depolymerisation at pH 6.4. k_2 (the rate constant for the loss of ThT fluorescence during fibril disassembly) and C_f were normalised to those calculated for β_2m fibrils fragmented for 0.5 h. Error bars are the standard deviation from a minimum of four independent repeats.

As for Figure 4.3.5, C_f and k_2 have been normalised with respect to those calculated for the fibril sample fragmented for 0.5 h. The proportionality coefficient calculated from the linear fit (black line) is only 0.15, showing that the increase in k_2 is not directly proportional to the increase in number of fibril ends as C_f increases.

To ensure that the small increase in k_2 as the number of fibril ends in solution increases is not an artefact of measuring fibril disassembly using ThT fluorescence, the release of soluble material was quantified (Section 2.2.8) to provide a second, independent observation for the rate of fibril depolymerisation. Figure 4.3.8 shows that no discernible difference is detectable in the amount of soluble material appearing during fibril disassembly over time between fibril samples fragmented for 0.5 h or 48 h. Thus, the lack of end-dependent kinetics is not a result of measuring fibril disassembly using ThT fluorescence. Therefore, at least kinetically, the processes of fibril elongation at low pH and depolymerisation at pH 6.4 are distinct, in that fibril polymerisation appears to occur at fibril ends, whilst this may not be the case for fibril depolymerisation.

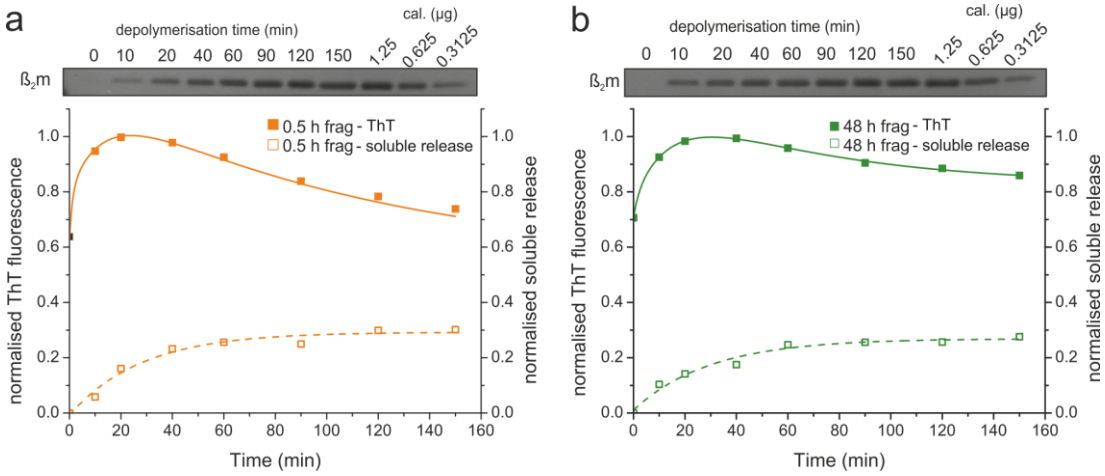

Figure 4.3.8 ThT fluorescence and the release of soluble material during fibril depolymerisation at pH 6.4. The release of soluble material was quantified during fibril depolymerisation as described in Section 2.2.8 at the time points after the initiation of fibril depolymerisation indicated on the gel. Gels bands corresponding to β_2m were quantified using the calibrant gel bands shown in (a) and (b). The release of soluble material was quantified for fibrils fragmented for 0.5 h (a) and 48 h (b) (clear squares) and is shown plotted with the corresponding ThT fluorescence measurements (filled squares). The ThT fluorescence is shown normalised to the highest ThT fluorescence reading within each sample and the release of soluble material is normalised betwee 0 and 30 µM (starting assay concentration.

There are several possible explanations for why the rate of fibril depolymerisation does not exhibit a direct linear relationship with the number of fibril ends. Firstly, the rate of fibril depolymerisation may be **length** dependent. This is not to be confused with end-dependency. Length dependent depolymerisation would mean that as fibrils become shorter, the rate at which species dissociate from fibril ends would slow down. For instance, fibrils that are fragmented to reduce length 4-fold exhibit only a 2-fold rate enhancement for the loss of ThT fluorescence in comparison with the unfragmented fibril sample. If the dissociation of species from fibril ends is twice as slow for these shorter fibrils than their longer counterparts, this would explain why the global rate of depolymerisation, as monitored by ThT fluorescence, has only exhibited a 2-fold increase (Figure 4.3.9a).

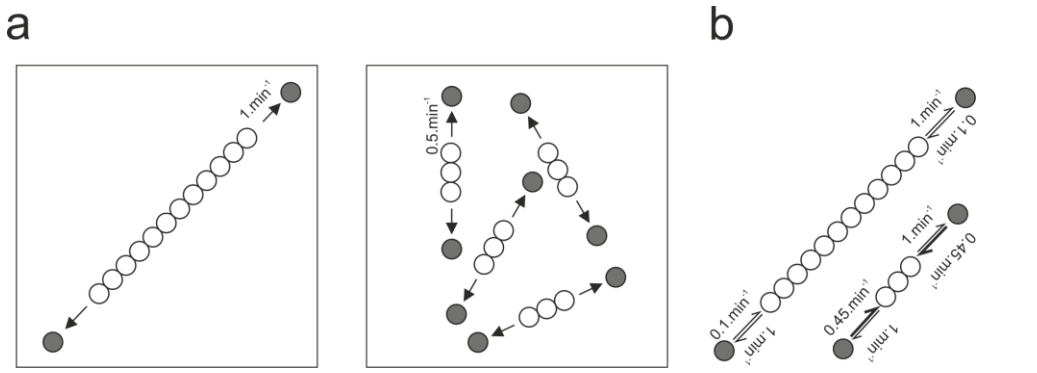

Figure 4.3.9 Why is the rate of fibril depolymerisation not end-dependent? (a) Fibril depolymerisation is length-dependent. Both boxes show fibril species of different lengths constructed from monomer equivalent concentrations. Reducing the fibril length 4-fold generates 4 times the number of fibril ends – the site of fibril depolymerisation. However the reduction in length leads to a reduction in the rate in which species are shed from fibril ends. (b) The fibril-oligomer distribution is altered upon reducing fibril length. The ThT decay constant is the sum of multiple individual rates for the inter-conversion of ThT positive and negative species. Reducing fibril length promotes greater back-exchange of oligomers with fibrils, thus reducing the rate of decay of ThT fluorescence in a length-dependent manner.

A second scenario could be that back-exchange between fibril ends and oligomers are greater upon reducing fibril length. The kinetics of depolymerisation monitored by ThT fluorescence is the sum of individual rates for the forward and back exchange between any number of given species that either exhibit ThT fluorescence or not. The simplest model, such as that outlined in the discussion of Chapter 3, would involve the conversion of ThT fluorescent fibrils into non-ThT fluorescent oligomers. If the equilibrium between these two species is modulated by changing the length of fibrils, such that more species were able to back exchange with fibrils upon a reduction in fibril length, this could result in a smaller than expected increase

in the rate of depolymerisation as monitored by ThT fluorescence (Figure 4.3.11b). The increased back exchange between oligomers and fibrils upon a reduction in fibril length may be due to the greater diffusivity of shorter fibrils in comparison with their longer counterparts. Evidence for the increased diffusivity of shorter fibrils is provided by the favourable surface deposition of shorter fibrils onto AFM imaging surfaces (360). The sequestration of longer fibrils into bundles upon diluting fibrils into near-neutral buffers (92) may mask fibril surfaces that are capable of exchanging with HMW, soluble species, therefore decreasing the rate at which oligomers back-exchange with fibrils.

Although FCS experiments did not show that soluble material can back-exchange with fibrils (Figure 3.3.11b and d), this does not rule out the scenario outlined in Figure 4.3.9b. To detect back-exchange between HMW species and fibrils within the experiments performed in Section 3.3.5 would require native monomeric R3C488 to initially interact with HMW species, which in-turn would need to interact with an unlabelled β_2m fibril. This labelled fibril would then be required to diffuse across the confocal volume in order for back-exchange to be detected. As fibrils pre-labelled with R3C488 are rarely encountered in the confocal volume during fibril depolymerisation experiments (Figure 3.3.6), the lack of detection of HMW species re-interacting with fibrils in the back-exchange FCS experiments (Section 3.3.5) may be due to the low frequency in which fibrils (fluorescently-labelled via the re-association of fluorescent, soluble species) are encountered within the confocal volume. Indeed, the establishment of an equilibrium during fibril depolymerisation (Figure 4.3.7, 48 h fibril sample) at pH 6.4, in which a significant proportion of ThT fluorescent material remains, suggests that soluble species do interact with fibrils, as outlined in Figure 4.3.11b. The back exchange phenomenon could be investigated by FCS as proposed in Section 3.3.5, but instead using 48 h fragmented fibrils, as opposed to unfragmented fibrils, to increase the diffusivity of fibril particles so that back exchange may be more readily observed.

Another explanation for why the rate of fibril depolymerisation may not appear to be end-dependent include the possible solution-induced fragmentation of longer fibril samples upon dilution into near-neutral buffers (Figure 4.3.10a). Dilution of fibrils formed at low pH into buffers with different pH values may alter the hydrogen bonding capacity of amino acid side chains involved in the formation of the steric

zipper motif. In addition, side chains that interdigitate to form the tightly packed dry protofilament interface may adopt new charge states (see Section 1.3.1 and 1.4.3). Such changes to amino acid side chain charges could lead to structural rearrangements within the fibril core observed by CD (Figure 2.3.8). Structural rearrangements may also lead to the increased ThT fluorescence observed at the initial stages of fibril depolymerisation assays (Figure 4.3.7). Interestingly, the equilibrium of fibril depolymerisation towards native β_2m is much favoured by increasing the pH by a single unit from pH 6.4 to pH 7.4 (Section 2.3.4). This suggests that histidine side chains may play an important role in the formation and maintenance of the fibril core, as the pK_a of the histidine side chain is close to these pH values (~pK_a 6.1). Increasing the pH from 6.4 to 7.4 may switch the side chain imidazole group from an H-bond donor to acceptor, thus potentially altering the H-bonding network in which the imidazole ring may be involved.

Although at pH 6.4 the histidine side chain should be predominantly uncharged (as pK_a is ~6.1), equivalent to the probable charge adopted by His residues upon dilution into pH 7.4 buffer, side chain pK_a values can be significantly influenced by the local environment in which residues find themselves (421). This has recently been shown for histidine residues within the colicin E7 immunity protein, where a folding intermediate was shown to have histidine pK_a values as high as 6.9±0.3 (422). The potential role of histidine residues in mediating the increased stability of fibrils and/or HMW soluble species at pH 6.4 is suggested by NMR, as His84 is one of the residues in which a chemical shift perturbation was detected during the initial stages of fibril depolymerisation (Figure 2.3.19bi). The protonation of His84 at pH 6.2 is also thought to be a critical event that enhances the amyloidogenicity of monomeric β_2m at near-neutral pH (157).

Although the pK_a of histidine residues is more pertinent to the differences in fibril depolymerisation at pH 7.4 or pH 6.4, other residue side chains, such as the carboxyl groups of aspartate and glutamate (pK_a values of 3.9 and 4.3 respectively) are likely to undergo changes in charge states upon dilution of fibrils into either pH 7.4 or 6.4 buffer that will alter their hydrogen bonding capacity exhibited at low pH. The change in the hydrogen bonding capacity of amino acid side chains may impact both the stability of the steric zipper motif of the cross-β core and the dry protofilament interface, leading to a reduction in the tensile strength of an amyloid fibril which

could result in increased fibril 'brittleness' and subsequent fibril fragmentation. If longer fibrils are more susceptible to this type of fragmentation, then this could potentially explain why k_2 does not scale with the number of fibril ends calculated within the orginal fibril population. This could be studied by quantifying changes to FLDs throughout the depolymerisation process using AFM to see whether a large-scale reduction of fibril lengths takes place during the initial stages of fibril depolymerisation.

The final possibility to be discussed is that fibril depolymerisation may not be strictly mediated through fibril ends (Figure 4.3.10b). Depolymerisation may be a combination of both the shedding of oligomers from fibril ends AND from random positions along the fibril axis. This may take place due to the possible reductions in the mechanical stability of β_2m fibrils for the reasons discussed above. Whether fibril depolymerisation takes place via this mechanism could be studied using FCS, by observing the rate at which soluble species reappear during depolymerisation from fibrils that incorporate R3C488 into different positions along the fibril axis. Fibrils in which R3C488 has been incorporated randomly during fibril elongation (by including R3C488 at the beginning of seeded growth) and those that have been 'end-capped' with R3C488 after fibril elongation has reached equilibrium, should exhibit distinct kinetics for the reappearance of soluble material if depolymerisation is mediated from fibril ends. These FCS experiments could be performed in addition to the AFM experiments discussed previously to ensure that any differences in the rate

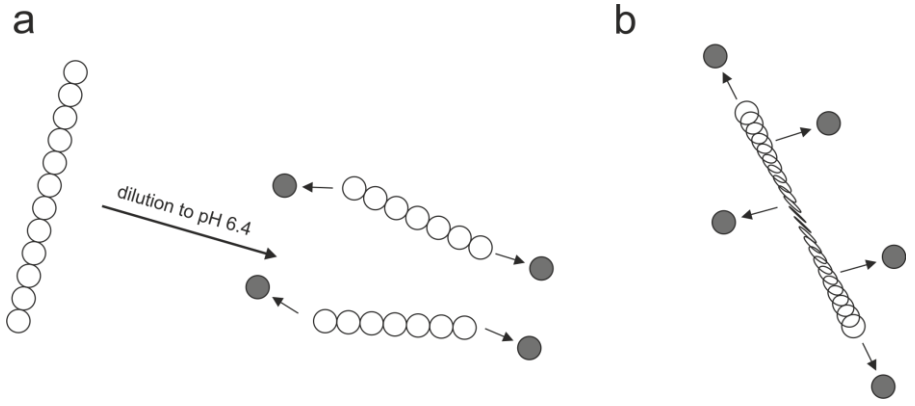

Figure 4.3.10 Potential mechanisms of fibril depolymerisation due to changes in fibril stability. (a) Dilution of fibrils formed at low pH into near-neutral pH buffers changes the H-bonding capacity of the fibril core and disrupts the interdigitated, dry protofilament interface. Such changes could induce fibril shearing to reduce the fibril length distribution and accelerate depolymerisation. (b) Fibril depolymerisation does not exclusively proceed from fibril ends. Due to changes in fibril stability as discussed oligomers predominantly dissociate from within the fibril core.

at which soluble material released during fibril depolymerisation and detected by FCS is not due to the fragmentation of fibrils to generate more fibril ends in solution (Figure 4.3.12a).

4.3.4 Identification of species that form during β_2m amyloid formation

The kinetic differences of polymerisation and depolymerisation raise the possibility that distinct species may form within each process. The most toxic species in amyloid disorders are reported to be those that are soluble and form prior to mature amyloid fibrils (20–22, 24–26, 166, 170–173, 183–185, 196, 209, 423). Highlighting structural differences between pre-fibrillar oligomers and those derived from mature amyloid fibrils during molecular shedding that are also cytotoxic would be a novel insight with important biological impact. Thus, a study was initiated to investigate structural differences that may exist between oligomers that form within the assembly cascade and those that form during molecular shedding.

To do this, FCS was employed as it provided the greatest success in identifying non-native oligomeric species that populate during fibril depolymerisation. To ensure that β_2m amyloid formation could be studied using FCS, control experiments were performed to test whether amyloid formation could proceed under FCS conditions. FCS requires the presence of small amounts of detergents in buffers (typically 0.01%-0.001% (*v/v*), see Section 4.2.4) to prevent the adsorption of material to the cover slip chamber. Adsorption of material can impede the detection threshold of the FCS experiment. Different species may also preferentially interact with the coverslip, artificially altering the perceived concentration of species in solution. Therefore, unseeded amyloid formation of 120 μM β_2m at pH 2 (at 25°C, 600 rpm – see Section 4.2.4) was studied in the presence and absence of 0.001% (*v/v*) Tween-20. ThT fluorescence was used to monitor fibril formation on a plate reader as described in Section 4.2.4. The rate of amyloid fibril formation in the presence and absence of Tween-20 is similar, although in the presence of Tween-20, the amplitude of ThT fluorescence within the stationary phase is substantially reduced (Figure 4.3.11a). Quantification of soluble material after fibril formation has reached equilibrium shows that the presence of this concentration of Tween-20 has not affected the fibril yield (Figure 4.3.11b). Therefore, Tween-20 must competitively inhibit the binding of ThT or lower the fluorescent yield of ThT when bound.

Negative stain TEM of fibrils grown in the presence and absence of Tween are morphologically similar (Figure 4.3.13c). Therefore fibril formation can be studied by FCS.

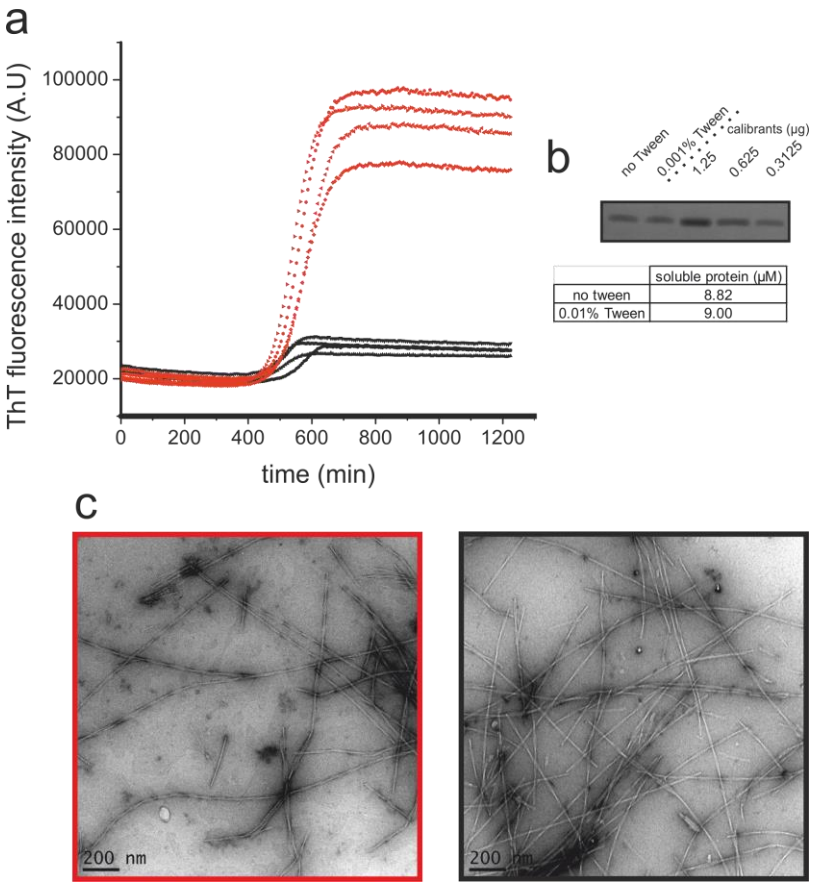

Figure 4.3.11 β_2m amyloid formation at pH 2 in the presence or absence of Tween-20. (a) *De novo* β_2m amyloid fibril formation was monitored by ThT fluorescence in low pH buffer in the presence (black) or absence (red) of 0.001% (*v*/v) Tween-20. (b)The fibril yield was determined by quantifying the amount of β_2m in the supernatant after centrifugation for 1 h at 16300 x *g*. Calibrants were used to determine the concentration of soluble material shown in (b). Negative stain TEM of fibrils formed in the presence (black) or absence (red) of 0.001% (*v/v*) Tween-20.

In order to detect amyloid formation by FCS, 18 nM R3C488 was added to 120 µM *wt* β_2m at pH 2. ACs were collected during amyloid formation by removing aliquots from the plate reader at various time points and immediately analysing the sample by FCS. As previously stated in Chapter 3, ACs displayed for the respective time points are the average of a minimum of 20 x 30 sec ACs with the corresponding time point the median of the collection window. Figure 4.3.12 shows that as aggregation proceeds, no change is detected in the amplitude of ACs for the first 300 min, suggesting that the majority of material remains soluble and predominantly low order. This observation is consistent with previous ESI-IMS-MS experiments

showing low order oligomers (<6mer) populate during the lag phase of β_2m amyloid assembly (383). After 300 min, G(0) increases significantly over the preceding time points (Figure 4.3.12). This shows that soluble species are being consumed into higher order material, thus lowering their relative concentration of low-order, soluble β_2m which manifests in the perceived increase in G(0). This is because of the inverse relationship between G(0) and the number of species detected during the acquisition of an AC (see Section 3.3.4, Equation 10). Note the increase in G(0) precedes that of the increase in ThT fluorescence (Figure 4.3.10a), suggesting that higher-order species populate prior to the formation of amyloid fibrils detected by ThT fluorescence. G(0) steadily increases from 300 min onwards, coinciding with the increase in ThT fluorescence and the consumption of β_2m into amyloid fibrils. The detection of amyloid fibrils at low pH is markedly improved in comparison with that at pH 6.4 or pH 7.4 as fibrils remain soluble and diffuse under fibril growth conditions.

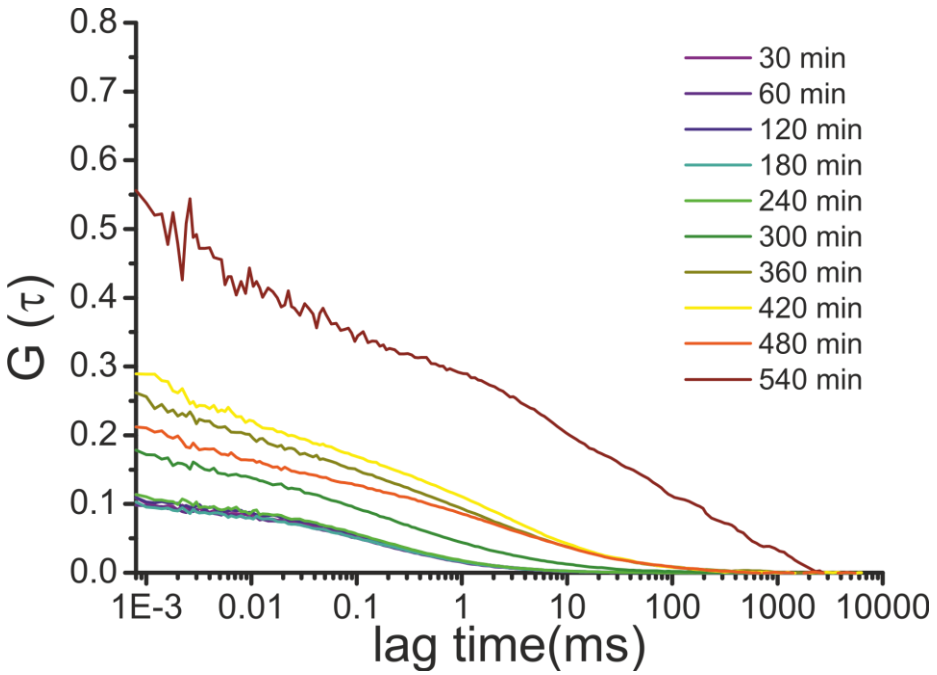

Figure 4.3.12 ACs collected during β_2m amyloid formation at pH 2. ACs displayed are the average of 20 x 30 sec individual acquisitions collected during the formation of 120 µM β_2m amyloid formation at pH 2.0. Time points displayed are the median of the collection window.

The distribution of species within ACs were extracted using MEM as previously described in Section 3.2.5. Tau distributions were then converted to apparent R_H distributions by calibration of the confocal volume as described in Section 3.2.3. The

resulting apparent R_H distributions of species populating during unseeded β_2m fibril formation at pH 2 are shown in Figure 4.3.13.

For the first 180 min of β_2m amyloid formation at pH 2, the apparent R_H

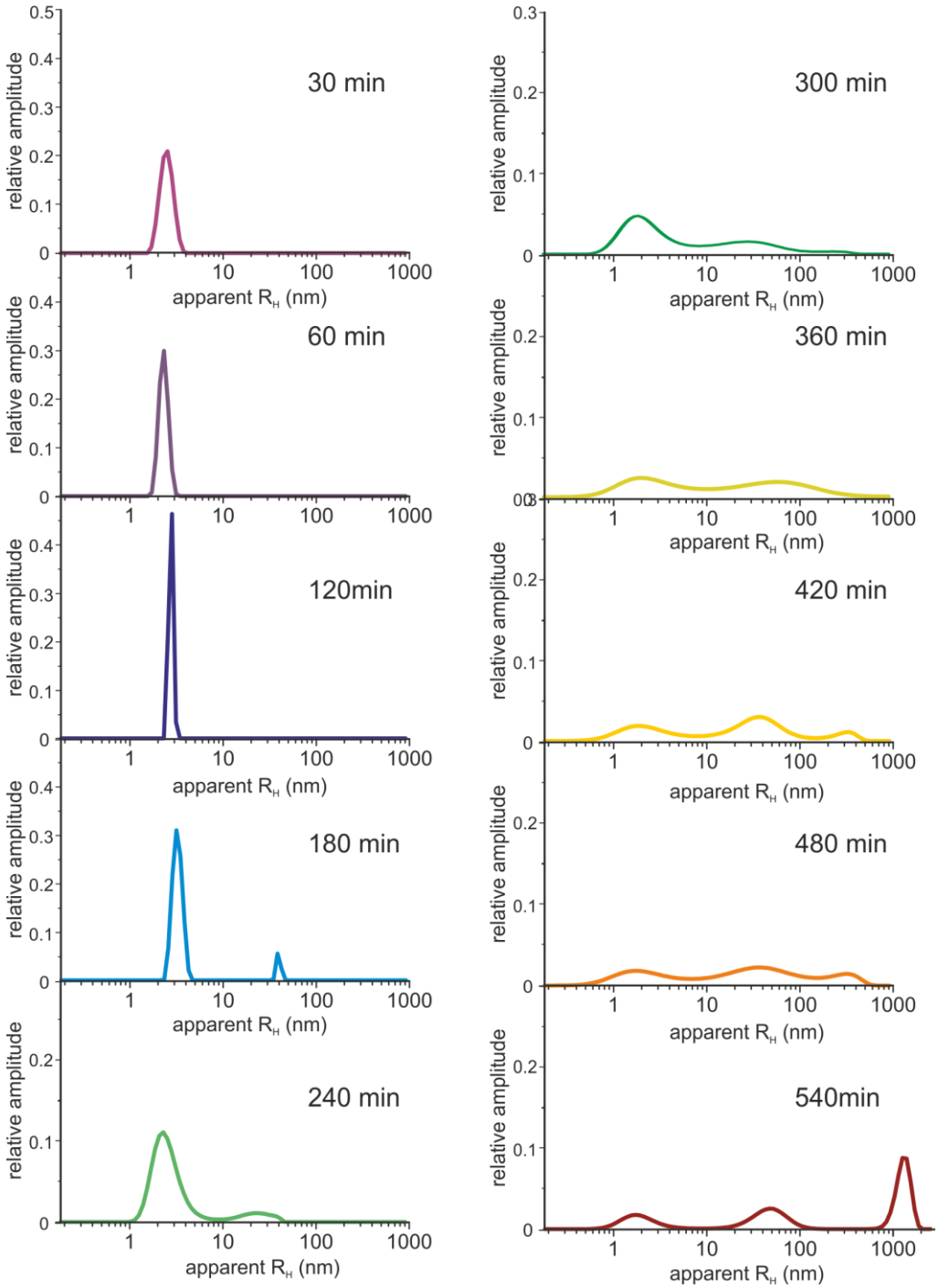

Figure 4.3.13 MEM distribution of species formed during β_2m amyloid formation. 120 µM β_2m with 18 nM R3C488 amyloid formation was monitored at low pH using FCS. Aliquots were removed from the fibril formation assay and immediately analysed by FCS. Each time point distribution was extracted from 20 x 30 sec ACs. The time point indicates the median of the collection window.

distributions are dominated by the presence of a LMW peak (Figure 4.3.13, Table 4.3.7). These species are likely to correspond to the unfolded monomer and/or LMW oligomers similar to those observed from comparative ESI-IMS-MS studies. The peak centre ranges from 1.8-3.3 nm (Table 4.3.7), which is consistent with apparent R_H values of native monomer controls calculated by FCS in Chapter 3 (Figure 3.3.7). The narrow distribution of the LMW peak in the absence of higher order species suggests a high degree of homogeneity. The exact identity of species within the LMW peak cannot be resolved by FCS and therefore may contain a range of LMW oligomers that have been shown to form during β_2m amyloid formation by other techniques (383, 387). In general, in order to resolve two species by FCS, a doubling of the apparent R_H is required. The doubling of apparent R_H is equivalent to an 8-fold increase in hydrodynamic volume (V_H):

$$V_h = {}^4/_3 \pi {R_h}^3 \quad (3)$$

and as D_o is inversely proportional to the cubic root of the mass of a protein (424):

$$D_o \propto \frac{1}{\sqrt[3]{M}} \quad (4)$$

where M is the molecular weight of a protein, then an 8-fold increase in mass is also required for a 2-fold reduction of D_o, which is inversely proportional to R_H. Therefore the lower order species observed by ESI-IMS-MS (286, 383) are unlikely to be resolvable by FCS.

Table 4.3.7 Apparent R_H distributions of species populated during β_2m amyloid formation at low pH.

	Peak centre (nm)		
time (min)	**LMW**	**HMW**	**Fibrils**
30	2.6	-	-
60	2.4	-	-
120	2.9	-	-
180	3.3	-	-
240	2.1	28.4	-
300	1.9	35.2	-
360	2.1	75.1	-
420	1.9	48.7	472.5
480	1.7	48.7	472.5
540	1.7	60.5	2148.4

After 240 min a second species appears with an apparent R_H centred at 28 nm. As time proceeds, the relative concentration of the HMW peak increases in comparison

with that of the LMW peak (Figure 4.3.15). This suggests that LMW species are consumed into HMW aggregates prior to the formation of β_2m amyloid fibrils. There is also an increase in the apparent R_H of HMW species as time proceeds (Table 4.3.7). Apart from t = 360 min, where the apparent R_H of HMW species is ~75 nm, the increase is gradual, from 28 nm (at 240 min) to 60.5 nm after 540 min. Interestingly, the large increase in apparent R_H of HMW species detected at 360 min is the last time point measured before fibril formation proceeds (Figure 4.3.11a). Therefore, there might be a critical mass, or aggregate size that is required, before fibril formation can begin.

After 360 min an additional species can be observed with an apparent R_H >100 nm. The formation of this peak is coincident with an increase in ThT fluorescence, suggesting these species are likely to be mature amyloid fibrils. Moreover, the relative concentration of these species increases over time in comparison with LMW and HMW species. This is concurrent with an increase in apparent R_H of the large species observed 540 min into the aggregation landscape in excess of 1000 nm (Table 4.3.7 – fibrils). This shows that fibrils are continuously being elongated during the aggregation landscape. How the relative concentration of each species changes in solution over time during the assembly is shown in Figure 4.3.14. The

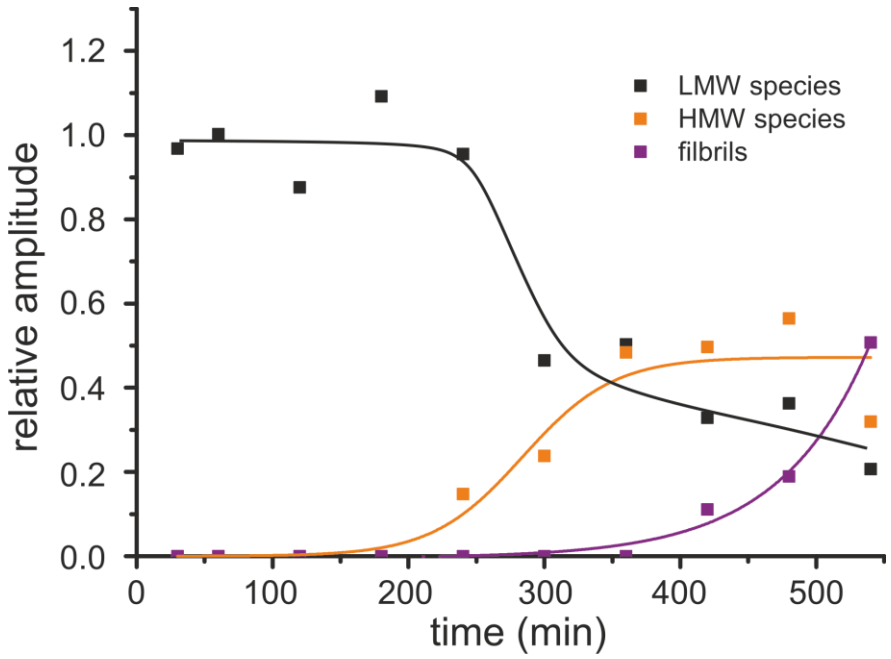

Figure 4.3.14 The relative population of species formed during β_2m amyloid formation. The relative amplitude of LMW species (black), HMW species (orange) and fibrils (purple) forming as a function of time and extracted from ACs using MEM. Lines are visual guides and are fitted.

relative amplitude of species has been normalised to the amplitude of LMW species observed at t = 30 min.

4.4 Discussion

This Chapter aimed to resolve the mechanism by which fibril depolymerisation proceeds and whether species that form within the lag phase of amyloid fibril formation are structurally distinct or homologous to those that populate during molecular shedding. The discoveries relating to the mechanism of fibril depolymerisation, the potential implications, and future work required to fully elucidate the mechanism were discussed in detail in Section 4.3.3 and will therefore not be reviewed here once more.

For the characterisation of pre-fibrillar oligomers that form during the lag phase of β_2m amyloid assembly, FCS has proved successful in identifying at least three distinct populations of species that form at different stages during amyloid formation. For the first 180 min of amyloid formation, the lag phase is dominated by a LMW peak with an apparent R_H consistent with that observed for native monomer controls performed in Chapter 3. As discussed in Section 4.3.3, FCS is unlikely to be able to resolve the presence of additional LMW oligomers that have been shown to populate in addition to monomer during the lag phase of β_2m amyloid formation under similar conditions (Figure 4.4.1a). This is because only 6mers and below have been observed by ESI-IMS-MS of β_2m amyloid formation at low pH, whereas an 8-fold increase in mass is required for the 2-fold increase in apparent R_H which is typically required to resolve species by FCS (Section 4.3.4, Equations 3 and 4). Therefore the slight increase in apparent R_H of the LMW peak from 30 to 180 min is consistent with the formation of LMW oligomers that cannot be resolved by FCS, but were seen by analytical ultracentrifugation under similar assembly conditions (Figure 4.4.1) (387). In order to elucidate whether these LMW species are forming under the conditions used for FCS experiments, AUC could be repeated.

Interestingly, the HMW species that form after 180 min, but before the onset of amyloid fibril formation (Figure 4.3.16), were not detected in AUC experiments performed by Smith et al in (387). Amorphous aggregate deposition preceding the formation of amyloid fibrils has been shown for β_2m aggregation under similar conditions by AFM analysis (Figure 4.4.1b and c) (155). Some of these species are

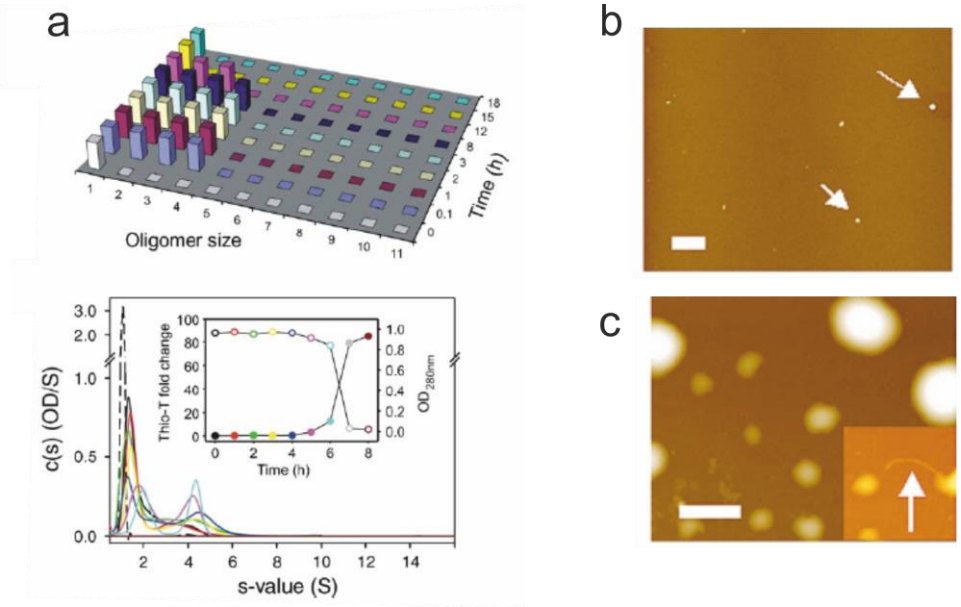

Figure 4.4.1 Pre-fibrillar oligomers previously identified during β_2m amyloid formation. (a) AUC performed during β_2m amyloid formation under similar conditions to those used in Section 4.3.3. AUC revealed that LMW oligomers up to tetramers were frequently observed during the lag phase of β_2m assembly (387). (b) and (c) Representative AFM images of species populated during β_2m amyloid assembly at low pH. Images were taken 17% and 31% into the lag phase (lag phase defined as the time it takes for a 10% increase in ThT fluorescence to be reached (155).

similar in apparent size to those observed during FCS experiments, although the amorphous aggregates predominantly observed by AFM as the lag phase proceeds are significantly larger than those observed by FCS (Figure 4.4.1b) (typically between 300 -1 µm in diameter) (155). This suggests that the HMW species detected here, which do increase in apparent R_H before the onset of amyloid fibril elongation, but not to such an extent as previously shown, may be a novel pre-fibrillar species that forms during β_2m amyloid formation at low pH.

The data presented here provides a starting point from which a more comprehensive analysis of the structural comparison of pre-fibrillar oligomers and those that form through molecular shedding can be performed. From these initial observations, the apparent R_H of HMW pre-fibrillar species are similar to those that form during depolymerisation at pH 6.4 (Figure 3.3.8). However, they are consistently larger. It would be interesting to investigate the structural properties of these pre-fibrillar species in a similar manner to which molecular shedded oligomers formed during depolymerisation were assessed. The structure of pre-fibrillar oligomers formed at low pH could be studied by CD throughout the lag phase. This will provide information as to the secondary structure of LMW and HMW species and whether

either begins to propagate significant β-sheet secondary structure prior to the formation of fibrils begin. The HMW species observed to form after 180 min of the lag phase may be protofilament assemblies of β_2m incapable of binding or increasing the fluorescent yield of ThT. The β_2m fibril is composed of six individual protofilaments that arrange into two crescent shaped half-fibrils that stack back-to-back along the fibril axis (Figure 1.4.3). Protofilaments may form prior to the assembly of ThT-fluorescent mature amyloid fibrils. Similar ANS binding assays to those performed on oligomers formed during molecular shedding could be performed to probe the surface-exposed hydrophobicity of the oligomers. AFM and negative stain-EM could also be used to probe the gross morphology of HMW pre-fibrillar species whose formation precedes that of the mature amyloid fibril. Characterising pre-fibrillar oligomers in this way would therefore allow a comparison between these and oligomers generated during molecular shedding to take place. If the two oligomer populations are found to be significantly different, this could hold important consequences within disease, as it expands the repertoire of soluble species that are capable of causing cytotoxicity. This would also further illustrate the importance of detailed investigations that uncover mechanisms of fibril-mediated cellular dysfunction.

CHAPTER 5

5.1 Discussion

Amyloid toxicity is a complicated, integrated process, involving the formation of multiple potentially cytotoxic species that mediate cellular disruption through a variety of distinct mechanisms. For the treatment of amyloid diseases, especially those that target toxic aggregates, it is likely that the array of species that disrupt cellular homeostasis in models of disease will need to be characterised before effective palliative or curative treatments can be developed. This includes those species that are formed *in vitro*, as several examples of species that were initially characterised *in vitro* have been found to occur in cells (82, 113, 170, 184). Thus, studying mechanisms of amyloid formation and toxicity *in vitro* contribute significantly towards our collective understanding of the processes underlying amyloid diseases.

Work presented in this thesis has focused primarily on elucidating the mechanism by which β_2m amyloid fibrils cause membrane disruption *in vitro*. The hypothesis of this work was borne out of the observation made by Goodchild *et al*, which showed that disruption of liposomes by β_2m amyloid fibrils is dependent upon pH, where a ~2-fold increase in the extent of membrane disruption is observed upon reducing the pH by a single unit, from pH 7.4 to 6.4 (341). This, coupled with the reduced extent of β_2m fibril-mediated liposome disruption in the presence of the known fibril stabiliser LMW heparin (78, 342), prompted an investigation into the role of fibril dynamics in mediating the disruption of membranes. This was the primary focus of Chapters 2 and 3.

Why is β_2m fibril-mediated membrane disruption pH-dependent?

Several literature examples have highlighted the ability of amyloid fibrils to 'recycle' molecules between the fibrillar and soluble forms under conditions of fibril growth (188, 238, 242, 243, 425). Similarly, kinetic analysis of the response of β_2m amyloid fibrils formed at low pH upon dilution into pH 7.4 or 6.4 buffers revealed that soluble material is released as a consequence destabilising β_2m fibrils by changing the solution conditions. The soluble material formed under both conditions

was then shown to be responsible for up to 80% of the membrane disruption potential of β_2m fibrils under both conditions. Paradoxically, the extent of membrane disruption is not directly related to the concentration of material released during depolymerisation; the kinetic amplitude of fibril depolymerisation is significantly greater at pH 7.4, but the released soluble material is only half as membrane-active as that formed during depolymerisation at pH 6.4. As native β_2m monomer is incapable of disrupting liposomal membranes, the membrane disruption activity exhibited by soluble material must be caused by the formation of one or more non-native, membrane-active species that is/are significantly more populated upon fibril depolymerisation at pH 6.4. This was subsequently confirmed using NMR and ESI-IMS-MS, which showed that the appearance of native β_2m during fibril depolymerisation at pH 6.4 is delayed significantly with respect to the loss of fibrillar material (Figure 5.1.1). This is the first example that subtle changes in

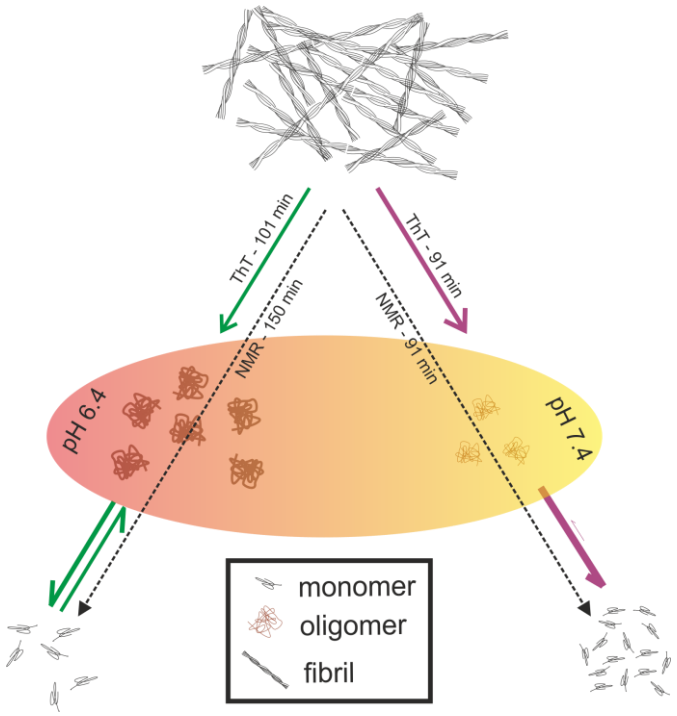

Figure 5.1.1 The kinetic mechanism of β_2m fibril depolymerisation. Upon dilution into pH 7.4 (purple) or pH 6.4 (green) buffer, β_2m fibrils undergo depolymerisation to release soluble material responsible for membrane disruption. Comparison between the time constant for the loss of ThT fluorescence (loss of fibrillar material – double headed arrow) and the appearance of native β_2m (measured by NMR – dashed line), reveals that, at pH 6.4, a non-native, NMR-invisible species is significantly populated, leading to the delayed appearance of native β_2m . It is this species that is presumably responsible for the increased membrane disruption at pH 6.4 (ellipsoid, red to orange indicates the membrane-activity of non-native species generated under either condition).

solution conditions can impact upon the cytotoxic capacity of an amyloid fibril by modulating the concentration of membrane-active soluble species that are initially populated upon fibril depolymerisation.

Subsequently, work presented in Chapter 3 attempted to characterise the non-native, soluble species that are responsible for membrane disruption using different biophysical methods. MEMFCS identified a HMW species, with an apparent R_H of ~20 nm, which is significantly more populated upon depolymerisation at pH 6.4. The apparent size distribution of these species was confirmed by negative-stain TEM. Although FCS rarely detected HMW species upon fibril depolymerisation at pH 7.4, the ability of soluble material generated during depolymerisation at this pH to cause membrane disruption suggests that non-native species must form, as native β_2m monomer cannot cause liposome dye release. Indeed, further analysis by CD and ANS binding experiments revealed that non-native species that are at least partially unstructured and possess surface-exposed hydrophobicity do form during fibril depolymerisation at pH 7.4. These properties were shared with species that populate during fibril depolymerisation at pH 6.4, although a significantly greater proportion of soluble material displays surface-exposed hydrophobic patches and is unstructured at this pH. The exposure of hydrophobic patches at the surface of amyloid oligomers is a feature thought to be responsible for driving the interaction between lipid bilayers and aggregates that leads to membrane disruption (see Section 1.3.6).

Does molecular shedding contribute to β_2m fibril-mediated cellular disruption?

Although the work presented in this thesis is an *in vitro* investigation, the secondary aim was to test whether the observations made were applicable to the mechanism by which β_2m fibrils cause metabolic defects in cells. Since 2009, when Xue *et al* first showed that incubating cells with β_2m amyloid fibrils causes metabolic defects (245, 347), work has been ongoing to elucidate the mechanism by which this takes place. Subsequently, several observations have been made; i) preventing fibril internalisation via endocytosis rescues cells against fibril-mediated cellular disruption; ii) once internalised, fibrils are trafficked through the endocytic pathway and localise with lysosomes, and; iii) fibril internalisation impairs the lysosome proteolytic machinery and causes membrane trafficking defects (340).

In Chapter 2, a chemical cross-linking strategy designed to reduce (at least in-part) the extent of fibril depolymerisation, resulted a modest, but significant, inhibition in the metabolic defects associated with β_2m fibril incubation. The inhibition of fibril toxicity through the reduction of molecular shedding was corroborated by an independent set of experiments which showed that the molecular chaperone, Hsp70, is able to prevent fibril depolymerisation in a dose-dependent manner. Hsp70 was also able to restore cellular metabolic activity in the presence of β_2m fibrils and to restore lysosomal proteolysis to basal levels. Hsp70 was significantly better at reducing the metabolic defects induced by the presence of β_2m fibrils than the chemical cross-linking strategy. This is likely to be due to the concerted anti-amyloid activities of Hsp70 reported in the literature (236, 370, 373, 376–381). Nevertheless, these results indicate that the molecular shedding of cytotoxic species is a contributing factor to β_2m fibril-mediated cellular disruption.

Can molecular shedding be a contributing factor within other amyloid disorders?

The advantage of working with β_2m as a model system is that both the biophysical nature of β_2m amyloid aggregation and the mechanisms of β_2m amyloid-associated toxicity have been characterised in great detail (78, 92, 100, 155, 157, 159, 304, 329, 331, 332, 336, 387, 426–430). Therefore, the context of this work can be integrated into existing hypotheses of β_2m amyloid toxicity to refine the potential mechanism by which β_2m fibrils cause metabolic defects. The *in vitro* observations made and presented in Chapter 2 were integrated with the established phenomena discussed above to put forward a model of β_2m fibril-mediated toxicity. This suggests that the localised environment of specific endocytic compartments may be most susceptible to β_2m amyloid toxicity by tuning the molecular shedding equilibrium in favour of the generation of membrane-active oligomers (Section 2.4).

Chapter 2 also discussed the relevance of molecular shedding to other amyloidogenic aggregates. Many amyloids (especially those deposited extracellularly) are trafficked within the endocytic pathway, thus encountering different environments, one or more of which may favour the molecular shedding of cytotoxic species (11, 98, 108, 188, 218, 220, 244). Evidence for this is provided by the cytoplasmic penetration of soluble particles that are trafficked through the endocytic pathway to seed amyloid formation in previously healthy cells (216–218, 246). In addition, the dissociation of

soluble species from plaques of $A\beta_{42}$ in mice models of disease have been shown to generate an oligomeric 'halo' within which cells are most susceptible to amyloid toxicity (343). Finally, a recent series of small molecule screening experiments identified a set of compounds that bind to the fibril core formed from the $A\beta_{16-21}$ fragment (431). Several of these compounds were shown to inhibit Aβ fibril toxicity markedly. Although not proven in their study, the authors speculate that the inhibitory effect of small molecules is due to the stabilisation of the amyloid fibril core upon binding of the small molecules, thus preventing the dissociation of cytotoxic species. All in all, this series of experiments suggests that amyloid fibrils, through the action of molecular shedding, are likely to be an important reservoir of toxicity in other amyloidogenic systems.

Are species generated during molecular shedding a novel class of β_2m-derived oligomers?

The inception of the work described in Chapter 4 was inspired from the same studies outlined above and follows on from the work presented in Chapters 2 and 3. Briefly, having established that fibril membrane disruption is predominantly mediated through the molecular shedding of soluble species, Chapter 4 aims to elucidate why the length-dependent membrane disruption potential of β_2m amyloid fibrils (and cellular disruption, see Section 2.1) does not linearly scale with the number of fibril ends within a fibril population. The fragmentation of β_2m fibrils, which typically leads to a 4-fold reduction in the weight average fibril length, only induces an ~2-fold increase in membrane disruption potential under a variety of different conditions, and in the presence of a variety of different lipid compositions (245, 341). As discussed in Section 4.1, the polymerisation of amyloid fibrils and the recycling of soluble species within the stationary phase of amyloid formation (Figure 1.3.4a), are generally end-dependent processes. Thus, it would be reasonable to assume that molecular shedding induced upon fibril destabilisation would be similarly mediated from fibril ends.

It turns out that establishing the mechanism of fibril depolymerisation is not that straightforward. By monitoring the length dependent rate of fibril depolymerisation (Figure 4.3.7) and the release of soluble material (Figure 4.3.9), the difference in the extent of membrane disruption potential is equivalent to the difference in

depolymerisation kinetics between unfragmented and 48 h fragmented fibril samples. Why the rate of depolymerisation, unlike the rate of polymerisation (Figure 4.3.2), does not linearly correlate with the number of fibril ends poses an intellectually challenging question which is discussed at length in Section 4.3.3 and will not be repeated here.

Finally, the differences in the kinetics of β_2m fibril polymerisation and depolymerisation prompted an investigation of the structural characterisation of species that form in the lag phase of β_2m amyloid assembly. Highlighting differences in the structural properties of pre-fibrillar oligomers (frequently reported as the agents of toxicity) and those that form during molecular shedding would expand the morphological features of soluble species able to form from a single precursor through competing pathways. The potential discovery would hold important consequences as to how best to combat amyloid toxicity *in vivo*. Many therapeutic strategies are designed to divert the formation of amyloid through distinct mechanisms or to kinetically modulate the aggregation pathway (Section 1.3.8). Diverting amyloid formation would therefore require the characterisation of novel species formed through the action of small molecules to ensure they do not exhibit toxicity. In addition, the action of a small molecule on the entire ensemble of amyloidogenic species likely to be found *in vivo* would have to be investigated, as small molecules may have additional effects on other amyloidogenic species that are not being specifically targeted (342).

The initial observations made by MEMFCS show the evolution of three distinct species that populate at different times throughout the lag phase of β_2m assembly. The apparent R_H of the intermediate, HMW species formed in the lag phase of β_2m amyloid fibril assembly is similar to that formed via molecular shedding, although this pre-fibrillar species is somewhat larger (according to apparent R_H - ~20 nm for molecular shedded HMW species and 30 – 75 nm for pre-fibrillar species). With the limited structural characterisation of species performed so far, it is too early to tell whether these pre-fibrillar speices are distinct from those that form during molecular shedding, although MEMFCS has provided a starting point from which a more comprehensive analysis can begin.

5.2 Future directions

As is probably the case with the majority of PhD projects, attempting to answer a single question has led to the opening of Pandora's Box. There are now a wealth of new directions in which this research can be taken. If I could start a second PhD to follow on from this one, there would be three main questions that I would address. Firstly, I would like to finish the structural characterisation of pre-fibrillar oligomers in order to draw comparisons between the structural properties of these HMW species and those that form through molecular shedding. Secondly, it would be interesting to investigate in more detail the reasons for why the molecular shedding equilibrium is so dramatically altered upon the slight reduction in pH from 7.4 to 6.4. More specifically, the role of histidine residues in maintaining the stability of β_2m fibrils at pH 6.4 could be investigated for the reasons outlined in Section 4.3.3. As has been discussed (Section 4.3.3), His84 is thought to play an important role in initiating the formation of amyloid aggregation at near-neutral pH of the β_2m variant ΔN6 (157). It was also shown to be one of the residues that exhibit a non-native chemical shift within the early stages of fibril depolymerisation at pH 6.4 (as detected by NMR (Figure 2.3.19)). His84 also participates in the formation cross-β core of β_2m fibrils formed at low pH (117, 409). In lieu of this, does mutating His84, or other His residues within β_2m (*wt* β_2m has four His residues in total), prevent the formation of β_2m amyloid fibrils at low pH? If not, does it affect the pH dependent fibril depolymerisation observed for *wt* β_2m fibrils formed at low pH?

Finally, and most interestingly from a therapeutic perspective, a more detailed analysis of the mechanism by which Hsp70 modulates the kinetic stability of β_2m amyloid fibrils at near-neutral pH should be performed. A discussed in Sections 1.3.6 and 2.3.5, modulation of the proteostatic network is becoming an increasingly suggested method for correcting the metabolic defects associated with amyloid deposition and toxicity.

Investigating the mode of binding of Hsp70 to β_2m fibrils by cryoEM would be an exciting question to pursue. It would be particularly interesting to study β_2m fibril:Hsp70 complexes at the two molar ratios used to rescue fibril depolymerisation in a dose-dependent manner. Such a study could indicate whether chaperone binding is observed along the entire fibril axis or is localised to particular regions of the fibril

structure. Such observations as to the mechanism of the inhibition of fibril depolymerisation may inform as to the sites from which molecular shedding takes place. In addition, studying Hsp70:β_2m amyloid complexes by FCS would also be insightful. FCCS could be performed using differentially labelled β_2m fibrils and Hsp70 to monitor the interaction between amyloid species and the chaperone at different times after the initiation of fibril depolymerisation. Cross-correlating ACs between Hsp70 and amyloid species could reveal whether Hsp70 additionally interacts with the membrane-active HMW species shown to form during molecular shedding. Such an observation may explain why Hsp70 rescues β_2m fibril-mediated toxicity to a significantly greater extent than chemical cross-linking of amyloid fibrils.

5.3 Concluding remark

In the grand scheme of things, how much the work presented here contributes towards a more comprehensive understanding of the processes that underlie amyloid toxicity will be known in time. I hope that the main aim of this project, to add to the growing body of evidence that indicates the importance mature amyloid fibrils in facilitating amyloid toxicity, has been achieved. And I hope that the avenues of research opened as a result of this project will provide fruitful, challenging, but ultimately exciting work for enthusiastic successors for several years to come.

Bibliography

1. Pepys, M. B. (2006) Amyloidosis. *Annu. Rev. Med.* **57**, 223–241

2. Chiti, F., and Dobson, C. M. (2006) Protein misfolding, functional amyloid, and human disease. *Annu. Rev. Biochem.* **75**, 333–366

3. Buxbaum, J. N., and Linke, R. P. (2012) A molecular history of the amyloidoses. *J. Mol. Biol.* **421**, 142–59

4. Knowles, T. P. J., Vendruscolo, M., and Dobson, C. M. (2014) The amyloid state and its association with protein misfolding diseases. *Nat. Rev. Mol. Cell Biol.* **15**, 384–396

5. Olshansky, S., Passaro, D., Hershow, R., Jayden, J., Carnes, B., Brody, J., Hayflick, L., Allison, D., and Ludwig, D. (2005) A potential decline in life expectancy in the United States in the 21st century. *N. Engl. J. Med.* **352**, 1138–1145

6. Douglas, P. M., and Dillin, A. (2010) Protein homeostasis and aging in neurodegeneration. *J. Cell Biol.* **190**, 719–29

7. Taylor, R. C., and Dillin, A. (2011) Aging as an event of proteostasis collapse. *Cold Spring Harb. Perspect. Biol.* **3**, a004440

8. Lindquist, S. L., and Kelly, J. W. (2011) Chemical and biological approaches for adapting proteostasis to ameliorate protein misfolding and aggregation diseases: progress and prognosis. *Cold Spring Harb. Perspect. Biol.* **3**, a004507

9. Nahri, L., Wood, S., Steavenson, S., Jiang, Y., May Wu, G., Anafi, D., Kaufman, S. ., Martin, F., Sitney, K., Denis, P., Louis, J., Wypych, J., Leona Biere, A., and Citron, M. (1999) Both familial Parkinson's disease mutations accelerate α-synuclein aggregation. *J. Biol. Chem.* **274**, 9843–9846

10. Valleix, S., Gillmore, J., Bridoux, F., Magione, P., Dogan, A., Nedelec, B., Boimard, M., Touchard, G., Goujon, J., Lacombe, C., Lozeron, P., Adams, D., Lacroix, C., Maisonobe, T., Plante-Bordeneuve, V., Vrana, J., Theis, J., Giorgetti, S., Porcari, R., Ricagno, S., Bologenesi, M., Stoppini, M., Delpech, M., Pepys, M., Hawkins, P., and Bellotti, V. (2012) Hereditary systemic amyloidosis due to Asp76Asn variant β2-microglobulin. *N. Engl. J. Med.* **366**, 2276–2283

11. Münch, C., and Bertolotti, A. (2010) Exposure of hydrophobic surfaces initiates aggregation of diverse ALS-causing superoxide dismutase-1 mutants. *J. Mol. Biol.* **399**, 512–25

12. Lashuel, H. A., Lai, Z., and Kelly, J. W. (1998) Characterization of the transthyretin acid denaturation pathways by analytical ultracentrifugation: implications for wild-type, V30M, and L55P amyloid fibril formation. *Biochemistry*. **37**, 17851–64

13. Kim, H. J., Kim, N. C., Wang, Y. D., Scarborough, E. a, Moore, J., Diaz, Z., MacLea, K. S., Freibaum, B., Li, S., Molliex, A., Kanagaraj, A. P., Carter, R., Boylan, K. B., Wojtas, A. M., Rademakers, R., Pinkus, J. L., Greenberg, S. a, Trojanowski, J. Q., Traynor, B. J., Smith, B. N., Topp, S., Gkazi, A.-S., Miller, J.,

Shaw, C. E., Kottlors, M., Kirschner, J., Pestronk, A., Li, Y. R., Ford, A. F., Gitler, A. D., Benatar, M., King, O. D., Kimonis, V. E., Ross, E. D., Weihl, C. C., Shorter, J., and Taylor, J. P. (2013) Mutations in prion-like domains in hnRNPA2B1 and hnRNPA1 cause multisystem proteinopathy and ALS. *Nature*. **495**, 467–73

14. Kitada, T., Asakawa, S., and Hattori, N. (1998) Mutations in the parkin gene cause autosomal recessive juvenile parkinsonism. *Nature*. **169**, 166–169

15. Roses, a D. (1996) Apolipoprotein E alleles as risk factors in Alzheimer's disease. *Annu. Rev. Med.* **47**, 387–400

16. Harold, D., Abraham, R., Hollingworth, P., Sims, R., Gerrish, A., Hamshere, M. L., Pahwa, J. S., Moskvina, V., Dowzell, K., Williams, A., Jones, N., Thomas, C., Stretton, A., Morgan, A. R., Lovestone, S., Powell, J., Proitsi, P., Lupton, M. K., Brayne, C., Rubinsztein, D. C., Gill, M., Lawlor, B., Lynch, A., Morgan, K., Brown, K. S., Passmore, P. a, Craig, D., McGuinness, B., Todd, S., Holmes, C., Mann, D., Smith, a D., Love, S., Kehoe, P. G., Hardy, J., Mead, S., Fox, N., Rossor, M., Collinge, J., Maier, W., Jessen, F., Schürmann, B., Heun, R., van den Bussche, H., Heuser, I., Kornhuber, J., Wiltfang, J., Dichgans, M., Frölich, L., Hampel, H., Hüll, M., Rujescu, D., Goate, A. M., Kauwe, J. S. K., Cruchaga, C., Nowotny, P., Morris, J. C., Mayo, K., Sleegers, K., Bettens, K., Engelborghs, S., De Deyn, P. P., Van Broeckhoven, C., Livingston, G., Bass, N. J., Gurling, H., McQuillin, A., Gwilliam, R., Deloukas, P., Al-Chalabi, A., Shaw, C. E., Tsolaki, M., Singleton, A. B., Guerreiro, R., Mühleisen, T. W., Nöthen, M. M., Moebus, S., Jöckel, K.-H., Klopp, N., Wichmann, H.-E., Carrasquillo, M. M., Pankratz, V. S., Younkin, S. G., Holmans, P. a, O'Donovan, M., Owen, M. J., and Williams, J. (2009) Genome-wide association study identifies variants at CLU and PICALM associated with Alzheimer's disease. *Nat. Genet.* **41**, 1088–93

17. Bentahir, M., Nyabi, O., Verhamme, J., Tolia, A., Horré, K., Wiltfang, J., Esselmann, H., and De Strooper, B. (2006) Presenilin clinical mutations can affect gamma-secretase activity by different mechanisms. *J. Neurochem.* **96**, 732–42

18. Hardy, J., and Higgins, G. (1992) Alzheimer's disease: The amyloid cascade hypothesis. *Science*. **256**, 184–185

19. Sipe, J., Benson, M., Buxbaum, J., Ikeda, S., Merlini, G., M, S., and Westermark, P. (2012) Amyloid fibril protein nomenclature: 2012 recommendations from the Nomenclature Committee of the International Society of Amyloidosis. *Amyloid*. **19**, 167–170

20. Bucciantini, M., Giannoni, E., Chiti, F., Baroni, F., Formigli, L., Zurdo, J., Taddei, N., Ramponi, G., Dobson, C. M., and Stefani, M. (2002) Inherent toxicity of aggregates implies a common mechanism for protein misfolding diseases. *Nature*. **416**, 507–511

21. Kayed, R., Head, E., Thompson, J. L., McIntire, T. M., Milton, S. C., Cotman, C. W., and Glabe, C. G. (2003) Common structure of soluble amyloid oligomers implies common mechanism of pathogenesis. *Science*. **300**, 486–489

22. Klein, W. L. (2002) Aβ toxicity in Alzheimer's disease: globular oligomers (ADDLs) as new vaccine and drug targets. *Neurochem. Int.* **41**, 345–352

23. Shankar, G. M., Li, S., Mehta, T. H., Garcia-Munoz, A., Shepardson, N. E., Smith, I., Brett, F. M., Farrell, M. a, Rowan, M. J., Lemere, C. a, Regan, C. M., Walsh, D. M., Sabatini, B. L., and Selkoe, D. J. (2008) Amyloid-beta protein dimers isolated directly from Alzheimer's brains impair synaptic plasticity and memory. *Nat. Med.* **14**, 837–42

24. Stroud, J. C., Liu, C., Teng, P. K., and Eisenberg, D. (2012) Toxic fibrillar oligomers of amyloid-β have cross-β structure. *Proc. Natl. Acad. Sci. U. S. A.* **109**, 7717–7722

25. Benilova, I., Karran, E., and De Strooper, B. (2012) The toxic Aβ oligomer and Alzheimer's disease: an emperor in need of clothes. *Nat. Neurosci.* **15**, 349–357

26. Bieschke, J., Herbst, M., Wiglenda, T., Friedrich, R. P., Boeddrich, A., Schiele, F., Kleckers, D., Lopez del Amo, J. M., Grüning, B. a, Wang, Q., Schmidt, M. R., Lurz, R., Anwyl, R., Schnoegl, S., Fändrich, M., Frank, R. F., Reif, B., Günther, S., Walsh, D. M., and Wanker, E. E. (2012) Small-molecule conversion of toxic oligomers to nontoxic β-sheet-rich amyloid fibrils. *Nat. Chem. Biol.* **8**, 93–101

27. Lednev, I. K. (2014) Amyloid fibrils: the eighth wonder of the world in protein folding and aggregation. *Biophys. J.* **106**, 1433–1435

28. Arrasate, M., Mitra, S., Schweitzer, E. S., Segal, M. R., and Finkbeiner, S. (2004) Inclusion body formation reduces levels of mutant huntingtin and the risk of neuronal death. *Nature*. **431**, 805–10

29. Anfinsen, C. B. (1973) Principles that govern the folding of protein chains. *Science*. **181**, 223–30

30. Harms, M. J., and Thornton, J. W. (2013) Evolutionary biochemistry: revealing the historical and physical causes of protein properties. *Nat. Rev. Genet.* **14**, 559–71

31. Hietpas, R. T., Jensen, J. D., and Bolon, D. N. a (2011) Experimental illumination of a fitness landscape. *Proc. Natl. Acad. Sci. U. S. A.* **108**, 7896–901

32. Fowler, D. M., Araya, C. L., Fleishman, S. J., Kellogg, E. H., Stephany, J. J., Baker, D., and Fields, S. (2010) High-resolution mapping of protein sequence-function relationships. *Nat. Methods*. **7**, 741–6

33. Schonbrun, J., and Dill, K. a (2003) Fast protein folding kinetics. *Proc. Natl. Acad. Sci. U. S. A.* **100**, 12678–82

34. White, D. a, Buell, A. K., Knowles, T. P. J., Welland, M. E., and Dobson, C. M. (2010) Protein aggregation in crowded environments. *J. Am. Chem. Soc.* **132**, 5170–5

35. Salceda, S., and Caro, J. (1997) Hypoxia-inducible factor 1 (HIF-1) protein is rapidly degraded by the ubiquitin proteasome system under normoxic conditions: it's stabilization by hypoxia depends on redox-induced changes. *J. Biol. Chem.* **272**, 22642–22647

36. Verzijl, N., DeGroot, J., Thorpe, S. R., Bank, R. a, Shaw, J. N., Lyons, T. J., Bijlsma, J. W., Lafeber, F. P., Baynes, J. W., and TeKoppele, J. M. (2000) Effect of collagen turnover on the accumulation of advanced glycation end products. *J. Biol. Chem.* **275**, 39027–31

37. Prabakaran, S., Lippens, G., Steen, H., and Gunawardena, J. (2012) Post-translational modification: nature's escape from genetic imprisonment and the basis for dynamic information encoding. *WIREs Syst. Biol. Med.* **4**, 565–583

38. Madian, A., and Regnier, E. (2010) Proteomic identification of carbonylated proteins and their oxidation sites. *J. Proteome Res.* **9**, 3766–3780

39. Wolff, S., Weissman, J. S., and Dillin, A. (2014) Differential scales of protein quality control. *Cell*. **157**, 52–64

40. Pechmann, S., Willmund, F., and Frydman, J. (2013) The ribosome as a hub for protein quality control. *Mol. Cell*. **49**, 411–21

41. Willmund, F., del Alamo, M., Pechmann, S., Chen, T., Albanèse, V., Dammer, E. B., Peng, J., and Frydman, J. (2013) The cotranslational function of ribosome-associated Hsp70 in eukaryotic protein homeostasis. *Cell*. **152**, 196–209

42. O'Brien, E. P., Vendruscolo, M., and Dobson, C. M. (2012) Prediction of variable translation rate effects on cotranslational protein folding. *Nat. Commun.* **3**, 868

43. O'Brien, E. P., Vendruscolo, M., and Dobson, C. M. (2014) Kinetic modelling indicates that fast-translating codons can coordinate cotranslational protein folding by avoiding misfolded intermediates. *Nat. Commun.* **5**, 2988

44. Zhou, M., Guo, J., Cha, J., Chae, M., Chen, S., Barral, J. M., Sachs, M. S., and Liu, Y. (2013) Non-optimal codon usage affects expression, structure and function of clock protein FRQ. *Nature*. **495**, 111–5

45. Richter, K., Haslbeck, M., and Buchner, J. (2010) The heat shock response: life on the verge of death. *Mol. Cell*. **40**, 253–66

46. Ron, D., and Walter, P. (2007) Signal integration in the endoplasmic reticulum unfolded protein response. *Nat. Rev. Mol. Cell Biol.* **8**, 519–29

47. Schröder, M., and Kaufman, R. J. (2005) The mammalian unfolded protein response. *Annu. Rev. Biochem.* **74**, 739–89

48. Scheuner, D., Song, B., McEwen, E., Liu, C., Laybutt, R., Gillespie, P., Saunders, T., Bonner-Weir, S., and Kaufman, R. J. (2001) Translational control is required for the unfolded protein response and in vivo glucose homeostasis. *Mol. Cell*. **7**, 1165–76

49. Harding, H. P., Novoa, I., Zhang, Y., Zeng, H., Wek, R., Schapira, M., and Ron, D. (2000) Stress-Induced Gene Expression in Mammalian Cells. *Mol. Cell*. **6**, 1099–1108

50. Kozutsumi, Y., Segal, M., Normington, K., Gething, M., and Sambrook, J. (1988) The presence of malfolded proteins in the endoplasmic reticulum signals the induction of glucose-regulated proteins. *Nature*. **332**, 462–464

51. Kim, Y. E., Hipp, M. S., Bracher, A., Hayer-Hartl, M., and Hartl, F. U. (2013) Molecular chaperone functions in protein folding and proteostasis. *Annu. Rev. Biochem.* **82**, 323–55

52. Kaushik, S., and Cuervo, A. M. (2012) Chaperone-mediated autophagy: a unique way to enter the lysosome world. *Trends Cell Biol.* **22**, 407–17

53. Kaganovich, D., Kopito, R., and Frydman, J. (2008) Misfolded proteins partition between two distinct quality control compartments. *Nature*. **454**, 1088–95

54. Duttler, S., Pechmann, S., and Frydman, J. (2013) Principles of cotranslational ubiquitination and quality control at the ribosome. *Mol. Cell*. **50**, 379–93

55. Sontag, E. M., Vonk, W. I. M., and Frydman, J. (2014) Sorting out the trash: the spatial nature of eukaryotic protein quality control. *Curr. Opin. Cell Biol.* **26**, 139–46

56. Wang, F., Durfee, L. a, and Huibregtse, J. M. (2013) A cotranslational ubiquitination pathway for quality control of misfolded proteins. *Mol. Cell*. **50**, 368–78

57. Kamhi-Nesher, S., Shenkman, M., Tolchinsky, S., Fromm, S. V, Ehrlich, R., and Lederkremer, G. Z. (2001) A novel quality control compartment derived from the endoplasmic reticulum. *Mol. Biol. Cell*. **12**, 1711–23

58. Kroemer, G., Mariño, G., and Levine, B. (2010) Autophagy and the integrated stress response. *Mol. Cell*. **40**, 280–93

59. Varshavsky, A. (2012) The ubiquitin system, an immense realm. *Annu. Rev. Biochem.* **81**, 167–76

60. Van Oosten-Hawle, P., Porter, R. S., and Morimoto, R. I. (2013) Regulation of organismal proteostasis by transcellular chaperone signaling. *Cell*. **153**, 1366–78

61. Neufeld, E. F. (1991) Lysosomal storage diseases. *Annu. Rev. Biochem.* **60**, 257–280

62. Rowe, S. M., Miller, S., and Sorscher, E. J. (2005) Cystic fibrosis. *N. Engl. J. Med.* **352**, 1992–2001

63. Jahn, T. R., and Radford, S. E. (2005) The Yin and Yang of protein folding. *FEBS J.* **272**, 5962–70

64. Virchow, R. (1857) neue beobachtungen über amyloid degeneration. *Virchows Arch. Pathol. Anat. Physiol. Klin. Med.* **11**, 188–189

65. Pras, M., Schubert, M., Zucker-Franklin, D., Rimon, a, and Franklin, E. C. (1968) The characterization of soluble amyloid prepared in water. *J. Clin. Invest.* **47**, 924–33

66. Fändrich, M., and Dobson, C. M. (2002) The behaviour of polyamino acids reveals an inverse side chain effect in amyloid structure formation. *EMBO J.* **21**, 5682–90

67. Dobson, C. M. (2003) Protein folding and misfolding. *Nature*. **426**, 884–90

68. Sunde, M., Serpell, L. C., Bartlam, M., Fraser, P. E., Pepys, M. B., and Blake, C. C. (1997) Common core structure of amyloid fibrils by synchrotron X-ray diffraction. *J. Mol. Biol.* **273**, 729–39

69. Jahn, T. R., Makin, O. S., Morris, K. L., Marshall, K. E., Tian, P., Sikorski, P., and Serpell, L. C. (2010) The common architecture of cross-beta amyloid. *J. Mol. Biol.* **395**, 717–27

70. Sawaya, M. R., Sambashivan, S., Nelson, R., Ivanova, M. I., Sievers, S. a, Apostol, M. I., Thompson, M. J., Balbirnie, M., Wiltzius, J. J. W., McFarlane, H. T., Madsen, A. Ø., Riekel, C., and Eisenberg, D. (2007) Atomic structures of amyloid cross-beta spines reveal varied steric zippers. *Nature*. **447**, 453–7

71. Nelson, R., Sawaya, M. R., Balbirnie, M., Madsen, A. Ø., Riekel, C., Grothe, R., and Eisenberg, D. (2005) Structure of the cross-beta spine of amyloid-like fibrils. *Nature*. **435**, 773–8

72. Knowles, T. P. J., and Buehler, M. J. (2011) Nanomechanics of functional and pathological amyloid materials. *Nat. Nanotechnol.* **6**, 469–79

73. Knowles, T. P. J., Waudby, C. a, Devlin, G. L., Cohen, S. I. a, Aguzzi, A., Vendruscolo, M., Terentjev, E. M., Welland, M. E., and Dobson, C. M. (2009) An analytical solution to the kinetics of breakable filament assembly. *Science*. **326**, 1533–7

74. Li, D., Furukawa, H., Deng, H., Liu, C., Yaghi, O. M., and Eisenberg, D. S. (2014) Designed amyloid fibers as materials for selective carbon dioxide capture. *Proc. Natl. Acad. Sci. U. S. A.* **111**, 191–6

75. Baldwin, A. J., Knowles, T. P. J., Tartaglia, G. G., Fitzpatrick, A. W., Devlin, G. L., Shammas, S. L., Waudby, C. a, Mossuto, M. F., Meehan, S., Gras, S. L., Christodoulou, J., Anthony-Cahill, S. J., Barker, P. D., Vendruscolo, M., and Dobson, C. M. (2011) Metastability of native proteins and the phenomenon of amyloid formation. *J. Am. Chem. Soc.* **133**, 14160–3

76. Baldwin, A. J., Bader, R., Christodoulou, J., MacPhee, C. E., Dobson, C. M., and Barker, P. D. (2006) Cytochrome display on amyloid fibrils. *J. Am. Chem. Soc.* **128**, 2162–3

77. Westermark, G. T., Johnson, K. H., and Westermark, P. (1999) Staining methods for identification of amyloid in tissue. *Methods Enzymol.* **309**, 3–25

78. Myers, S. L., Jones, S., Jahn, T. R., Morten, I. J., Tennent, G. A., Hewitt, E. W., and Radford, S. E. (2006) A Systematic Study of the Effect of Physiological Factors on beta2-microglobulin Amyloid Formation at Neutral pH. *Biochemistry*

79. Naiki, H., Higuchi, K., Hosokawa, M., and Takeda, T. (1989) Fluorometric determination of amyloid Fibrils in vitro using the fluorescent dye , thioflavine T. *Anal. Biochem.* **177**, 244–249

80. O'Nuallain, B., and Wetzel, R. (2002) Conformational Abs recognizing a generic amyloid fibril epitope. *Proc. Natl. Acad. Sci. U. S. A.* **99**, 1485–1490

81. Glabe, C. G. (2008) Structural classification of toxic amyloid oligomers. *J. Biol. Chem.* **283**, 29639–43

82. Jahn, T. R., Tennent, G. a, and Radford, S. E. (2008) A common β-sheet architecture underlies in vitro and in vivo β2-microglobulin amyloid fibrils. *J. Biol. Chem.* **283**, 17279–86

83. Nelson, R., and Eisenberg, D. S. (2006) Structural models of amyloid-like fibrils. *Adv. Protein Chem.* **73**, 235–282

84. Scherzinger, E., Sittler, A., K, S., Heiser, V., Lurz, R., Hasenbank, R., Bates, G., Lehrach, H., and Wanker, E. (1999) Self-assembly of polyglutamine-containing huntingtin fragments into amyloid-like fibrils: implications for Huntington's disease pathology. *Proc. Natl. Acad. Sci. U. S. A.* **96**, 4604–4609

85. Scherzinger, E., Lurz, R., Turmaine, M., Mangiarini, L., Hollenbach, B., Hasenbank, R., Bates, G. P., Davies, S. W., Lehrach, H., and Wanker, E. E. (1997) Huntingtin-encoded polyglutamine expansions form amyloid-like protein aggregates in vitro and in vivo. *Cell*. **90**, 549–58

86. Elam, J. S., Taylor, A. B., Strange, R., Antonyuk, S., Doucette, P. a, Rodriguez, J. a, Hasnain, S. S., Hayward, L. J., Valentine, J. S., Yeates, T. O., and Hart, P. J. (2003) Amyloid-like filaments and water-filled nanotubes formed by SOD1 mutant proteins linked to familial ALS. *Nat. Struct. Biol.* **10**, 461–7

87. Qiang, W., Yau, W.-M., Luo, Y., Mattson, M. P., and Tycko, R. (2012) Antiparallel β-sheet architecture in Iowa-mutant β-amyloid fibrils. *Proc. Natl. Acad. Sci. U. S. A.* **109**, 4443–8

88. Liu, C., Zhao, M., Jiang, L., Cheng, P. N., Park, J., Sawaya, M. R., Pensalfini, A., Gou, D., Berk, A. J., Glabe, C. G., Nowick, J., and Eisenberg, D. (2012) Out-of-register β-sheets suggest a pathway to toxic amyloid aggregates. *Proc. Natl. Acad. Sci. U. S. A.* **109**, 20913–8

89. Zandomeneghi, G., Krebs, M. R. H., Mccammon, M. G., Fändrich, M., Biotechnologie, M., and Jena, D.- (2004) FTIR reveals structural differences between native beta-sheet proteins and amyloid fibrils. *Protein Sci.* **13**, 3314–3321

90. Colletier, J.-P., Laganowsky, A., Landau, M., Zhao, M., Soriaga, A. B., Goldschmidt, L., Flot, D., Cascio, D., Sawaya, M. R., and Eisenberg, D. (2011) Molecular basis for amyloid-beta polymorphism. *Proc. Natl. Acad. Sci. U. S. A.* **108**, 16938–43

91. Fitzpatrick, A., Debelouchina, G. T., Bayro, M. J., Clare, D. K., Caporini, M. a, Bajaj, V. S., Jaroneic, C., Wang, L., Ladizhansky, V., Muller, S., Macphee, C. E., Waudby, Christopher aMott, H., De Simone, A., Knowles, T. P. J., Saibil, H. R., Vendruscolo, M., Orlova, E. V, Griffin, R. G., and Dobson, C. M. (2013) Atomic structure and hierarchical assembly of a cross-β amyloid fibril. *Proc. Natl. Acad. Sci. U. S. A.* **110**, 5468–5473

92. White, H. E., Hodgkinson, J. L., Jahn, T. R., Cohen-Krausz, S., Gosal, W. S., Müller, S., Orlova, E. V, Radford, S. E., and Saibil, H. R. (2009) Globular tetramers of β2-microglobulin assemble into elaborate amyloid fibrils. *J. Mol. Biol.* **389**, 48–57

93. Mossuto, M. F., Dhulesia, A., Devlin, G., Frare, E., Kumita, J. R., de Laureto, P. P., Dumoulin, M., Fontana, A., Dobson, C. M., and Salvatella, X. (2010) The non-core

regions of human lysozyme amyloid fibrils influence cytotoxicity. *J. Mol. Biol.* **402**, 783–796

94. Su, Y., Sarell, C. J., Eddy, M. T., Debelouchina, G. T., Andreas, L. B., Pashley, C. L., Radford, S. E., and Griffin, R. G. (2014) Secondary structure in the core of amyloid fibrils formed from human β2m and its truncated variant ΔN6. *J. Am. Chem. Soc.* **136**, 6313–6325

95. Petkova, A. T., Leapman, R. D., Guo, Z., Yau, W.-M., Mattson, M. P., and Tycko, R. (2005) Self-propagating, molecular-level polymorphism in Alzheimer's β-amyloid fibrils. *Science*. **307**, 262–265

96. Petkova, A. T., Yau, W., and Tycko, R. (2006) Experimental constraints on quaternary structure in Alzheimer 's β-amyloid fibrils. *Biochemistry*. **45**, 498–512

97. Paravastu, A. K., Leapman, R. D., Yau, W., and Tycko, R. (2008) Molecular structural basis for polymorphism in Alzheimer's β-amyloid fibrils. *Proc. Natl. Acad. Sci. U. S. A.* **105**, 18349–18354

98. Bousset, L., Pieri, L., Ruiz-Arlandis, G., Gath, J., Jensen, P. H., Habenstein, B., Madiona, K., Olieric, V., Böckmann, A., Meier, B. H., and Melki, R. (2013) Structural and functional characterization of two alpha-synuclein strains. *Nat. Commun.* **4**, 2575

99. Buell, A. K., Galvagnion, C., Gaspar, R., Sparr, E., Vendruscolo, M., Knowles, T. P. J., Linse, S., and Dobson, C. M. (2014) Solution conditions determine the relative importance of nucleation and growth processes in α-synuclein aggregation. *Proc. Natl. Acad. Sci. U. S. A.* **111**, 7671–7676

100. Kad, N. M., Thomson, N. H., Smith, D. P., Smith, D. a, and Radford, S. E. (2001) Beta(2)-microglobulin and its deamidated variant, N17D form amyloid fibrils with a range of morphologies in vitro. *J. Mol. Biol.* **313**, 559–71

101. Chatani, E., Yagi, H., Naiki, H., and Goto, Y. (2012) Polymorphism of β2-microglobulin amyloid fibrils manifested by ultrasonication-enhanced fibril formation in trifluoroethanol. *J. Biol. Chem.* **287**, 22827–37

102. Macchi, F., Hoffmann, S. V, Carlsen, M., Vad, B., Imparato, A., Rischel, C., and Otzen, D. E. (2011) Mechanical stress affects glucagon fibrillation kinetics and fibril structure. *Langmuir*. **27**, 12539–49

103. Dzwolak, W., Smirnovas, V., Jansen, R., and Winter, R. (2004) Insulin forms amyloid in a strain-dependent manner: An FTIR spectroscopic study. *Protein Sci.* 10.1110/ps.03607204.ogy

104. Gosal, W. S., Morten, I. J., Hewitt, E. W., Smith, D. A., Thomson, N. H., and Radford, S. E. (2005) Competing pathways determine fibril morphology in the self-assembly of beta2-microglobulin into amyloid. *J. Mol. Biol.* **351**, 850–64

105. Bolognesi, B., Kumita, J. R., Barros, T. P., Esbjorner, E. K., Luheshi, L. M., Crowther, D. C., Wilson, M. R., Dobson, C. M., Favrin, G., and Yerbury, J. J. (2010) ANS binding reveals common features of cytotoxic amyloid species. *ACS Chem. Biol.* **5**, 735–40

106. Debelouchina, G. T., Platt, G. W., Bayro, M. J., Radford, S. E., and Griffin, R. G. (2010) Magic angle spinning NMR analysis of beta2-microglobulin amyloid fibrils in two distinct morphologies. *J. Am. Chem. Soc.* **132**, 10414–23

107. Mossuto, M. F., Bolognesi, B., Guixer, B., Dhulesia, A., Agostini, F., Kumita, J. R., Tartaglia, G. G., Dumoulin, M., Dobson, C. M., and Salvatella, X. (2011) Disulfide bonds reduce the toxicity of the amyloid fibrils formed by an extracellular protein. *Angew. Chem. Int. Ed. Engl.* **50**, 7048–51

108. Guo, J. L., Covell, D. J., Daniels, J. P., Iba, M., Stieber, A., Zhang, B., Riddle, D. M., Kwong, L. K., Xu, Y., Trojanowski, J. Q., and Lee, V. M. Y. (2013) Distinct α-synuclein strains differentially promote tau inclusions in neurons. *Cell*. **154**, 103–17

109. Frederick, K. K., Debelouchina, G. T., Kayatekin, C., Dorminy, T., Jacavone, A. C., Griffin, R. G., and Lindquist, S. (2014) Distinct prion strains are defined by amyloid core structure and chaperone binding site dynamics. *Chem. Biol.* **21**, 295–305

110. Tanaka, M., Collins, S. R., Toyama, B. H., and Weissman, J. S. (2006) The physical basis of how prion conformations determine strain phenotypes. *Nature*. **442**, 585–589

111. Toyama, B. H., Kelly, M. J. S., Gross, J. D., and Weissman, J. S. (2007) The structural basis of yeast prion strain variants. *Nature*. **449**, 233–237

112. Tuite, M. F., Howard, M. J., and Xue, W.-F. (2014) Dynamic prions revealed by magic. *Chem. Biol.* **21**, 172–173

113. Lu, J.-X., Qiang, W., Yau, W.-M., Schwieters, C. D., Meredith, S. C., and Tycko, R. (2013) Molecular structure of β-amyloid fibrils in Alzheimer's disease brain tissue. *Cell*. **154**, 1257–68

114. Norlin, N., Hellberg, M., Filippov, A., Sousa, A. a, Gröbner, G., Leapman, R. D., Almqvist, N., and Antzutkin, O. N. (2012) Aggregation and fibril morphology of the Arctic mutation of Alzheimer's Aβ peptide by CD, TEM, STEM and in situ AFM. *J. Struct. Biol.* **180**, 174–89

115. Tycko, R., Sciarretta, K. L., Orgel, J. P. R. O., and Meredith, S. C. (2009) Evidence for novel beta-sheet structures in Iowa mutant beta-amyloid fibrils. *Biochemistry*. **48**, 6072–84

116. Cloe, A., Orgel, J., Sachleben, J., Tycko, R., and Meredith, S. (2011) Japanese mutant Aβ (ΔE22-Aβ1− 39) forms fibrils instantaneously, with low-thioflavin T fluorescence: seeding of wild-Type Aβ1− 40 into atypical Fibrils by ΔE22-. *Biochemistry*. **50**, 2026–2039

117. Sarell, C. J., Woods, L. a, Su, Y., Debelouchina, G. T., Ashcroft, A. E., Griffin, R. G., Stockley, P. G., and Radford, S. E. (2013) Expanding the repertoire of amyloid polymorphs by co-polymerization of related protein precursors. *J. Biol. Chem.* **288**, 7327–7337

118. Sarell, C. J., Stockley, P. G., and Radford, S. E. (2013) Assessing the causes and consequences of co-polymerization in amyloid formation. *Prion*. **7**, 359–68

119. Surmacz-Chwedoruk, W., Nieznańska, H., Wójcik, S., and Dzwolak, W. (2012) Cross-seeding of fibrils from two types of insulin induces new amyloid strains. *Biochemistry*. **51**, 9460–9

120. Tycko, R. (2011) Solid-state NMR studies of amyloid fibril structure. *Annu. Rev. Phys. Chem.* **62**, 279–99

121. Wasmer, C., Lange, A., Van Melckebeke, H., Siemer, A. B., Riek, R., and Meier, B. H. (2008) Amyloid fibrils of the HET-s(218-289) prion form a β solenoid with a triangular hydrophobic core. *Science*. **319**, 1523–6

122. Debelouchina, G., Bayro, M. J., Fitzpatrick, A. W., Ladizhansky, V., Colvin, M., Caporini, M. a, Jaroneic, C., Bajaj, V. S., Rosay, M., MacPhee, C., Vendruscolo, M., Maas, W., Dobson, C. M., and Griffin, R. G. (2013) Higher order amyloid fibril structure by MAS NMR and DNP spectroscopy. *J. Am. Chem. Soc.* **135**, 19237–19247

123. Jiménez, J. L., Nettleton, E. J., Bouchard, M., Robinson, C. V, Dobson, C. M., and Saibil, H. R. (2002) The protofilament structure of insulin amyloid fibrils. *Proc. Natl. Acad. Sci. U. S. A.* **99**, 9196–201

124. Jiménez, J. L., Guijarro, J. I., Orlova, E., Zurdo, J., Dobson, C. M., Sunde, M., and Saibil, H. R. (1999) Cryo-electron microscopy structure of an SH3 amyloid fibril and model of the molecular packing. *EMBO J.* **18**, 815–21

125. Vilar, M., Chou, H.-T., Lührs, T., Maji, S. K., Riek-Loher, D., Verel, R., Manning, G., Stahlberg, H., and Riek, R. (2008) The fold of alpha-synuclein fibrils. *Proc. Natl. Acad. Sci. U. S. A.* **105**, 8637–42

126. Uptain, S. M., and Lindquist, S. (2002) Prions as protein-based genetic elements. *Annu. Rev. Microbiol.* **56**, 703–41

127. Newby, G. a, and Lindquist, S. (2013) Blessings in disguise: biological benefits of prion-like mechanisms. *Trends Cell Biol.* **23**, 251–9

128. Cooper, T. G. (2002) Transmitting the signal of excess nitrogen in Saccharomyces cerevisiae from the Tor proteins to the GATA factors: connecting the dots. *FEMS Microbiol. Rev.* **26**, 223–38

129. Patino, M. M., Liu, J. J., Glover, J. R., and Lindquist, S. (1996) Support for the prion hypothesis for inheritance of a phenotypic trait in yeast. *Science*. **273**, 622–6

130. Serio, T., Cashikar, A., Kowal, A., Sawicki, G., Mosleshi, J., Serpell, L., Arnsdorf, M., and Lindquist, S. L. (2000) Nucleated Conformational Conversion and the Replication of Conformational Information by a Prion Determinant. *Science*. **289**, 1317–1321

131. Alberti, S., Halfmann, R., King, O., Kapila, A., and Lindquist, S. (2009) A systematic survey identifies prions and illuminates sequence features of prionogenic proteins. *Cell*. **137**, 146–58

132. Halfmann, R., Jarosz, D. F., Jones, S. K., Chang, A., Lancaster, A. K., and Lindquist, S. (2012) Prions are a common mechanism for phenotypic inheritance in wild yeasts. *Nature*. **482**, 363–8

133. Holmes, D. L., Lancaster, A. K., Lindquist, S., and Halfmann, R. (2013) Heritable remodeling of yeast multicellularity by an environmentally responsive prion. *Cell*. **153**, 153–65

134. Shorter, J., and Lindquist, S. (2005) Prions as adaptive conduits of memory and inheritance. *Nat. Rev. Genet. Genet.* **6**, 435–50

135. Fowler, D. M., Koulov, A. V, Alory-Jost, C., Marks, M. S., Balch, W. E., and Kelly, J. W. (2006) Functional amyloid formation within mammalian tissue. *PLoS Biol.* **4**, e6

136. Kato, M., Han, T. W., Xie, S., Shi, K., Du, X., Wu, L. C., Mirzaei, H., Goldsmith, E. J., Longgood, J., Pei, J., Grishin, N. V, Frantz, D. E., Schneider, J. W., Chen, S., Li, L., Sawaya, M. R., Eisenberg, D., Tycko, R., and McKnight, S. L. (2012) Cell-free formation of RNA granules: low complexity sequence domains form dynamic fibers within hydrogels. *Cell*. **149**, 753–67

137. Han, T. W., Kato, M., Xie, S., Wu, L. C., Mirzaei, H., Pei, J., Chen, M., Xie, Y., Allen, J., Xiao, G., and McKnight, S. L. (2012) Cell-free formation of RNA granules: bound RNAs identify features and components of cellular assemblies. *Cell*. **149**, 768–79

138. Kwon, I., Kato, M., Xiang, S., Wu, L., Theodoropoulos, P., Mirzaei, H., Han, T., Xie, S., Corden, J. L., and McKnight, S. L. (2013) Phosphorylation-regulated binding of RNA polymerase II to fibrous polymers of low-complexity domains. *Cell*. **155**, 1049–60

139. Si, K., Choi, Y.-B., White-Grindley, E., Majumdar, A., and Kandel, E. R. (2010) Aplysia CPEB can form prion-like multimers in sensory neurons that contribute to long-term facilitation. *Cell*. **140**, 421–35

140. Majumdar, A., Cesario, W. C., White-Grindley, E., Jiang, H., Ren, F., Khan, M. R., Li, L., Choi, E. M.-L., Kannan, K., Guo, F., Unruh, J., Slaughter, B., and Si, K. (2012) Critical role of amyloid-like oligomers of Drosophila Orb2 in the persistence of memory. *Cell*. **148**, 515–29

141. Chapman, M. R., Robinson, L. S., Pinkner, J. S., Roth, R., Heuser, J., Hammar, M., Normark, S., and Hultgren, S. J. (2002) Role of Escherichia coli curli operons in directing amyloid fiber formation. *Science*. **295**, 851–5

142. Hammer, N. D., Schmidt, J. C., and Chapman, M. R. (2007) The curli nucleator protein, CsgB, contains an amyloidogenic domain that directs CsgA polymerization. *Proc. Natl. Acad. Sci. U. S. A.* **104**, 12494–9

143. Blanco, L. P., Evans, M. L., Smith, D. R., Badtke, M. P., and Chapman, M. R. (2012) Diversity, biogenesis and function of microbial amyloids. *Trends Microbiol.* **20**, 66–73

144. Maury, C. P. J. (2009) The emerging concept of functional amyloid. *J. Intern. Med.* **265**, 329–34

145. Münch, J., Rücker, E., Ständker, L., Adermann, K., Goffinet, C., Schindler, M., Wildum, S., Chinnadurai, R., Rajan, D., Specht, A., Giménez-Gallego, G., Sánchez, P. C., Fowler, D. M., Koulov, A., Kelly, J. W., Mothes, W., Grivel, J.-C., Margolis, L., Keppler, O. T., Forssmann, W.-G., and Kirchhoff, F. (2007) Semen-derived amyloid fibrils drastically enhance HIV infection. *Cell*. **131**, 1059–1071

146. Xue, W.-F., Homans, S. W., and Radford, S. E. (2008) Systematic analysis of nucleation-dependent polymerization reveals new insights into the mechanism of amyloid self-assembly. *Proc. Natl. Acad. Sci. U. S. A.* **105**, 8926–8931

147. Collins, S. R., Douglass, A., Vale, R. D., and Weissman, J. S. (2004) Mechanism of prion propagation: amyloid growth occurs by monomer addition. *PLoS Biol.* **2**, e321

148. Ferrone, F. (1999) Analyis of Protein Aggregation Kinetics. *Methods Enzymol.* **309**, 256–274

149. Knowles, T. P. J., Waudby, C. a, Devlin, G. L., Cohen, S. I. a, Aguzzi, A., Vendruscolo, M., Terentjev, E. M., Welland, M. E., and Dobson, C. M. (2009) An analytical solution to the kinetics of breakable filament assembly. *Science*. **326**, 1533–7

150. Xue, W.-F., and Radford, S. E. (2013) An imaging and systems modeling approach to fibril breakage enables prediction of amyloid behavior. *Biophys. J.* **105**, 2811–9

151. Arosio, P., Cukalevski, R., Frohm, B., Knowles, T., and Linse, S. (2014) Quantification of the concentration of Aβ42 propagons during the lag phase by an amyloid chain reaction assay. *J. Am. Chem. Soc.* **136**, 219–225

152. Cohen, S. I., Linse, S., Luheshi, L. M., Hellstrand, E., White, D. a, Rajah, L., Otzen, D. E., Vendruscolo, M., Dobson, C. M., and Knowles, T. P. J. (2013) Proliferation of amyloid-β42 aggregates occurs through a secondary nucleation mechanism. *Proc. Natl. Acad. Sci. U. S. A.* **110**, 9758–9763

153. Lee, J., Culyba, E. K., Powers, E. T., and Kelly, J. W. (2011) Amyloid-β forms fibrils by nucleated conformational conversion of oligomers. *Nat. Chem. Biol.* **7**, 602–9

154. Hurshman, A. R., White, J. T., Powers, E. T., and Kelly, J. W. (2004) Transthyretin aggregation under partially denaturing conditions is a downhill polymerization. *Biochemistry*. **43**, 7365–81

155. Kad, N. M., Myers, S. L., Smith, D. P., Alastair Smith, D., Radford, S. E., and Thomson, N. H. (2003) Hierarchical Assembly of β2-Microglobulin Amyloid In Vitro Revealed by Atomic Force Microscopy. *J. Mol. Biol.* **330**, 785–797

156. Buell, A. K., Dhulesia, A., Mossuto, M. F., Cremades, N., Kumita, J. R., Dumoulin, M., Welland, M. E., Knowles, T. P. J., Salvatella, X., and Dobson, C. M. (2011) Population of nonnative states of lysozyme variants drives amyloid fibril formation. *J. Am. Chem. Soc.* **133**, 7737–7743

157. Eichner, T., Kalverda, A. P., Thompson, G. S., Homans, S. W., and Radford, S. E. (2011) Conformational conversion during amyloid formation at atomic resolution. *Mol. Cell*. **41**, 161–172

158. Neudecker, P., Robustelli, P., Cavalli, A., Walsh, P., Lundström, P., Zarrine-Afsar, A., Sharpe, S., Vendruscolo, M., and Kay, L. E. (2012) Structure of an intermediate state in protein folding and aggregation. *Science*. **336**, 362–6

159. Jahn, T. R., Parker, M. J., Homans, S. W., and Radford, S. E. (2006) Amyloid formation under physiological conditions proceeds via a native-like folding intermediate. *Nat. Struct. Mol. Biol.* **13**, 195–201

160. Kelly, J. (1998) The alternative conformations of amyloidogenic proteins and their multi-step assembly pathways. *Curr. Opin. Struct. Biol.* **8**, 101–106

161. Dhulesia, A., Cremades, N., Kumita, J. R., Hsu, S.-T. D., Mossuto, M. F., Dumoulin, M., Nietlispach, D., Akke, M., Salvatella, X., and Dobson, C. M. (2010) Local cooperativity in an amyloidogenic state of human lysozyme observed at atomic resolution. *J. Am. Chem. Soc.* **132**, 15580–8

162. Kim, L., Dyson, H., Kelly, J., and Wright, P. (2013) Localized Structural Fluctuations Promote Amyloidogenic Conformations in Transthyretin. *J. Mol. Biol.* **425**, 977–988

163. Glabe, C. G. (2008) Structural classification of toxic amyloid oligomers. *J. Biol. Chem.* **283**, 29639–43

164. Gong, Y., Chang, L., Viola, K. L., Lacor, P. N., Lambert, M. P., Finch, C. E., Krafft, G. a, and Klein, W. L. (2003) Alzheimer's disease-affected brain: presence of oligomeric A beta ligands (ADDLs) suggests a molecular basis for reversible memory loss. *Proc. Natl. Acad. Sci. U. S. A.* **100**, 10417–22

165. Lambert, M. P., Barlow, a K., Chromy, B. a, Edwards, C., Freed, R., Liosatos, M., Morgan, T. E., Rozovsky, I., Trommer, B., Viola, K. L., Wals, P., Zhang, C., Finch, C. E., Krafft, G. a, and Klein, W. L. (1998) Diffusible, nonfibrillar ligands derived from Abeta1-42 are potent central nervous system neurotoxins. *Proc. Natl. Acad. Sci. U. S. A.* **95**, 6448–53

166. Kuperstein, I., Broersen, K., Benilova, I., Rozenski, J., Jonckheere, W., Debulpaep, M., Vandersteen, A., Segers-Nolten, I., Van Der Werf, K., Subramaniam, V., Braeken, D., Callewaert, G., Bartic, C., D'Hooge, R., Martins, I. C., Rousseau, F., Schymkowitz, J., and De Strooper, B. (2010) Neurotoxicity of Alzheimer's disease Aβ peptides is induced by small changes in the Aβ42 to Aβ40 ratio. *EMBO J.* **29**, 3408–20

167. Shankar, G. M., Leissring, M. a, Adame, A., Sun, X., Spooner, E., Masliah, E., Selkoe, D. J., Lemere, C. a, and Walsh, D. M. (2009) Biochemical and immunohistochemical analysis of an Alzheimer's disease mouse model reveals the presence of multiple cerebral Abeta assembly forms throughout life. *Neurobiol. Dis.* **36**, 293–302

168. Matsumura, S., Shinoda, K., Yamada, M., Yokojima, S., Inoue, M., Ohnishi, T., Shimada, T., Kikuchi, K., Masui, D., Hashimoto, S., Sato, M., Ito, A., Akioka, M.,

Takagi, S., Nakamura, Y., Nemoto, K., Hasegawa, Y., Takamoto, H., Inoue, H., Nakamura, S., Nabeshima, Y., Teplow, D. B., Kinjo, M., and Hoshi, M. (2011) Two distinct amyloid beta-protein (Abeta) assembly pathways leading to oligomers and fibrils identified by combined fluorescence correlation spectroscopy, morphology, and toxicity analyses. *J. Biol. Chem.* **286**, 11555–62

169. Lesné, S., Koh, M. T., Kotilinek, L., Kayed, R., Glabe, C. G., Yang, A., Gallagher, M., and Ashe, K. H. (2006) A specific amyloid-β protein assembly in the brain impairs memory. *Nature*. **440**, 352–7

170. Reed, M. N., Hofmeister, J. J., Jungbauer, L., Welzel, A. T., Yu, C., Sherman, M. a, Lesné, S., LaDu, M. J., Walsh, D. M., Ashe, K. H., and Cleary, J. P. (2011) Cognitive effects of cell-derived and synthetically derived Aβ oligomers. *Neurobiol. Aging*. **32**, 1784–94

171. Cleary, J. P., Walsh, D. M., Hofmeister, J. J., Shankar, G. M., Kuskowski, M. a, Selkoe, D. J., and Ashe, K. H. (2005) Natural oligomers of the amyloid-beta protein specifically disrupt cognitive function. *Nat. Neurosci.* **8**, 79–84

172. Hartley, D. M., Zhao, C., Speier, A. C., Woodard, G. a, Li, S., Li, Z., and Walz, T. (2008) Transglutaminase induces protofibril-like amyloid beta-protein assemblies that are protease-resistant and inhibit long-term potentiation. *J. Biol. Chem.* **283**, 16790–800

173. Kayed, R., Pensalfini, A., Margol, L., Sokolov, Y., Sarsoza, F., Head, E., Hall, J., and Glabe, C. (2009) Annular protofibrils are a structurally and functionally distinct type of amyloid oligomer. *J. Biol. Chem.* **284**, 4230–7

174. Nussbaum, J. M., Schilling, S., Cynis, H., Silva, A., Swanson, E., Wangsanut, T., Tayler, K., Wiltgen, B., Hatami, A., Rönicke, R., Reymann, K., Hutter-Paier, B., Alexandru, A., Jagla, W., Graubner, S., Glabe, C. G., Demuth, H.-U., and Bloom, G. S. (2012) Prion-like behaviour and tau-dependent cytotoxicity of pyroglutamylated amyloid-β. *Nature*. **485**, 651–5

175. Necula, M., Kayed, R., Milton, S., and Glabe, C. G. (2007) Small molecule inhibitors of aggregation indicate that amyloid beta oligomerization and fibrillization pathways are independent and distinct. *J. Biol. Chem.* **282**, 10311–24

176. Lasagna-Reeves, C. a, Glabe, C. G., and Kayed, R. (2011) Amyloid-β annular protofibrils evade fibrillar fate in Alzheimer disease brain. *J. Biol. Chem.* **286**, 22122–30

177. Lasagna-Reeves, C. a, and Kayed, R. (2011) Astrocytes contain amyloid-β annular protofibrils in Alzheimer's disease brains. *FEBS Lett.* **585**, 3052–7

178. Chávez-Gutiérrez, L., Bammens, L., Benilova, I., Vandersteen, A., Benurwar, M., Borgers, M., Lismont, S., Zhou, L., Van Cleynenbreugel, S., Esselmann, H., Wiltfang, J., Serneels, L., Karran, E., Gijsen, H., Schymkowitz, J., Rousseau, F., Broersen, K., and De Strooper, B. (2012) The mechanism of γ-Secretase dysfunction in familial Alzheimer disease. *EMBO J.* **31**, 2261–74

179. Walsh, D. M., Hartley, D., Kusumoto, Y., Fexoui, Y., Condron, M., Lomakin, A., Benedek, G., Selkow, D., and Teplow, D. (1999) Amyloid β-protein

fibrillogenesis:Stucture and biological activity of protofibrillar intermediates. *J. Biol. Chem.* **274**, 25945–25952

180. Conway, K. a, Harper, J. D., and Lansbury, P. T. (1998) Accelerated in vitro fibril formation by a mutant alpha-synuclein linked to early-onset Parkinson disease. *Nat. Med.* **4**, 1318–20

181. Conway, K. A., Lee, S., Rochet, J., Ding, T. T., Williamson, R. E., and Lansbury, P. T. (2000) Acceleration of oligomerization , not fibrillization , is a shared property of both alpha-synuclein mutations linked to early-onset Parkinson's disease: Implications for pathogenesis and therapy. *Proc. Natl. Acad. Sci. U. S. A.* **97**, 571–576

182. Caughey, B., and Lansbury, P. T. (2003) Protofibrils, pores, fibrils, and neurodegeneration: separating the responsible protein aggregates from the innocent bystanders. *Annu. Rev. Neurosci.* **26**, 267–98

183. Karpinar, D. P., Balija, M. B. G., Kügler, S., Opazo, F., Rezaei-Ghaleh, N., Wender, N., Kim, H.-Y., Taschenberger, G., Falkenburger, B. H., Heise, H., Kumar, A., Riedel, D., Fichtner, L., Voigt, A., Braus, G. H., Giller, K., Becker, S., Herzig, A., Baldus, M., Jäckle, H., Eimer, S., Schulz, J. B., Griesinger, C., and Zweckstetter, M. (2009) Pre-fibrillar alpha-synuclein variants with impaired beta-structure increase neurotoxicity in Parkinson's disease models. *EMBO J.* **28**, 3256–68

184. Winner, B., Jappelli, R., Maji, S. K., Desplats, P. A., Boyer, L., and Aigner, S. (2011) In vivo demonstration that α -synuclein oligomers are toxic. *Proc. Natl. Acad. Sci. U. S. A.* **108**, 4194–4199

185. Danzer, K. M., Haasen, D., Karow, A. R., Moussaud, S., Habeck, M., Giese, A., Kretzschmar, H., Hengerer, B., and Kostka, M. (2007) Different species of alpha-synuclein oligomers induce calcium influx and seeding. *J. Neurosci.* **27**, 9220–32

186. Tsigelny, I. F., Crews, L., Desplats, P., Shaked, G. M., Sharikov, Y., Mizuno, H., Spencer, B., Rockenstein, E., Trejo, M., Platoshyn, O., Yuan, J. X.-J., and Masliah, E. (2008) Mechanisms of hybrid oligomer formation in the pathogenesis of combined Alzheimer's and Parkinson's diseases. *PLoS One*. **3**, e3135

187. Lorenzen, N., Nielsen, S. B., Buell, A. K., Kaspersen, J. D., Arosio, P., Vad, B. S., Paslawski, W., Christiansen, G., Valnickova-Hansen, Z., Andreasen, M., Enghild, J. J., Pedersen, J. S., Dobson, C. M., Knowles, T. P. J., and Otzen, D. E. (2014) The role of stable α-synuclein oligomers in the molecular events underlying amyloid formation. *J. Am. Chem. Soc.* **136**, 3859–3868

188. Cremades, N., Cohen, S. I. a, Deas, E., Abramov, A. Y., Chen, A. Y., Orte, A., Sandal, M., Clarke, R. W., Dunne, P., Aprile, F. a, Bertoncini, C. W., Wood, N. W., Knowles, T. P. J., Dobson, C. M., and Klenerman, D. (2012) Direct observation of the interconversion of normal and toxic forms of α-synuclein. *Cell*. **149**, 1048–1059

189. Valko, M., Leibfritz, D., Moncol, J., Cronin, M. T. D., Mazur, M., and Telser, J. (2007) Free radicals and antioxidants in normal physiological functions and human disease. *Int. J. Biochem. Cell Biol.* **39**, 44–84

190. Campioni, S., Mannini, B., Zampagni, M., Pensalfini, A., Parrini, C., Evangelisti, E., Relini, A., Stefani, M., Dobson, C. M., Cecchi, C., and Chiti, F. (2010) A causative link between the structure of aberrant protein oligomers and their toxicity. *Nat. Chem. Biol.* **6**, 140–7

191. Kinnunen, P. K. J. (2009) Amyloid formation on lipid membrane surfaces. *Open Biol. J.* **2**, 163–175

192. Relini, A., Marano, N., and Gliozzi, A. (2013) Misfolding of amyloidogenic proteins and their interactions with membranes. *Biomolecules*. **4**, 20–55

193. Gorbenko, G. P., and Kinnunen, P. K. J. (2006) The role of lipid-protein interactions in amyloid-type protein fibril formation. *Chem. Phys. Lipids*. **141**, 72–82

194. Nicoll, A. J., Panico, S., Freir, D. B., Wright, D., Terry, C., Risse, E., Herron, C. E., O'Malley, T., Wadsworth, J. D. F., Farrow, M. a, Walsh, D. M., Saibil, H. R., and Collinge, J. (2013) Amyloid-β nanotubes are associated with prion protein-dependent synaptotoxicity. *Nat. Commun.* **4**, 2416

195. Walsh, D. M., Lomakin, A., Benedek, G. B., Condron, M. M., and Teplow, D. B. (1997) Amyloid-β protein fibrillogenesis: detection of a protofibrillar intermediate. *J. Biol. Chem.* **272**, 22364–22372

196. Last, N. B., and Miranker, A. D. (2013) Common mechanism unites membrane poration by amyloid and antimicrobial peptides. *Proc. Natl. Acad. Sci. U. S. A.* **110**, 6382–6387

197. Cao, P., Abedini, A., Wang, H., Tu, L.-H., Zhang, X., Schmidt, A. M., and Raleigh, D. P. (2013) Islet amyloid polypeptide toxicity and membrane interactions. *Proc. Natl. Acad. Sci. U. S. A.* **110**, 19279–84

198. Quist, A., Doudevski, I., Lin, H., Azimova, R., Ng, D., Frangione, B., Kagan, B., Ghiso, J., and Lal, R. (2005) Amyloid ion channels: a common structural link for protein-misfolding disease. *Proc. Natl. Acad. Sci. U. S. A.* **102**, 10427–32

199. Demuro, A., Smith, M., and Parker, I. (2011) Single-channel Ca(2+) imaging implicates Aβ1-42 amyloid pores in Alzheimer's disease pathology. *J. Cell Biol.* **195**, 515–24

200. Demuro, A., Mina, E., Kayed, R., Milton, S. C., Parker, I., and Glabe, C. G. (2005) Calcium dysregulation and membrane disruption as a ubiquitous neurotoxic mechanism of soluble amyloid oligomers. *J. Biol. Chem.* **280**, 17294–300

201. Engel, M. F. M., Khemtémourian, L., Kleijer, C. C., Meeldijk, H. J. D., Jacobs, J., Verkleij, A. J., de Kruijff, B., Killian, J. A., and Höppener, J. W. M. (2008) Membrane damage by human islet amyloid polypeptide through fibril growth at the membrane. *Proc. Natl. Acad. Sci. U. S. A.* **105**, 6033–8

202. Engel, M. F. M. (2009) Membrane permeabilization by Islet Amyloid Polypeptide. *Chem. Phys. Lipids*. **160**, 1–10

203. Zhao, H., Tuominen, E. K. J., and Kinnunen, P. K. J. (2004) Formation of amyloid fibers triggered by phosphatidylserine-containing membranes. *Biochemistry*. **43**, 10302–7

204. Iyer, A., Petersen, N. O., Claessens, M. M. A. E., and Subramaniam, V. (2014) Amyloids of Alpha-Synuclein Affect the Structure and Dynamics of Supported Lipid Bilayers. *Biophys. J.* **106**, 2585–2594

205. Last, N. B., Rhoades, E., and Miranker, A. D. (2011) Islet amyloid polypeptide demonstrates a persistent capacity to disrupt membrane integrity. *Proc. Natl. Acad. Sci. U. S. A.* **108**, 9460–5

206. Laganowsky, A., Liu, C., Sawaya, M. R., Whitelegge, J. P., Park, J., Zhao, M., Pensalfini, A., Soriaga, A. B., Landau, M., Teng, P. K., Cascio, D., Glabe, C., and Eisenberg, D. (2012) Atomic view of a toxic amyloid small oligomer. *Science*. **335**, 1228–31

207. Lee, C.-C., Sun, Y., and Huang, H. W. (2010) Membrane-mediated peptide conformation change from alpha-monomers to beta-aggregates. *Biophys. J.* **98**, 2236–45

208. Sun, Y., Lee, C.-C., Chen, T.-H., and Huang, H. W. (2010) Kinetic process of beta-amyloid formation via membrane binding. *Biophys. J.* **99**, 544–52

209. Sokolov, Y., Kozak, J. A., Kayed, R., Chanturiya, A., Glabe, C., and Hall, J. E. (2006) Soluble amyloid oligomers increase bilayer conductance by altering dielectric structure. *J. Gen. Physiol.* **128**, 637–47

210. Canale, C., Torrassa, S., Rispoli, P., Relini, A., Rolandi, R., Bucciantini, M., Stefani, M., and Gliozzi, A. (2006) Natively folded HypF-N and its early amyloid aggregates interact with phospholipid monolayers and destabilize supported phospholipid bilayers. *Biophys. J.* **91**, 4575–88

211. Freir, D. B., Nicoll, A. J., Klyubin, I., Panico, S., Mc Donald, J. M., Risse, E., Asante, E. a, Farrow, M. a, Sessions, R. B., Saibil, H. R., Clarke, A. R., Rowan, M. J., Walsh, D. M., and Collinge, J. (2011) Interaction between prion protein and toxic amyloid β assemblies can be therapeutically targeted at multiple sites. *Nat. Commun.* **2**, 336

212. Laurén, J., Gimbel, D. a, Nygaard, H. B., Gilbert, J. W., and Strittmatter, S. M. (2009) Cellular prion protein mediates impairment of synaptic plasticity by amyloid-beta oligomers. *Nature*. **457**, 1128–32

213. Narayan, P., Ganzinger, K. a, McColl, J., Weimann, L., Meehan, S., Qamar, S., Carver, J. a, Wilson, M. R., St George-Hyslop, P., Dobson, C. M., and Klenerman, D. (2013) Single molecule characterization of the interactions between amyloid-β peptides and the membranes of hippocampal cells. *J. Am. Chem. Soc.* **135**, 1491–8

214. Bucciantini, M., Nosi, D., Forzan, M., Russo, E., Calamai, M., Pieri, L., Formigli, L., Quercioli, F., Soria, S., Pavone, F., Savistchenko, J., Melki, R., and Stefani, M. (2012) Toxic effects of amyloid fibrils on cell membranes: the importance of ganglioside GM1. *FASEB J.* **26**, 818–31

215. Powers, E. T., and Powers, D. L. (2006) The kinetics of nucleated polymerizations at high concentrations: amyloid fibril formation near and above the "supercritical concentration". *Biophys. J.* **91**, 122–32

216. Münch, C., O'Brien, J., and Bertolotti, A. (2011) Prion-like propagation of mutant superoxide dismutase-1 misfolding in neuronal cells. *Proc. Natl. Acad. Sci. U. S. A.* **108**, 3548–53

217. Ren, P.-H., Lauckner, J. E., Kachirskaia, I., Heuser, J. E., Melki, R., and Kopito, R. R. (2009) Cytoplasmic penetration and persistent infection of mammalian cells by polyglutamine aggregates. *Nat. Cell Biol.* **11**, 219–25

218. Clavaguera, F., Bolmont, T., Crowther, R. A., Abramowski, D., Frank, S., Probst, A., Fraser, G., Stalder, A. K., Beibel, M., Staufenbiel, M., Jucker, M., Goedert, M., and Tolnay, M. (2009) Transmission and spreading of tauopathy in transgenic mouse brain. *Nat. Cell Biol.* **11**, 909–914

219. Frost, B., Jacks, R. L., and Diamond, M. I. (2009) Propagation of tau misfolding from the outside to the inside of a cell. *J. Biol. Chem.* **284**, 12845–52

220. Williams, T. L., Johnson, B. R. G., Urbanc, B., Jenkins, a T. a, Connell, S. D. a, and Serpell, L. C. (2011) Aβ42 oligomers, but not fibrils, simultaneously bind to and cause damage to ganglioside-containing lipid membranes. *Biochem. J.* **439**, 67–77

221. Olzscha, H., Schermann, S. M., Woerner, A. C., Pinkert, S., Hecht, M. H., Tartaglia, G. G., Vendruscolo, M., Hayer-Hartl, M., Hartl, F. U., and Vabulas, R. M. (2011) Amyloid-like aggregates sequester numerous metastable proteins with essential cellular functions. *Cell.* **144**, 67–78

222. Bennett, E. J., Shaler, T. a, Woodman, B., Ryu, K.-Y., Zaitseva, T. S., Becker, C. H., Bates, G. P., Schulman, H., and Kopito, R. R. (2007) Global changes to the ubiquitin system in Huntington's disease. *Nature*. **448**, 704–8

223. Kabashi, E., Agar, J. N., Taylor, D. M., Minotti, S., and Durham, H. D. (2004) Focal dysfunction of the proteasome: a pathogenic factor in a mouse model of amyotrophic lateral sclerosis. *J. Neurochem.* **89**, 1325–35

224. Boulevard, C., and Blanchard (1988) Ubiquitin is a common factor in intermediate filament inclusion bodies of diverse type in man, including those of Parkinson's disease, Pick's disease and Alzheimer's disease, as well as rosenthal fibries in cerebeller astrocytomas, cytoplasmic bodies in m. *J. Pathol.* **155**, 9–15

225. Park, S.-H., Kukushkin, Y., Gupta, R., Chen, T., Konagai, A., Hipp, M. S., Hayer-Hartl, M., and Hartl, F. U. (2013) PolyQ Proteins Interfere with Nuclear Degradation of Cytosolic Proteins by Sequestering the Sis1p Chaperone. *Cell.* **154**, 134–145

226. Yu, A., Shibata, Y., Shah, B., Calamini, B., Lo, D. C., and Morimoto, R. I. (2014) Protein aggregation can inhibit clathrin-mediated endocytosis by chaperone competition. *Proc. Natl. Acad. Sci. U. S. A.* **111**, E1481–90

227. Treusch, S., Hamamichi, S., Goodman, J. L., Matlack, K. E. S., Chung, C. Y., Baru, V., Shulman, J. M., Parrado, A., Bevis, B. J., Valastyan, J. S., Han, H., Lindhagen-Persson, M., Reiman, E. M., Evans, D. a, Bennett, D. a, Olofsson, A., DeJager, P. L.,

Tanzi, R. E., Caldwell, K. a, Caldwell, G. a, and Lindquist, S. (2011) Functional links between Aβ toxicity, endocytic trafficking, and Alzheimer's disease risk factors in yeast. *Science (80-.).* **334**, 1241–1245

228. Outeiro, T. F., and Lindquist, S. (2003) Yeast cells provide insight into alpha-synuclein biology and pathobiology. *Science*. **302**, 1772–5

229. Kuwahara, T., Koyama, A., Koyama, S., Yoshina, S., Ren, C.-H., Kato, T., Mitani, S., and Iwatsubo, T. (2008) A systematic RNAi screen reveals involvement of endocytic pathway in neuronal dysfunction in alpha-synuclein transgenic C. elegans. *Hum. Mol. Genet.* **17**, 2997–3009

230. Tardiff, D. F., Jui, N. T., Khurana, V., Tambe, M. a, Thompson, M. L., Chung, C. Y., Kamadurai, H. B., Kim, H. T., Lancaster, A. K., Caldwell, K. a, Caldwell, G. a, Rochet, J.-C., Buchwald, S. L., and Lindquist, S. (2013) Yeast reveal a "druggable" Rsp5/Nedd4 network that ameliorates α-synuclein toxicity in neurons. *Science*. **342**, 979–83

231. Chung, C. Y., Khurana, V., Auluck, P. K., Tardiff, D. F., Mazzulli, J. R., Soldner, F., Baru, V., Lou, Y., Freyzon, Y., Cho, S., Mungenast, A. E., Muffat, J., Mitalipova, M., Pluth, M. D., Jui, N. T., Schüle, B., Lippard, S. J., Tsai, L.-H., Krainc, D., Buchwald, S. L., Jaenisch, R., and Lindquist, S. (2013) Identification and rescue of α-synuclein toxicity in Parkinson patient-derived neurons. *Science*. **342**, 983–7

232. Matlack, K. E. S., Tardiff, D. F., Narayan, P., Hamamichi, S., Caldwell, K. a, Caldwell, G. a, and Lindquist, S. (2014) Clioquinol promotes the degradation of metal-dependent amyloid-β (Aβ) oligomers to restore endocytosis and ameliorate Aβ toxicity. *Proc. Natl. Acad. Sci. U. S. A.* **111**, 4013–4018

233. Moreno, J. a, Radford, H., Peretti, D., Steinert, J. R., Verity, N., Martin, M. G., Halliday, M., Morgan, J., Dinsdale, D., Ortori, C., Barrett, D., Tsaytler, P., Bertolotti, A., Willis, A. E., Bushell, M., and Mallucci, G. R. (2012) Sustained translational repression by eIF2α-P mediates prion neurodegeneration. *Nature*. **485**, 507–11

234. Kim, H.-J., Raphael, A. R., Ladow, E. S., McGurk, L., Weber, R. a, Trojanowski, J. Q., Lee, V. M.-Y., Finkbeiner, S., Gitler, A. D., and Bonini, N. M. (2013) Therapeutic modulation of eIF2α phosphorylation rescues TDP-43 toxicity in amyotrophic lateral sclerosis disease models. *Nat. Genet.* **46**, 152–160

235. Leitman, J., Barak, B., Benyair, R., Shenkman, M., Ashery, U., Hartl, F. U., and Lederkremer, G. Z. (2014) ER stress-induced eIF2-alpha phosphorylation underlies sensitivity of striatal neurons to pathogenic huntingtin. *PLoS One*. **9**, e90803

236. Pemberton, S., Madiona, K., Pieri, L., Kabani, M., Bousset, L., and Melki, R. (2011) Hsc70 protein interaction with soluble and fibrillar alpha-synuclein. *J. Biol. Chem.* **286**, 34690–34699

237. Narayan, P., Meehan, S., Carver, J. a, Wilson, M. R., Dobson, C. M., and Klenerman, D. (2012) Amyloid-β oligomers are sequestered by both intracellular and extracellular chaperones. *Biochemistry*. **51**, 9270–6

238. Narayan, P., Orte, A., Clarke, R. W., Bolognesi, B., Hook, S., Ganzinger, K. a, Meehan, S., Wilson, M. R., Dobson, C. M., and Klenerman, D. (2012) The

extracellular chaperone clusterin sequesters oligomeric forms of the amyloid-β(1-40) peptide. *Nat. Struct. Mol. Biol.* **19**, 79–83

239. Muchowski, P. J., Schaffar, G., Sittler, a, Wanker, E. E., Hayer-Hartl, M. K., and Hartl, F. U. (2000) Hsp70 and hsp40 chaperones can inhibit self-assembly of polyglutamine proteins into amyloid-like fibrils. *Proc. Natl. Acad. Sci. U. S. A.* **97**, 7841–6

240. McGlinchey, R. P., Jiang, Z., and Lee, J. C. (2014) Molecular Origin of pH-Dependent Fibril Formation of a Functional Amyloid. *Chembiochem*. **20892**, 1–5

241. Petrovska, I., Nüske, E., Munder, M. C., Kulasegaran, G., Malinovska, L., Kroschwald, S., Richter, D., Fahmy, K., Gibson, K., Verbavatz, J.-M., and Alberti, S. (2014) Filament formation by metabolic enzymes is a specific adaptation to an advanced state of cellular starvation. *Elife*. **3**, e02409

242. Carulla, N., Caddy, G. L., Hall, D. R., Zurdo, J., Gairí, M., Feliz, M., Giralt, E., Robinson, C. V, and Dobson, C. M. (2005) Molecular recycling within amyloid fibrils. *Nature*. **436**, 554–558

243. Sánchez, L., Madurga, S., Pukala, T., Vilaseca, M., López-Iglesias, C., Robinson, C. V, Giralt, E., and Carulla, N. (2011) Aβ40 and Aβ42 amyloid fibrils exhibit distinct molecular recycling properties. *J. Am. Chem. Soc.* **133**, 6505–8

244. Soura, V., Stewart-Parker, M., Williams, T. L., Ratnayaka, A., Atherton, J., Gorringe, K., Tuffin, J., Darwent, E., Rambaran, R., Klein, W., Lacor, P., Staras, K., Thorpe, J., and Serpell, L. C. (2012) Visualization of co-localization in Aβ42-administered neuroblastoma cells reveals lysosome damage and autophagosome accumulation related to cell death. *Biochem. J.* **441**, 579–90

245. Xue, W.-F., Hellewell, A. L., Gosal, W. S., Homans, S. W., Hewitt, E. W., and Radford, S. E. (2009) Fibril fragmentation enhances amyloid cytotoxicity. *J. Biol. Chem.* **284**, 34272–34282

246. Clavaguera, F., Lavenir, I., Falcon, B., Frank, S., Goedert, M., and Tolnay, M. (2013) "Prion-like" templated misfolding in tauopathies. *Brain Pathol.* **23**, 342–9

247. Pieri, L., Madiona, K., Bousset, L., and Melki, R. (2012) Fibrillar α-synuclein and huntingtin exon 1 assemblies are toxic to the cells. *Biophys. J.* **102**, 2894–2905

248. Orrenius, S., Zhivotovsky, B., and Nicotera, P. (2003) Regulation of cell death: the calcium-apoptosis link. *Nat. Rev. Mol. Cell Biol.* **4**, 552–65

249. Martins, I. C., Kuperstein, I., Wilkinson, H., Maes, E., Vanbrabant, M., Jonckheere, W., Van Gelder, P., Hartmann, D., D'Hooge, R., De Strooper, B., Schymkowitz, J., and Rousseau, F. (2008) Lipids revert inert Abeta amyloid fibrils to neurotoxic protofibrils that affect learning in mice. *EMBO J.* **27**, 224–233

250. Balch, W. E., Morimoto, R. I., Dillin, A., and Kelly, J. W. (2008) Adapting proteostasis for disease intervention. *Science*. **319**, 916–9

251. Coelho, T. (1996) Familial amyloid polyneuropathy: New developments in genetics and treatment. *Curr. Opin. Neurol.* **9**, 355–359

252. Monaco, H., Rizzi, M., and Coda, A. (1995) Structure of a complex of two plasma proteins: transthyretin and retinol binding protein. *Science*. **268**, 1039–1041

253. Colon, W., and Kelly, J. W. (1992) Partial denaturation of transthyretin is sufficient for amyloid fibril formation in vitro. *Biochemistry*. **31**, 8654–60

254. Lai, Z., Colón, W., and Kelly, J. W. (1996) The acid-mediated denaturation pathway of transthyretin yields a conformational intermediate that can self-assemble into amyloid. *Biochemistry*. **35**, 6470–82

255. Johnson, S. M., Connelly, S., Fearns, C., Powers, E. T., and Kelly, J. W. (2012) The transthyretin amyloidoses: from delineating the molecular mechanism of aggregation linked to pathology to a regulatory-agency-approved drug. *J. Mol. Biol.* **421**, 185–203

256. Saraiva, M. (1995) Transthyretin mutations in health and disease. *Hum. Mutat.* **5**, 191–196

257. Sekijima, Y., Wiseman, R. L., Matteson, J., Hammarström, P., Miller, S. R., Sawkar, A. R., Balch, W. E., and Kelly, J. W. (2005) The biological and chemical basis for tissue-selective amyloid disease. *Cell*. **121**, 73–85

258. Hurshman Babbes, A. R., Powers, E. T., and Kelly, J. W. (2008) Quantification of the thermodynamically linked quaternary and tertiary structural stabilities of transthyretin and its disease-associated variants: the relationship between stability and amyloidosis. *Biochemistry*. **47**, 6969–84

259. Jiang, X., Buxbaum, J. N., and Kelly, J. W. (2001) The V122I cardiomyopathy variant of transthyretin increases the velocity of rate-limiting tetramer dissociation, resulting in accelerated amyloidosis. *Proc. Natl. Acad. Sci. U. S. A.* **98**, 14943–8

260. Coelho, T., Carvalho, M., Saraiva, M., Alves, I., Almeida, M., and Costa, P. (1993) A strikingly benign evolution of FAP in an individual found to be a compound heterozygote for two TTR mutations: TTR Met-30 and TTR Met-119. *J. Rheumatol.* **20**, 179

261. Coelho, T., Chorao, R., Sausa, A., Alves, I., Torres, M., and Saraiva, M. (1996) Compound heterozygotes of transthyretin Met30 and transthyretin M119 are protected from the devastating effects of familial amyloid polyneuropathy. *Neurosmucular Disord.* **6**, 27

262. Hammarström, P., Wiseman, R. L., Powers, E. T., and Kelly, J. W. (2003) Prevention of transthyretin amyloid disease by changing protein misfolding energetics. *Science*. **299**, 713–6

263. Razavi, H., Palaninathan, S. K., Powers, E. T., Wiseman, R. L., Purkey, H. E., Mohamedmohaideen, N. N., Deechongkit, S., Chiang, K. P., Dendle, M. T. a, Sacchettini, J. C., and Kelly, J. W. (2003) Benzoxazoles as transthyretin amyloid fibril inhibitors: synthesis, evaluation, and mechanism of action. *Angew. Chem. Int. Ed. Engl.* **42**, 2758–61

264. Purkey, H. E., Dorrell, M. I., and Kelly, J. W. (2001) Evaluating the binding selectivity of transthyretin amyloid fibril inhibitors in blood plasma. *Proc. Natl. Acad. Sci. U. S. A.* **98**, 5566–71

265. Sambamurti, K., Greig, N. H., Utsuki, T., Barnwell, E. L., Sharma, E., Mazell, C., Bhat, N. R., Kindy, M. S., Lahiri, D. K., and Pappolla, M. a (2011) Targets for AD treatment: conflicting messages from γ-secretase inhibitors. *J. Neurochem.* **117**, 359–74

266. Lemere, C. a, and Masliah, E. (2010) Can Alzheimer disease be prevented by amyloid-beta immunotherapy? *Nat. Rev. Neurol.* **6**, 108–19

267. Sehgal, N., Gupta, A., Valli, R. K., Joshi, S. D., Mills, J. T., Hamel, E., Khanna, P., Jain, S. C., Thakur, S. S., and Ravindranath, V. (2012) Withania somnifera reverses Alzheimer's disease pathology by enhancing low-density lipoprotein receptor-related protein in liver. *Proc. Natl. Acad. Sci. U. S. A.* **109**, 3510–3515

268. Cramer, P. E., Cirrito, J. R., Wesson, D. W., Lee, C. Y. D., Karlo, J. C., Zinn, A. E., Casali, B. T., Restivo, J. L., Goebel, W. D., James, M. J., Brunden, K. R., Wilson, D. a, and Landreth, G. E. (2012) ApoE-directed therapeutics rapidly clear β-amyloid and reverse deficits in AD mouse models. *Science*. **335**, 1503–6

269. Strittmatter, W. J., Saunders, a M., Schmechel, D., Pericak-Vance, M., Enghild, J., Salvesen, G. S., and Roses, a D. (1993) Apolipoprotein E: high-avidity binding to beta-amyloid and increased frequency of type 4 allele in late-onset familial Alzheimer disease. *Proc. Natl. Acad. Sci. U. S. A.* **90**, 1977–81

270. Veeraraghavalu, K., Zhang, C., Miller, S., Hefendehl, J. K., Rajapaksha, T. W., Ulrich, J., Jucker, M., Holtzman, D. M., Tanzi, R. E., Vassar, R., and Sisodia, S. S. (2013) Comment on "ApoE-directed therapeutics rapidly clear β-amyloid and reverse deficits in AD mouse models". *Science*. **340**, 924–f

271. Fitz, N. F., Cronican, A. a, Lefterov, I., and Koldamova, R. (2013) Comment on "ApoE-directed therapeutics rapidly clear β-amyloid and reverse deficits in AD mouse models". *Science*. **340**, 924–c

272. Price, A. R., Xu, G., Siemienski, Z. B., Smithson, L. a, Borchelt, D. R., Golde, T. E., and Felsenstein, K. M. (2013) Comment on "ApoE-directed therapeutics rapidly clear β-amyloid and reverse deficits in AD mouse models". *Science*. **340**, 924–d

273. Tesseur, I., Lo, A. C., Roberfroid, A., Dietvorst, S., Van Broeck, B., Borgers, M., Gijsen, H., Moechars, D., Mercken, M., Kemp, J., D'Hooge, R., and De Strooper, B. (2013) Comment on "ApoE-directed therapeutics rapidly clear β-amyloid and reverse deficits in AD mouse models". *Science*. **340**, 924–e

274. Fountaine, T. M., and Wade-martins, R. (2007) RNA Interference-Mediated Knockdown of a -Synuclein Protects Human Dopaminergic Neuroblastoma Cells From MPP + Toxicity and Reduces Dopamine Transport. *J. neuoscience Res.* **363**, 351–363

275. Benson, M., Smith, R., Hung, G., Kluve-Beckerman, B., Showalter, A., Sloop, K., and Monia, B. (2010) Suppression of choroid plexus transthyretin levels by antisense oligonucleotide treatment. *Amyloid*. **17**, 43–49

276. Ehrnhoefer, D. E., Duennwald, M., Markovic, P., Wacker, J. L., Engemann, S., Roark, M., Legleiter, J., Marsh, J. L., Thompson, L. M., Lindquist, S., Muchowski, P. J., and Wanker, E. E. (2006) Green tea (-)-epigallocatechin-gallate modulates early events in huntingtin misfolding and reduces toxicity in Huntington's disease models. *Hum. Mol. Genet.* **15**, 2743–51

277. Bieschke, J., Russ, J., Friedrich, R. P., Ehrnhoefer, D. E., Wobst, H., Neugebauer, K., and Wanker, E. E. (2010) EGCG remodels mature alpha-synuclein and amyloid-beta fibrils and reduces cellular toxicity. *Proc. Natl. Acad. Sci. U. S. A.* **107**, 7710–5

278. Ehrnhoefer, D. E., Bieschke, J., Boeddrich, A., Herbst, M., Masino, L., Lurz, R., Engemann, S., Pastore, A., and Wanker, E. E. (2008) EGCG redirects amyloidogenic polypeptides into unstructured, off-pathway oligomers. *Nat. Struct. Mol. Biol.* **15**, 558–66

279. Liu, F.-F., Dong, X.-Y., He, L., Middelberg, A. P. J., and Sun, Y. (2011) Molecular insight into conformational transition of amyloid β-peptide 42 inhibited by (-)-epigallocatechin-3-gallate probed by molecular simulations. *J. Phys. Chem. B.* **115**, 11879–87

280. Wu, C., Lei, H., Wang, Z., Zhang, W., and Duan, Y. (2006) Phenol red interacts with the protofibril-like oligomers of an amyloidogenic hexapeptide NFGAIL through both hydrophobic and aromatic contacts. *Biophys. J.* **91**, 3664–72

281. Arosio, P., Vendruscolo, M., Dobson, C. M., and Knowles, T. P. J. (2014) Chemical kinetics for drug discovery to combat protein aggregation diseases. *Trends Pharmacol. Sci.* **35**, 127–135

282. Tu, L.-H., Noor, H., Cao, P., and Raleigh, D. P. (2014) Aspirin, Diabetes, and Amyloid: Re-examination of the Inhibition of Amyloid Formation by Aspirin and Ketoprofen. *ACS Chem. Biol.* **9**, 1632–7

283. Cheng, B., Gong, H., Xiao, H., Petersen, R. B., Zheng, L., and Huang, K. (2013) Inhibiting toxic aggregation of amyloidogenic proteins: a therapeutic strategy for protein misfolding diseases. *Biochim. Biophys. Acta*. **1830**, 4860–71

284. Mason, J., Kokkoni, N., Stott, K., and Doig, A. (2003) Design strategies for anti-amyloid agents. *Curr. Opin. Struct. Biol.* **13**, 526–532

285. Landau, M., Sawaya, M. R., Faull, K. F., Laganowsky, A., Jiang, L., Sievers, S. A., Liu, J., Barrio, J. R., and Eisenberg, D. (2011) Towards a Pharmacophore for Amyloid. *PLoS Biol.* **9**, e1001080

286. Woods, L. a, Platt, G. W., Hellewell, A. L., Hewitt, E. W., Homans, S. W., Ashcroft, A. E., and Radford, S. E. (2011) Ligand binding to distinct states diverts aggregation of an amyloid-forming protein. *Nat. Chem. Biol.* **7**, 730–9

287. Abelein, A., Lang, L., Lendel, C., Gräslund, A., and Danielsson, J. (2012) Transient small molecule interactions kinetically modulate amyloid β peptide self-assembly. *FEBS Lett.* **586**, 3991–5

288. Porat, Y., Abramowitz, A., and Gazit, E. (2006) Inhibition of amyloid fibril formation by polyphenols: structural similarity and aromatic interactions as a common inhibition mechanism. *Chem. Biol. Drug Des.* **67**, 27–37

289. Härd, T., and Lendel, C. (2012) Inhibition of amyloid formation. *J. Mol. Biol.* **421**, 441–65

290. Bartolini, M., and Andrisano, V. (2010) Strategies for the inhibition of protein aggregation in human diseases. *Chembiochem.* **11**, 1018–35

291. Sievers, S. a, Karanicolas, J., Chang, H. W., Zhao, A., Jiang, L., Zirafi, O., Stevens, J. T., Münch, J., Baker, D., and Eisenberg, D. (2011) Structure-based design of non-natural amino-acid inhibitors of amyloid fibril formation. *Nature*. **475**, 96–100

292. Zhang, H., Xu, L.-Q., and Perrett, S. (2011) Studying the effects of chaperones on amyloid fibril formation. *Methods*. **53**, 285–94

293. Pul, R., Dodel, R., and Stangel, M. (2011) Antibody-based therapy in Alzheimer's disease. *Expert Opin. Biol. Ther.* **11**, 343–357

294. Weggen, S., Rogers, M., and Eriksen, J. (2007) NSAIDs: small molecules for prevention of Alzheimer's disease or precursors for future drug development? *Trends Pharmacol. Sci.* **28**, 536–43

295. Sharma, A. K., Pavlova, S. T., Kim, J., Finkelstein, D., Hawco, N. J., Rath, N. P., Kim, J., and Mirica, L. M. (2012) Bifunctional compounds for controlling metal-mediated aggregation of the aβ42 peptide. *J. Am. Chem. Soc.* **134**, 6625–36

296. Forloni, G., Colombo, L., Girola, L., Tagliavini, F., and Salmona, M. (2001) Anti-amyloidogenic activity of tetracyclines: studies in vitro. *FEBS Lett.* **487**, 404–7

297. Yoo, S. Il, Yang, M., Brender, J. R., Subramanian, V., Sun, K., Joo, N. E., Jeong, S.-H., Ramamoorthy, A., and Kotov, N. a (2011) Inhibition of amyloid peptide fibrillation by inorganic nanoparticles: functional similarities with proteins. *Angew. Chem. Int. Ed. Engl.* **50**, 5110–5

298. Cohen, F. E., and Kelly, J. W. (2003) Therapeutic approaches to protein-misfolding diseases. *Nature*. **426**, 905–9

299. Cheng, P.-N., Liu, C., Zhao, M., Eisenberg, D., and Nowick, J. S. (2012) Amyloid β-sheet mimics that antagonize protein aggregation and reduce amyloid toxicity. *Nat. Chem.* **4**, 927–33

300. Zheng, J., Liu, C., Sawaya, M. R., Vadla, B., Woods, R. J., Eisenberg, D., Goux, W. J., and Nowick, J. S. (2011) Macrocyclic β-sheet peptides that inhibit the aggregation of a tau-derived hexapeptide. *J. Am. Chem. Soc.* **133**, 3144–3157

301. Spencer, R. K., Li, H., and Nowick, J. S. (2014) X-ray Crystallographic Structures of Trimers and Higher-Order Oligomeric Assemblies of a Peptide Derived from Aβ17-36. *J. Am. Chem. Soc.* 10.1021/ja5017409

302. Liu, C., Sawaya, M. R., Cheng, P.-N., Zheng, J., Nowick, J. S., and Eisenberg, D. (2011) Characteristics of amyloid-related oligomers revealed by crystal structures of macrocyclic β-sheet mimics. *J. Am. Chem. Soc.* **133**, 6736–44

303. Pham, J. D., Chim, N., Goulding, C. W., and Nowick, J. S. (2013) Structures of oligomers of a peptide from β-amyloid. *J. Am. Chem. Soc.* **135**, 12460–7

304. Giorgetti, S., Raimondi, S., Pagano, K., Relini, A., Bucciantini, M., Corazza, A., Fogolari, F., Codutti, L., Salmona, M., Mangione, P., Colombo, L., De Luigi, A., Porcari, R., Gliozzi, A., Stefani, M., Esposito, G., Bellotti, V., and Stoppini, M. (2011) Effect of tetracyclines on the dynamics of formation and destructuration of beta2-microglobulin amyloid fibrils. *J. Biol. Chem.* **286**, 2121–31

305. Palhano, F. L., Lee, J., Grimster, N. P., and Kelly, J. W. (2013) Toward the molecular mechanism(s) by which EGCG treatment remodels mature amyloid fibrils. *J. Am. Chem. Soc.* **135**, 7503–10

306. Woods, L. A., Radford, S. E., and Ashcroft, A. E. (2013) Advances in ion mobility spectrometry-mass spectrometry reveal key insights into amyloid assembly. *Biochim. Biophys. Acta*. **1834**, 1257–68

307. Bleiholder, C., Do, T. D., Wu, C., Economou, N. J., Bernstein, S. S., Buratto, S. K., Shea, J.-E., and Bowers, M. T. (2013) Ion mobility spectrometry reveals the mechanism of amyloid formation of Aβ(25-35) and its modulation by inhibitors at the molecular level: epigallocatechin gallate and scyllo-inositol. *J. Am. Chem. Soc.* **135**, 16926–37

308. Young, L. M., Cao, P., Raleigh, D. P., Ashcroft, A. E., and Radford, S. E. (2014) Ion mobility spectrometry-mass spectrometry defines the oligomeric intermediates in amylin amyloid formation and the mode of action of inhibitors. *J. Am. Chem. Soc.* **136**, 660–70

309. Cheng, B., Gong, H., Li, X., Sun, Y., Zhang, X., Chen, H., Liu, X., Zheng, L., and Huang, K. (2012) Silibinin inhibits the toxic aggregation of human islet amyloid polypeptide. *Biochem. Biophys. Res. Commun.* **419**, 495–9

310. Powers, E. T., Morimoto, R. I., Dillin, A., Kelly, J. W., and Balch, W. E. (2009) Biological and chemical approaches to diseases of proteostasis deficiency. *Annu. Rev. Biochem.* **78**, 959–91

311. Moreno, J., Halliday, M., Molloy, C., Radford, H., Verity, N., Axten, J. M., Ortori, C., Willis, A. E., Fischer, P. M., Barrett, D., and Mallucci, G. R. (2013) Oral treatment targeting the unfolded protein response prevents neurodegeneration and clinical disease in prion-infected mice. *Sci. Transl. Med.* **5**, 206ra138

312. Salloway, S., Sperling, R., Fox, N. C., Blennow, K., Klunk, W., Raskind, M., Sabbagh, M., Honig, L. S., Porsteinsson, A. P., Ferris, S., Reichert, M., Ketter, N., Nejadnik, B., Guenzler, V., Miloslavsky, M., Wang, D., Lu, Y., Lull, J., Tudor, I. C., Liu, E., Grundman, M., Yuen, E., Black, R., and Brashear, H. R. (2014) Two phase 3 trials of bapineuzumab in mild-to-moderate Alzheimer's disease. *N. Engl. J. Med.* **370**, 322–33

313. Becker, J. W., and Reeke, G. N. (1985) Three-dimensional structure of beta 2-microglobulin. *Proc. Natl. Acad. Sci. U. S. A.* **82**, 4225–9

314. Cunningham, J. (1976) Structure and significane of beta-2-microglobulin. *Fed. Proc.* **35**, 1171–1176

315. Isenman, D. E., Painter, R. H., and Dorrington, K. J. (1975) The structure and function of immunoglobulin domains: studies with beta-2-microglobulin on the role of the intrachain disulfide bond. *Proc. Natl. Acad. Sci. U. S. A.* **72**, 548–52

316. Hill, D. M., Kasliwal, T., Schwarz, E., Hebert, A. M., Chen, T., Gubina, E., Zhang, L., and Kozlowski, S. (2003) A dominant negative mutant beta 2-microglobulin blocks the extracellular folding of a major histocompatibility complex class I heavy chain. *J. Biol. Chem.* **278**, 5630–8

317. Bjorkman, P., Saper, M., and Samraoui, B. (1987) Structure of the human class I histocompatibility antigen HLA-A2. *Nature*. **329**, 506–512

318. Sundin, D., Cohen, M., Dahl, R., Falk, S., and Molitoris, B. (1994) Characterisation of the beta-2-microglobulin endocytic pathway in rat proximal tubule cells. *Am. J. Physiol.* **267**, F380–F389

319. Floege, J., and Ehlerding, G. (1996) Beta-2-microglobulin-associated amyloidosis. *Nephron*. **72**, 9–26

320. Koch, K. (1992) Dialysis-related amyloidosis. *Kidney Int.* **41**, 1416–1429

321. Miyata, T., Jadoul, M., Kurokawa, K., and Van Ypersele De Strihou, C. (1998) Beta-2-Microglobulin Renal Disease. *J Am Soc Nephrol*. **9**, 1723–1735

322. Bardin, T., and KuntzD (1987) The arthropy of chronic hemodialysis. *Clin. Exp. Rheumatol.* **5**, 379–386

323. Ferreira, A., Urefia, P., Ang, K. S., Simon, P., Morieux, C., and Souberbielle, J. (1995) Nephrology Dialysis Transplantation. *Nephrol Dial Transpl.* **10**, 1701–1707

324. Homma, M., F, G., M, I., and Arakawa, M. (1989) Collagen binding affinity of beta-2-microglobulin, a preprotein of haemadialysis-associated amyloidosis. *Nephron*. **53**, 37–40

325. Giorgetti, S., Rossi, A., Mangione, P., Raimondi, S., Marini, S., Stoppini, M., Corazza, A., Viglino, P., Esposito, G., Cetta, G., Merlini, G., and Bellotti, V. (2005) Beta-2-Microglobulin isoforms display an heterogeneous affinity for type I collagen. *Protein Sci.* **14**, 696–702

326. Campistol, J., Sole, M., Bombi, J., Rodriguez, R., Mirapeix, E., Munoz-Gomez, J., and Revert, O. (1992) In vitro spontaneous synthesis of beta-2-microglobulin amyloid fibrils in peripheral blood mononuclear cell culture. *Am. J. Pathol.* **141**, 241–247

327. Connors, L., Shirahama, T., Skinner, M., Fenves, A., and Cohen, A. (1985) In vitro formation of amyloid fibrils from intact beta-2-microglobulin. *Biochem. Biophys. Res. Commun.* **131**, 1063–1068

328. Linke, R. P., Hampl, H., Lobeck, H., Ritz, E., Bommer, J., Waldherr, R., and Eulitz, M. (1989) Lysine-specific cleavage of beta 2-microglobulin in amyloid deposits associated with hemodialysis. *Kidney Int.* **36**, 675–81

329. Esposito, G., Michelutti, R., Verdone, P., Viglino, P., Hernandez, H., Robinson, C. V, Amoresano, A., Dal Piaz, F., Monti, M., Pucci, P., Mangione, P., Stoppini, M., Merlini, G., Ferri, G., and Bellotti, V. (2000) Removal of the N-terminal hexapeptide from human β2-microglobulin facilitates protein aggregation and fibril formation. *Protein Sci.* **9**, 831–845

330. Mcparland, V. J., Kad, N. M., Kalverda, A. P., Brown, A., Kirwin-jones, P., Hunter, M. G., Sunde, M., and Radford, S. E. (2000) Partially Unfolded States of Beta-2-microglobulin and Amyloid Formation in Vitro. *Biochemistry*. **39**, 8735–8746

331. Eichner, T., and Radford, S. E. (2009) A Generic Mechanism of β2-Microglobulin Amyloid Assembly at Neutral pH Involving a Specific Proline Switch. *J. Mol. Biol.* **386**, 1312–1326

332. Karamanos, T. K., Kalverda, A. P., Thompson, G. S., and Radford, S. E. (2014) Visualization of transient protein-protein interactions that promote or inhibit amyloid assembly. *Mol. Cell*. **55**, 214–226

333. Jones, S., Smith, D. P., and Radford, S. E. (2003) Role of the N and C-terminal Strands of Beta 2-Microglobulin in Amyloid Formation at Neutral pH. *J. Mol. Biol.* **330**, 935–941

334. Morgan, C. J., Gelfand, M., Atreya, C., and Miranker, a D. (2001) Kidney dialysis-associated amyloidosis: a molecular role for copper in fiber formation. *J. Mol. Biol.* **309**, 339–45

335. Yamamoto, S., Yamaguch, I., Hasegawa, K., Tsutsumi, S., Goto, Y., Gejyo, F., and Naiki, H. (2004) Glycosaminoglycans Enhance the Trifluoroethanol-Induced Extension of 2-Microglobulin-Related Amyloid Fibrils at a Neutral pH. *J. Am. Soc. Nephrol.* **15**, 126–133

336. Mcparland, V. J., Kad, N. M., Kalverda, A. P., Brown, A., Kirwin-jones, P., Hunter, M. G., Sunde, M., and Radford, S. E. (2000) Partially Unfolded States of and Amyloid Formation in Vitro †. *Biochemistry*. **39**, 8735–8746

337. Smith, D. P., Jones, S., Serpell, L. C., Sunde, M., and Radford, S. E. (2003) A Systematic Investigation into the Effect of Protein Destabilisation on Beta 2-Microglobulin Amyloid Formation. *J. Mol. Biol.* **330**, 943–954

338. Debelouchina, G. T., Platt, G. W., Bayro, M. J., Radford, S. E., and Griffin, R. G. (2010) Intermolecular Alignment in Amyloid Fibrils. *J. Am. Chem. Soc.* **132**, 17077–17079

339. Sarell, C. J., Woods, L. a, Su, Y., Debelouchina, G. T., Ashcroft, A. E., Griffin, R. G., Stockley, P. G., and Radford, S. E. (2013) Expanding the repertoire of amyloid polymorphs by co-polymerization of related protein precursors. *J. Biol. Chem.* **288**, 7327–37

340. Jakhria, T., Hellewell, A. L., Porter, M. Y., Jackson, M. P., Tipping, K. W., Xue, W.-F., Radford, S. E., and Hewitt, E. W. (2014) β2-microglobulin amyloid fibrils are nanoparticles that disrupt lysosomal membrane protein trafficking and inhibit protein degradation by lysosomes. *J. Biol. Chem.*

341. Goodchild, S. C., Sheynis, T., Thompson, R., Tipping, K. W., Xue, W.-F., Ranson, N. A., Beales, P. A., Hewitt, E. W., and Radford, S. E. (2014) β2-microglobulin amyloid fibril-induced membrane disruption is enhanced by endosomal lipids and acidic pH. *PLoS One*. **9**, e 104492

342. Sheynis, T., Friediger, A., Xue, W.-F., Hellewell, A. L., Tipping, K. W., Hewitt, E. W., Radford, S. E., and Jelinek, R. (2013) Aggregation modulators interfere with membrane interactions of β2-microglobulin fibrils. *Biophys. J.* **105**, 745–55

343. Koffie, R. M., Meyer-Luehmann, M., Hashimoto, T., Adams, K. W., Mielke, M. L., Garcia-Alloza, M., Micheva, K. D., Smith, S. J., Kim, M. L., Lee, V. M., Hyman, B. T., and Spires-Jones, T. L. (2009) Oligomeric amyloid beta associates with postsynaptic densities and correlates with excitatory synapse loss near senile plaques. *Proc. Natl. Acad. Sci. U. S. A.* **106**, 4012–7

344. Morel, B., Varela, L., and Conejero-Lara, F. (2010) The thermodynamic stability of amyloid fibrils studied by differential scanning calorimetry. *J. Phys. Chem. B.* **114**, 4010–9

345. Williams, A. D., Portelius, E., Kheterpal, I., Guo, J., Cook, K. D., Xu, Y., and Wetzel, R. (2004) Mapping Aβ Amyloid Fibril Secondary Structure Using Scanning Proline Mutagenesis. *J. Mol. Biol.* **335**, 833–842

346. Shammas, S. L., Knowles, T. P. J., Baldwin, A. J., Macphee, C. E., Welland, M. E., Dobson, C. M., and Devlin, G. L. (2011) Perturbation of the stability of amyloid fibrils through alteration of electrostatic interactions. *Biophys. J.* **100**, 2783–91

347. Xue, W., Hellewell, A. L., Hewitt, E. W., and Radford, S. E. (2010) When size matters. *Prion.* **4**, 20–25

348. Macia, E., Ehrlich, M., Massol, R., Boucrot, E., Brunner, C., and Kirchhausen, T. (2006) Dynasore, a cell-permeable inhibitor of dynamin. *Dev. Cell*. **10**, 839–50

349. Porter, M. Y., Routledge, K. E., Radford, S. E., and Hewitt, E. W. (2011) Characterization of the response of primary cells relevant to dialysis-related amyloidosis to β2-microglobulin monomer and fibrils. *PLoS One*. **6**, e27353

350. Berthelot, K., Cullin, C., and Lecomte, S. (2013) What does make an amyloid toxic: morphology, structure or interaction with membrane? *Biochimie*. **95**, 12–19

351. Freeman, D., Cedillos, R., Choyke, S., Lukic, Z., McGuire, K., Marvin, S., Burrage, A. M., Sudholt, S., Rana, A., O'Connor, C., Wiethoff, C. M., and Campbell, E. M. (2013) Alpha-synuclein induces lysosomal rupture and cathepsin dependent reactive oxygen species following endocytosis. *PLoS One*. **8**, e62143

352. Laganowsky, A., Liu, C., Sawaya, M. R., Whitelegge, J. P., Park, J., Zhao, M., Pensalfini, A., Soriaga, A. B., Landau, M., Teng, P. K., Cascio, D., Glabe, C., and

Eisenberg, D. (2012) Atomic view of a toxic amyloid small oligomer. *Science*. **335**, 1228–1231

353. Engel, M. F. M., vandenAkker, C. C., Schleeger, M., Velikov, K. P., Koenderink, G. H., and Bonn, M. (2012) The polyphenol EGCG inhibits amyloid formation less efficiently at phospholipid interfaces than in bulk solution. *J. Am. Chem. Soc.* **134**, 14781–8

354. Lee, J.-H., Hong, C.-S., Lee, S., Yang, J.-E., Park, Y. Il, Lee, D., Hyeon, T., Jung, S., and Paik, S. R. (2012) Radiating amyloid fibril formation on the surface of lipid membranes through unit-assembly of oligomeric species of α-synuclein. *PLoS One*. **7**, e47580

355. Sciacca, M. F. M., Brender, J. R., Lee, D.-K., and Ramamoorthy, A. (2012) Phosphatidylethanolamine enhances amyloid fiber-dependent membrane fragmentation. *Biochemistry*. **51**, 7676–84

356. Stefani, M. (2010) Biochemical and biophysical features of both oligomer/fibril and cell membrane in amyloid cytotoxicity. *FEBS J.* **277**, 4602–13

357. Uversky, V. N. (2010) Mysterious oligomerization of the amyloidogenic proteins. *FEBS J.* **277**, 2940–53

358. Milanesi, L., Sheynis, T., Xue, W.-F., Orlova, E. V, Hellewell, A. L., Jelinek, R., Hewitt, E. W., Radford, S. E., and Saibil, H. R. (2012) Direct three-dimensional visualization of membrane disruption by amyloid fibrils. *Proc. Natl. Acad. Sci. U. S. A.* **109**, 20455–20460

359. Gill, S., and Hippel, P. Von (1989) Calculation of protein extinction coefficients from amino acid sequence data. *Anal. Biochem.* **182**, 319–26

360. Xue, W.-F., Homans, S. W., and Radford, S. E. (2009) Amyloid fibril length distribution quantified by atomic force microscopy single-particle image analysis. *Protein Eng. Des. Sel.* **22**, 489–96

361. Schanda, P., Kupce, E., and Brutscher, B. (2005) SOFAST-HMQC experiments for recording two-dimensional heteronuclear correlation spectra of proteins within a few seconds. *J. Biomol. NMR*. **33**, 199–211

362. Janson, J., Ashley, R. H., Harrison, D., McIntyre, S., and Butler, P. C. (1999) The mechanism of islet amyloid polypeptide toxicity is membrane disruption by intermediate-sized toxic amyloid particles. *Diabetes*. **48**, 491–8

363. Lee, C.-C., Sun, Y., and Huang, H. W. (2012) How type II diabetes-related islet amyloid polypeptide damages lipid bilayers. *Biophys. J.* **102**, 1059–68

364. Kobayashi, T., Beuchat, M.-H., Chevallier, J., Makino, A., Mayran, N., Escola, J.-M., Lebrand, C., Cosson, P., Kobayashi, T., and Gruenberg, J. (2002) Separation and characterization of late endosomal membrane domains. *J. Biol. Chem.* **277**, 32157–32164

365. Kobayashi, T., Beuchat, M. H., Lindsay, M., Frias, S., Palmiter, R. D., Sakuraba, H., Parton, R. G., and Gruenberg, J. (1999) Late endosomal membranes rich in lysobisphosphatidic acid regulate cholesterol transport. *Nat. Cell Biol.* **1**, 113–118

366. Kobayashi, T., Stang, E., Fang, K. S., de Moerloose, P., Parton, R. G., and Gruenberg, J. (1998) A lipid associated with the antiphospholipid syndrome regulates endosome structure and function. *Nature*. **392**, 193–7

367. Martins, I. C., Kuperstein, I., Wilkinson, H., Maes, E., Vanbrabant, M., Jonckheere, W., Van Gelder, P., Hartmann, D., D'Hooge, R., De Strooper, B., Schymkowitz, J., and Rousseau, F. (2008) Lipids revert inert Abeta amyloid fibrils to neurotoxic protofibrils that affect learning in mice. *EMBO J.* **27**, 224–33

368. Wolfe, L. S., Calabrese, M. F., Nath, A., Blaho, D. V, Miranker, A. D., and Xiong, Y. (2010) Protein-induced photophysical changes to the amyloid indicator dye thioflavin T. *Proc. Natl. Acad. Sci. U. S. A.* **107**, 16863–16868

369. Park, S.-H., Kukushkin, Y., Gupta, R., Chen, T., Konagai, A., Hipp, M. S., Hayer-Hartl, M., and Hartl, F. U. (2013) PolyQ proteins interfere with nuclear degradation of cytosolic proteins by sequestering the Sis1p chaperone. *Cell*. **154**, 134–45

370. Fonte, V., Kapulkin, W. J., Taaft, A., Fluet, A., Friedman, D., and Link, C. D. (2002) Interaction of intracellular beta amyloid peptide with chaperone proteins. *Proc. Natl. Acad. Sci. U. S. A.* **99**, 9439–9444

371. Alavez, S., Vantipalli, M. C., Zucker, D. J. S., Klang, I. M., and Lithgow, G. J. (2011) Amyloid-binding compounds maintain protein homeostasis during ageing and extend lifespan. *Nature*. **472**, 226–9

372. Neef, D. W., Jaeger, A. M., and Thiele, D. J. (2011) Heat shock transcription factor 1 as a therapeutic target in neurodegenerative diseases. *Nat. Rev. Drug Discov.* **10**, 930–44

373. Warrick, J. M., Chan, H. Y., Gray-Board, G. L., Chai, Y., Paulson, H. L., and Bonini, N. M. (1999) Suppression of polyglutamine-mediated neurodegeneration in Drosophila by the molecular chaperone HSP70. *Nat. Genet.* **23**, 425–8

374. Auluck, P. K., and Bonini, N. M. (2002) Pharmacological prevention of Parkinson disease in Drosophila. *Nat. Med.* **8**, 1185–6

375. Cooley, C. B., Ryno, L. M., Plate, L., Morgan, G. J., Hulleman, J. D., Kelly, J. W., and Wiseman, R. L. (2014) Unfolded protein response activation reduces secretion and extracellular aggregation of amyloidogenic immunoglobulin light chain. *Proc. Natl. Acad. Sci. U. S. A.* **111**, 13046–13051

376. Huang, C., Cheng, H., Hao, S., Zhou, H., Zhang, X., Gao, J., Sun, Q.-H., Hu, H., and Wang, C.-C. (2006) Heat shock protein 70 inhibits alpha-synuclein fibril formation via interactions with diverse intermediates. *J. Mol. Biol.* **364**, 323–336

377. Chai, Y., Koppenhafer, S. L., Bonini, N. M., and Paulson, H. L. (1999) Analysis of the role of heat shock protein (Hsp) molecular chaperones in polyglutamine disease. *J. Neurosci.* **19**, 10338–47

378. Dedmon, M. M., Christodoulou, J., Wilson, M. R., and Dobson, C. M. (2005) Heat shock protein 70 inhibits alpha-synuclein fibril formation via preferential binding to prefibrillar species. *J. Biol. Chem.* **280**, 14733–40

379. Danzer, K. M., Ruf, W. P., Putcha, P., Joyner, D., Hashimoto, T., Glabe, C., Hyman, B. T., and McLean, P. J. (2011) Heat-shock protein 70 modulates toxic extracellular α-synuclein oligomers and rescues trans-synaptic toxicity. *FASEB J.* **25**, 326–336

380. Roodveldt, C., Bertoncini, C. W., Andersson, A., van der Goot, A. T., Hsu, S.-T., Fernández-Montesinos, R., de Jong, J., van Ham, T. J., Nollen, E. a, Pozo, D., Christodoulou, J., and Dobson, C. M. (2009) Chaperone proteostasis in Parkinson's disease: stabilization of the Hsp70/alpha-synuclein complex by Hip. *EMBO J.* **28**, 3758–3770

381. Wang, A. M., Miyata, Y., Klinedinst, S., Peng, H.-M., Chua, J. P., Komiyama, T., Li, X., Morishima, Y., Merry, D. E., Pratt, W. B., Osawa, Y., Collins, C. a, Gestwicki, J. E., and Lieberman, A. P. (2013) Activation of Hsp70 reduces neurotoxicity by promoting polyglutamine protein degradation. *Nat. Chem. Biol.* **9**, 112–118

382. Bleiholder, C., Dupuis, N. F., Wyttenbach, T., and Bowers, M. T. (2011) Ion mobility-mass spectrometry reveals a conformational conversion from random assembly to β-sheet in amyloid fibril formation. *Nat. Chem.* **3**, 172–7

383. Smith, D. P., Radford, S. E., and Ashcroft, A. E. (2010) Elongated oligomers in β2 -microglobulin amyloid assembly revealed by ion mobility spectrometry-mass spectrometry. *Proc. Natl. Acad. Sci. U. S. A.* **107**, 6794–6798

384. Smith, D. P., Knapman, T. W., Campuzano, I., Malham, R. W., Berryman, J. T., Radford, S. E., and Ashcroft, A. E. (2009) Deciphering drift time measurements from travelling wave ion mobility spectrometry-mass spectrometry studies. *Eur. J. mass Spectrom.* **15**, 113–30

385. Bernstein, S., Dupuis, N., and Lazo, N. (2009) Amyloid-β protein oligomerization and the importance of tetramers and dodecamers in the aetiology of Alzheimer's disease. *Nat. Chem.* **1**, 326 – 331

386. Hall, Z., and Robinson, C. V (2012) Do charge state signatures guarantee protein conformations? *J. Am. Soc. Mass Spectrom.* **23**, 1161–8

387. Smith, A. M., Jahn, T. R., Ashcroft, A. E., and Radford, S. E. (2006) Direct observation of oligomeric species formed in the early stages of amyloid fibril formation using electrospray ionisation mass spectrometry. *J. Mol. Biol.* **364**, 9–19

388. Xie, H., Hou, S., Jiang, J., Sekutowicz, M., Kelly, J., and Bacskai, B. J. (2013) Rapid cell death is preceded by amyloid plaque-mediated oxidative stress. *Proc. Natl. Acad. Sci. U. S. A.* **110**, 7904–9

389. Haustein, E., and Schwille, P. (2007) Fluorescence correlation spectroscopy: novel variations of an established technique. *Annu. Rev. Biophys. Biomol. Struct.* **36**, 151–169

390. Orte, A., Clarke, R., Balasubramanian, S., and Klenerman, D. (2006) Determination of the fraction and stoichiometry of femtomolar levels of biomolecular complexes in

an excess of monomer using single-molecule, two-color coincidence detection. *Anal. Chem.* **78**, 7707–15

391. Orte, A., Clarke, R., and Klenerman, D. (2010) Single-molecule two-colour coincidence detection to probe biomolecular associations. *Biochem. Soc. Trans.* **38**, 914–8

392. Orte, A., Birkett, N. R., Clarke, R. W., Devlin, G. L., Dobson, C. M., and Klenerman, D. (2008) Direct characterization of amyloidogenic oligomers by single-molecule fluorescence. *Proc. Natl. Acad. Sci. U. S. A.* **105**, 14424–9

393. Eigen, M., and Rigler, R. (1994) Sorting single molecules: application to diagnostics and evolutionary biotechnology. *Proc. Natl. Acad. Sci. U. S. A.* **91**, 5740–7

394. Schwille, P., Meyer-Almes, F. J., and Rigler, R. (1997) Dual-color fluorescence cross-correlation spectroscopy for multicomponent diffusional analysis in solution. *Biophys. J.* **72**, 1878–86

395. Kim, S. a, Heinze, K. G., Waxham, M. N., and Schwille, P. (2004) Intracellular calmodulin availability accessed with two-photon cross-correlation. *Proc. Natl. Acad. Sci. U. S. A.* **101**, 105–10

396. Bacia, K., Kim, S. A., and Schwille, P. (2006) Fluorescence cross-correlation spectroscopy in living cells. *Nat. Methods.* **3**, 83–89

397. Bieschke, J., Giese, a, Schulz-Schaeffer, W., Zerr, I., Poser, S., Eigen, M., and Kretzschmar, H. (2000) Ultrasensitive detection of pathological prion protein aggregates by dual-color scanning for intensely fluorescent targets. *Proc. Natl. Acad. Sci. U. S. A.* **97**, 5468–73

398. Pitschke, M., Prior, R., Haupt, M., and Riesner, D. (1998) Detection of single amyloid β-protein aggregates in the cerebrospinal fluid of Alzheimer's patients by fluorescence correlation spectroscopy. *Nat. Med.* **4**, 832–834

399. Ohta, S., Kawai-Noma, S., Kitamura, A., Pack, C.-G., Kinjo, M., and Taguchi, H. (2013) The interaction of Hsp104 with yeast prion Sup35 as analyzed by fluorescence cross-correlation spectroscopy. *Biochem. Biophys. Res. Commun.* **442**, 28–32

400. Müller, J. D., Chen, Y., and Gratton, E. (2000) Resolving heterogeneity on the single molecular level with the photon-counting histogram. *Biophys. J.* **78**, 474–86

401. Ossato, G., Digman, M. a, Aiken, C., Lukacsovich, T., Marsh, J. L., and Gratton, E. (2010) A two-step path to inclusion formation of huntingtin peptides revealed by number and brightness analysis. *Biophys. J.* **98**, 3078–85

402. Zijlstra, N., Claessens, M. M. A. E., Blum, C., and Subramaniam, V. (2014) Elucidating the Aggregation Number of Dopamine-Induced α-Synuclein Oligomeric Assemblies. *Biophys. J.* **106**, 440–446

403. Sengupta, P., Garai, K., Balaji, J., Periasamy, N., and Maiti, S. (2003) Measuring size distribution in highly heterogeneous systems with fluorescence correlation spectroscopy. *Biophys. J.* **84**, 1977–1984

404. Garai, K., Sahoo, B., Kaushalya, S. K., Desai, R., and Maiti, S. (2007) Zinc Lowers Amyloid- Toxicity by Selectively Precipitating Aggregation. *Biochemistry*. **46**, 10655–10663

405. Garai, K., Sengupta, P., Sahoo, B., and Maiti, S. (2006) Selective destabilization of soluble amyloid beta oligomers by divalent metal ions. *Biochem. Biophys. Res. Commun.* **345**, 210–5

406. Sengupta, P., Garai, K., Sahoo, B., Shi, Y., Callaway, D. J. E., and Maiti, S. (2003) The Amyloid Beta Peptide (ABeta 1-40) Is Thermodynamically Soluble at Physiological Concentrations. *Biochemistry*. **42**, 10506–10513

407. Krichevsky, O., and Bonnet, G. (2002) Fluorescence correlation spectroscopy : the technique and its applications. *Reports Prog. Phys.* **65**, 251–297

408. Elson, E. L. (2013) *Brief introduction to fluorescence correlation spectroscopy.*, 1st Ed., Elsevier Inc., **518**, 11–41

409. Ladner, C. L., Chen, M., Smith, D. P., Platt, G. W., Radford, S. E., and Langen, R. (2010) Stacked sets of parallel, in-register beta-strands of β2-microglobulin in amyloid fibrils revealed by site-directed spin labeling and chemical labeling. *J. Biol. Chem.* **285**, 17137–17147

410. Doeven, M. K., Folgering, J. H. a, Krasnikov, V., Geertsma, E. R., van den Bogaart, G., and Poolman, B. (2005) Distribution, lateral mobility and function of membrane proteins incorporated into giant unilamellar vesicles. *Biophys. J.* **88**, 1134–42

411. Tang, G., Peng, L., Baldwin, P. R., Mann, D. S., Jiang, W., Rees, I., and Ludtke, S. J. (2007) EMAN2: an extensible image processing suite for electron microscopy. *J. Struct. Biol.* **157**, 38–46

412. Scheres, S. H. W. (2012) RELION: implementation of a Bayesian approach to cryo-EM structure determination. *J. Struct. Biol.* **180**, 519–30

413. Platt, G. W., Xue, W.-F., Homans, S. W., and Radford, S. E. (2009) Probing dynamics within amyloid fibrils using a novel capping method. *Angew. Chem. Int. Ed. Engl.* **48**, 5705–7

414. Wilkins, D. K., Grimshaw, S. B., Dobson, C. M., Jones, J. A., and Smith, L. J. (1999) Articles Hydrodynamic Radii of Native and Denatured Proteins Measured by Pulse Field Gradient NMR Techniques. *Biochemistry*

415. Kelly, S. M., Jess, T. J., and Price, N. C. (2005) How to study proteins by circular dichroism. *Biochim. Biophys. Acta*. **1751**, 119–139

416. Cardamone, M., and Puri, N. K. (1992) Spectrofluorimetric assessment of the surface hydrophobicity of proteins. *Biochem. J.* **282**, 589–93

417. Carulla, N., Zhou, M., Giralt, E., Robinson, C. V, and Dobson, C. M. (2010) Structure and intermolecular dynamics of aggregates populated during amyloid fibril formation studied by hydrogen/deuterium exchange. *Acc. Chem. Res.* **43**, 1072–9

418. Bitan, G., and Teplow, D. B. (2004) Rapid photochemical cross-linking--a new tool for studies of metastable, amyloidogenic protein assemblies. *Acc. Chem. Res.* **37**, 357–64

419. Fawzi, N. L., Ying, J., Ghirlando, R., Torchia, D. a, and Clore, G. M. (2011) Atomic-resolution dynamics on the surface of amyloid-β protofibrils probed by solution NMR. *Nature*. **480**, 268–272

420. Hellewell, A. L. (2011) *The cytotoxicity of amyloid fibrils*. Ph.D. thesis, Univeristy of Leeds

421. Pace, C. N., Grimsley, G. R., and Scholtz, J. M. (2009) Protein ionizable groups: pK values and their contribution to protein stability and solubility. *J. Biol. Chem.* **284**, 13285–9

422. Hansen, A. L., and Kay, L. E. (2014) Measurement of histidine pKa values and tautomer populations in invisible protein states. *Proc. Natl. Acad. Sci. U. S. A.* **111**, E1705–12

423. Walsh, D. M., Klyubin, I., Fadeeva, J. V, Cullen, W. K., Anwyl, R., Wolfe, M. S., Rowan, M. J., and Selkoe, D. J. (2002) Naturally secreted oligomers of amyloid beta protein potently inhibit hippocampal long-term potentiation in vivo. *Nature*. **416**, 535–539

424. Haglund, B. O., Sundelöf, L.-O., Upadrashta, S. M., and Wurster, D. E. (1996) Effect of SDS Micelles on Rhodamine-B Diffusion in Hydrogels. *J. Chem. Educ.* **73**, 889–893

425. Carulla, N., Zhou, M., Giralt, E., Robinson, C. V, and Dobson, C. M. (2010) Structure and intermolecular dynamics of aggregates populated during amyloid fibril formation studied by hydrogen/deuterium exchange. *Acc. Chem. Res.* **43**, 1072–9

426. Gosal, W. S., Morten, I. J., Hewitt, E. W., Smith, D. A., Thomson, N. H., and Radford, S. E. (2005) Competing pathways determine fibril morphology in the self-assembly of beta2-microglobulin into amyloid. *J. Mol. Biol.* **351**, 850–864

427. Chiti, F., De Lorenzi, E., Grossi, S., Mangione, P., Giorgetti, S., Caccialanza, G., Dobson, C. M., Merlini, G., Ramponi, G., and Bellotti, V. (2001) A partially structured species of beta 2-microglobulin is significantly populated under physiological conditions and involved in fibrillogenesis. *J. Biol. Chem.* **276**, 46714–46721

428. Colombo, M., de Rosa, M., Bellotti, V., Ricagno, S., and Bolognesi, M. (2012) A recurrent D-strand association interface is observed in β-2 microglobulin oligomers. *FEBS J.* **279**, 1131–1143

429. Domanska, K., Vanderhaegen, S., Srinivasan, V., Pardon, E., Dupeux, F., Marquez, J. a, Giorgetti, S., Stoppini, M., Wyns, L., Bellotti, V., and Steyaert, J. (2011) Atomic structure of a nanobody-trapped domain-swapped dimer of an amyloidogenic beta2-microglobulin variant. *Proc. Natl. Acad. Sci. U. S. A.* **108**, 1314–1319

430. Diomede, L., Soria, C., Romeo, M., Giorgetti, S., Marchese, L., Mangione, P. P., Porcari, R., Zorzoli, I., Salmona, M., Bellotti, V., and Stoppini, M. (2012) C. elegans

expressing human β2-microglobulin: a novel model for studying the relationship between the molecular assembly and the toxic phenotype. *PLoS One*. **7**, e52314

431. Jiang, L., Liu, C., Leibly, D., Landau, M., Zhao, M., Hughes, M. P., and Eisenberg, D. S. (2013) Structure-based discovery of fiber-binding compounds that reduce the cytotoxicity of amyloid beta. *Elife*. **2**, e00857

432. Coelho, T., Maia, L., Martins Da Silva, A., Waddington Cruz, M., Plante-Bordeneuve, V., and Lozeron, P. (2011) A comprehensive evaluation of the disease-modifying effects of tafimidis in patients with transthyretin type familial amyloid polyneuropathy. *Neurology*. **76**, A111 supplement 4

433. Verdone, G., Corazza, A., Viglino, P., Pettirossi, F., Giorgetti, S., Mangione, P., Andreola, A., Stoppini, M., Bellotti, V., and Esposito, G. (2002) The solution structure of human beta-2-microglobulin reveals the prodromes of its amyloid transition. *Protein Sci.* **11**, 487–499

434. Jahn, T. R., and Radford, S. E. (2005) *Amyloid Proteins: The Beta Sheet Conformation and Diseases*

435. http://www.olympusmicro.com/primer/java/jablonski/jabintro/